

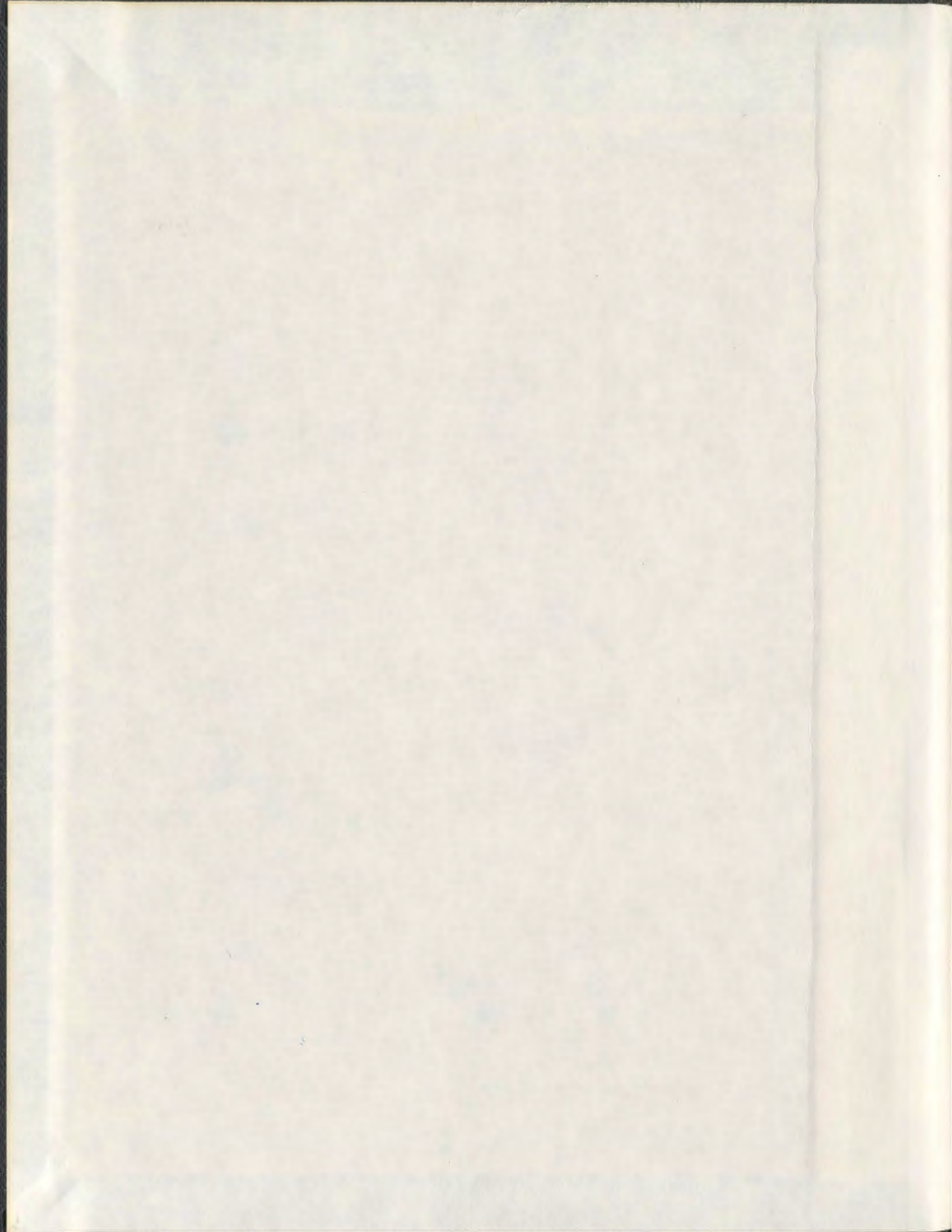
**FAILURE MECHANISMS OF SUCTION CAISSON
FOUNDATIONS IN CLAY UNDER VERTICAL AND
INCLINED PULLOUT LOADS**

CENTRE FOR NEWFOUNDLAND STUDIES

**TOTAL OF 10 PAGES ONLY
MAY BE XEROXED**

(Without Author's Permission)

HANDAYANU



001311



INFORMATION TO USERS

This manuscript has been reproduced from the microfilm master. UMI films the text directly from the original or copy submitted. Thus, some thesis and dissertation copies are in typewriter face, while others may be from any type of computer printer.

The quality of this reproduction is dependent upon the quality of the copy submitted. Broken or indistinct print, colored or poor quality illustrations and photographs, print bleedthrough, substandard margins, and improper alignment can adversely affect reproduction.

In the unlikely event that the author did not send UMI a complete manuscript and there are missing pages, these will be noted. Also, if unauthorized copyright material had to be removed, a note will indicate the deletion.

Oversize materials (e.g., maps, drawings, charts) are reproduced by sectioning the original, beginning at the upper left-hand corner and continuing from left to right in equal sections with small overlaps.

**ProQuest Information and Learning
300 North Zeeb Road, Ann Arbor, MI 48106-1346 USA
800-521-0600**

UMI[®]

NOTE TO USERS

Page(s) not included in the original manuscript are unavailable from the author or university. The manuscript was microfilmed as received.

100, 199, 297

This reproduction is the best copy available.

UMI[®]



**National Library
of Canada**

**Acquisitions and
Bibliographic Services**

**395 Wellington Street
Ottawa ON K1A 0N4
Canada**

**Bibliothèque nationale
du Canada**

**Acquisitions et
services bibliographiques**

**395, rue Wellington
Ottawa ON K1A 0N4
Canada**

Your file *Votre référence*

Our file *Notre référence*

The author has granted a non-exclusive licence allowing the National Library of Canada to reproduce, loan, distribute or sell copies of this thesis in microform, paper or electronic formats.

The author retains ownership of the copyright in this thesis. Neither the thesis nor substantial extracts from it may be printed or otherwise reproduced without the author's permission.

L'auteur a accordé une licence non exclusive permettant à la Bibliothèque nationale du Canada de reproduire, prêter, distribuer ou vendre des copies de cette thèse sous la forme de microfiche/film, de reproduction sur papier ou sur format électronique.

L'auteur conserve la propriété du droit d'auteur qui protège cette thèse. Ni la thèse ni des extraits substantiels de celle-ci ne doivent être imprimés ou autrement reproduits sans son autorisation.

0-612-73547-8

Canada

Failure Mechanisms of Suction Caisson Foundations in Clay Under Vertical and Inclined Pullout Loads

By

©Handayanu

**A thesis submitted to the
School of Graduate Studies
in partial fulfilment of the
requirements for the degree of
Doctor of Philosophy**

**Faculty of Engineering and Applied Science
Memorial University of Newfoundland**

November, 2001

St. John's

Newfoundland

Abstract

A suction caisson typically consists of a hollow cylinder or a cluster of cylinders made of steel or concrete with a closed top. This novel foundation consists of massive cells, typically 10 to 30 meters in diameter and up to 40 to 50 meters deep. The caissons will form a tight seal with the soft submarine sediments, and provide the necessary uplift resistance, when pressure reduction is created below the closed top. In this study, finite element method was used to investigate the development of suction force, based on D'Arcy's law, by implementing some user subroutines provided in ABAQUS. Contact between suction caisson and soil surface was simulated using a contact surface model. Soil material was modelled as a porous medium and its plastic behaviour was characterized using a modified camclay model.

The study to validate the results of the above numerical analysis used four laboratory tests carried out in different locations, for different purposes and with different set-ups. The test data used are the Massachusetts Institute of Technology (MIT) suction caisson tests [Cauble, 1997], University of Texas at Austin suction caisson tests [El-Gharbawy, 1998], Indian Institute of Technology (IIT) Madras (India) friction single pile tests [Prasad, 1992], and suction caisson tests [Rao et al., 1997]. All these tests gave a total of twenty-nine experimental results to validate results from finite element analyses. In addition, scale model analyses for 1g, ng, and prototype models were also carried out. Failure patterns observed in soil were modelled by relevant soil failure models available in literature. Moreover, comparison of 3D and axisymmetric-asymmetric analyses for inclined pullout loads with different inclination angle and anchor point attachments, were also carried out.

Suction pressure generation in suction caisson model finite element analyses consistently gave close matches with results obtained from laboratory vertical pullout tests carried out at MIT, University of Texas at Austin, and IIT Madras. Suction pressure development, carried out in this study, simulated the suction force or pressure (built up below the caisson top) properly, and the difference between good numerical and experimental results ranging between 0.3% to 7% (based on suction force) for the MIT tests, 10% to 20% (based on suction pressure) for the Texas tests, and 22.7% to 26% for the IIT Madras tests by Rao et al. However, less accurate results ranged from 27% to 70%.

The finite element models gave a stiffer displacement response and as such did not match very well with some (especially University of Texas) of the experimental measurements.

Based on the combined contours of shear stress to shear strength ratios (based on direct shear tests and triaxial extension tests) under vertical and inclined pullout loads, failure surfaces similar to the failure surfaces obtained for the Snorre suction caisson model pullout tests (carried out by the Norwegian Geotechnical Institute [Andersen et al., 1993]) were obtained in this study.

Acknowledgements

I am deeply indebted to my supervisor, Dr. A. Swamidas, for his patient and kind supervision, and consistent encouragement during the course of this study. I would also like to express my thanks to him for the financial support (towards my fees) during the later periods of my study here at Memorial, when my main financial support was over. I would also like to thank other members of my supervisory committee, Dr. K. Munaswamy and Dr. M. Booton, for the time they spent on reading my proposal and thesis as well as suggestions they made for the revision.

The computer and software support by the Centre of Computer Aided Engineering (CCAЕ), Faculty of Engineering and Applied Science is gratefully acknowledged.

The financial support for this work was provided by the Indonesian Government through the HEP project and is gratefully acknowledged.

A special word of thanks is due to my colleagues and friends who helped me during my study.

Finally, I would like to express my thanks to my dear wife Dinik Prasetiasih and my son Arief Handi Putra for their support and patience, to whom I am dedicating this work.

Table of Contents

Abstract	ii
Acknowledgements.....	iii
Table of Contents	iv
List of Tables.....	viii
List of Figures	x
List of Abbreviations and Symbols.....	xviii
Chapter 1: Introduction.....	1
1.1. General	1
1.2. Offshore Anchoring Systems	3
1.3. Definition of Suction Foundation	4
1.4. Relevance of Suction Anchors.....	5
1.5. Interaction with environment.....	7
1.6. Thesis Objectives and Scope.....	8
1.7. Organization.....	10
Chapter 2 Literature Review: Suction Anchor for Offshore Structures	12
2.1. Introduction.....	12
2.2. Suction Anchor for Offshore Application.....	12
2.3. Large Scale Field Tests on Suction Anchor.....	16
2.4. Laboratory Model Studies on Suction Anchor	21
2.4.1. <i>1g Model Tests</i>	21
2.4.2. <i>Centrifuge model Tests</i>	32
2.5. Analytical Studies on Suction Anchor Foundations.....	35
2.5.1. <i>Use of Semi-empirical Formulation</i>	35
2.5.2. <i>Numerical/Finite Element Analyses</i>	43
2.6. Definition of Soil as a Multi-Phase Medium	47
2.6.1. <i>Mechanics of Porous Media</i>	47
2.6.2. <i>Soil Constitutive Models</i>	50
2.7. Summary	55
Chapter 3 Theoretical Foundations: Analytical Procedure, Model Characterization and Data Interpretation	58
3.1. Introduction.....	58
3.2. Methodology	59
3.3. General Formulation for the Governing Equation of Porous Media	60

3.3.1. General Formulation for Static and Dynamic Response of Soil as a Porous Media	60
3.3.2. ABAQUS Formulation for Static and Dynamic Response of Soil as a Porous Media using Axisymmetric Elements Allowing Asymmetric Deformation in ABAQUS	72
Interpolation	72
Deformation Gradient and Increments in Strain and Rotation	76
Virtual work	78
Pressure Loads and Load Stiffness	80
Pore Pressure Elements in Hybrid Formulation	84
3.3.3. Plasticity Models in ABAQUS	85
3.3.4. Process of Integration in Plasticity Models	89
3.3.5. Critical State Models	95
3.4. Effect of Parameter β and K in Cam Clay Model	106
3.5. Contact Surface	110
3.6. Suction Force Generation	112
3.7. Failure Mode Identification	116
3.8. Model to Prototype Relationships	117
3.8.1. 1g Model to Prototype Relationships	118
3.8.2. ng Model to Prototype Relationships	119
3.9. Skempton's Soil Strength Criteria	120
3.10. Summary	121

Chapter 4 Comparison Of Numerical Results With Experimental Data from 1g Models..... 123

4.1. Introduction	123
4.2. Massachusetts Institute of Technology Tests [Cauble, 1997]	123
4.2.1. Test Geometry and Instrumentation	124
4.2.2. Test Loading Schedule	125
4.2.3. Test Quality	127
4.2.4. Soil Properties	127
4.2.5. Monotonic Pullout Test Results	131
4.3. Tests at University of Texas at Austin [El-Gharbawy, 1998]	132
4.3.1. Test Geometry and Instrumentation	133
4.3.2. Test Loading Schedule	133
4.3.3. Soil Properties	134
4.3.4. Monotonic Pullout Test Results	135
4.4. Indian Institute of Technology (IIT), Madras (India) Tests [Prasad, 1992]	137
4.4.1. Test Geometry and Instrumentation	137
4.4.2. Test Loading Schedule	137
4.4.3. Soil Properties	138
4.4.4. Monotonic Pullout Test Results	138
4.5. IIT Madras (India) Tests [Rao et al, 1997]	140
4.5.1. Test Geometry and Instrumentation	140
4.5.2. Test Loading Schedule	141

4.5.3. <i>Soil Properties</i>	141
4.5.4. <i>Monotonic Pullout Test Results</i>	142
4.6. Results from Finite Element Analyses	144
4.6.1. <i>Results of MIT Model Tests</i>	145
4.6.2. <i>Results of University of Texas at Austin Model Tests</i>	155
4.6.3. <i>Results of IIT Madras Model Tests [Prasad, 1992]</i>	165
4.6.4. <i>Results of IIT Madras Model Tests [Rao et al, 1997]</i>	170
4.7. Summary	178
Chapter 5 Scale Models and Failure Mode Analysis	180
5.1. Introduction.....	180
5.2. Scale Model Analysis.....	181
5.2.1. <i>1g Model Analysis</i>	183
5.2.2. <i>Prototype Analysis</i>	187
5.2.3. <i>ng Model Analysis</i>	194
5.3. Failure Modes Analysis	199
5.4. Summary	213
Chapter 6 Suction Caisson Subjected to Inclined Pullout Loading using Two-Dimensional and Three-Dimensional Analyses	215
6.1. Introduction.....	215
6.2. Comparison of Results from Axisymmetric (with Asymmetric Loading) and Three-Dimensional Finite Element Models.....	216
6.3. Summary	226
Chapter 7 Suction Caisson Under Inclined Pullout Load: Effect of Pullout Anchor Inclination and Location.....	228
7.1. Introduction.....	228
7.2. Axisymmetric Model	228
7.2.1. <i>Model Definition</i>	228
7.2.2. <i>Pullout Scenarios</i>	229
7.2.3. <i>Presentation and Discussion of Results</i>	231
7.3. Failure Behaviour of Suction Caisson System under Inclined Pullout Loads based on Shear Stress to Shear Strength ratios	243
7.4. Summary	255
Chapter 8 Conclusions and Recommendations	257
8.1 Overview of Study.....	257
8.2 Findings and Conclusions	260
8.3 Recommendations for future work.....	264
References	266
Appendix A1 Subroutines used for suction force generation.....	282
Appendix A2 MIT Models Analyses Results [Cauble, 1997]	287

Appendix A3 Results from Analyses of Texas Models [El-Gharbawy, 1998].....	299
Appendix A4 Results from Analyses of Indian Institute of Technology (IIT) Models [Prasad, 1992]	306
Appendix A5 Results of Analyses of Indian Institute of Technology (IIT) Models [Rao et al., 1997]	310

List of Tables

Table 3.1. Scaling relations [Scott, 1979]	120
Table 4.2.1. Tests loading schedule of MIT laboratory tests	126
Table 4.2.2 Quality assessment for individual test control and instrumentation [Cauble, 1997]	127
Table 4.2.3 Test results from MIT laboratory tests	132
Table 4.3.1 Short-term pullout (undrained loading).....	134
Table 4.3.2 Long-term pullout (drained loading).....	134
Table 4.3.3. Consolidation and shearing stress parameters of test soil [El-Gharbawy, 1998]	135
Table 4.3.4. Short-term pullout (undrained loading) test results.....	136
Table 4.3.5. Long-term pullout (drained loading) test results.....	136
Table 4.4.1. Index properties of soil sample	138
Table 4.4.2 Test results of single friction pile.....	139
Table 4.5.1. Properties of soil sample [Rao et al. 1997]	141
Table 4.6.1 Finite element analysis results of MIT model tests.....	148
Table 4.6.2 Components in Christensen's equation for test data	153
Table 4.6.3 Components in Christensen's equation for analysis data.....	153
Table 4.6.4 Ratio of components in Christensen's equation between laboratory tests and finite element analyses results	155
Table 4.6.5 Short term pullout (undrained loading) analysis results.....	158
Table 4.6.6 Long-term pullout (drained loading) analysis results	158
Table 4.6.7 Components in Christensen's equation for undrained tests data.....	162
Table 4.6.8 Components in Christensen's equation for undrained analyses data	163
Table 4.6.9 Ratio of components in Christensen's equation between laboratory tests and finite element analysis results for undrained loading	163
Table 4.6.10 Bulk and swelling moduli coefficients.....	166
Table 4.6.11 Results from finite element analysis (Laboratory test values)	167
Table 4.6.12 Bulk and swelling moduli coefficients.....	170
Table 4.6.13 Results from finite element analysis (laboratory test values)	171
Table 4.6.14 Components in Christensen's equation for tests data.....	176
Table 4.6.15 Components in Christensen's equation for analyses data	177
Table 4.6.16 Ratio of components in Christensen's equation between laboratory tests and finite element analysis results	177
Table 5.2.1 Salient system properties for 1g small model	183
Table 5.2.2 Scale value from 1g small model to prototype.....	187
Table 5.2.3 Salient system properties for prototype.....	188
Table 5.2.4 Expected and actual force values obtained for the prototype.....	190
Table 5.2.5 Salient system properties for ng scale model	196
Table 5.2.6 Expected force values for the prototype from the ng	199

Table 5.2.7 Suction pressure (at the inside top) at maximum pullout capacity	199
Table 5.3.1 Procedure for identifying failure modes.....	202
Table 6.2.1 Force components comparison between two and four Fourier components of axisymmetric models, and 3D-model	219
Table 7.2.1 Salient soil properties for RBBC.....	229
Table A.2.1. Tests loading schedule of MIT laboratory tests	288
Table A.2.2 Finite element analysis results of MIT model tests.....	289
Table A.3.1 Short-term pullout (undrained loading).....	299
Table A.3.2 Long-term pullout (drained loading).....	299
Table A.3.3 Short term pullout (undrained loading) analysis results.....	300
Table A.3.4 Long-term pullout (drained loading) analysis results.....	301
Table A.4.1 Results from finite element analyses (Laboratory test values).....	306
Table A.5.1 Results from finite element analyses (laboratory test values).....	311

List of Figures

Figure 1.4.1 Sketch of Snorre Tension Leg Platform (TLP) system [Støve et al., 1992] ...	5
Figure 1.4.2 Suction caissons installed in the North Sea for Snorre TLP. [Støve et al., 1992].....	7
Figure 2.4.1 Schematic of a hydrostatic caisson [Brown and Nacci, 1971].....	23
Figure 2.4.2 Test setup of MIT suction foundation studies [Cauble, 1997]	30
Figure 2.4.3 Typical suction foundation geometry of University of Texas (Austin) tests [El-Gharbawy, 1998]	31
Figure 2.5.1 Definition of notations for the suction pile [Christensen et al, 1991].....	36
Figure 2.5.2 Failure mechanism #1, for clay [Christensen et al. 1991].	38
Figure 2.5.3 Failure mechanism #2, for clay [Christensen et al, 1991]	39
Figure 2.5.4 Failure mechanism #3, for clay [Christensen et al, 1991]	39
Figure 3.3.1 Total and effective stresses in soil [Lewis & Schrefler, 1987]	61
Figure 3.3.2 Axisymmetric 8-node quadratic with reduced integration points element [HKS, 1998]	73
Figure 3.3.3 Displacement and rotation in r- θ plane [HKS, 1998]	75
Figure 3.3.4 Tangent elastic matrix for displacement update process [HKS, 1998].....	92
Figure 3.3.5 Cam-clay yield and critical state surfaces in principle stress space [HKS, 1998]	95
Figure 3.3.6a Shear test response on the dry side of critical state ($t > M_p$) [HKS, 1998].....	103
Figure 3.3.6b Shear test response on the dry side of critical state ($t > M_p$) [HKS, 1998].....	103
Figure 3.3.7a Shear test response on the dry side of critical state ($t < M_p$) [HKS, 1998].....	104
Figure 3.3.7b Shear test response on the dry side of critical state ($t < M_p$) [HKS, 1998].....	104
Figure 3.3.8 Cam-clay yield surface in p-q plane [HKS, 1998].....	105
Figure 3.3.9 Cam-clay surfaces in the deviatoric plane [HKS, 1998]	105
Figure 3.4.1 MIT suction caisson foundation model mesh	107
Figure 3.4.2 Force–displacement curve of MIT test model with $K = 1$ and $\beta = 1$	107
Figure 3.4.3 Force–displacement curve of MIT test model with $K = 0.78$ and $\beta = 1$	108
Figure 3.4.4 Force–displacement curve of MIT test model with $K = 0.78$ and $\beta = 0.9$..	109
Figure 3.4.5 Force–displacement curve of MIT test model with $K = 0.78$ and $\beta = 0.8$..	109
Figure 3.4.6 Stress state of element 49 and 344 in p-q plane.....	110
Figure 3.5.1 Contact surface model defined by a pair of master surface (BSURF) and slave surface (ASURF) [ABAQUS, 1998].....	112
Figure 3.5.2 Contact surface model defined by a pair of slide line element (ISL element) and nodes at master surface (slide line) [ABAQUS, 1998].....	113
Figure 3.6.1 Flowchart of suction force generation.	115
Figure 4.4.1. Pullout tests of single pile, dia. = 13.8 mm, IIT Madras [Prasad, 1992] ...	139
Figure 4.4.2. Pullout tests of single pile, dia. = 18.0 mm, IIT Madras [Prasad, 1992] ..	140

Figure 4.5.1. Pullout load – displacement curve of suction anchor, LI = 0.6 [Rao et al. 1997]	142
Figure 4.5.2. Variation of ultimate pullout load with liquidity index (LI) [Rao et al. 1997]	143
Figure 4.5.3. Variation of suction pressure with deformation for different L/D ratio [Rao et al, 1997]	143
Figure 4.5.4. Influence of soil consistency on suction pressure. L/D = 2 [Rao et al, 1997].	144
Figure 4.6.1 MIT suction caisson foundation model mesh	147
Figure 4.6.2. Total force-displacement curves of laboratory test results (CET3) and FEM analysis results.....	149
Figure 4.6.3. Wall force-displacement curves of laboratory test results (CET3) and FEM analysis results.....	150
Figure 4.6.4. Suction force-displacement curves of laboratory test results (CET3) and FEM analysis results.....	151
Figure 4.6.5 University of Texas suction foundation model mesh for L/D = 6.	157
Figure 4.6.6. Force-displacement curve of STCC2 for undrained loading	160
Figure 4.6.7. Displacement-time curve of STCC2 for drained loading (at caisson head top center)	161
Figure 4.6.8 IIT suction foundation model mesh for L/D = 25. D = 13.8 mm.	167
Figure 4.6.9 Force-displacement curve of single pile pullout test, Dia.: 13.8 mm. L/D = 25. IIT Madras model.	168
Figure 4.6.10 Force-displacement curve of single pile pullout test, Dia.: 18.0 mm. L/D = 15. IIT Madras model.	169
Figure 4.6.11 IIT suction foundation model mesh for L/D = 1, D = 75 mm.	172
Figure 4.6.12 Pullout load–displacement curve, for L/D = 1, LI = 0.6	173
Figure 4.6.13 Suction pressure–displacement curve, for L/D = 1, LI = 0.6	174
Figure 4.6.14 Pullout capacity–liquidity index (LI) curve, for L/D = 1	175
Figure 5.2.1 1g Finite Element Model Mesh.....	182
Figure 5.2.2 Prototype Finite Element Model Mesh.....	182
Figure 5.2.3 Horizontal stress state acting on the walls of 1g model.....	185
Figure 5.2.4 Pullout Forces of 1g model.....	186
Figure 5.2.5 Contour of shear stress state at maximum pullout capacity of 1g model ...	186
Figure 5.2.6 Contour of pore pressure distribution at maximum pullout capacity of 1g model	187
Figure 5.2.7 Horizontal stress state of prototype structure.....	190
Figure 5.2.8 Pullout forces of prototype with no decay in fluid velocity.....	191
Figure 5.2.9 Contour of shear stress state at maximum pullout capacity of prototype with no decay in fluid velocity	191
Figure 5.2.10 Contour of pore pressure distribution at maximum pullout capacity of prototype with no decay in fluid velocity.....	192
Figure 5.2.11 Pullout forces of prototype with decay in fluid velocity.....	192
Figure 5.2.12 Contour of shear stress state at maximum pullout capacity of prototype with decay in fluid velocity	193

Figure 5.2.13 Contour of pore pressure distribution at maximum pullout capacity of prototype with decay in fluid velocity	193
Figure 5.2.14 Horizontal stress state of ng model	195
Figure 5.2.15 Pullout forces of ng model.....	196
Figure 5.2.16 Contour of shear stress state at maximum pullout capacity of ng model .	197
Figure 5.2.17 Contour of pore pressure distribution at maximum pullout capacity of ng model	197
Figure 5.3.1 Contours of shear stress to shear strength ratio based on direct simple shear tests of the model with $L/D = 0.4$ at peak pullout capacity (step = 3, increment = 25). Failure between the wall and soil has begun to occur on the inside wall of caisson, but has not occurred on the outside wall.....	204
Figure 5.3.2 Contours of shear stress to shear strength ratio based on triaxial tests of the model with $L/D = 0.4$ at peak pullout capacity (step = 3, increment = 25). Conditions favourable to extensional shear failure occurs on the outside of suction caisson wall, but not on the inside	204
Figure 5.3.3 Contours of shear stress to shear strength ratio based on direct simple shear tests of the model with $L/D = 0.4$ at failure (step = 3, increment = 57). Failure has not occurred between the outside wall of caisson and the soil (except at some local points). It is almost at the final failure stage due to direct shear on the inside wall of caisson.	205
Figure 5.3.4 Contours of shear stress to shear strength ratio based on triaxial tests of the model with $L/D = 0.4$ at failure (step = 3, increment = 57). Conditions favourable to extensional shear failure occur over the outside and inside of caisson walls: possible tensile failure also occurs at the caisson bottom soon after the occurrence of above shear failure.	205
Figure 5.3.5 Load-displacement curve of $L/D = 0.4$ model. Units: Force (N), Displacement (cm).....	206
Figure 5.3.6 Contours of shear stress to shear strength ratio based on direct simple shear tests of the model with $L/D = 1$, at peak pullout capacity (step = 3, increment = 45). Direct shear failure is progressing along the outside caisson wall, but it is not developing on the inside wall at all.	207
Figure 5.3.7 Contours of shear stress to shear strength ratio based on triaxial tests of the model with $L/D = 1$, at peak pullout capacity (step = 3, increment = 48). Extensional shear failure conditions have developed almost over the whole length of outside caisson wall, but have not developed at all on the inside or at the base.....	208
Figure 5.3.8 Contours of shear stress to shear strength ratio based on direct simple shear tests of the model with $L/D = 1$, at failure (step = 3, increment = 48). Direct simple shear failure conditions have developed almost along the whole length of the caisson outside wall, but have not developed at all on the inside.....	208

Figure 5.3.9	Contours of shear stress to shear strength ratio based on triaxial tests of the model with $L/D = 1$, at failure (step = 3, increment = 48). Extensional shear failure conditions occur almost along the whole cross sectional area of suction caisson at its base, along with general shear failure conditions on the outside wall.....	209
Figure 5.3.10	Load-displacement curve of $L/D = 1.0$ model. Units: Force (N), Displacement (cm).....	209
Figure 5.3.11	Contours of shear stress to shear strength ratio based on direct simple shear tests of the model with $L/D = 2.1$ at peak pullout capacity (step = 3, increment = 253). Conditions favourable to direct simple shear failure occur over almost the whole length of caisson outside wall, but do not occur on the inside. Also failure occurs resulting from direct shear stresses at the base of the caisson foundation.....	211
Figure 5.3.12	Contours of shear stress to shear strength ratio based on triaxial tests of the model with $L/D = 2.1$, at peak pullout capacity (step = 3, increment = 253). Conditions favourable to extensional shear failure occur along the base of suction caisson showing that tensile failure has occurred at the base. In addition, extensional shear failure seems to be occurring in the soil surrounding the suction caisson outside wall.	211
Figure 5.3.13	Contours of shear stress to shear strength ratio based on direct simple shear tests of the model with $L/D = 2.1$, at failure (step = 3, increment = 97). Conditions favourable to direct simple shear failure occur along most of the outside wall; not along the inside wall. Also the shear stress contour has become greater than one along the base of the foundation showing tension failure resulting from shear.	212
Figure 5.3.14	Contour of shear stress to shear strength ratio based on triaxial tests of the model with $L/D = 2.1$, at failure (step = 3, increment = 97). Conditions favourable to extensional shear failure occur in the soil body at the base of suction caisson and around the caisson wall. Hence it is a combination of tension and general shear failure scenarios.	212
Figure 5.3.15	Load-displacement curve of $L/D = 2.1$ model. Units: Force (N), Displacement (cm).....	213
Figure 6.2.1	Force-displacement curve of total forces component from axisymmetric and 3-D model	220
Figure 6.2.2	Force-displacement curve of wall force component from axisymmetric and 3-D model	221
Figure 6.2.3	Force-displacement curve of suction force component from axisymmetric and 3-D model	222
Figure 6.2.4	Shear stress to shear strength ratio contour based on DSS test, cross section of three-dimensional model.....	223
Figure 6.2.5	Shear stress to shear strength ratio contour based on TE test, cross section of three-dimensional model.....	223
Figure 6.2.6	Shear stress to shear strength ratio contour based on DSS test, cross section of axisymmetric model.....	224

Figure 6.2.7 Shear stress to shear strength ratio contour based on TE test, cross section of axisymmetric model.....	224
Figure 6.2.8 Pore pressure contour, cross section view of three-dimensional model	225
Figure 6.2.9 Pore pressure contour, cross section of axisymmetric model	225
Figure 7.2.1 Mesh and pullout scenario for the three different anchor points	230
Figure 7.2.2 Total resistance-displacement curve at 0.02 m anchor point below the soil surface.....	234
Figure 7.2.3 Total resistance-displacement curve at 0.025 m anchor point below the soil surface.....	235
Figure 7.2.4 Total resistance-displacement curve at 0.038 m anchor point below the soil surface.....	236
Figure 7.2.5 Wall resistance-displacement curve at 0.02 m anchor point below the soil surface.....	237
Figure 7.2.6 Wall resistance-displacement curve at 0.025 m anchor point below the soil surface.....	238
Figure 7.2.7 Wall resistance-displacement curve at 0.038 m anchor point below the soil surface.....	239
Figure 7.2.8 Suction resistance-displacement curve at 0.02 m anchor point below the soil surface.....	240
Figure 7.2.9 Suction resistance-displacement curve at 0.025 m anchor point below the soil surface.....	241
Figure 7.2.10 Suction resistance-displacement curve at 0.038 m anchor point below the soil surface.....	242
Figure 7.2.11 Plate anchor in clay	243
Figure 7.3.1 Contour of ratio of shear stress to shear strength based on DSS test of pullout with inclined angle of 5° and anchor point at 0.02 m below the soil surface.....	245
Figure 7.3.2 Contour of ratio of shear stress to shear strength based on TE test of pullout with inclined angle of 5° and anchor point at 0.02 m below the soil surface.....	245
Figure 7.3.3 Contour of ratio of shear stress to shear strength based on DSS test of pullout with inclined angle of 20° and anchor point at 0.02 m below the soil surface.....	246
Figure 7.3.4 Contour of ratio of shear stress to shear strength based on TE test of pullout with inclined angle of 20° and anchor point at 0.02 m below the soil surface.....	246
Figure 7.3.5 Contour of ratio of shear stress to shear strength based on DSS test of pullout with inclined angle of 60° and anchor point at 0.02 m below the soil surface.....	247
Figure 7.3.6 Contour of ratio of shear stress to shear strength based on TE test of pullout with inclined angle of 60° and anchor point at 0.02 m below the soil surface.....	247
Figure 7.3.7 Contour of ratio of shear stress to shear strength based on DSS test of pullout with inclined angle of 5° and anchor point at 0.025 m below the soil surface.....	248

Figure 7.3.8 Contour of ratio of shear stress to shear strength based on TE test of pullout with inclined angle of 5° and anchor point at 0.025 m below the soil surface.....	248
Figure 7.3.9 Contour of ratio of shear stress to shear strength based on DSS test of pullout with inclined angle of 20° and anchor point at 0.025 m below the soil surface.....	249
Figure 7.3.10 Contour of ratio of shear stress to shear strength based on TE test of pullout with inclined angle of 20° and anchor point at 0.025 m below the soil surface.....	249
Figure 7.3.11 Contour of ratio of shear stress to shear strength based on DSS test of pullout with inclined angle of 60° and anchor point at 0.025 m below the soil surface.....	250
Figure 7.3.12 Contour of ratio of shear stress to shear strength based on TE test of pullout with inclined angle of 60° and anchor point at 0.025 m below the soil surface.....	250
Figure 7.3.13 Contour of ratio of shear stress to shear strength based on DSS test of pullout with inclined angle of 5° and anchor point at 0.038 m below the soil surface.....	251
Figure 7.3.14 Contour of ratio of shear stress to shear strength based on TE test of pullout with inclined angle of 5° and anchor point at 0.038 m below the soil surface.....	251
Figure 7.3.15 Contour of ratio of shear stress to shear strength based on DSS test of pullout with inclined angle of 20° and anchor point at 0.038 m below the soil surface.....	252
Figure 7.3.16 Contour of ratio of shear stress to shear strength based on TE test of pullout with inclined angle of 20° and anchor point at 0.038 m below the soil surface.....	252
Figure 7.3.17 Contour of ratio of shear stress to shear strength based on DSS test of pullout with inclined angle of 60° and anchor point at 0.038 m below the soil surface.....	253
Figure 7.3.18 Contour of ratio of shear stress to shear strength based on TE test of pullout with inclined angle of 60° and anchor point at 0.038 m below the soil surface.....	253
Figure 7.3.19 Contour of ratio of shear stress to shear strength based on DSS test of pullout with inclined angle of 90° and anchor point at 0.038 m below the soil surface.....	254
Figure 7.3.20 Contour of ratio of shear stress to shear strength based on TE test of pullout with inclined angle of 90° and anchor point at 0.038 m below the soil surface.....	254
Figure 7.3.21 Failure surface of Snorre suction caisson [Andersen et al, 1993].....	255
Figure A.2.1 Total force-displacement curves of laboratory test results (CET3) and FEM analysis results.....	290
Figure A.2.2 Wall force-displacement curves of laboratory test results (CET3) and FEM analysis results.....	290

Figure A.2.3 Suction force-displacement curves of laboratory test results (CET3) and FEM analysis results.....	291
Figure A.2.4 Total force-displacement curves of laboratory test results (CET4) and FEM analysis results.....	291
Figure A.2.5 Wall force-displacement curves of laboratory test results (CET4) and FEM analysis results.....	292
Figure A.2.6 Suction force-displacement curves of laboratory test results (CET4) and FEM analysis results.....	292
Figure A.2.7 Total force-displacement curves of laboratory test results (CET5) and FEM analysis results.....	293
Figure A.2.8 Wall force-displacement curves of laboratory test results (CET5) and FEM analysis results.....	293
Figure A.2.9 Suction force-displacement curves of laboratory test results (CET5) and FEM analysis results.....	294
Figure A.2.10 Total force-displacement curves of laboratory test results (CET6) and FEM analysis results.....	294
Figure A.2.11 Wall force-displacement curves of laboratory test results (CET6) and FEM analysis results.....	295
Figure A.2.12 Suction force-displacement curves of laboratory test results (CET6) and FEM analysis results.....	295
Figure A.2.13 Total force-displacement curves of laboratory test results (CET7) and FEM analysis results.....	296
Figure A.2.14 Wall force-displacement curves of laboratory test results (CET7) and FEM analysis results.....	296
Figure A.2.15 Suction force-displacement curves of laboratory test results (CET7) and FEM analysis results.....	297
Figure A.2.16 Total force-displacement curves of laboratory test results (CET8) and FEM analysis results.....	297
Figure A.2.17 Wall force-displacement curves of laboratory test results (CET8) and FEM analysis results.....	298
Figure A.2.18 Suction force-displacement curves of laboratory test results (CET8) and FEM analysis results.....	298
Figure A.3.1 Force-displacement curve of STCC2 for undrained loading	302
Figure A.3.2 Force-displacement curve of STCC4 for undrained loading	302
Figure A.3.3 Force-displacement curve of STCC6 for undrained loading	303
Figure A.3.4 Force-displacement curve of STCC12 for undrained loading	303
Figure A.3.5 Displacement-time curve of STCC2 for drained loading (at caisson head top center)	304
Figure A.3.6 Displacement-time curve of STCC4 for drained loading (at caisson head top center)	304
Figure A.3.7 Displacement-time curve of STCC4 for drained loading (at caisson head top center)	305
Figure A.3.8 Displacement-time curve of STCC4 for drained loading (at caisson head top center)	305

Figure A.4.1 Force-displacement curve of single pile pullout test. Dia.: 13.8 mm, L/D = 15, IIT Madras model.	307
Figure A.4.2 Force-displacement curve of single pile pullout test, Dia.: 13.8 mm. L/D = 25, IIT Madras model.	307
Figure A.4.3 Force-displacement curve of single pile pullout test. Dia.: 13.8 mm. L/D = 40, IIT Madras model.	308
Figure A.4.4 Force-displacement curve of single pile pullout test. Dia.: 18.0 mm, L/D = 15, IIT Madras model.	308
Figure A.4.5 Force-displacement curve of single pile pullout test. Dia.: 18.0 mm, L/D = 25, IIT Madras model.	309
Figure A.4.6 Force-displacement curve of single pile pullout test, Dia.: 18.0 mm. L/D = 40, IIT Madras model.	309
Figure A.5.1 Pullout load–displacement curve. for L/D = 1, LI = 0.6	311
Figure A.5.2 Suction pressure–displacement curve, for L/D = 1, LI = 0.6	312
Figure A.5.3 Pullout load–displacement curve. for L/D = 1.5, LI = 0.6	312
Figure A.5.4 Suction pressure–displacement curve. for L/D = 1.5, LI = 0.6	313
Figure A.5.5 Pullout load–displacement curve, for L/D = 2, LI = 0.6	313
Figure A.5.6 Suction pressure–displacement curve, for L/D = 2, LI = 0.6	314
Figure A.5.7 Pullout load–displacement curves obtained from analyses, for LI = 0.8 ..	314
Figure A.5.8 Pullout load–displacement curves obtained from analyses. for LI = 0.6 ..	315
Figure A.5.9 Pullout load–displacement curves obtained from analyses, for LI = 0.4 ..	315
Figure A.5.10 Suction pressure–displacement curves obtained from analyses, for LI = 0.8	316
Figure A.5.11 Suction pressure–displacement curves obtained from analyses, for LI = 0.6	316
Figure A.5.12 Suction pressure–displacement curves obtained from analyses. for LI = 0.4	317

List of Abbreviations and Symbols

FSH = Ultimate load for Shear Failure.

FTS = Ultimate load for Tension Failure.

FGS = Ultimate load for General Shear Failure.

FTS' = Modified ultimate load for tension failure.

LL, PL = Liquid limit and plastic limit respectively.

PI = plasticity index.

RBBC = Resedimented Boston Blue Clay

A_i = interior cross sectional area of the pile.

A_{se} = external surface area of the pile.

A_{so} = outside area of the pile.

A_s = pile shaft area.

A_{si} = inner side area of pile.

A_t = tip area of the pile.

A_i , A_e = interior and exterior cross sectional areas of the pile, respectively.

A = cross sectional area of the bottom caisson.

B = the well known strain matrix.

b_i = body forces.

C_c = coefficient of consolidation.

C_s = coefficient of swelling.

C_u = undrained compressive strength of soil.

c_u^{avg} = average undrained shear strength of soil in contact with pile shaft.

c = a constant.

d = external diameter of pile.

D = caisson diameter.

$d\varepsilon$ = total strain of the skeleton.

D_T = total modulus of solid phase.

$d\varepsilon_c$ = the creep strain = $c dt$.

$d\varepsilon_p = -\delta_{ij} (dp/(3K_s))$ represents the overall volumetric strains caused by uniform compression of the particle by the pressure of the pore fluid (K_s is the bulk modulus of the solid phase).

$d\varepsilon_0$ = represents all other strains not directly associated with stress changes (i.e., swelling, thermal, chemical, and others).

$d(..)$ = derivative symbol.

$d\lambda_i$ = the rate of change for time, dt , for a rate-dependent model or is a scalar measuring the amount of the plastic flow rate on the i th system.

e_1 = intercept of the virgin consolidation line with the voids ratio axis in a plot of void ratio versus pressure stress.

E = Young's modulus.

F_w, F_c = the caisson wall and cap force respectively.

f = friction coefficient.

f_i = yield function for the i th system.

F = forces matrix.

F = total deformation matrix.

F_b = breakout force.

F_s = force resulting from the pressure difference.

F_{so} = shear forces between soil and anchor skirt surface.

f_s = side shear open top pile model.

$[F]$ = deformation gradient matrix.

F_{tot} = total force.

G = a constant shear modulus.

$G^p(\theta)$ = trigonometric functions.

g, h = isoparametric coordinates.

g_i = the flow potential function for the i th system.

G_{sec} = secant shear modulus.

G_s = Specific gravity.

H^m = polynomial interpolation functions.

h = depth of penetration.

H_α = a set of hardening parameters.

H_c = height of soil sample.

i_r, i_z = unit vector direction.

$[I]$ = unit matrix.

J = The Jacobian matrix.

K_w = bulk modulus of water.

k_{ij} = permeability of the soil.

K = stiffness matrix.

K_T, K_S = porous medium bulk modulus and solid phase bulk modulus.

k = permeability.

K_0 = coefficient at rest of soil stress.

L = caisson length.

L/D = length to diameter ratio.

\mathbf{M} = mass matrix.

\mathbf{M} = stress ratio in p-t or p-q plane.

M_c = Critical State ratio.

N_c = bearing capacity factor.

N_c^* = bearing capacity factor.

n = porosity.

N^u and N^p = approximate shape functions.

p_0 = initial value of the equivalent pressure stress.

p_d = hydrostatic pressure generated on top of the anchor.

p_r = average pressure acting on fracture cone surface.

$\lambda\Delta p$ = the anchor capacity resulting from suction (psi).

Δp = suction to which the test anchor was subjected (psi).

P_{top} = water pressure at top.

P_{tip} = pore pressure in the pile section (soil plug) at base level.

p = pore pressure.

q_0 = the anchor capacity at the no-pump (pump to generate suction) condition (psi).

q = end bearing.

Q = applied tensile load.

Q_a = applied tensile force.

Q_s = suction force.

Q, P = bearing capacity.

R_i = the viscous drag force.

S_u = undrained shear strength averaged at depth of $D/2$ below the caisson rim.

$\text{Sym} ()$ = symmetric part of.

s_{uTE} = shear strength of soil in Triaxial Extension test.

s_{uDSS} = shear strength of soil in Direct Simple Shear test.

\bar{t} = the prescribed traction vector on part of the boundary Γ_t .

T_e = contribution to breakout capacity from exterior shear stresses.

T_i = contribution to breakout capacity from interior shear stresses.

T = horizontal component of the load.

T = the temperature.

$T_{a\max}$ = maximum shear stress.

u = pore pressure below top of pile.

u_t = pore pressure below tip.

\dot{u} = solid velocity.

\bar{u} and \bar{p} = a finite set of parameters.

\dot{U} = velocity of porous fluid.

\ddot{u} = acceleration.

\bar{u} , \bar{p} = a finite set of parameters.

\dot{u}, \dot{w} = solid velocity and relative velocity of fluid (water) to solid, respectively.

W_s = buoyant weight of soil.

W_a = buoyant weight of the anchor.

W_p = buoyant weight of pump.

W_p = submerged pile weight.

W_s = submerged soil plug weight.

W_w = hydrostatic force to top cap of the pile.

W_p = submerged weight of pile.

W_{plug} = submerged weight of the plug.

W' = buoyant weight of the pile.

W' = buoyant weight of suction pile.

W_p = total weight of the pile exclude soil plug.

\dot{w} = relative velocity of fluid (water) to solid.

w_i = relative displacement of water to solid.

w_c = water content.

\mathbf{X} = reference position vector.

X, R, Z = reference position value.

$\mathbf{x}, \mathbf{z}, \mathbf{r}$ = vectors.

α = non-dimensional constant.

α_c, α_i = dimensionless factors (according to API, 1987).

α = empirical coefficient.

β, θ = parameters.

δ = interface friction angle.

δ_{ij} = Kronecker delta.

δ_w, δ_c = the caisson wall and cap displacement respectively.

∇ = derivative operator.

$\dot{\epsilon}$ = strain rate.

λ = slope of virgin consolidation line in $e:\log p'$ diagram.

λ = a constant.

γ' = buoyant unit weight of the soil.

γ = unit weight of soil.

γ' = effective unit weight of soil.

$\dot{\gamma}_a$ = average shear strain rate.

γ = shear strain.

κ = slope of swelling line in $e:\log p'$ diagram.

ρ_f = mass density of fluid phase.

ρ_s = mass density of solid phase.

ρ_f = mass density of fluid phase.

ρ_s = mass density of solid phase.

σ'_{ij} = effective stress.

σ_{ij} = total stress.

σ_t = tensile strength of soil.

σ_n = normal stress on pile surface.

σ_h = total horizontal stress between soil plug and interior pile wall at base level or if coefficient of earth pressure at rest is 1.0 in the undrained state.

σ'_{vc} = effective vertical compression.

$\zeta_s, \zeta_i, \zeta_d$ = caisson shape factor, inclination factor, and depth factor, respectively.

ϕ'_p = effective friction angle at peak.

τ_{max} = maximum shear stress.

ν = Poisson's ratio.

Chapter 1: Introduction

1.1. General

Recently, oil exploration and production have moved into deep sea with great water depths. Deepwater structures have been developed for the North Sea, Campos Basin, and Gulf of Mexico. In the Gulf of Mexico, some production platforms have been proposed even for water depths of 2,000 meters. The high costs of the fixed steel jacket platforms and other types of offshore structures in these great depths make floating structures economically attractive for deep waters, wherein the ice concentration is minimal and mobile ice masses are absent.

There are many types of deep water concepts: catenary anchored floating platforms (semisubmersibles and tankers), tension leg platforms (TLPs), guyed towers, compliant piled towers, articulated towers, subsea systems, and spars [Le Blanc, 1996]. Catenary anchored floaters that allow six degrees of freedom motions are economically suitable for marginal fields with small number of risers; of these floating structures semisubmersibles, with smaller water plane area, are more reliable and preferable in rough seas than tankers, owing to their greater stability. On the other hand TLPs, which are also compliant structures having lateral movements of surge, sway, and yaw but restrained heave, pitch, and roll motions, have been found to be the most suitable for non-marginal fields with large numbers of risers. Guyed towers are framed platforms designed

by incorporating guy lines, centered pile foundations and buoyancy tanks that offset the topside weight completely. The compliant piled tower is designed to sway as a rigid beam about a base pivot in a manner similar to the guyed tower; however, instead of clustering piles near the center at the bottom of tower, they are moved out to the edge of the structure and increased in number. For deep water, these piles are extended upwards through ungrouted guides to a point approximately midway up the tower. Articulated towers are column shaped or mixed column and truss structures, which are attached to the seabed at a single articulation point, and maintain their position by the buoyancy forces. Subsea systems require very high underwater technology for remote operation and a large investment for the integrated functioning of submerged production system (SPS), subsea satellite wells, christmas trees, and subsea pipelines that transfer oil/gas to the storage platform or onshore storage. Spar systems, such as the Oryx Neptune unit, which has already been installed for the Viosca Knoll Block 826 (in Norway) and Chevron Genesis unit, which is being fabricated for the Green Canyon Block 205 (in the Gulf of Mexico), are compliant structures for extremely deep waters depths up to 3,000 meters. Spar systems are floating long mono cylindrical column shaped hull structures, with or without oil storage, and moored by mooring lines to the seabed. Spar systems, due to their geometry, are considered having superior performance to other systems, especially for the extreme water depth [Le Blanc, 1996].

In spite of the availability of such a large number of deepwater concepts, the tension leg platform (TLP) concept was chosen as the best possible production structure

for the Gulf of Mexico deepwater area [MIT, 1992]. TLP structures are anchored to their foundations with flexible tendons or tethers. Due to the dynamic ocean environment of winds and waves, foundations of these structures are subjected to varying levels of static and dynamic tensile loading. These loadings have to be resisted by the uplift shaft reverse resistance offered by these foundations. In particular, the anchoring systems provided for these floating offshore structures play a very important role in resisting the environmental loads exerted on these floating structures.

1.2. Offshore Anchoring Systems

Many types of anchoring systems are used for such deepwater offshore structures. These are known as high capacity anchoring systems and some of these systems currently applied to offshore structures are high capacity drag anchors, anchor piles, base-plate and deadweight anchors, and suction anchors (or caissons). High capacity drag anchors can only resist horizontal loads; therefore, they are usually used for semisubmersible or tanker mooring system anchors. These drag anchors usually resist the environmental loads with a maximum load inclination of 10° to the horizontal plane. Therefore, they need very long chain lines to satisfy the load inclination requirements. Also, drag anchors need to be proof-loaded on site. Gravity base plate and deadweight anchors are very reliable anchors that will resist upward vertical and possibly horizontal forces. These gravity base anchors are generally installed by controlled submergence, and then ballasted or weighted down by high-density materials. This technique of anchoring structures is used very little in deepwater due to difficulties experienced in transporting,

handling, and installing the dead weights. Anchor piles are usually driven from above or below water either by hammer or by vibrodriver. Even though the anchor piles can resist both vertical and horizontal loads, in deepwater installations they usually require special tools for driving, and require large safety factors to be used in their design. Another anchoring concept that has become popular recently is the suction caisson (or anchor), which has been used for many deepwater structures (i.e. Snorre & Heidrun fields in Norwegian sector of the North Sea, and Marlim field in the Gulf of Mexico).

1.3. Definition of Suction Foundation

A suction caisson typically consists of a hollow cylinder or a cluster of cylinders made of steel or concrete with a closed top. Installation of the suction caisson would require: (i) Penetration of subsea soil foundation by deadweight and (ii) Pressure reduction under the cylinder head using pumps that create downward differential pressure. During installation, the rate of penetration can be controlled by the magnitude of the applied suction. When the design penetration depth is reached, the pumps are shut off, disconnected and retrieved; then any space between the soil plug and the top cap of the caisson is grouted with special cement mix. This novel foundation consists of massive cells, typically 10 to 30 meters in diameter and up to 40 to 50 meters deep. Clusters of cells can be floated to the platform site and lowered to the seabed to anchor the foundation to seabed. The caissons will form a tight seal with the soft submarine sediments, and provide the necessary uplift resistance.

1.4. Relevance of Suction Caissons

The production platforms utilized for the deepwater areas of the Gulf of Mexico were mainly TLP structures. These structures (shown in Figure 1.4.1) were massive semisubmersible structures weighing 50,000 to 100,000 tonnes, and anchored to the sea floor by 12 to 16 vertical tendons attached to deeply embedded piles.

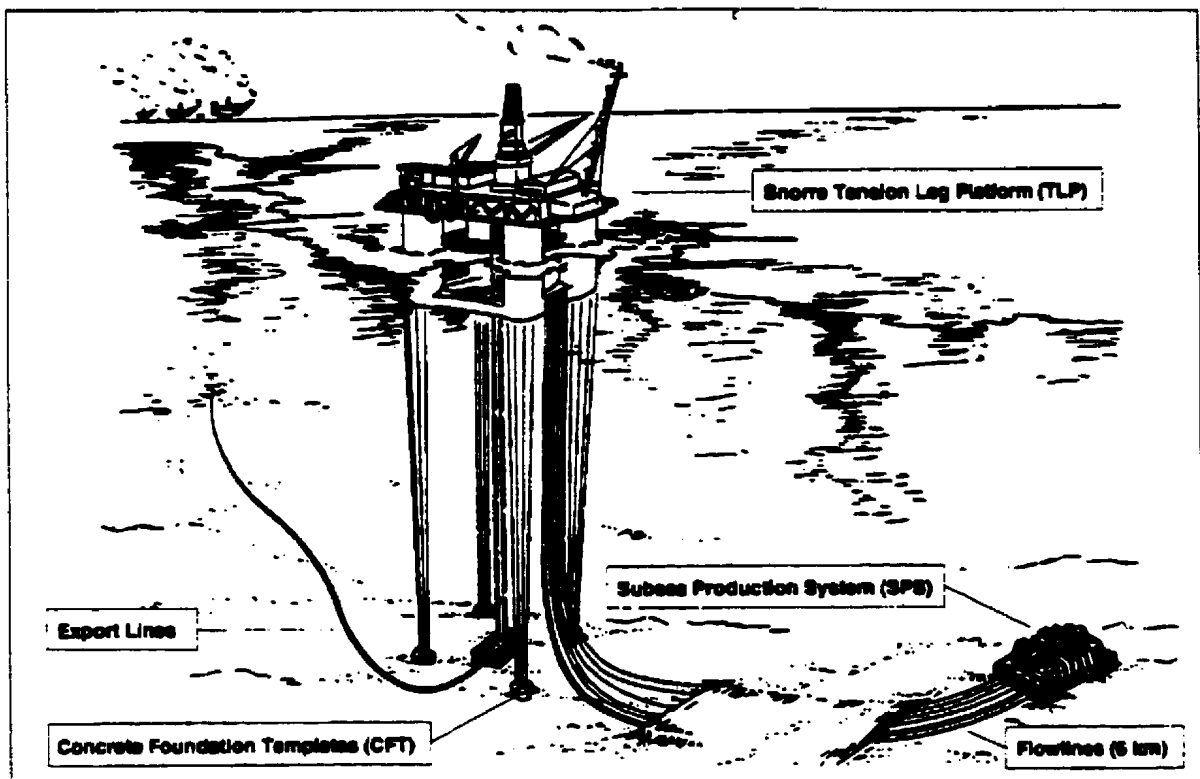


Figure 1.4.1 Sketch of Snorre Tension Leg Platform (TLP) system [Støve et al., 1992]

Each of these tendons had to carry a tensile load of about 14,000 to 60,000 tonnes. The piles used for anchoring these tendons, were more than 100 meters long, and had to be driven into the seabed by underwater hammers operating on the sea floor, for example,

Auger TLP piles were about 140 meters long (427 ft.) [Ulbricht et al., 1994]. The technical requirement of driving piles of such length, in 1000 to 2000 m water depths, calls for innovation and overcoming of great technical challenges for (pile driving) equipment manufacturers. It also presents serious safety problems for personnel aboard the support vessel, which must stand by throughout the installation process. Therefore, an alternate anchorage system was found to be necessary; thus a new class of structures called suction caissons have been utilized during the last decade.

A typical suction caisson system, shown in Figure 1.4.2, has been successfully installed in the Snorre TLP during June 1991 [Christophersen et al., 1992] and in the Heidrun TLP during July 1994 [Munkejord, 1996]. Moreover, due to the increased availability of recoverable oil from the Snorre field, the production has been increased by almost 100 per cent, viz., from 190,000 to 360,000 bopd since the field development plan was formulated in 1987 [Saga petroleum, 1997]. Up to now there has been no adverse report on the performance of the Snorre TLP foundation. Certainly, this must primarily be due to the excellent foundation support provided for the TLP structure. Therefore, this typical anchor would find a wide usage during the coming years in other offshore contexts. Moreover, suction caissons have also been proved to offer great potential for cost savings and installation operational safety [Saga petroleum, 1997].

1.5. Interaction with environment

Once in position, the suction caisson anchors the superstructure to the seabed. Pullout resistance of suction caisson is determined by factors as follows: (i) effect of wall friction, (ii) soil weight contained within the cells, (iii) ballast provided at the top of the caisson and, (iv) reverse-end-bearing or passive suction during uplift. These caissons can resist both vertical and horizontal loads. For example, the maximum design loads for the Snorre TLP caisson was given as a pretension load of 6950 tonnes and a maximum tension of 14200 tonnes [Fines et al., 1991].

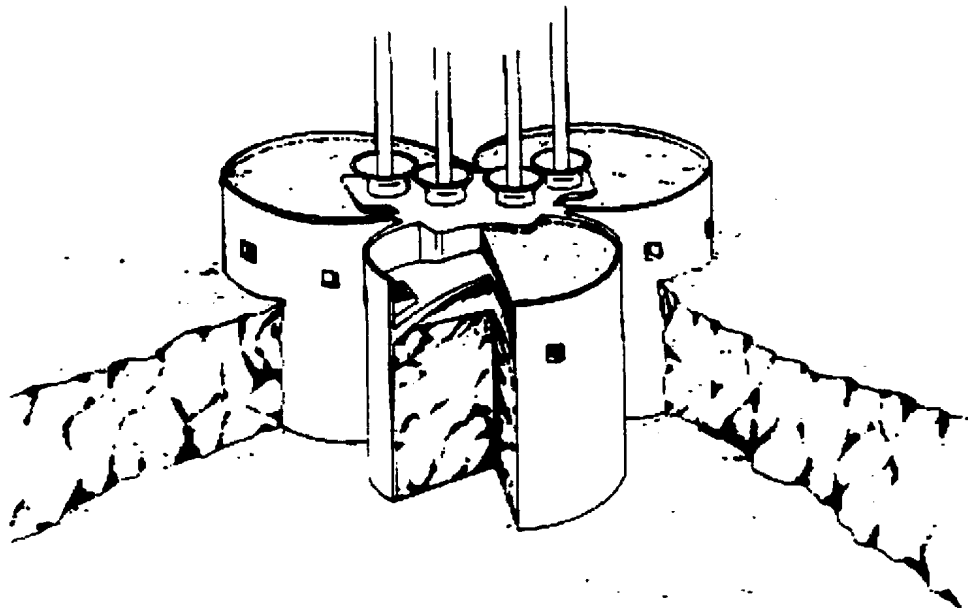


Figure 1.4.2 Suction caissons installed in the North Sea for Snorre TLP [Støve et al., 1992]

In addition, the effectiveness of anchorage provided is also dependent on suction forces that dissipate with time as pore pressures dissipate inside the caissons. The amount of tensile resistance developed by suction forces, during the sudden pull out condition, depends on the rate and duration of the applied load as well as on the drainage length and hydraulic conductivity of the surrounding soils.

1.6. Thesis Objectives and Scope

Since suction caissons have been proven to offer savings and safety, they seem to be usable for the next generation TLP structures. Earlier studies related to suction foundation have been considered under five main areas: i) suction application during installation, ii) prediction of caisson set-up performance, iii) prediction of soil reaction forces for TLP applications, iv) effects of caisson geometry, and v) influence of soil properties (mainly soft clays) [Andersen & Myers, 1995].

A number of small-scale experiments (including those in a centrifuge) and some medium-scale field tests have been carried out to examine the feasibility and behaviour of suction anchors. Some numerical studies have been carried out to validate the results of experiments. However, the various mechanisms of interaction developed by suction caissons have not been clearly understood. Even though they resist the vertical pull out forces by developing frictional resistance and negative back pressure, and the inclined loads by developing lateral bearing resistance, the interactive behaviour of the caisson

and soil system in the presence of a dynamic component of environmental load has not been analytically investigated in detail. Moreover, the location of cable attachment point with respect to the foundation height as well as the characteristic behaviour of soil resistance under varying rates of loading need to be examined in detail. Suction caisson capacity to the full range of the TLP loading conditions (during sudden pullout) would provide another interesting investigation. Moreover internally partitioned suction anchors would provide additional increases in shear/tensile resistance. The examination of these characteristics of suction anchors would assist in making a reliable prediction of anchor performance for various critical loading conditions.

Therefore this thesis was focussed on achieving the following objectives:

- To model and calibrate a numerical analysis procedure for suction foundation based on existing available small-scale laboratory tests data: MIT Tests [Cauble, 1997], University of Texas at Austin Tests [El-Gharbawy, 1998], and IIT Madras (India) Tests [Rao et al., 1997; Prasad, 1992];
- To develop a procedure that will be implemented in ABAQUS [HKS, 1998] finite element software to simulate the behaviour of suction foundations under static and dynamic (quasi-static) loads considering suction fluid pressures developed within the caisson;
- To identify the failure conditions observed in experiments through analysis;
- To verify scaling of model tests from numerical analysis simulating 1 g, prototype, and ng models; and

- To compute the pullout resistance of tension foundations under inclined loads, investigating the influence of load inclination of anchor attachment points.

1.7. Organization

This thesis is divided into 8 chapters. Chapter 1 contains introductory information including offshore anchoring systems, and the relevance and definition of suction foundations. It also outlines the thesis objectives and scope.

Chapter 2 presents a literature review on the state-of-the-art of suction foundations for offshore application. The chapter begins with studies on suction caissons for offshore applications; thereafter, early field and laboratory studies on large scale and small scale suction foundations are reviewed. It is followed by a review of analytical and numerical studies on suction caissons using semi-empirical formulations and finite element procedures.

Chapter 3 contains some details of the theoretical background giving numerical formulations used in ABAQUS, including suction force generation and failure mode identification (using external sub-routines). It also outlines the procedures used for reconciling l_g , n_g , and prototype values during model tests. In chapter 4, comparison of numerical results with experimental data is presented, including application of suction force generation.

Chapter 5 includes multi scaling model analyses to verify consistency of the model approach for l_g , prototype, and n_g models. Also in this chapter, failure mode

identification analyses are carried out to explore three known failure modes for suction foundation under pullout: shear failure, tension failure, and general shear (reverse end bearing) failure.

Chapter 6 contains comparison between three-dimensional model analyses of suction foundation with axisymmetric model analyses (having symmetric loading capabilities) of suction foundation to observe any significant difference between these two types of element application. Chapter 7 considers inclined loads on a tension foundation verifying the asymmetric loading analysis with the three-dimensional model and the comparison of results with existing theoretical formulations.

Finally, Chapter 8 lists the salient findings and conclusions of the thesis.

Chapter 2 Literature Review: Suction Caisson for Offshore Structures

2.1. Introduction

Since suction caissons have been recently used successfully in some offshore structure foundations, producing significant savings, it would be interesting and profitable to investigate their behaviour in order to understand failure mechanisms, nature of interaction with surrounding soil under varying loading conditions, and characterize and evaluate some of the basic design formulations. Many model studies, and large-scale field test programs, have been carried out to understand suction caisson behaviour and to verify the formulations made for predicting its response to the applied forces, using semi-empirical equations. Very few detailed analytical studies have been carried out using numerical procedures to understand the interactive behaviour of suction caisson-soil system. In order to understand the state of the art of these investigations, a literature review was carried out and the results of this search are reported below.

2.2. Suction Caissons for Offshore Application

The first commercial application of the suction caisson was in 1980 when the Dansk Boreselskab A/S (DANBOR) ordered two Catenary Anchor Leg Mooring (CALM), for Gorm field in the Danish sector of the North Sea, in approximately 40m water depth [Senpere and Auvergne, 1982]. The soil condition consisted of a sandy layer at top (5 to 6m) followed by soft clay (0 to 2m) overlying stiff clay. There were six

anchor chains of 0.09525m (3.75 inches) diameter and six suction caissons of 3.5m diameter and 8.5m to 9m height designed for each CALM. To meet the specific requirement and environmental conditions, both the chain and the suction caissons were designed to resist a force of 200 tonnes that acted horizontally at mudline. To date no adverse report has been made on its proper functioning.

The second application was on the Snorre TLP in June 1991 [Støve et al., 1992]. The Snorre field was located in more than 300m water depth of the North Sea. The soil profile consisted of thick clay layers, interspersed with soft clay to stiff clay, overlying clayey sand. The Snorre TLP was anchored by four Concrete Foundation Templates (CFT). Each CFT or the suction caisson was a three-celled concrete structure of 720 m² base area and 20 m height with individual cell diameter of 17m and skirt wall thickness of 0.35m. The CFT was designed to reach its target penetration of 12m. As noted already in Chapter 1, this type of anchor caisson is functioning well and is able to take the extra loads imposed on the foundation by the introduction of an additional process module.

The third application was on the Heidrun TLP in July 1994 [Munkejord, 1996]. The Heidrun field was located in 345m water depth in the northern part of Haltenbanken area, approximately 100 nautical miles from the west coast of mid-Norway. The Heidrun TLP was anchored by four CFT. Each CFT was a nineteen-celled concrete structure of 1500 m² base area and 26.45m height with each individual cell diameter of 9m. The CFT was designed to a penetration depth of 5m.

The fourth application presented in this section is for a permanent mooring for the process and accommodation barge in the Nkossa field of the Gulf of Guinea in July/August 1995 [Colliat et al., 1995, 1996]. The Nkossa field was located at 170 m

water depth in the offshore area of Western Africa. The soil profile was sandy clay overlying normally consolidated clay. There were 12 mooring lines equipped with 5m diameter and 13 m high steel suction caissons to moor a process and accommodation barge. There were two types of caissons chosen with ultimate holding capacities of 4850 kN and 5920 kN each, respectively, and 12.5 m penetration to fulfil the design requirements.

A paper showing the suction caisson as a cost effective method of installing mooring systems for both FPSO's (Floating Production System and Off-loading) and MODU's (Mobile Offshore Drilling Units) was presented [Hagen et al., 1998]. The paper especially focused on time and cost effectiveness from design, planning, and installation processes that can be achieved by a simple caisson design giving short fabrication time and requiring simple installation procedures.

A review of important contributions from the geotechnical profession to offshore development, from the early piled and gravity based foundations to the new lightweight skirted foundation concepts was presented by Suzanne Lacasse (Lacasse, 1999). The review highlights achievements and challenges over the past 25 years in geotechnical practice, which included areas of site and soil investigations, in situ testing, laboratory testing, model testing, foundation design, deep water development, skirt foundations and anchors, risk analysis, and observational methods. Some highlighted needs were on the need of higher quality data to calibrate design procedures, and some aspects of foundation design such as: (i) foundations on calcareous soils, silt, and permafrost, (ii) statistics and risk analysis in site investigation, (iii) application of dynamic measurements during installation, and (iv) focus on rational approach for pile design. Cost savings

became the main reason for the success of skirt foundations and anchors. Geotechnical design became an essential part of developing a skirt foundation solution. The design included analysis of skirt penetration, capacity, soil stiffness and displacements. Geotechnical calculation procedures are now well developed and have been verified, but not all aspects have yet been presented in the public domain because of confidentiality clauses associated with research underway [Lacasse, 1999]. Another application of skirted foundation was for support of near-shore submarine pipelines that worked well in the presence of uneven seabed and unstable slope.

The principles of skirt foundations and anchors in clay and their applicability for various types of offshore platforms and different types of loading were presented including procedures for penetration analyses and calculation of capacity [Andersen and Jostad, 1999]. The paper discusses various factors that influence geometry, installation, short term capacity, capacity under long term loads, fixed or retrievable cap and optimal load attachment point. Calculation procedures have been shown for penetration analyses and for holding capacities. The holding capacity of an anchor was significantly higher if the load was applied at an optimal depth below the seabed instead of at top of anchor. Set-up effects along the outside skirt wall after skirt penetration may not permit regaining of full shear strength for skirts penetrating by underpressure. It was believed that skirt anchors can be used to hold large permanent pullout loads, both for TLPs and taut leg mooring systems.

A paper showing the importance of geotechnical principles due to the installation of bucket foundations in dense sand has been presented [Erbrich and Tjelta, 1999]. The topic especially focused on suction pressure application in order to increase static driving

force and reduce penetration resistance during installation process. An examination of the distribution of seepage flows, and a determination of the onset of critical conditions were carried out by a series of finite element analyses using ABAQUS. Piping and boiling failures have been proven difficult to induce and appear to require substantial pre-loosening of the soil (due to installation procedures) before unstable conditions arise.

2.3. Large Scale Field Tests on Suction Caissons

During 1976 preliminary experiments were conducted on relatively small suction caissons in a very shallow lake. The results of these tests showed that the force required to reach full penetration was considerably lower than would be expected from generally accepted soil mechanics considerations [Hogervorst, 1980]. The promising results obtained from these studies led to full scale tests in order to exclude scaling effects. Suction trials were conducted, over two years, in the Netherlands under the Shell Offshore Research Program at a number of inshore locations having sandy soils and over consolidated clay soils [Hogervorst, 1980]. Steel suction caissons, of 3.8m diameter and between 5m and 10m length with a wall thickness of 16mm, were used in these studies.

The tests showed that the initial penetration of caissons into soil under their own weight provided sufficient sealing for subsequent decompression of the inside of the piles. The tests demonstrated that the suction caisson concept could be categorized as an easy handling (light weight) installation. Also, it required simple installation equipment and provided rapid installation. Moreover, loads could be applied instantly with high holding capacities in all directions. In these tests, holding capacities of the order of 200 t

of static loads were measured (measured to calculated holding capacity ratios varied between 1.08 and 1.33). It was also observed that there was no boundary drag during the installation and showed possibility of the suction caisson recovery. The tests also showed that installation was not hampered by the presence of small obstacles in the ground or by non-vertical positioning of the pile. Also, in sandy soils it was observed that the sand inside the caisson could become liquefied, thus eliminating internal pile friction. However, only static loads were applied in these studies instead of static, dynamic and cyclic loads. Ultimate suction caisson resistance calculation was based on equilibrium conditions of moment and lateral forces.

In 1985 Statoil [Tjelta et. al, 1986] conducted a field investigation to verify the suitability of the Gullfaks C skirt foundation. The field tests consisted of two 6.5 m outer diameter, 23 m high, and 35 mm thick steel caissons attached to a concrete shell foundation having 22 m penetration of its full skirt length into the seabed. These caissons were successfully installed in a seabed of 10 m of clay overlying 10 m of sand. The active suction force was applied thereafter and the suitability of installing large foundation units of this type under actual field conditions was examined. The observations showed that wall friction which was significantly influenced by water pressure inside the caisson (approximately 50%) was increased by suction and decreased by excess pore pressure. Penetration rate had a small influence on tip penetration resistance. The cyclic failure load after consolidation was approximately 50% of precyclic penetration force. Also, the soil reactions were believed to be highly dependent on soil permeability and time.

Another field test for a gravity structure was conducted by J&W Offshore on behalf of Norsk Hydro and Saga Petroleum [Andréasson et al., 1988]. The test specimens

consisted of seven steel cell model foundations with a cell diameter of 0.6 m, a skirt length of 0.6 m and an additional dome height of 0.2 m. The tests were conducted on a soft clay site in the vicinity of Gothenburg, Norway, with a range of penetration of 0.3 to 0.5 m. The foundation was installed by means of suction and subjected to a combination of static and cyclic loads simulating the loading conditions of deep water concrete platform. The test results showed that considerable reductions in rocking spring stiffness (defined as the overturning moment relative to the centre of rotation per unit rotation) could develop even at low to intermediate load levels with correspondingly high hysteresis damping (approximately 20%), reasonably high foundation capacity, and small shake down settlements. The foundation capacity under cyclic loading was of the order of 70% of the static capacity.

A series of field tests, on modelled specimens, were carried out by the Norwegian Geotechnical Institute (NGI) [Dyvik et al., 1993] on behalf of Saga Petroleum A.S. and its partners to decide on the basic configuration and loading conditions for a suction caisson to be used for the Snorre field. The tests were addressed to provide verification results for the predictions made for these tests, using analytical foundation design procedures, developed by NGI, for the design of offshore gravity structures [Dyvik et al., 1989; Andersen et al., 1989]. The procedure also included calculations and interpretation of stability performance of the structure. Earlier, a laboratory program of static and cyclic triaxial and direct simple tests had to be carried out to determine the static/cyclic shear strength and deformation characteristics of the soil at site. The distribution of static shear stress, variation of cyclic shear strength along the potential failure surface, and the safety factor were determined in an iterative manner. The safety factor was dependent on a

coefficient defined as the ratio of shear strength to applied shear stress.

In addition to giving the partial safety factors and the location of critical failure surfaces, the calculations also indicated whether the critical failure will be based on large average platform displacements, large cyclic platform displacements, or a combination of the two. This was deduced from the relative values of static and cyclic shear strains obtained for the critical condition. The limitation of the above procedure is that all soil elements were assumed to be subjected to the same shear stress history; in addition, the redistribution that occurs during cyclic loading could also cause the stress history for the most severely loaded elements to differ from the shear stress history assumed when the cyclic shear strength curves were established.

These comparisons provided a means for checking the validity of design procedures used for suction caissons before they were applied to the design of actual TLP tether anchors. It was believed that the use of 1-g environment model tests to check calculation procedures was as valid as centrifuge tests. The 1-g model tests could be performed in such a way that some limitations could be accounted for in the calculations.

The model geometry basically consisted of four circular cells, with 869 mm internal diameter and 914 mm outer diameter each. The base area, enclosed by the skirt compartments, was about 2.8m^2 . The skirts were 900 mm long and 22.5 mm thick. The model was constructed of welded steel with an approximate weight of 37 kN in air and 33 kN in water. During the penetration process, the model was lowered and it penetrated into the clay by self-weight. Then it was followed by the suction penetration to give the full penetration of 820 mm (equal to prototype penetration of 13.0 m). It was found that the soil inside the skirt compartment had heaved to almost 80 mm.

One static test and three cyclic tests were carried out on the model. The static model test was loaded to failure with actuator rams in displacement control. For cyclic model tests, three cyclic load controlled tests with a cyclic period of 10 seconds were carried out. The test program included 26 to 32 load parcels (cases) for all the three cyclic model tests. Load parcels had been arranged so as to reflect the peak part of a 100-year storm that had been scaled for the prototype, anticipating a large cyclic load increase of 80%. Based on measured results, the observations showed that the penetration resistance at full penetration was approximately equal to the submerged weight of the model, and the cyclic load capacity was smaller than static load capacity. The primary failure mode was small cyclic displacements and large permanent (average) displacements. Eccentric cyclic loading produced much lower cyclic failure loads and larger displacements.

A paper showing soil-structure interaction of the Draupner E bucket foundation during storm conditions was presented [Svanø et al., 1997]. The platform was extensively instrumented which provided useful data that enabled such numerical analyses providing greater accuracy. Design assumptions regarding dynamic stiffness and pore pressure dissipation were verified, and mechanisms for pore pressure generation during storm conditions were studied. It was found that the generated excess pore pressure was related to redistribution of load bearing between skirts and base plate due to the action of wave loads, and the resulting hydraulic gradients were well below critical, and no effects of stiffness degradation were seen.

A study that correlated laboratory analyses results and full scale on site tests result was presented by El-Gharbawy et al. (1999). All small scale laboratory tests studies and full-scale on-site tests were addressed to study on design of suction foundations for Gulf

of Mexico. Model caissons had L/D ratios of 2, 4, 6, and 12, with a diameter of 0.1016m (4 in). Six full-scale models had an L/D ratio of 5, with a prototype diameter of 3.7 m (12 ft.). Full-scale tests were performed in 1200 to 3000 m (4000 to 10,000 ft.) deep water depths. From full-scale installation, the self-weight penetration was observed to be one-half of the computed installation penetration. From self-weight penetration observations, the geotechnical properties of the foundation material were assessed and estimates were made of the required installation suction pressures and the vertical holding capacity of each of the anchors.

2.4. Laboratory Model Studies on Suction Caisson

2.4.1. 1g Model Tests

Since it has been known for a long time that a suction anchor could provide more saving and safety than a conventional anchor, it has generated many laboratory research studies to provide understanding of its behaviour, including its interaction with surrounding soils, the ultimate resistance developed, the cyclic behaviour and the failure mechanism. The review of these laboratory studies and analyses will be carried out in the following paragraphs.

Earlier laboratory studies on suction caissons were conducted: (i) To show the suction caisson performance in terms of resistance to weight ratio when subjected to pullout loads [Brown and Nacci, 1971] and (ii) To study the efficiency and break-out resistance of suction caisson as a function of anchor diameter, skirt length, soil strength

properties, soil-anchor friction, and suction capacity [Wang et al., 1975]. The tests showed that foundation capacity increased linearly with increasing suction on a constant skirt length to diameter ratio. The increase in the foundation capacity resulted from increased suction and increased internal friction angle of the test soils. Guha (1978) carried out tests on the break out of objects from underconsolidated sediments. The research only considered surficial ocean sediments, which were generally cohesive and highly under consolidated, having very low shear strength, high liquidity index and negligible friction angle. The study considered only adhesion and cohesion properties to be of primary importance. It used an artificial soil sediment having properties comparable to those of ocean sediments: only one type of soil was used for all the tests. Types of objects tested were spherical, flat plate, square prism, and cube. It was observed that the adhesive resistance was dependent on surface roughness of the embedded object and the cohesion of soil. The first laboratory tests with cyclic loads [Larsen, 1989] were conducted in order to compare the reduction in horizontal pullout capacity due to a cyclic load. The tests showed that the horizontal ultimate pullout capacity of the suction foundation on fine-grained soils depended on the load and its time variation.

Brown and Nacci (1971) defined the force equilibrium by the following equation (see Figure.2.4.1.), viz.,

$$F_b = W_a + W_p + W_s + F_{so} + F_s \quad (2.5)$$

where:

W_s = buoyant weight of soil; W_a = buoyant weight of the caisson;

W_p = buoyant weight of pump; F_b = breakout force;

F_s = force resulting from the pressure difference = $\pi D^2 (p_d - p_r)/4$

F_{so} = shear forces between soil and caisson skirt surface;

p_d = hydrostatic pressure generated on top of the caisson;

p_f = average pressure acting on fracture cone surface; and

D = internal diameter

There were 29 run tests carried out using 0.254 m (10 inches) diameter model in loose and dense sand. The hydrostatic caisson gave high reaction to weight ratio compare to conventional anchor.

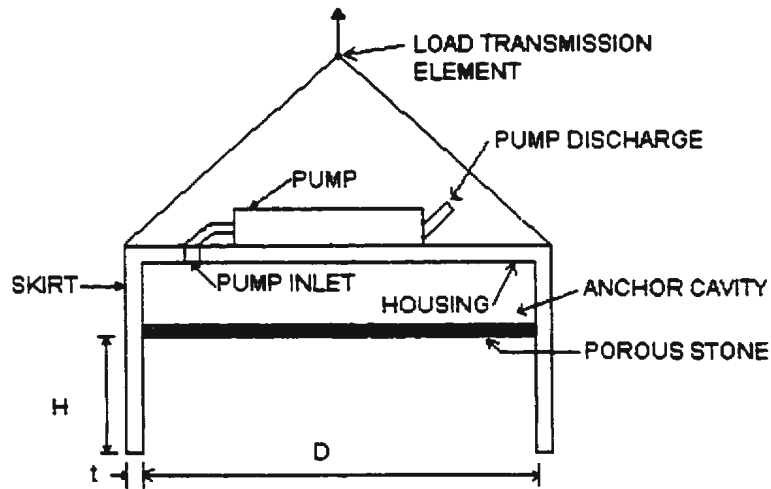


Figure 2.4.1 Schematic of a hydrostatic caisson [Brown and Nacci, 1971]

Wang et al. (1975) developed an equation to express foundation capacity q as follows:

$$q = q_o + \lambda \Delta p \text{ (psi)} \quad (2.6)$$

where q_o = the foundation capacity at the no-pump (pump to generate suction) condition

(psi). Δp = suction to which the test suction caisson was subjected (psi). $\lambda \Delta p$ = the foundation capacity resulting from suction (psi) and λ = a constant. It was also found that long-skirt suction foundation possessed greater values of q_0 than short-skirt caissons, primarily attributable to the greater soil wedge attached to the caisson after pullout and to the greater friction or adhesion along the exterior surface of the caisson walls. The caisson capacity increased with increasing suction, and λ depended greatly upon the internal friction angle of the test soil. It showed that the greater the internal friction angle, the greater the rate of anchor capacity increases.

Larsen (1989) found that the test results of ultimate horizontal pullout capacities of caisson foundations in sand were 30 to 60% higher than those obtained from Brinch Hansen (1961) and Broms (1964) formulae. This was due to the calculation method that considered only horizontal normal stresses on the outside of the caisson (and neglected the bottom friction and normal stresses), and the model size scale effects that could not be properly estimated. Further, in clay, the ultimate pullout capacity under cyclic loads was 1/2 to 2/3 times static ultimate pullout capacity for normally consolidated clays. It was found that the penetration resistance was primarily dependent on the friction force exerted on the outside of caisson during down suction. Also, the intrusion of surface material inside the caisson was unavoidable during down suction.

Steensen-Bach (1992) investigated short suction caissons in sands and in clays. From laboratory tests, it was found that the increased break-out resistance was proportional to the suction developed inside the caisson for sands, and to the suction induced transition from local failure along the shaft to a reversed bearing capacity failure

for clays. Recent observations of three different failure mechanisms (general shear failure, local shear failure, and local tension failure - details given later) in Kaolinite clay was also confirmed to be the case for other clay types. If suction was allowed to develop below the pile top, general shear failure (in terms of reversed bearing capacity failure) dominated tests in clay. The tensile strength was exceeded only after some displacements occurred during general shear failure; and the bearing capacity factors, N , were sensitive to the undrained shear strength, time of regeneration, break out velocity, and embedment ratio. In sands, the reverse bearing capacity failure was not important. Failure occurred as local shear failure along the pile shaft. However due to the development of suction below the caisson top, higher breakout capacity could be obtained at breakout velocities above a certain level. The equations for breakout forces in clay medium were as follows [Steensen-Bach, 1992]:

- For general shear failure:

$$F = W_p + W_s + W_w + \alpha c_u A_{sc} + (Nc_u - q)A_e \quad (2.7)$$

However, the value of N for the vertical equilibrium should be governed by the following equation, viz.,

$$-uA_i + \alpha c_u A_{si} = W_s + (Nc_u - q)A_i \quad (2.8)$$

- For local tension failure:

$$F = W_p + W_s + W_w + \alpha c_u A_{sc} + \sigma_t A_e \quad (2.9)$$

- For local shear failure:

$$F = \alpha c_u (A_{sc} + A_{si}) + W_p + W_w + A_t u_t \quad (2.10)$$

Determination of the breakout capacity of suction foundations, in sand, is usually

regarded as dependent only on the unit shaft resistance, and is expressed generally as:

$$\tau = a + \sigma_n \tan \delta; \quad \text{and} \quad \text{for sand: } a = 0. \quad (2.11)$$

Depending on breakout velocity, a transient state between drained states (no suction at all) and entirely undrained failure can be defined, and increased breakout capacity due to suction has been suggested using the following equation:

$$F = W_p + T_e + T_i + uA_i \quad (2.12)$$

The variables in equations (2.7) to (2.12) are given by

W_p = submerged caisson weight;

W_s = submerged soil plug weight;

W_w = hydrostatic force to top cap of the caisson;

α = non-dimensional constant;

c_u = mean undrained shear strength;

A_i = interior cross sectional area of the caisson;

A_{se} = external surface area of the caisson;

A_{si} = internal surface area of the caisson;

A_e = exterior cross sectional area of the caisson;

q = total stress at caisson tip;

u = pore pressure below top of caisson;

u_t = pore pressure below tip;

A_t = point area of caisson;

T_e = contribution to breakout capacity from exterior shear stresses;

T_i = contribution to breakout capacity from interior shear stresses;

δ = interface friction angle;

σ_t = tensile strength of soil; and

σ_n = normal stress on caisson surface.

Iskander et al. (1993) performed tests to investigate the behaviour of suction caissons in sand. The tests included installation and pullout resistances of the suction caisson. The studies showed that an appropriate initial penetration was required to perform suction penetration. Soil heave inside the pile resulted in significant reduction of soil penetration resistance. The high suction force applied to the specimen was also found to reduce the frictional capacity of suction caissons. It was found that suction was the dominant parameter contributing to the short-term pullout capacity. Also, during pullout, the frictional capacity was increased and suction was sufficiently developed to retain the soil plug. The side shear for sealed top model was calculated as follows:

$$f_s = (Q_a - Q_s - W_p - W_{\text{plug}})/A_{s0} \quad (2.13)$$

where:

Q_a = applied tensile force;

Q_s = suction force;

W_p = submerged weight of caisson;

W_{plug} = submerged weight of the plug;

A_{s0} = outside area of the caisson.

For open top suction caisson models, the side shear was calculated as follows:

$$f_s = (Q - W_p)/(A_{si} + A_{s0}) \quad (2.14)$$

where:

Q = applied tensile load;

A_{si} = inner side area of caisson.

It was found that the calculated values of f_s (according to API - RP2A,1992) and measured values of f_s were in good agreement.

Jones et al. (1994) carried out studies on the behaviour of suction caissons under various installation and pullout conditions using an instrumented double-walled pile model. A laboratory test tank containing fine-grained sand was used to perform all the tests. It was observed that liquefaction occurred during installation. A significant increase in tensile load capacity was observed during rapid pullout. The increase in tensile load capacity was generated by pressure differences that developed under the suction caisson top, and by the increase of external side shear.

Recently laboratory tests have been carried out to examine the behaviour of suction caissons in soft marine clays [Rao et al., 1997]. The tests were aimed to examine the influence of soil consistency and embedment ratio (L/D , length to diameter ratio) on the pullout behaviour of suction caissons and on the variation of suction pressure at the top of the soil plug. Two different models were considered from the installation point of view: surface and buried suction caissons, applying short-term monotonic loads. These tests showed that closed end suction caissons resisted more loads than open-end caissons, and showed the development of reversed end bearing introduced by Finn and Byrne (1972). It was observed that displacements were required to mobilize a large pullout capacity; a significant increase in pullout capacity occurred when liquidity index (LI) changed from 0.8 to 0.4 for this particular Indian marine clay, and suction pressures were not dependent on L/D ratios. Also, buried caisson foundations were found to be superior to surface caisson foundations' pullout capacities which were proportional to the burying depth ratios.

MIT (Massachusetts Institute of Technology, Cambridge, Massachusetts, USA) studies on suction foundation were carried out to address suction foundation applications for tension foundations. especially for a typical tension leg platform [Cauble, 1997]. A special apparatus, which was called as Caisson Element Test (CET), was developed to do the installation simulation, set-up, and axial tension loading of a miniature caisson in uniformly saturated clay. The CET cell comprised of five components: i) a sealed test chamber that contained a consolidated clay sample, ii) a model caisson having a unique two-pieces design that enabled independent control of the caisson wall and cap, iii) a driving system, which controlled displacements of the caisson wall and cap, and applied total stress on the clay surface, iv) a continuous automated feedback control system that could simulate various stages during the suction foundation tests, and v) an instrumentation package, which provided input signals for feedback control and data for test interpretation. The clay sample used was from Resedimented Boston Blue Clay (RBBC) using methods developed previously at MIT.

Suction caisson foundation model geometry was arranged to have a length of 0.0508 m., wall thickness of 0.00145 m., and outside diameter of 0.0508 m. The test chamber was designed to have a diameter of 0.305 m, and the soil samples height was 0.12 to 0.14 m (Figure 2.4.2). In each test the clay element was consolidated from the virgin compression range to a consolidation stress of $\sigma'_{vc} = 73.5$ kPa. The pullout tests were planned at a low speed of 0.0003 m/min., and at a fast speed of 0.003 m/min. The results from low speed tests gave 225.6 N of total maximum pullout resistance consisting of a maximum friction force of 137.34 N and a maximum suction force of 88.26 N.

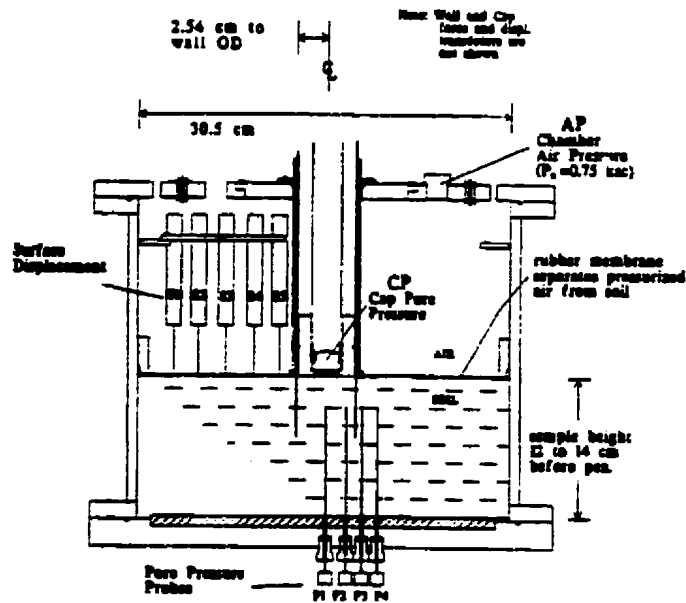


Figure 2.4.2 Test setup of MIT suction foundation studies [Cauale, 1997]

At the University of Texas, Austin, Texas, USA, studies on suction foundations were carried out with reference to applications in the Gulf of Mexico area. The study was also carried out to explore the potential for using suction foundation with aspect ratios larger than 2, and for examining their behavior under cyclic loads (El-Gharbawy, 1998).

A clay sample was prepared from Kaolinite clay (El-Gharbawy, 1998). Using certain mixing procedures and consolidation schedules, a good sample was prepared for the tests. Tank chamber geometry used was 0.762 m diameter and the soil sample height was 0.762 m. Ranges of acrylic suction foundation model length to diameter ratios varied

as 2, 4, 6, with a standard outer diameter of 0.1016 m, and a wall thickness of 0.003175 m (Figure 2.4.3). An additional model with a length to diameter ratio of 12 was made of steel tube, with a standard outer diameter of 0.0508 m and a thickness to diameter ratio of 0.03125 (El-Gharbawy, 1998).

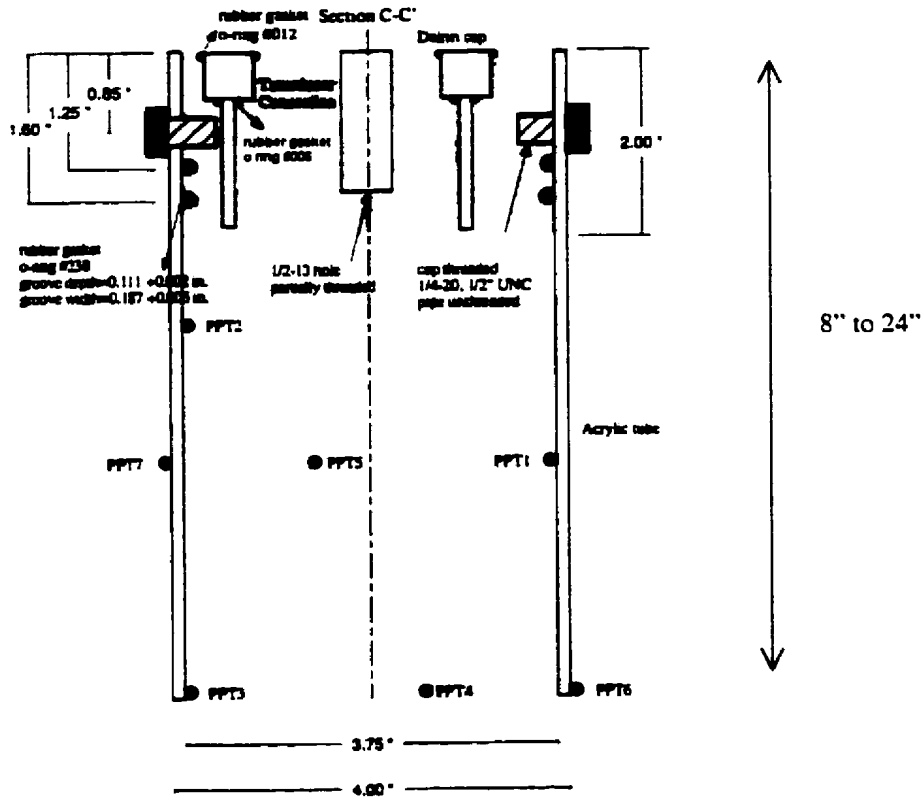


Figure 2.4.3 Typical suction foundation geometry of University of Texas (Austin) tests [El-Gharbawy, 1998]

One of the test results showed that the maximum pullout resistance force was around 178 N, when significant displacements occurred.

Results of one of the earliest deepwater geotechnical site investigations (January 1996) [NGI, 1996] concerning the design of suction caissons in the Marlim field of Gulf of Mexico were presented by Jeanjean et al. (1998). Extensive results from monotonic and cyclic laboratory testing program were presented and discussed with some results shown in simple design diagrams. The Marlim site soil characteristics were believed to be representative of large areas of Gulf of Mexico that can reduce costs of soil investigations and laboratory tests.

A paper highlighting application of suction caissons was presented by Alhayari (1998). Application was for two SBM FPSO projects for the Curlew site in Central North Sea (90 meters water depth) and Aquila in Adriatic Sea (850 meters water depth). One part of the paper presented model test results performed for the testing of water injection system used in Curlew project. It was proved that suction caissons could be installed in harder soils (very dense sand) without much difficulty. In the other part highlighting the Aquila project it was observed that the limitations in terms of water depth were mainly due to the ROV capabilities and other installation requirements, and not due to the concept of the suction caisson itself.

2.4.2. Centrifuge Model Tests

Several centrifuge tests were carried out on scaled models to study the behaviour of suction caissons [Renzi et al., 1991]. In these tests, load application considered both static and cyclic loads along with the proper modelling of the body force in the soil. From the results of one of the centrifuge tests it was observed that dissipation of penetration-

induced pore pressures in clay, especially those inside the caisson, was very slow. Also, it was observed that application of a cyclic load that simulated the tidal variations did not cause critical conditions in the soil; the pore pressures generated were small and caisson displacement was negligible. Calculation of the bearing capacity was made as follows:

$$Q = \alpha A_s c_u^{ave} + (c_u N_c + \gamma' h) A_t - W' \quad (2.15)$$

where:

W' = buoyant weight of the caisson; γ' = buoyant unit weight of the soil;

h = depth of penetration; A_t = base area of the caisson;

A_s = caisson shaft area; α = empirical coefficient;

c_u = undrained shear strength of soil in the zone of caisson base;

c_u^{ave} = average undrained shear strength of soil in contact with caisson shaft;

N_c = bearing capacity factor, given as 9.

Renzi and Maggioni (1994) conducted a study, using centrifuge tests, on a single skirt pile (or caisson) to examine the aspects of installation, bearing capacity, and long term behaviour under cyclic loading using suction anchors. The tests also included reconsolidation of soils to represent original field conditions. The tests found that the penetrability of the suction caisson was sufficient to reach its desired depth by its own weight and suction force. Also, the resistance to penetration could be estimated using a simple method developed for caisson bearing capacity calculation. The equation was as follows:

$$Q = \alpha A_s c_u^{ave} + (c_u N_c^* + \gamma' h) A_t - W' \quad (2.16)$$

where :

$$c_u = (q_c - \gamma h)/N_c ; \text{ and } N_c = N_c^*$$

A bearing capacity test indicated that, in case of skirt cap contribution, adequate values of undrained failure loads could be estimated using a simple method for calculation of the bearing capacity of a shallow foundation. The equation was as follows:

$$P = c_u N_c^* A_c + \gamma' h A_t - W' ; \quad (2.17)$$

with:

$$N_c^* = (\pi + 2)(1.2 + 0.4 \tan(\alpha))$$

where:

Q, P = bearing capacity;

d = external diameter of caisson;

c_u = undrained shear strength of soil in the zone of pile base or in the zone below the caisson tip;

c_u^{avg} = average undrained shear strength of soil in contact with the caisson shaft;

N_c^* = bearing capacity factor;

α = empirical coefficient;

A_s = caisson shaft area (inside and outside skirt) in contact with soil;

γ = unit weight of soil;

A_c = cap area of the soil;

γ' = effective unit weight of soil;

A_t = tip area of the caisson;

h = depth of penetration below the mudline;

W' = buoyant weight of suction caisson.

Fuglsang and Steensen-Bach (1991) also carried out model tests, especially for long-skirted suction caissons with penetration larger than one diameter. In this study model tests and centrifuge tests were performed. All the tests were essentially in undrained condition. The failure mechanism in clay at the base of the suction caisson was similar to a reverse bearing capacity problem. It was observed that 1g test may lead to no relevant failure mechanism.

Another centrifuge study, carried out by Clukey and Morrison (1993), investigated and evaluated the behaviour of single cylindrical shell steel suction caissons with an L/D ratio of about 2, under loading and soil conditions typical of deepwater Gulf of Mexico. It was found that the dominant portion (60% to 70%) of uplift capacity was derived from the reverse end bearing or suction at the bottom of the caisson.

Morrison et al. (1994) and Clukey et al. (1995), investigated the static uplift loading and cyclic loading conditions to model suction caissons of a TLP through centrifuge tests. The tests showed that suction caisson foundation satisfied the referenced field test results and satisfied the design criteria for a 100-year design storm in the Gulf of Mexico.

2.5. Analytical Studies on Suction Caisson Foundations

2.5.1. Use of Semi-empirical Formulation

Christensen et al. (1991) defined failure mechanisms for suction caisson

For clay:

- Failure mechanism #1: Shear failure along the shaft

$$F_1 = W_p + F_u^{ext} - F_u^{int} + T_e + T_i - F_u^{tip} ; \quad (2.18)$$

where:

$$F_u^{ext} = A_e \gamma_w d_1 ; \quad F_u^{int} = A_i P_{top} ;$$

$$F_u^{tip} = P_{up} (A_e - A_i) \equiv 0;$$

The variables are defined as follows:

W_p = total weight of the caisson excluding soil plug;

$T_e = P_e c_u \alpha_e \min(a_3, a_2)$; $T_i = a_1 P_i c_u \alpha_i$;

P_{top} = water pressure at top;

P_{up} = pore pressure in the caisson section (soil plug) at base level;

α_e, α_i = dimensionless factors (according to API, 1987).

- Failure mechanism #2: Tension failure at caisson tip

$$F_2 = W_p + W_s + F_u^{ext} + T_e + F_t ; \quad (2.19)$$

where:

W_s = total weight of soil inside caisson;

$F_t = A_i \min (\sigma_t ; -P_{up})$; $\sigma_t = 2c_u - \sigma_h$ = tensile strength in soil plug at bottom level;

σ_h = total horizontal stress between soil plug and interior caisson wall at base level or if

coefficient of earth pressure at rest is 1.0 in the undrained state:

$$\sigma_h = \max (\sigma_{lim} ; (W_s - T_i)/A_i) .$$

$$\sigma_{lim} = \gamma_w (d_2 + a_2), \text{ equal to lower bound of } \sigma_h .$$

- Failure mechanism #3: General shear failure

$$F_3 = W_p + F_u^{ext} + T_c + W_s + N C_u A_c - q_{tip} A_c \quad (2.20)$$

with:

$$N = \min (9 ; 6.2(1 + 0.35 a_2/D_c)) ; \quad q_{tip} = d_2 \gamma_w + a_2 \gamma_m$$

For sand:

- Fully Drained State:

$$F = W_p + F_u^{ext} - F_u^{int} - F_u^{tip} + T_c + T_i = W'_p + T_c + T_i \quad (2.21)$$

where:

W_p = effective weight of the caisson:

$$T_c = 0.1 \gamma' a_3 (2a_2 - a_3) P_c ; \quad \text{for: } a_2 \geq a_3$$

$$T_c = 0.1 \gamma' a_2^2 P_c ; \quad \text{for: } a_2 < a_3$$

$$T_i = \gamma' A_i a_1 - \gamma' A_i^2 / (k_r P_i) (1 - \exp(-k_r a_1 P_i / A_i))$$

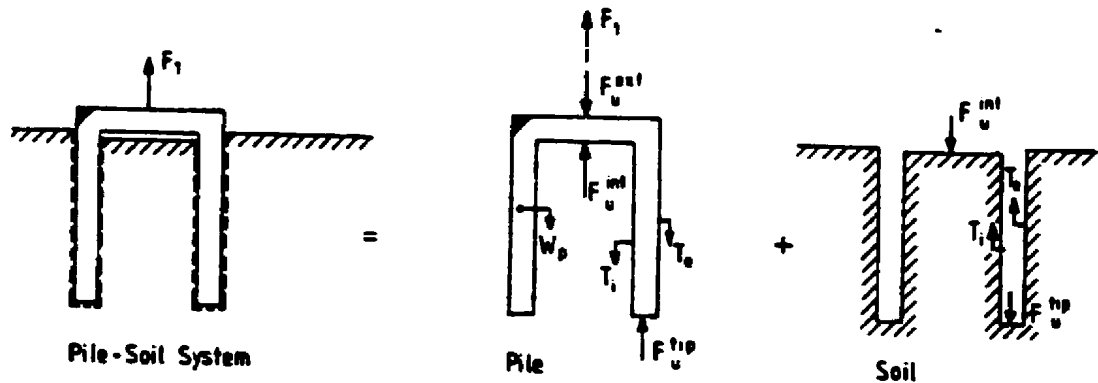


Figure 2.5.2 Failure mechanism #1, for clay [Christensen et al, 1991].

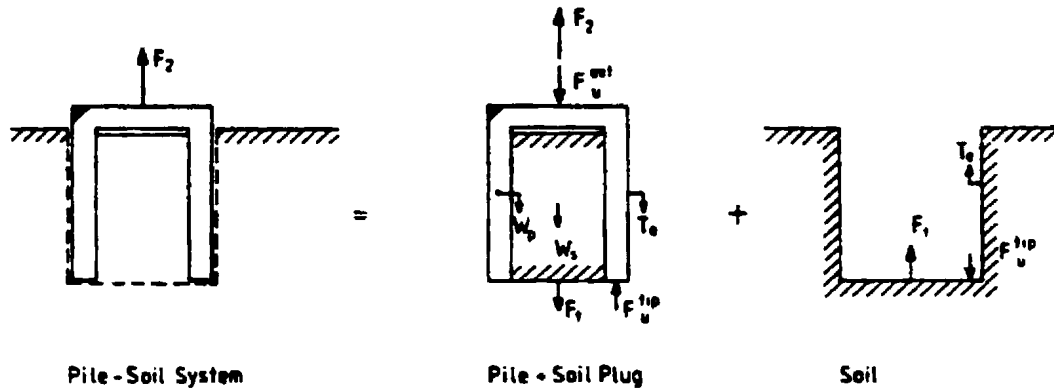


Figure 2.5.3 Failure mechanism #2, for clay [Christensen et al, 1991].

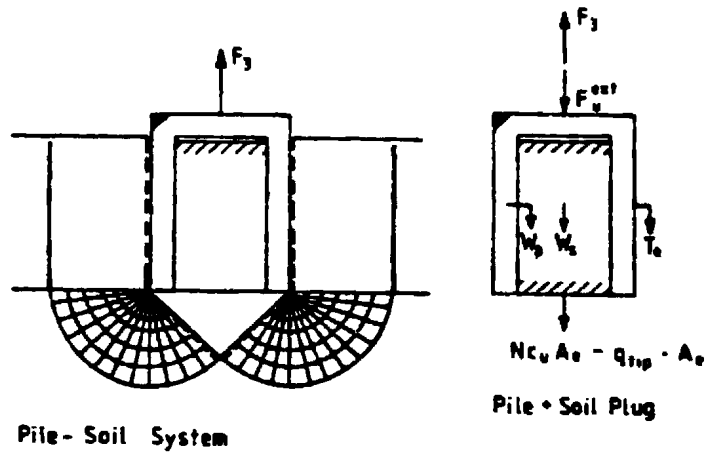


Figure 2.5.4 Failure mechanism #3, for clay [Christensen et al, 1991].

- Transient states:

The limiting transient state that may be interesting is not necessarily the one where cavitation develops at top of the soil column inside the caisson. A lower pullout capacity was found for the above condition, where upward gradients would lift the soil in the caisson: and the upward velocity, v , of the caisson that was required for this to happen was determined as:

$$v = kh_v/(D_f + a_1) ; \quad D_f = \pi D_i^2/(4\beta D_e) \quad (2.22)$$

where:

k = permeability of soil

D_i , D_e = internal and external diameters of the pile, respectively; $\beta = 2$ to 4;

h_o = the difference in hydraulic head (potential) between sea floor and top of soil inside the caisson;

Therefore the total pullout resistance of a suction caisson is given by:

$$F = W_p + F_u^{ext} - F_u^{int} + T_c + T_i \quad (2.23)$$

where:

$$F_u^{ext} = A_e d_1 \gamma_w ;$$

$$F_u^{int} = A_i p_{i,top} = A_i (-h_o + d_1 + t) \gamma_w ;$$

$$T_c = 0.1(\gamma' + i_2' \gamma_w) a_2^2 P_c ; \quad \text{for: } a_2 < a_3 ;$$

$$T_c = 0.1(\gamma' + i_2' \gamma_w) a_3 (2a_2 - a_3) P_c ; \quad \text{for: } a_2 \geq a_3 ;$$

$$T_i = \gamma'' A_i a_1 - \gamma'' A_i^2 (1 - \exp(-0.11 a_1 P_i / A_i)) / (0.11 P_i) ;$$

$$\gamma'' = \max(0, \gamma' + i_1 \gamma_w).$$

$$i_1 = (h_x - h_o) / a_1 \quad (<0)$$

$$i_2 = h_x / (D_f + a_2) \quad (>0)$$

$$h_x = h_0 D_f / (D_f + a_1)$$

If the buoyant weight of the suction caisson is W'_p , then equation (2.23) becomes:

$$F = W'_p + T_c + T_i + \gamma_w h_0 A_i \quad (2.24)$$

where:

$$h_0 = \min((\gamma' / \gamma_w) (D_f + a_1), H); \quad H = a_2 + d_2 - a_1 + d_0$$

A_i, A_e = interior and exterior cross sectional areas of the caisson, respectively.

The break-out capacity for suction caissons in sands, under drained condition, was dependent on effective suction caisson weight, inside wall shear force, and outside wall shear force. Further, for transient conditions, the break-out capacity was dependent on suction caisson weight, varying hydrostatic force, inside wall shear force, and outside wall shear force. Finally, it was observed that the suction effect contribution was significant and mainly influenced by embedded pile length, and permeability of soil; for clays, it was also influenced by the variation of undrained shear strength.

Andersen et al. (1992, 1993) presented a procedure to calculate the pullout capacity of suction caissons in clays. The method determined the cyclic shear strength of soil at the site using cyclic triaxial and direct simple shear test results from the laboratory which were run under conditions that simulated the in-situ stress conditions along the potential failure surface as close as possible. The results obtained from the above procedure could provide information on failure load, type and location of critical failure surface, and the failure modes (such as large cyclic displacement failure, or large

permanent displacements, or combination of the previous modes). The static and dynamic displacements were predicted using a finite element program. The predicted displacements were in good agreement for lower static loads, but a little higher for higher loads. Further, all the displacements of the cyclic model tests were within the range of the predicted displacements. However, results of higher eccentricity model had lower values. This deviation of predicted displacements of cyclic model tests might be due to the use of approximate normalized stress-strain curves that assumed independence of the stress path to compute the approximate displacements.

Since reverse end bearing was known to be the dominant part of the overall soil resistance for clays, Clukey and Morrison (1993) derived simple analytical formula for the suction caisson end bearing capacity from the bearing capacity formula of shallow foundations with shape factor, inclination factor, and depth factor correction. The compressive end bearing at the bottom of the caisson was defined as follows:

$$F_c = q A \quad (2.31)$$

where:

q = unit end bearing ;

A = cross sectional area of the bottom caisson.

The unit end bearing was defined for an undrained ($\varphi = 0$) total stress case:

$$q = N_c S_u \zeta_s \zeta_i \zeta_d + N_\gamma \gamma' L \quad (2.32)$$

where:

N_c = bearing capacity factor for a strip footing resting at the ground surface;

N_γ = bearing capacity factor for over burden pressure;

S_u = undrained shear strength averaged at depth of $D/2$ below the caisson rim;

ζ_s , ζ_i , ζ_d = caisson shape factor, inclination factor, and depth factor, respectively.

The bearing capacity factor was 5.14 ($= 2 + \pi$) for a uniform shear strength soil deposit. The inclination factor, ζ_i , was approximated by the following expression (Kulhawy et al., 1983):

$$\zeta_i = 6 T / (S_u N_c \pi D^2); \text{ with } T = \text{horizontal component of the load.}$$

The shape factor, ζ_s , for a cylindrical footing was taken as 1.2. For compressive loading, the following expression was used for the depth factor with a linearly increasing shear strength profile:

$$\zeta_d = 1 + 0.18 \tan^{-1} (D/L)$$

where:

D = caisson diameter;

L = caisson length.

2.5.2. Numerical/Finite Element Analyses

The first finite element model used for calculating skirt foundation capacities was developed for a gravity skirt foundation by Veritec [Andréasson et al., 1988]. The finite element analysis was aimed to verify foundation stiffness in terms of the rotational spring stiffness obtained from laboratory tests. A nonlinear elastic program AXIPLN was used for simulation. The soil foundation model was idealized as a plane strain footing having material behaviour similar to Duncan & Chang type hyperbolic models. Undrained shear strength was used with an initial shear modulus. From the results, it was concluded that

finite element analysis could be used for prediction of deformation behaviour, failure surface and static capacity. However, the finite element analysis did not consider large deformation analysis.

A finite element model for suction caissons was first implemented for Snorre CFT. The model was idealized as a single cylinder using a special finite element code developed by NGI called INFIDEL [Andersen et al., 1993]. Clay soil was assumed to be incompressible and weightless. Static shear strength and cyclic shear strength were determined from the principal stress directions calculated in the finite element analysis, and modified shear strength and cyclic shear strength formulations. In addition, formulations to define the tangential shear modulus were also used. From the static analysis, all the displacement components (rotation, horizontal, and vertical) were closely matched with experimental results for up to 75% of the failure load. For loads that exceeded 75% of failure load, the finite element analysis gave greater results than the experimental results, possibly caused by a stiffer response from the finite element analysis. Also, results from cyclic loads tests were in the range of upper and lower bound of results from finite element analysis. However, the finite element results did not show components of pullout resistance that are generally identified as shear and suction forces.

Clukey and Morrison (1993) carried out a finite element analysis along with laboratory centrifuge tests to evaluate the suction capacity of caissons for a TLP application. The finite element method used the ABAQUS computer program utilising 8-noded quadrilateral axi-symmetric elements with reduced integration points, and using a tri-linear model for stress-strain behaviour of the soil. Full suction was implied in the

analysis by maintaining contact between soil and caisson nodes at the top of the caisson during loading, but the pore pressure dissipation was not taken into account. Finite element analyses accurately predicted the load-displacement behaviour up to 0.6m (2ft.) of vertical displacement for 31.27m (102.6 ft.) depth of embedment of the prototype (diameter of 15.21m (49.9 ft.)). A good agreement was achieved for the centrifuge test (at 100g) having a suction efficiency of 92%. However, the finite element analysis did not consider the condition where separation may occur between the caisson top and the soil plug inside.

Hansteen and Höeg (1994) carried out a finite element analysis of a single cylindrical caisson used as a suction caisson. The emphasis of the analysis was on soil-structure interaction and determination of the contact stress between the embedded cylinder and the inside and outside soils using the INFIDEL finite element program developed by the NGI. The caisson was subjected to a cyclic tension load inclined at 6° from the vertical. The saturated soil was assumed to behave in an undrained manner. According to the finite element analysis, there were four different kinds of load carrying mechanisms: (i) vertical underpressure under the caisson top cap, (ii) inside and (iii) outside shear along the skirt walls, and (iv) underpressure under the skirt tip circumference. Depending on the values of the parameters and load levels studied, mechanism (i) carried between 24% and 43% of the applied loads, mechanism (ii) between 3% and 26%, mechanism (iii) between 25% and 49%, and mechanism (iv) between 10% and 17%. Results obtained with elliptic cross section (with axis ratio of 1.4) of the caisson differed significantly from results obtained with circular cross section. The difference between circular to elliptic of load distribution for suction, inside shear, out

side shear, and skirt tip was 8.8%, -4.4%, -2.3% and -1.1%, respectively. This indicated that minor changes in geometry and configuration of the skirts could change the load sharing significantly during soil-structure interaction.

Maeno et al. (1995) simulated the frequency response of seabed around a suction caisson subject to the mooring load of a floating structure. The seabed was assumed to be a fluid-saturated poroelastic medium whose behavior was governed by Biot's theory of wave propagation, and the suction caisson was modelled as a rigid and hollow cylinder with a cap at the top. The effect of skirt length on both the displacement response of suction pile anchor and that of seabed was investigated utilizing the permeability characteristics.

An analysis of skirt foundations and suction caissons in sand subjected to cyclic loading was presented by Jostad et al. (1997). The study assessed a method for analysing the behaviour of skirt foundations and suction caissons in water-saturated sand subjected to combined static and cyclic loading. The main purpose was to develop a procedure for calculation of accumulated pore pressure under undrained cyclic loading. The pore pressure accumulation procedure was implemented into a finite element program for coupled stress equilibrium and pore water flow problems. Including an elasto-plastic constitutive model for calculation of the average effective stresses, the method was able to model redistribution of the average stresses between the skirt and the foundation base during the loading history. The correctness of the finite element analysis results was demonstrated by back-calculation of a laboratory model test of a skirt foundation, in dense sand, subjected to a loading history representative of the storm loading on the most loaded leg of a jacket platform in the North Sea. It was shown that the results agreed very

well both in absolute values and trends with the measured pore pressure and displacement. However, the numerical method underestimated the deformations due to accumulated shear strains, when the cyclic shear stress was high.

2.6. Definition of Soil as a Multi-Phase Medium

A common definition of soil as a porous medium involves defining the mechanical properties of the constituents, their respective volume fractions, and the considerations of the type of soil micro structure. However, other soil material definition as porous media can be derived by treating soil as a three-phase medium incorporating average pore size as a material parameter [Pietruszczak and Pande, 1996].

2.6.1. Mechanics of Porous Media

Soil is a mixture of mineral grains with various fluids. Soils consist of an assemblage of particles with different sizes and shapes. The voids of the particle skeletons are filled with water and air or gas. Therefore, soil in general must be looked at as one-phase (dry soil), two-phase (fully saturated soil), or multi-phase (partially saturated soil) material. The material condition is governed by the stresses and displacement of each material phase (solid, water, gas). The stresses developed in the soil skeleton (solid phase) are called effective stresses [Terzaghi,1943], and those in the fluid phase are called the pore fluid pressures.

However, in general, the multi-phase condition is more common in real nature. The early classical work of Terzaghi(1943) and Rendulic (1936) on the consolidation

problem was followed by the more explicit work of Biot (1941), Florin (1942) and others [Zienkiewicz et al., 1977; Schiffman et al., 1964]; these were valid for quasi static situations only. The theory for an elastic porous medium was first developed by Biot [1955, 1956, 1957, 1972, 1977, 1978]. Further formulations, considering the soil as a general mixture, were derived through formal linearization of the field and constitutive equations to reduce to Biot's linear poroelastic model [ie., Bowen (1982)]. However, from experimental observations, it was found that the stress-strain behaviour of the soil skeleton was non-linear, anisotropic, hysteretic, and path dependent. An extension of Biot's theory to the non-linear inelastic range was derived by Prévost [1980].

Soil also has been viewed as a multi-phase medium using the modern theory of mixtures; this was first developed by Truesdell and Taupin [1960]. Others such as Green and Naghdi [1965] and Eringen and Ingram [1965] extended this formulation. Sandhu and Wilson [1969] were the first to study linear elastic consolidation in a finite element context. Zienkiewicz and Bettess [1982] derived the general formulation for soils and other saturated media under transient and dynamic conditions considering the inertial component of the system also. Various simplifications and assumptions were considered by generalizing the Biot's formulation. The approximations consisted of: (i) Medium speed phenomena where the inertial component of fluid was negligible compared to that of solid; (ii) Very slow phenomena (consolidation equation) where inertial components of both solid and fluid were negligible; (iii) Very rapid phenomena (undrained behavior) where the displacement, velocity and acceleration of fluid were negligible or the permeability became very small, so that the kinematical and inertial components of both solid and fluid could be neglected [Zienkiewicz and Bettess,1982]. A useful

classification, based on parametric study of the importance of fluid and solid accelerations, showed that the wave load problems may be categorized as the slow type phenomena (solid and fluid accelerations are unimportant) [Zienkiewicz and Bettess,1982]. However, a partially drained condition could be suspected to occur in the intermediate to high porous media. This condition may be governed by the elemental size of the numerical model.

Zienkiewicz et al. [1984] tried to revise and generalize Biot's formula using a numerical procedure for dynamic behavior of two-phase saturated porous media. The formulation included revision of the definition of effective stress of the porous media including nonlinear material and large deformation behavior. Several approximations including variables in discretized form, fluid compressibility and incompressible options were modeled. Chohan et al. [1991] defined a procedure for dynamic response analysis of saturated soils using Laplace transform to suppress the time variables and linearization of the Laplace transform. The procedure was applied to one-dimensional wave propagation in a linear elastic material and in flow-saturated elastic soil layer with weak, strong, and moderate coupling. However, for the case where the excitation was discontinuous, significant error was obtained in the solution. This error was explained as that occurring due to the limitations of the finite element approximation. Also, the method seemed to be uneconomical when it was applied for large eigenvalue problems.

Zienkiewicz et al. [1990a, 1990b] verified the numerical results of static and dynamic analysis for one and two-dimensional models with those of laboratory tests conducted on a soil media subjected to an earthquake. The model included material non-linearity and large deformation behaviour of the two-phase media. A three dimensional

analysis of soil/water coupling problems using elasto-viscoplastic constitutive equations was carried out by Ohta et al. [1991]; the elasto-viscoplastic model was first proposed by Sekiguchi and Ohta [1977]. The analysis addressed the simulation of ground deformation and behaviour of pore water pressure during an earthquake excitation. The analysis also showed that Sandhu-Wilson equation [1969] and Christian equation [1968] had no essential differences. A multi-phase flow analysis in a deforming porous media was carried out by Li and Zienkiewicz [1992]. The detailed derivation of the interaction of two immiscible porous fluids was also carried out. The displacement of solid, the pressure and saturation of the wetting fluids were taken as primary unknowns of the model. A generalized Galerkin's procedure was devised to establish the coupled finite element equation set in u-p-S form. Unconditionally stable direct and staggered solution procedures were used for the time domain numerical solution. Further, Meroi et al. [1995] considered the topic of large strain behavior of porous media under static and dynamic loads, and developed solutions for saturated and unsaturated conditions. The procedure was addressed to analyze soil as a three-phase material incorporating non-linear behavior of solid phase.

2.6.2. Soil Constitutive Models

Seabed soil condition is generally made up of specific combinations of different types of soils. The stratigraphy of seabed soil can be one of these soil types: gravel, sand, silt, clay or a combination of them. Some examples of soil types available at offshore oil sites are given as: (i) Hibernia (typical) soils: very dense to dense sand [Clark and

Guigné, 1988]; (ii) Gulf of Mexico: clay; and (iii) Snorre field: clay. Since, the general soil conditions in offshore sites are of two major groups, viz., sand and clay, the main interest would be that of sand and clay constitutive models.

Soil deformation behaviour under a given load is very complex and very difficult to obtain from any one test method. However, using a mathematical idealization, soil behaviour can be possibly predicted for its stress-strain relationship under different loading conditions. Recent developments in computer technology and numerical methods have increased the possibility to analyze any complex problem in soil mechanics. However, the validity of the material constitutive model depends on its mathematical formulation consistency for the general cases. A soil constitutive model should reflect some of the basic requirements in any solution procedure [Prévost,1987]: completeness, simplicity, and physical representation. Completeness means that it is able to represent material stress and strain behaviour for all stress and strain paths. This property is essential for practical application. The desired simplicity of a constitutive model will relate to the use of a small number of standard or simple material tests to obtain soil parameters. The correct physical representation of a material in mechanics will describe the elastic and plastic material properties. However, from experimental observations [Prévost, 1978] it was stated that: (a) Yielding of soil is anisotropic (stress-induced) and dependent on effective mean normal stresses; (b) A coupling exists between plastic volume changes and changes in shear stress; and (c) Dense or loose soil expands or contracts in volume during pure shear. In order to describe material plasticity, one needs: (1) Yield condition: specifying stress state initiating plastic flow; (2) Flow rule: describing relation of plastic strain-rate vector to that of stress and stress-rate vectors; and

(3) Hardening rule: yield conditions get modified during plastic flow.

In addition to these three conditions, a full definition of the plastic model requires a description of the nature of hardening, whether isotropic, kinematic or a combination thereof. As long as only monotonic loading conditions are being considered, the nature of hardening is irrelevant [Baker et al., 1982]. On the other hand, the nature of hardening must be specified if cyclic behaviour of soil is being investigated.

Several constitutive models have been developed recently to characterize the soil behaviour. They can be grouped as single to multi-yield surface as well as associative and non-associative plasticity.

Some of the well known classical plasticity models are Tresca, Von Mises, Mohr-Coulomb, and Drucker-Prager. They usually follow associative plasticity rule and are isotropic in nature. Further, a cap model was proposed to represent the realistic soil material behaviour [Drucker et al., 1955; Henkel, 1960; Parry, 1960; Roscoe et al., 1958]. However, a limitation was found for the cap model due to the stress-induced anisotropy and hence, was considered to be incapable of representing soil behaviour under cyclic loading [Prévost, 1987]. In 1968, the Cambridge group [Scott, 1985] began to develop the critical state theory which referred to constant volume state condition of soil. Then followed the development of the cam clay model which modeled both the volumetric and shearing behaviour of soil. An important theoretical development in plasticity was made by Iwan [1967] and Mròz [1967]. They showed how continuous yielding could be represented by a set of nested yield surfaces in stress space. The notions of kinematic and isotropic hardening/softening plasticity rules could give rise to the soil characterization having considerable flexibility. The concept was then adopted and enlarged by Prévost

[1977, 1978, 1985] and by Mròz [1980]. Material behaviour concept based on stress state distance from yield or bounding surface was constructed initially by Dafalias [Dafalias and Popov (1975 and 1977), Dafalias and Herrmann (1980), Dafalias (1986)], and later developed by others [e.g. Aboim and Roth, 1982; Gaboussi and Momen, 1982; Mròz and Pietruszczak, 1983a, 1983b; Bardet, 1986, 1990; Crouch and Wolf, 1994].

Iwan plasticity theory required large computational and storage requirements for the multi-surface theory, while the bounding surface theory was not able to correctly represent material behaviour when the stress state rotated around the hydrostatic axis. In order to clarify certain problems associated with the above models, the idea of material memory, indexed to the cumulative plastic strain, was employed in the endochronic theory developed by Valanis and Read [1982], and specialized for soils by Bazant and Krizek [1976].

The cap model has recently been modified for time dependent plasticity behaviour [Katona, 1984; Hsieh et al., 1990; Borja et al., 1990], by applying Perzyna's elastic/viscoplastic theory [1966] and employing associative rule to both yield surface of modified cam clay theory and von Mises cylinder inscribed in the cam clay ellipsoid. Another method called Spatial Mobilized Plane (SPM) method, has been developed to extend the triaxial elastoplastic constitutive model to the three-dimensional stress-strain model developed by Nakai and others [Nakai and Mihara, 1984; Nakai and Matsuoka, 1983]. The viscoplasticity model seems to assist the proper modelling of soil behaviour especially in linear and non-linear creep problems using associative or non-associative plasticity rules [Zienkiewicz and Corneau, 1974; Zienkiewicz et al., 1975; Adachi et al., 1987]. A detailed parameter estimation procedure for an elasto-viscoplastic finite element

analysis was developed by Iizuka and Ohta [1987].

However, a proper model for soil behaviour should retain the extreme versatility and accuracy of the simple multi-surface J_2 -theory [Prévost, 1977,1978] in describing observed nonlinear hysteretic shear behaviour, and shear stress-induced anisotropic effects and reflect the strong dependency of the shear dilatancy on the effective stress ratio in both cohesionless [Rowe, 1962; Luong, 1980; Luong & Touati, 1983] and cohesive soils [Hicher, 1985]. Therefore, the conical yield surface should be used for the purpose [Prévost, 1987].

The initial and induced anisotropy of clays has been clearly established by experiments [Amarasinghe and Parry, 1975; Bishop, 1966; Duncan and Seed, 1966; Saada and Bianchini, 1975]. Several constitutive models have been proposed to model the anisotropic clay behaviour. Prévost [1978], and Mròz & Pietruszczak [1983a, 1983b] simulated the clay behaviour using multi-yield-surface plasticity (MYSP) which was originally proposed by Iwan [1967] and Mròz [1967]. The procedure was quite complicated with complex mathematical formulations, numerous material constants, internal variables, and cumbersome finite element implementations. Anandarajah and Dafalias [1986] described the clay behaviour with bounding surface plasticity first introduced by Dafalias and Popov [1975], and Krieg [1975]. However, it produced excessive large artificial ratchetting, a phenomenon which was characterized by the cyclic accumulation of deformation [Hashiguchi, 1993]. A new constitutive model called Scaled Memory model has been recently proposed by Bardet which describes anisotropic behaviour of clay and hysteretic material behaviour [1995a, 1996], and also demonstrated various cyclic stress-strain responses of clays and sands [1995b]. It is capable of

eliminating the artificial ratcheting of bounding surface plasticity and needs less material variables and gives a more realistic stress-strain curve of soil than multi-yield surface plasticity model.

2.7. Summary

Suction caisson investigations have been carried out on large/small scale specimens, field/laboratory tests and through numerical computer models. The salient characteristics of the suction foundation can be reviewed as follows:

- Due to the development of suction forces, below the caisson top, significantly increased breakout capacity could be obtained at breakout velocity above a certain level.
- A transient state, between drained states and entirely undrained failure, is obtained depending on breakout velocities.
- The increase in the tensile load capacity was dependent on the pressure difference that developed under the caisson top, and on the increase of external side shear.
- For cyclic loads the horizontal ultimate pull-out capacity, of the caisson on fine grained soils, was dependent on the load and its time variation.
- Three failure mechanisms of suction caisson foundations were identified for clay medium, viz., shear failure along the shaft, tensile failure at pile tip, and bearing capacity failure. However for sand only one failure mechanism was identified, viz., shear failure along the shaft.

Based on a parametric study concerning the importance of fluid and solid

accelerations, Zienkiewicz and Bettess (1982) showed that the wave load type problem may be characterized as a slow phenomenon (solid and fluid accelerations are unimportant). However, a partial drained condition could be suspected to occur in the medium to high porous media. This condition may be governed by the elemental size of the numerical model. Most of the soil material characterization has considered anisotropic behaviour using associative and non-associative flow rules, and dilatancy seems to be an important factor for the extension condition. Under monotonic loading, the nature of hardening seems to be irrelevant [Baker et al., 1982]; on the other hand, the nature of hardening has to be specified if cyclic behaviour of soil is investigated.

The profiles of plasticity potential and yielding surface of sand do not coincide, and the direction of the plastic strain increments deviates by a certain angle from the normal to the failure surface; and non-associative flow rule would be required in plasticity theory [Meyerhof, 1982]. Normality to the yield surface would lead to an associative flow rule for an ideal material with friction angle equal to dilatancy angle. For cohesive-frictional soils a general plastic potential including anisotropy is difficult to establish, and the direction of the plastic strain increments may not be unique and depend on many different factors. However, for normally-consolidated and lightly over-consolidated clays of low sensitivity the plastic potential and yield surface are similar. But the direction of the plastic strain increments deviates by a certain angle from the normal to the failure surface, thus requiring a non-associative flow rule.

The study proposed in this investigation is on the breakout capacity of suction caisson foundations using finite element models where large deformation and material non-linearity are taken into account. From this study, a detailed load deformation

characterization of a commonly present seabed material will be made and relevant equations developed for the vertical and inclined static/dynamic pullout loading on a suction anchor foundation. Material model for soil material will use Cam clay model developments and the analytical procedure would be implemented and solved using the ABAQUS finite element program [HKS,1998].

Chapter 3 Theoretical Foundations: Analytical Procedure, Model Characterization and Data Interpretation

3.1. Introduction

In the previous sections, it has been shown that a number of suction caisson foundations have been installed and they have proved to be a good alternative to the conventional pile foundations. However, the tension static load for the TLP structure, for example, may gradually eliminate the bearing capacity of the foundation due to dissipation of (internally generated) suction force and thus reduce the foundation strength. Moreover, the nature of environmental dynamic loads may contribute to this condition due to pore pressure build-up during the repeated wave loadings. Therefore, analysis using the porous media concept for the soil should incorporate the consideration of pore pressure influences. Recently, there have been many field and laboratory studies to investigate the behaviour of suction caisson foundations dealing with pullout load deformation responses. But none of them has been related to the basic soil parameters, i.e., particle size characteristics, void ratio, relative density, permeability, Over Consolidation Ratio (OCR) as well as scale effects of model to prototype ratio; very few studies have been related to the effect of static pullout and transverse loads on this particular type of foundation. It is obvious that for such investigations numerical models are more convenient than physical models. While modeling by finite element procedure, axisymmetric elements are known to be capable of modeling transverse deformations through the use of Fourier series representation for load deformation behaviour.

However, the capacity provided for employing Fourier approximation of this deformation is limited and the use of higher order fourier approximations leads to uneconomic solution times. In addition since a large amount of deformation is experienced during pullout, a large deformation formulation needs to be used in the analyses.

3.2. Methodology

In the present analytical investigations, the cylindrical suction caisson foundation is assumed to be already installed on the sea floor. The load cases applied will be based on typical wave loads applied as static pretension to the TLP tether including its inclination and loading rate. From the theory of soil mechanics, the distance limit of stress influence is greater than 1.5 times the width of the foundation base. However, for the problem under consideration, the size required for finite element modeling may be different due to the consideration of large deformation, and extreme load situations. Material for the suction foundation is assumed to be either concrete or steel, and the soil is clay. Influence of geometric variables, such as L, D, and t, will also be considered. Comparison of the present results with previous laboratory results will be made. Based on the results, analysis of additional complex loading configurations also will be considered.

Since extreme loads induce large deformations in soil, a proper nonlinear material behaviour will be used for modelling soil medium. Nonlinear response of soils will use the soil stress-strain curve and its volumetric behaviour obtained from triaxial and direct shear tests; these behavioural properties will be converted to three dimensional stress strain relations. For concrete or steel material (used for the suction caisson), the standard material behaviour definition provided in the computer program ABAQUS will

be used.

3.3. General Formulation for the Governing Equation of Porous Media

In order to accommodate pore pressure influence in the analysis of saturated soil medium, it is necessary to describe the soil material as a two-phase media. Soil is assumed to consist of two phases, viz., solid and fluid (water) phases. However, soil also has a non-linear constitutive behaviour, which is manifested even from the beginning of loading. Therefore, due to consideration of extreme loads, large deformation and non-linear material properties have to be properly modelled in the numerical implementation of the solution procedure.

3.3.1. General Formulation for Static and Dynamic Response of Soil as a Porous Medium

The formulation of material behaviour for a multi-phase media requires considerations of mass and momentum conservation conditions, which define continuity of the fluid and solid phases, as well as force equilibrium conditions. Moreover, to account for large deformation behaviour, appropriate stress-strain relationships should also be applied.

Constitutive relationship of the two-phase media

Use of the conventional effective stress concept gives (see Figure 3.3.1),

$$\sigma'_{ij} = \sigma_{ij} + \delta_{ij}p \quad (3.1)$$

where: σ'_{ij} = effective stress; σ_{ij} = total stress; δ_{ij} = Kronecker delta; and

p = pore pressure.

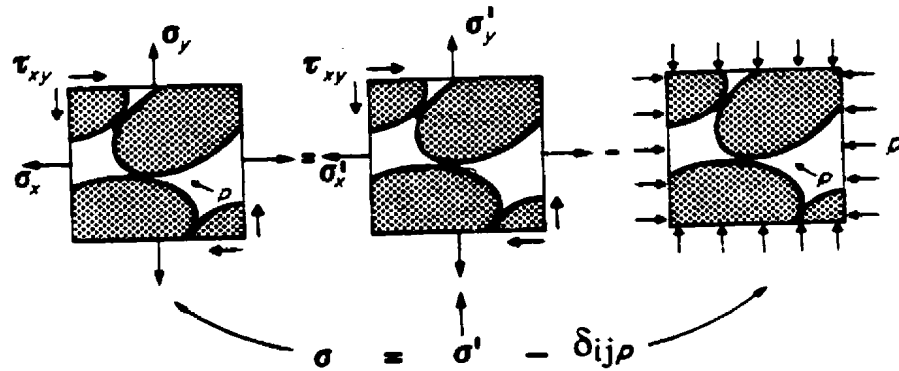


Figure 3.3.1 Total and effective stresses in soil [Lewis & Schrefler, 1987].

The constitutive equation relating the effective stress to the strain of the skeleton is independent of pore pressure, p , and for a general non-linear material can be written in an incremental form, thus allowing plasticity effects to be incorporated. The general form for effective stress rate is given by

$$d\sigma' = D_T(d\varepsilon - d\varepsilon_c - d\varepsilon_p - d\varepsilon_0) \quad (3.1a)$$

where:

$d\varepsilon$ = total strain of the skeleton,

D_T = total modulus of solid phase,

$d\varepsilon_c$ = the creep strain = $c dt$

$d\varepsilon_p = -\delta_{ij} (dp/(3K_s))$ represents the overall volumetric strains caused by uniform compression of the particle by the pressure of the pore fluid (K_s is the bulk modulus of the solid phase), and

$d\varepsilon_0$ = represents all other strains not directly associated with stress changes (i.e., swelling, thermal, chemical, and others).

The modified effective stress concept given by Zienkiewicz and Bettess [1982] states:

$$\sigma'_{ij} = \sigma_{ij} + \alpha \delta_{ij} p \quad (3.2)$$

where:

$$\alpha = \delta_{ij}^T \delta_{ji} - \frac{\delta_{ij}^T D_T \delta_{ij}}{3K_S} = 1 - K_T/K_S \leq 1 \quad (3.2a)$$

and K_T and K_S are porous medium bulk modulus and solid phase bulk modulus, respectively. The constitutive equation in rate form, accounting for Jaumann stress rate (representing material independence during large deformation [Khan & Huang, 1995; Cheng & Tsui, 1992; Zienkiewicz et al., 1990a]) in the last two terms for finite deformation, is given by,

$$d\sigma'_{ij} = D_{ijkl} (d\varepsilon_{kl} - d\varepsilon_{kl}^0) + \sigma'_{ik} d\omega_{kj} + \sigma'_{jk} d\omega_{ki} \quad (3.3)$$

$$d\varepsilon_{ij} = \frac{1}{2} (du_{i,j} + du_{j,i}); \quad d\omega_{ij} = \frac{1}{2} (du_{j,i} - du_{i,j}) \quad (3.4)$$

Since fluid velocity is relative, it is considered in relation to solid particle velocity, and gives the real velocity of porous fluid:

$$\dot{U} = \dot{u} + \dot{w} / n \quad (3.5)$$

where:

n = porosity; \dot{u} = solid velocity; and

\dot{w} = relative velocity of fluid (water) to solid.

Mass density of the porous media is given by

$$\rho = n\rho_f + (1-n)\rho_s \quad (3.5a)$$

where:

ρ_f = mass density of fluid phase; and ρ_s = mass density of solid phase.

Mass Conservation.

The continuity relationship showing the balance between inflow and outflow into or from a certain volume of soil from its surrounding surface is given by:

In Cartesian or Lagrangian form:

- For solid:

$$\begin{aligned} \frac{DM_s}{Dt} &= \frac{D}{Dt} \int (1-n)\rho_s dV = \int \left((1-n) \frac{\partial \rho_s}{\partial t} + (1-n) \rho_s \frac{\partial \dot{u}}{\partial x} \right) dV = 0 \\ (1-n) \frac{\partial \rho_s}{\partial t} + (1-n) \rho_s \frac{\partial \dot{u}}{\partial x} &= 0 \quad \Rightarrow \quad (1-n) \frac{1}{\rho_s} \frac{\partial \rho_s}{\partial t} + (1-n) \frac{\partial \dot{u}}{\partial x} = 0 \quad (3.6) \end{aligned}$$

- For fluid:

$$\frac{DM_w}{Dt} = \frac{D}{Dt} \int n\rho_w dV = \int \left(n \frac{\partial \rho_w}{\partial t} + n\rho_w \frac{\partial \dot{U}}{\partial x} \right) dV = 0$$

In spatial or Eulerian form:

$$\begin{aligned} n \frac{\partial \rho_w}{\partial t} + (\dot{w}/n)n \frac{\partial \rho_w}{\partial x} + n\rho_w \frac{\partial \dot{U}}{\partial x} &= 0 \\ \Rightarrow \frac{n}{\rho_w} \frac{\partial \rho_w}{\partial t} + \frac{\dot{w}}{\rho_w} \frac{\partial \rho_w}{\partial x} + n \frac{\partial \dot{u}}{\partial x} + \frac{\partial \dot{w}}{\partial x} &= 0 \quad (3.7) \end{aligned}$$

Addition of Equation (3.6) and (3.7), gives:

$$\frac{(1-n)}{\rho_s} \frac{\partial \rho_s}{\partial t} + (1-n) \frac{\partial \dot{u}}{\partial x} + \frac{n}{\rho_w} \frac{\partial \rho_w}{\partial t} + \frac{\dot{w}}{\rho_w} \frac{\partial \rho_w}{\partial x} + n \frac{\partial \dot{u}}{\partial x} + \frac{\partial \dot{w}}{\partial x} = 0$$

$$\Rightarrow \frac{(1-n) \partial \rho_s}{\rho_s \partial t} + \frac{\partial \dot{u}}{\partial x} + \frac{n \partial \rho_w}{\rho_w \partial t} + \frac{\dot{w} \partial \rho_w}{\rho_w \partial x} + \frac{\partial \dot{w}}{\partial x} = 0 \quad (3.8)$$

Considering the rate of volume change of solid, it is influenced by:

Rate of change of pressure, p , giving change of solid volume: $\frac{(1-n) \partial p}{K_s \partial t}$

Rate of change of effective stress, σ' , giving change of solid volume:

$$-\frac{1}{3K_s} \delta_{ij} \frac{\partial \sigma'}{\partial t}.$$

Hence, summation of the above definition gives the mass conservation conditions:

$$\frac{(1-n) \partial \rho_s}{\rho_s \partial t} = \frac{(1-n) \partial p}{K_s \partial t} - \frac{1}{3K_s} \delta_{ij} \frac{\partial \sigma'}{\partial t}$$

Substitution of Equation (3.2) into this equation represents mass conservation for solid phase as follows:

$$\frac{(1-n) \partial \rho_s}{\rho_s \partial t} = \frac{(1-n) \partial p}{K_s \partial t} - \frac{D_T}{3K_s} \delta_{ij} \tau \left(\frac{\partial \epsilon}{\partial t} - \frac{\delta_{ij}}{3K_s} \frac{\partial p}{\partial t} \right) \quad (3.9)$$

Moreover, mass conservation for the fluid is given as follows:

$$\frac{(1-n) \partial \rho_w}{\rho_s \partial t} = (\alpha - 1) \frac{\partial \epsilon}{\partial t} + \frac{(\alpha - n) \partial p}{K_s \partial t} \quad (3.10a)$$

$$\frac{n \partial \rho_w}{\rho_w \partial t} = \frac{n \partial p}{K_w \partial t} \quad (3.10b)$$

where K_w is the bulk modulus of water. Substitution of equations (3.9) and (3.10) into equation (3.8) gives

$$\alpha \dot{\epsilon} + \frac{(\alpha - n)}{K_s} \dot{p} + \frac{n}{K_w} \dot{p} + \dot{w}_x + \frac{\dot{w}}{\rho_w} \rho_w = 0 \quad (3.11)$$

Momentum conservation

The momentum principle for a collection of particles states that the time rate of change of the total momentum of a given set of particles equals the vector sum of all external forces acting on the particles of the set, provided Newton's Third Law of action and reaction governs the internal forces.

A. Overall momentum conservation for a unit volume of soil mixture is given by:

$$\sigma_{ij,j} - \rho \ddot{u}_i - n \rho_f \frac{d}{dt} \left(\frac{\dot{w}_i}{n} \right) + \rho b_i = 0 \quad (3.12)$$

where b_i = body forces

When the relative magnitude of accelerations of the fluid compared to solid phase is not significant, the relative acceleration terms of the fluid may be omitted [Zienkiewicz et al., 1980, 1982]. Consequently, the simplified equation can be given as:

$$\sigma_{ij,j} - \rho \ddot{u}_i + \rho b_i = 0 \quad (3.13)$$

Substituting for the definition of Equation (3.2) one obtains:

$$\sigma'_{ij,j} - \rho \ddot{u}_i + \rho b_i - \alpha p_{w,i} = 0 \quad (3.14)$$

However for a quasi-static condition, we may omit the inertial part. Therefore, the above two equations become as follows:

$$\sigma_{ij,j} + \rho b_i = 0 \quad (3.13a)$$

$$\sigma'_{ij,j} + \rho b_i - \alpha p_{w,i} = 0 \quad (3.14a)$$

B. Momentum equilibrium equation for the fluid is given by:

$$-n p_{,i} - R_i - n \rho_f \ddot{u}_i - n \rho_f \frac{d}{dt} \left(\frac{\dot{w}_i}{n} \right) + n \rho_f b_i = 0 \quad (3.15)$$

where R_i is the viscous drag force acting on fluid phase which can be written according to Darcy's law as:

$$k_{ij} R_j / n = w_i \quad (3.16)$$

where:

k_{ij} = permeability of the soil; and w_i = relative displacement of water to solid.

Substitution of Equation (3.16) in (3.15) gives:

$$-p_{w,i} - k_{ij}^{-1} w_j - \rho_f \ddot{u}_i - \rho_f \frac{d}{dt} (\dot{w}_i / n) + \rho_f b_i = 0 \quad (3.17)$$

By omitting the relative acceleration term in Equation (3.17) Darcy's velocity of the fluid phase can be given as:

$$w_j = k_{ij} (-\rho_f \ddot{u}_i + \rho_f b_i - p_{w,i})$$

The above equation is used to eliminate w in Equation (3.11) giving:

$$\alpha \dot{\epsilon}_{ii} - (k_{ij} p_{w,j})_{,i} + \frac{\dot{P}}{Q} + (k_{ij} \rho_f b_j)_{,i} - \{k_{ij} (\rho_f \ddot{u}_f)\}_{,i} = 0 \quad (3.18)$$

where :

$$\frac{1}{Q} = \frac{n}{K_T} + \frac{(\alpha - n)}{K_s}$$

However, again for a quasi-static condition, we may omit the inertial part. Therefore, the above equation becomes as follows:

$$\alpha \dot{\epsilon}_{ii} - (k_{ij} p_{w,j})_{,i} + \frac{\dot{P}}{Q} + (k_{ij} \rho_f b_j)_{,i} = 0 \quad (3.18a)$$

Discretization and numerical solution

To obtain a numerical solution a suitable discretization process becomes essential. Using finite element procedures for both spatial and time discretization, the spatial approximation is given by

$$\mathbf{u} = \mathbf{u}(t) = \mathbf{N}^u \bar{\mathbf{u}}(t) \quad \mathbf{p} = \mathbf{p}(t) = \mathbf{N}^p \bar{\mathbf{p}}(t) \quad (3.19)$$

where \mathbf{N}^u and \mathbf{N}^p are approximate shape functions and $\bar{\mathbf{u}}$ and $\bar{\mathbf{p}}$ are a finite set of parameters. Equations (3.14) and (3.18) can now be transformed into a set of algebraic equations in space with only time derivatives remaining by the use of an appropriate Galerkin statement. Thus pre-multiplying equation (3.14) by $[\mathbf{N}^u]^T$ and integrating over the spatial domain (after the use of Green's theorem and insertion of boundary conditions) results in:

$$\int_{\Omega} \mathbf{B}^T \boldsymbol{\sigma} d\Omega + \left[\int_{\Omega} \mathbf{N}^{uT} \rho \mathbf{N}^u d\Omega \right] \ddot{\mathbf{u}} = \mathbf{f}^{(1)} \quad (3.20)$$

where \mathbf{B} is the well known strain matrix relating the increments of strain and displacement,

$$d\boldsymbol{\varepsilon} = \mathbf{B} d\bar{\mathbf{u}}$$

The load vector $\mathbf{f}^{(1)}$ contains the body forces, boundary tractions, and prescribed boundary values.

$$\mathbf{f}^{(1)} = \int_{\Omega} \mathbf{N}^{uT} \rho \mathbf{b} d\Omega + \int_{\Gamma_1} \mathbf{N}^{uT} \bar{\boldsymbol{\tau}} d\Gamma \quad (3.21)$$

where $\bar{\boldsymbol{\tau}}$ is the prescribed traction vector on part of the boundary Γ_1 .

Substituting the definition of effective stresses in equation (3.20), one obtains

$$M\bar{u} + \int_{\Omega} B^T \sigma' d\Omega - Q\bar{p} - f^{(1)} = 0 \quad (3.22)$$

where : $M \equiv \int_{\Omega} N^{uT} \rho N^u d\Omega$ is the well known mass matrix and $Q = \int_{\Omega} B^T \alpha m N^p d\Omega$ is a coupling matrix with m being a vector equivalent to the Kronecker delta δ_{ij} . Both matrices are independent of the physical parameters of the problem (assuming constant values of α and ρ). The above discrete governing equation contains implicitly two unknown parameters \bar{u} and \bar{p} only, since the increments of stresses are given by the constitutive relation in terms of displacement increments. This relationship can be rewritten in vectorial notation as (see equation 3.3)

$$d\sigma' = D_T (B d\bar{u} - d\epsilon^0) + A^T \sigma' A B d\bar{u} \quad (3.23)$$

where A is a suitably defined matrix operator. The above allows σ' to be continuously integrated from the known initial values of the problem. The second governing equation (3.18) and its boundary conditions are similarly discretized using $[N^p]^T$ as the weighting function and this results in a set of ordinary differential equations of the form

$$Q^T \dot{\bar{u}} + H\bar{p} + S\dot{\bar{p}} - f^{(2)} = 0 \quad (3.24)$$

where Q is the matrix already defined in the previous equation, and $f^{(2)}$ represents force vector, incorporating body forces and the boundary conditions. The remaining matrices are defined below with

$$H = \int_{\Omega} (\nabla N^p)^T k \nabla N^p d\Omega \quad (3.25)$$

as the permeability matrix in which k is the matrix coefficients given by Equation (3.16).

$$S = \int_{\Omega} N^{p'} \frac{1}{Q} N^p d\Omega \quad (3.26)$$

is the compressibility matrix (frequently taken as zero) and

$$f^{(2)} = \int_{\Gamma_{-n}} N^{p'} k \frac{\partial p}{\partial n} d\Gamma - \int_{\Omega} \nabla N^{p'} k \rho_f b d\Omega + \left[\int_{\Omega} \nabla N^{p'} k \rho_f N^u d\Omega \right] \ddot{u} \quad (3.27)$$

To complete the numerical solution it is necessary to integrate the ordinary differential equations (3.22), (3.23), and (3.24) with respect to time.

It is needed to write the recurrence relation linking known values of \bar{u}_n , $\dot{\bar{u}}_n$, and \bar{p}_n available at time t_n with the values of \bar{u}_{n+1} , $\dot{\bar{u}}_{n+1}$, \bar{p}_{n+1} , which are valid at time $t + \Delta t$ and are the unknowns. If we assume that the Equations (3.22) and (3.24) have to be satisfied at each discrete time and $\ddot{\bar{u}}_n$ and $\dot{\bar{p}}_n$ are added to the known conditions at t_n with $\ddot{\bar{u}}_{n+1}$ and $\dot{\bar{p}}_{n+1}$ remaining as unknowns we require that

$$M \ddot{\bar{u}}_{n+1} + \left(\int_{\Omega} B^T \sigma' d\Omega \right)_{n+1} - Q \bar{p}_{n+1} - f_{n+1}^{(1)} = 0 \quad (3.28)$$

$$Q^T \dot{\bar{u}}_{n+1} + H_{n+1} \bar{p}_{n+1} + S_{n+1} \dot{\bar{p}}_{n+1} - f_{n+1}^{(2)} = 0 \quad (3.29)$$

and that Equation (3.23) is satisfied. The link between the successive values is provided by a truncated series expansion taken in the simplest case as

$$\dot{\bar{u}}_{n+1} = \dot{\bar{u}}_n + \ddot{\bar{u}}_n \Delta t + \Delta \ddot{\bar{u}}_n \beta_1 \Delta t \quad (3.30a)$$

$$\bar{u}_{n+1} = \bar{u}_n + \dot{\bar{u}}_n \Delta t + \frac{1}{2} \ddot{\bar{u}}_n \Delta t^2 + \frac{1}{2} \Delta \ddot{\bar{u}}_n \beta_2 \Delta t^2 \quad (3.30b)$$

$$\bar{p}_{n+1} = \bar{p}_n + \dot{\bar{p}}_n \Delta t + \Delta \dot{\bar{p}}_n \theta \Delta t \quad (3.30c)$$

where : $\Delta \ddot{\bar{u}}_n = \ddot{\bar{u}}_{n+1} - \ddot{\bar{u}}_n$ and $\Delta \dot{\bar{p}}_n = \dot{\bar{p}}_{n+1} - \dot{\bar{p}}_n$

are as yet undetermined quantities. The parameters β_1 , β_2 and θ are chosen in the range

0 - 1 but for unconditional stability of the recurrence scheme we require [Zienkiewicz & Taylor, 1985]

$$\beta_2 \geq \beta_1 \geq 1/2 \quad \text{and} \quad \theta \geq 1/2 ,$$

and their optimal choice is a matter of computational convenience, the discussion of which can be found in literature [Prévost, 1987]. Insertion of relations given in Equation (3.30) into Equations (3.28) and (3.29) yields a general nonlinear equation set in which only $\Delta \ddot{\bar{u}}_n$ and $\Delta \dot{\bar{p}}_n$ remain as unknowns.

This can be written as

$$\begin{aligned} \Psi_{n+1}^{(1)} &= M_{n+1} \Delta \ddot{\bar{u}}_n + P(u_{n+1}) - Q_{n+1} \theta \Delta t \Delta \dot{\bar{p}}_n - F_{n+1}^{(1)} = 0 \\ \Psi_{n+1}^{(2)} &= Q_{n+1}^T \beta_1 \Delta t \Delta \ddot{\bar{u}}_n + H_{n+1} \theta \Delta t \Delta \dot{\bar{p}}_n + S_{n+1} \Delta \dot{\bar{p}}_n - F_{n+1}^{(2)} = 0 \end{aligned} \quad (3.31)$$

where $F_{n+1}^{(1)}$ and $F_{n+1}^{(2)}$ can be evaluated explicitly from the information at time n and

$$P(u_{n+1}) = \int_{\Omega} B_{n+1}^T \sigma'_{n+1} d\Omega = \int_{\Omega} B^T \Delta \sigma'_n d\Omega + P(u_n) \quad (3.32)$$

$\Delta \sigma'_n$ is evaluated by integrating Equation (3.23) and \bar{u}_{n+1} is defined by Equation (3.30).

The equation will generally need to be solved by a convergent, iterative process using some form of the Newton procedure typically written as

$$J \begin{Bmatrix} \Delta \ddot{\bar{u}}_n \\ \Delta \dot{\bar{p}}_n \end{Bmatrix}^{l+1} = - \begin{Bmatrix} \Psi_{n+1}^{(1)} \\ \Psi_{n+1}^{(2)} \end{Bmatrix}^l ; \quad \text{where, } l \text{ is the iteration number.} \quad (3.33)$$

The Jacobian matrix can be written as

$$J \begin{bmatrix} \partial\Psi^{(1)}/\partial(\Delta\ddot{u}_n), & \partial\Psi^{(1)}/\partial(\Delta\dot{\bar{p}}_n) \\ \partial\Psi^{(2)}/\partial(\Delta\ddot{u}_n), & \partial\Psi^{(2)}/\partial(\Delta\dot{\bar{p}}_n) \end{bmatrix} = \begin{bmatrix} M + K_T & \beta_2 \frac{1}{2} \Delta t^2, & -Q\theta\Delta t^2 \\ Q^T \beta_1 \Delta t, & H_{n+1} \theta \Delta t + S_{n+1} \end{bmatrix} \quad (3.34)$$

where:

$$K_T = \int_{\Omega} B^T D_T B d\Omega + \int_{\Omega} B^T A^T \sigma' A B d\Omega \quad (3.35)$$

where K_T contains the well known tangent stiffness matrix and initial stiffness matrices evaluated in the current configuration.

While considering the long-term deformation of a suction anchor foundation, since consolidation is a quasistatic phenomenon, the inertial parts are neglected and Equations (3.28) and (3.29) get reduced to:

$$\begin{aligned} \int_{\Omega} B^T \sigma' d\Omega - Q\bar{p} - f^{(1)} &= 0 \\ Q^T \ddot{u} + H\bar{p} + S\dot{\bar{p}} - f^{(2)} &= 0 \\ f^{(1)} &= \int_{\Omega} N^{u^T} \rho \rho b d\Omega - \int_{\Omega} N^{u^T} r d\Omega + \int_{\Gamma_1} N^{u^T} \bar{t} d\Gamma \\ f^{(2)} &= \int_{\Gamma_n} N^{p^T} k \frac{\partial p}{\partial n} d\Gamma - \int_{\Omega} \nabla N^{p^T} k \rho_f b d\Omega \end{aligned} \quad (3.36)$$

These non-linear equations, obtained for quasi-static conditions, are solved in ABAQUS (1998) using Newton's method. Since the structural model and soil medium considered in this study (for analysis) are essentially axisymmetric, an axisymmetric model with possibilities for axisymmetric and asymmetric loading conditions (available in ABAQUS) is used in this study. The details of these formulations are given below for the sake of completing the above formulations.

3.3.2. ABAQUS Formulation for Static and Dynamic Response of Soil as a Porous Media using Axisymmetric Elements Allowing Asymmetric Deformation in ABAQUS

ABAQUS standard includes a library of solid elements whose geometry is initially axisymmetric and allows for asymmetric analysis in which deformation can occur about the plane $\theta = \pi/2$ in the (r, z, θ) cylindrical coordinate system of the model. The model geometry is defined in the r - z plane only. The displacements are the usual isoparametric interpolations with respect to r and z , augmented by Fourier expansions with respect to θ . Since the elements are written for deformation about the plane $\theta = \pi/2$ only, they cannot be used to model torsion of the structure about the original axis of symmetry. Because the elements are intended for asymmetric loading/deformation applications, the orthogonality properties associated with Fourier planes cannot be used to reduce the problem to a series of smaller, uncoupled cases, since the stiffness before projection onto the Fourier modes is not necessarily constant. For this reason these elements are significantly more expensive to use than the corresponding axisymmetric elements intended for axisymmetric deformations.

Interpolation

The undeformed geometry of the elements is taken to be axisymmetric with respect to the Z -axis of the coordinate system and, thus, independent of θ (see Figure 3.3.2). Taking \mathbf{i}_r , \mathbf{i}_z , and \mathbf{i}_θ to be unit vectors at a point in the radial, axial, and circumferential directions (in the undeformed state), the reference position \mathbf{X} of the point can be written as

$$\mathbf{X} = R \mathbf{i}_r + Z \mathbf{i}_z \quad (3.37)$$

where R is the original radius and Z is the position along z -axis. The displacement \mathbf{u} of the reference point is given by

$$\mathbf{u} = u_r \mathbf{i}_r + u_z \mathbf{i}_z + u_\theta \mathbf{i}_\theta \quad (3.38)$$

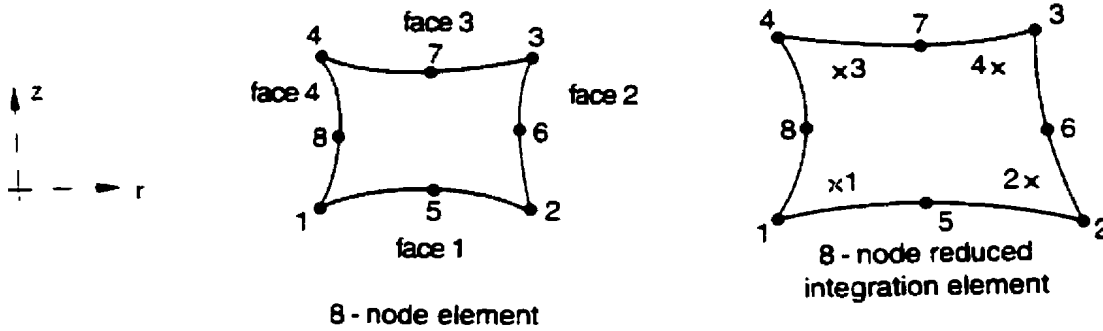


Figure 3.3.2 Axisymmetric 8-node quadratic with reduced integration points element [HKS, 1998]

The asymmetric equations associated with the above elements can be written, using Fourier series formulations as

$$u_\alpha = \sum_{m=1}^{m_1} H^m(g, h) \left(u_\alpha^{m0} + \sum_{p=1}^P (u_{\alpha r}^{mp} \cos p\theta + u_{\alpha s}^{mp} \sin p\theta) \right), \quad (\alpha = r, z, \theta) \quad (3.39)$$

where g, h are isoparametric coordinates in the original R - Z plane; H^m are polynomial interpolation functions and u_α^{m0} , $u_{\alpha r}^{mp}$, and $u_{\alpha s}^{mp}$ are solution amplitude values. m_1 is the number of terms used for interpolation with respect to g, h ; and P is the number of terms used in the Fourier interpolation with respect to θ . Purely axisymmetric deformation results when $P = 0$.

The number of variables to be considered in analysis are reduced by assuming that deformation is allowed only about one plane, $\theta = \pi/2$, so that the plane $\theta = 2n\pi$, n integer, is a plane of symmetry. The terms satisfying this condition are given as:

$$\begin{pmatrix} u_r \\ u_z \\ u_\theta \end{pmatrix} = \sum_{m=1}^{m_1} H^m(g, h) \left(\begin{pmatrix} u_r^{m0} \\ u_z^{m0} \\ 0 \end{pmatrix} + \sum_{p=1}^P \begin{pmatrix} u_{rc}^{mp} \\ u_{zc}^{mp} \\ 0 \end{pmatrix} \cos p\theta + \sum_{p=1}^P \begin{pmatrix} 0 \\ 0 \\ u_{\theta s}^{mp} \end{pmatrix} \sin p\theta \right) \quad (3.40)$$

For ease in calculation, u_r and u_z displacement components are used only at specific locations around the model between $\theta = 0$ and $\theta = \pi$ instead of the Fourier amplitudes u_r^{m0} and u_{rc}^{mp} (c is used for cos term and s for sin term). This is accurate only if the relative displacements in the θ -direction are small so that the interface conditions are considered with respect to u_r and u_z only; that is, in planes of constant θ . In addition, the subscripts c and s are omitted in the expression for radial, vertical, and circumferential displacements: $u_{rc}^{mp} \rightarrow u_r^{mp}$, $u_{zc}^{mp} \rightarrow u_z^{mp}$, and $u_{\theta s}^{mp} \rightarrow u_\theta^{mp}$. Equation (3.40) is then rewritten as:

$$\begin{pmatrix} u_r \\ u_z \\ u_\theta \end{pmatrix} = \sum_{m=1}^{m_1} H^m(g, h) \left(\sum_{p=1}^{P+1} G^p(\theta) \begin{pmatrix} u_r^{mp} \\ u_z^{mp} \\ 0 \end{pmatrix} + \sum_{p=1}^P \begin{pmatrix} 0 \\ 0 \\ u_\theta^{mp} \end{pmatrix} \sin p\theta \right) \quad (3.41)$$

where $G^p(\theta)$ are trigonometric functions and u_r^{mp} , u_z^{mp} and u_θ^{mp} are physical radial, axial, and circumferential displacements at $\theta = \pi(p-1)/P$ (see Figure 3.3.3). The G^p terms at the associated positions θ_p are taken as:

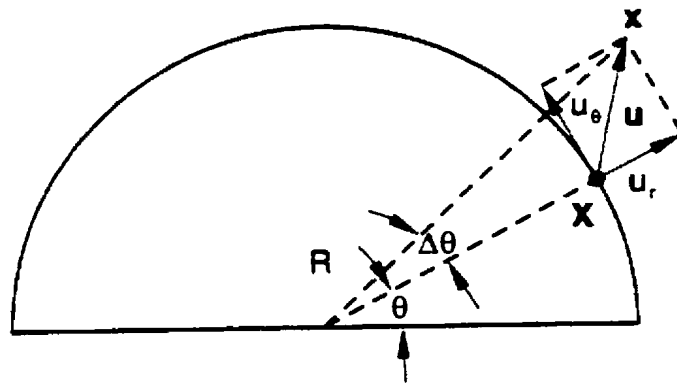


Figure 3.3.3 Displacement and rotation in r - θ plane [HKS, 1998]

$P = 1$:

$$G^1 = 1/2(1 + \cos \theta) \quad \text{and} \quad \theta_1 = 0$$

$$G^2 = 1/2(1 - \cos \theta) \quad \theta_2 = \pi$$

$P = 2$:

$$G^1 = 1/4(1 + 2 \cos \theta + \cos 2\theta) \quad \text{and} \quad \theta_1 = 0$$

$$G^2 = 1/2(1 - \cos 2\theta) \quad \theta_2 = \pi/2$$

$$G^3 = 1/4(1 - 2 \cos \theta + \cos 2\theta) \quad \theta_3 = \pi$$

$P = 3$:

$$G^1 = 1/6(1 + 2 \cos \theta + 2 \cos 2\theta + \cos 3\theta) \quad \text{and} \quad \theta_1 = 0$$

$$G^2 = 1/3(1 + \cos \theta - \cos 2\theta - \cos 3\theta) \quad \theta_2 = \pi/3$$

$$G^3 = 1/3(1 - \cos \theta - \cos 2\theta + \cos 3\theta) \quad \theta_3 = 2\pi/3$$

$$G^4 = 1/6(1 - 2 \cos \theta + 2 \cos 2\theta - \cos 3\theta) \quad \theta_4 = \pi$$

$P = 4$:

$$\begin{aligned}
G^1 &= 1/8(1 + 2 \cos \theta + 2 \cos 2\theta + 2 \cos 3\theta + \cos 4\theta) & \text{and } \theta_1 &= 0 \\
G^2 &= 1/4(1 + \sqrt{2} \cos \theta - \sqrt{2} \cos 3\theta - \cos 4\theta) & \theta_2 &= \pi/4 \\
G^3 &= 1/4(1 - 2 \cos \theta + \cos 4\theta) & \theta_3 &= \pi/2 \\
G^4 &= 1/4(1 - \sqrt{2} \cos \theta + \sqrt{2} \cos 3\theta - \cos 4\theta) & \theta_4 &= 3\pi/4 \\
G^5 &= 1/8(1 - 2 \cos \theta + 2 \cos 2\theta - 2 \cos 3\theta + \cos 4\theta) & \theta_5 &= \pi \quad (3.42)
\end{aligned}$$

$P = 4$ is the highest-order of interpolation available in ABAQUS with respect to θ in these elements; the elements become significantly more expensive as higher-order interpolation above $P = 4$ is used. It is also assumed that, full three-dimensional modeling is less expensive than using these elements when $P > 4$.

The integration scheme used in these elements consists of integration with respect to element coordinates in surfaces that were originally in the R-Z plane and integration with respect to θ . For the former the same scheme is used as in the case of corresponding purely axisymmetric elements (for example, either full or reduced Gauss integration in the isoparametric eight-noded quadrilaterals). For integration with respect to θ the trapezoidal rule is used, with the number of integration points set to $2(P + 1)$.

Deformation Gradient and Increments in Strain and Rotation

For a point in space, the deformation gradient vector \mathbf{F} is defined as the gradient of the current position vector \mathbf{x} with respect to the original position vector \mathbf{X} :

$$\mathbf{F} = \frac{\partial \mathbf{x}}{\partial \mathbf{X}} \quad (3.43)$$

The position \mathbf{x} can be described in terms of the position \mathbf{X} and the displacement \mathbf{u} by

$$\mathbf{x} = \mathbf{X} + \mathbf{u} = (R + u_r)\mathbf{i}_r + (Z + u_z)\mathbf{i}_z + u_\theta\mathbf{i}_\theta \quad (3.44)$$

and the gradient operator can be written in terms of partial derivatives with respect to the cylindrical coordinates by

$$\frac{\partial}{\partial \mathbf{X}} = \mathbf{i}_r \frac{\partial}{\partial R} + \mathbf{i}_z \frac{\partial}{\partial Z} + \mathbf{i}_\theta \frac{\partial}{R\partial\theta} \quad (3.45)$$

Since the radial and circumferential base vectors depend on the original circumferential coordinate θ , $\mathbf{i}_r = \mathbf{i}_r(\theta)$, $\mathbf{i}_\theta = \mathbf{i}_\theta(\theta)$, their partial derivatives with respect to θ are given by

$$\frac{\partial \mathbf{i}_r}{\partial \theta} = \mathbf{i}_\theta, \quad \frac{\partial \mathbf{i}_\theta}{\partial \theta} = -\mathbf{i}_r \quad (3.46)$$

With this result the deformation gradient can be written in a matrix form by

$$[\mathbf{F}] = \begin{bmatrix} 1 + \partial u_r / \partial R & \partial u_r / \partial Z & \partial u_r / R \partial \theta - u_\theta / R \\ \partial u_z / \partial R & 1 + \partial u_z / \partial Z & \partial u_z / R \partial \theta \\ \partial u_\theta / \partial R & \partial u_\theta / \partial Z & 1 + u_r / R + \partial u_\theta / R \partial \theta \end{bmatrix} \quad (3.47)$$

Strain and rotation increments are calculated from the integrated velocity gradient matrix, $\Delta \mathbf{L}$, defined as:

$$\Delta \mathbf{L} = \frac{\partial \Delta \mathbf{u}}{\partial \mathbf{x}_{t+\Delta t/2}} \quad (3.48)$$

where $\mathbf{x}_{t+\Delta t/2} = \mathbf{x}_t + \frac{1}{2}\Delta \mathbf{u} = \mathbf{x}_{t+\Delta t} - \frac{1}{2}\Delta \mathbf{u}$. This expression is not easily evaluated directly, since points that were in R-Z plane in the undeformed shape will no longer be located in the same plane after deformation. The gradient of $\Delta \mathbf{u}$ with respect to the reference state can be written in a matrix form as

$$[\Delta \mathbf{L}] = [\partial \Delta \mathbf{u} / \partial \mathbf{X}] \left[[\mathbf{F}] - \frac{1}{2} [\partial \Delta \mathbf{u} / \partial \mathbf{X}] \right]^{-1} \quad (3.49)$$

where

$$[\partial \Delta \mathbf{u} / \partial \mathbf{X}] = \begin{bmatrix} \partial \Delta u_r / \partial R & \partial \Delta u_r / \partial Z & \partial \Delta u_r / R \partial \theta - \partial \Delta u_\theta / R \\ \partial \Delta u_z / \partial R & \partial \Delta u_z / \partial Z & \partial \Delta u_z / R \partial \theta \\ \partial \Delta u_\theta / \partial R & \partial \Delta u_\theta / \partial Z & \partial \Delta u_\theta / R \partial \theta + \Delta u_r / R \end{bmatrix}$$

The strain increments are approximated as the symmetric part of $\Delta \mathbf{L}$, viz.,

$$[\Delta \boldsymbol{\varepsilon}] = \frac{1}{2} \left[[\Delta \mathbf{L}] + [\Delta \mathbf{L}]^T \right] \quad (3.50)$$

The volume strain increment is also modified in the fully integrated 8-node quadrilaterals (or reduced integration for 8-node quadrilaterals) to be independent of g and h in an r - Z plane, which yields,

$$[\Delta \bar{\boldsymbol{\varepsilon}}] = \frac{1}{2} \left[[\Delta \bar{\mathbf{L}}] + [\Delta \bar{\mathbf{L}}]^T \right],$$

$$\text{with } [\Delta \bar{\mathbf{L}}] = [\Delta \mathbf{L}] + \frac{1}{3} \left(\text{tr}(\Delta \mathbf{L}^0) - \text{tr}(\Delta \mathbf{L}) \right) [\mathbf{I}] \quad (3.51)$$

where $[\mathbf{I}]$ is the unit matrix, $\text{tr}(\Delta \mathbf{L}) = \Delta L_{rr} + \Delta L_{zz} + \Delta L_{\theta\theta}$ is the volume strain increment at the integration point, and $\text{tr}(\Delta \mathbf{L}^0)$ is the average value of volume strain increment over the R - Z plane of the element.

Virtual work

Virtual work method is used in the formulation of the equilibrium equation for the tension foundation. Equilibrium equation (by virtual work) requires linearization of the strain-displacement relationships. For fully integrated 8-node elements (or 8-node elements with reduced integration) the volume strain modification gives

$$\delta \bar{\boldsymbol{\varepsilon}} = \frac{1}{2} (\delta \bar{\mathbf{L}} + \delta \bar{\mathbf{L}}^T),$$

where

$$\delta \bar{\mathbf{L}} = \delta \mathbf{L} + \frac{1}{3} \left[\text{tr}(\delta \mathbf{L}^0) - \text{tr}(\delta \mathbf{L}) \right] \mathbf{I} \quad \text{and} \quad \delta \mathbf{L} = \frac{\partial \delta \mathbf{u}}{\partial \mathbf{x}} \quad (3.52)$$

The linearized strain-displacement relation formulation involves taking derivatives in the deformed shape ($\mathbf{x} = \mathbf{x}_{t+\Delta t}$). As given earlier, this can be written in matrix form as:

$$[\delta \mathbf{L}] = [\partial \delta \mathbf{u} / \partial \mathbf{X}] [\mathbf{F}]^{-1}, \quad (3.53)$$

where

$$[\partial \delta \mathbf{u} / \partial \mathbf{X}] = \begin{bmatrix} \partial \delta u_r / \partial R & \partial \delta u_r / \partial Z & \partial \delta u_r / R \partial \theta - \delta u_\theta / R \\ \partial \delta u_z / \partial R & \partial \delta u_z / \partial Z & \partial \delta u_z / R \partial \theta \\ \partial \delta u_\theta / \partial R & \partial \delta u_\theta / \partial Z & \partial \delta u_\theta / R \partial \theta + \delta u_r / R \end{bmatrix}$$

Interpolating in terms of nodal displacement variations, the derivatives of the displacements with respect to R, Z, and θ are obtained as,

$$\begin{aligned} \begin{Bmatrix} \partial u_r / \partial R \\ \partial u_z / \partial R \\ \partial u_\theta / \partial R \end{Bmatrix} &= \sum_{m=1}^{m_1} \frac{\partial H^m}{\partial R} \left(\sum_{p=1}^{P+1} G^p(\theta) \begin{Bmatrix} u_r^{mp} \\ u_z^{mp} \\ 0 \end{Bmatrix} + \sum_{p=1}^P \begin{Bmatrix} 0 \\ 0 \\ u_\theta^{mp} \end{Bmatrix} \sin p\theta \right), \\ \begin{Bmatrix} \partial u_r / \partial Z \\ \partial u_z / \partial Z \\ \partial u_\theta / \partial Z \end{Bmatrix} &= \sum_{m=1}^{m_1} \frac{\partial H^m}{\partial Z} \left(\sum_{p=1}^{P+1} G^p(\theta) \begin{Bmatrix} u_r^{mp} \\ u_z^{mp} \\ 0 \end{Bmatrix} + \sum_{p=1}^P \begin{Bmatrix} 0 \\ 0 \\ u_\theta^{mp} \end{Bmatrix} \sin p\theta \right), \\ \begin{Bmatrix} \partial u_r / \partial \theta \\ \partial u_z / \partial \theta \\ \partial u_\theta / \partial \theta \end{Bmatrix} &= \sum_{m=1}^{m_1} H^m \left(\sum_{p=1}^{P+1} \frac{G^p(\theta)}{\partial \theta} \begin{Bmatrix} u_r^{mp} \\ u_z^{mp} \\ 0 \end{Bmatrix} + \sum_{p=1}^P \begin{Bmatrix} 0 \\ 0 \\ u_\theta^{mp} \end{Bmatrix} \sin p\theta \right). \end{aligned} \quad (3.54)$$

Since u_r and u_z are dependent on local element coordinate g and h , they are related by

$$\begin{bmatrix} \frac{\partial H}{\partial g} \\ \frac{\partial H}{\partial h} \end{bmatrix} = \begin{bmatrix} \frac{\partial R}{\partial g} & \frac{\partial Z}{\partial g} \\ \frac{\partial R}{\partial h} & \frac{\partial Z}{\partial h} \end{bmatrix} \begin{bmatrix} \frac{\partial H}{\partial R} \\ \frac{\partial H}{\partial Z} \end{bmatrix} = [\mathbf{J}] \begin{bmatrix} \frac{\partial H}{\partial R} \\ \frac{\partial H}{\partial Z} \end{bmatrix}; \quad \text{therefore,} \quad \begin{bmatrix} \frac{\partial H}{\partial R} \\ \frac{\partial H}{\partial Z} \end{bmatrix} = [\mathbf{J}]^{-1} \begin{bmatrix} \frac{\partial H}{\partial g} \\ \frac{\partial H}{\partial h} \end{bmatrix},$$

where.

$$[J] = \begin{bmatrix} \frac{\partial H^1}{\partial g} & \frac{\partial H^2}{\partial g} & \frac{\partial H^3}{\partial g} \\ \frac{\partial H^1}{\partial h} & \frac{\partial H^2}{\partial h} & \frac{\partial H^3}{\partial h} \end{bmatrix} \cdot \begin{bmatrix} R_1 & Z_1 \\ R_2 & Z_2 \\ R_3 & Z_3 \end{bmatrix},$$

and, for a second order eight-noded quadrilateral element, the shape functions H^m are given by

$$\begin{bmatrix} H^1(g, h) \\ H^2(g, h) \\ H^3(g, h) \\ H^4(g, h) \\ H^5(g, h) \\ H^6(g, h) \\ H^7(g, h) \\ H^8(g, h) \end{bmatrix} = \begin{bmatrix} \frac{1}{4}(1-g)(1-h)(1+g+h) \\ \frac{1}{4}(1+g)(1-h)(1-g+h) \\ \frac{1}{4}(1+g)(1+h)(1-g-h) \\ \frac{1}{4}(1-g)(1+h)(1+g-h) \\ \frac{1}{2}(1-g)(1+g)(1-h) \\ \frac{1}{2}(1-h)(1+h)(1+g) \\ \frac{1}{2}(1-g)(1+g)(1+h) \\ \frac{1}{2}(1-h)(1+h)(1-g) \end{bmatrix} \quad (3.55)$$

Pressure Loads and Load Stiffness

For a geometrically symmetric problem, equivalent nodal loads due to applied surface pressures (due to soil and pore fluids) and body forces are readily calculated since the geometry is axisymmetric. For a geometrically asymmetric problem, the presence of body forces does not change the formulation because of the fixed direction of the forces and because the forces are proportional to the volume (which changes by a negligible

amount). However for surface pressures, the effect of non-axisymmetric (or asymmetric) deformations must be taken into account. The equivalent nodal loads associated with surface pressure p are obtained considering the virtual work contributions, viz.,

$$\int_A p \mathbf{n} \cdot \delta \mathbf{u} dA = \int_0^{2\pi} \int_{-1}^1 p \left(\frac{\partial \mathbf{x}}{\partial \xi} \times \frac{\partial \mathbf{x}}{\partial \theta} \right) \cdot \delta \mathbf{x} d\xi d\theta \quad (3.56)$$

where ξ is the parametric surface coordinate in the R-Z plane and

$$\mathbf{x} = r \mathbf{i}_r + z \mathbf{i}_z + u_\theta \mathbf{i}_\theta \quad (3.57)$$

with $r = R + u_r$ and $z = Z + u_z$. Hence, the current position of a point can be expressed as

$$\begin{Bmatrix} r \\ z \\ u_\theta \end{Bmatrix} = \sum_{m=1}^m h^m(\xi) \left(\sum_{p=1}^{p+1} G^p(\theta) \begin{Bmatrix} r^{mp} \\ z^{mp} \\ 0 \end{Bmatrix} + \sum_{p=1}^p \begin{Bmatrix} 0 \\ 0 \\ u_\theta^{mp} \end{Bmatrix} \sin p\theta \right) \quad (3.58)$$

Evaluating Equation (3.56),

$$\frac{\partial \mathbf{x}}{\partial \xi} = \frac{\partial r}{\partial \xi} \mathbf{i}_r + \frac{\partial z}{\partial \xi} \mathbf{i}_z + \frac{\partial u_\theta}{\partial \xi} \mathbf{i}_\theta, \quad \frac{\partial \mathbf{x}}{\partial \theta} = \left(\frac{\partial r}{\partial \theta} - u_\theta \right) \mathbf{i}_r + \frac{\partial z}{\partial \theta} \mathbf{i}_z + \left(r + \frac{\partial u_\theta}{\partial \theta} \right) \mathbf{i}_\theta \quad (3.59)$$

and,

$$\begin{aligned} \frac{\partial \mathbf{x}}{\partial \xi} \times \frac{\partial \mathbf{x}}{\partial \theta} = & \left[-\frac{\partial z}{\partial \xi} \left(r + \frac{\partial u_\theta}{\partial \theta} \right) + \frac{\partial u_\theta}{\partial \xi} \frac{\partial z}{\partial \theta} \right] \mathbf{i}_r + \left[-\frac{\partial u_\theta}{\partial \xi} \left(\frac{\partial r}{\partial \theta} - u_\theta \right) + \frac{\partial r}{\partial \xi} \left(r + \frac{\partial u_\theta}{\partial \theta} \right) \right] \mathbf{i}_z + \\ & \left[-\frac{\partial z}{\partial \xi} \frac{\partial z}{\partial \theta} + \frac{\partial z}{\partial \xi} \left(\frac{\partial r}{\partial \theta} - u_\theta \right) \right] \mathbf{i}_\theta \end{aligned} \quad (3.60)$$

Hence, the virtual work contribution is obtained as:

$$\begin{aligned} \int_A p \mathbf{n} \cdot \delta \mathbf{u} dA = & \int_0^{2\pi} \int_{-1}^1 -p \left\{ \left[\frac{\partial z}{\partial \xi} \left(r + \frac{\partial u_\theta}{\partial \theta} \right) - \frac{\partial u_\theta}{\partial \xi} \frac{\partial z}{\partial \theta} \right] \delta u_r + \right. \\ & \left. \left[\frac{\partial u_\theta}{\partial \xi} \left(\frac{\partial r}{\partial \theta} - u_\theta \right) - \frac{\partial r}{\partial \xi} \left(r + \frac{\partial u_\theta}{\partial \theta} \right) \right] \delta u_z + \left[\frac{\partial z}{\partial \xi} \frac{\partial z}{\partial \theta} - \frac{\partial z}{\partial \xi} \left(\frac{\partial r}{\partial \theta} - u_\theta \right) \right] \delta u_\theta \right\} d\xi d\theta \end{aligned} \quad (3.61)$$

The equivalent nodal forces are also obtained as follows using the interpolation function:

$$\begin{aligned}
F_r^{mp} &= \int_0^{2\pi} \int_{-1}^{+1} -ph^m(\xi) G^p(\theta) \left[\frac{\partial z}{\partial \xi} \left(r + \frac{\partial u_\theta}{\partial \theta} \right) - \frac{\partial u_\theta}{\partial \xi} \frac{\partial z}{\partial \theta} \right] d\xi d\theta \\
F_z^{mp} &= \int_0^{2\pi} \int_{-1}^{+1} -ph^m(\xi) G^p(\theta) \left[\frac{\partial u_\theta}{\partial \xi} \left(\frac{\partial r}{\partial \theta} - u_\theta \right) - \frac{\partial r}{\partial \xi} \left(r + \frac{\partial u_\theta}{\partial \theta} \right) \right] d\xi d\theta \\
F_\theta^{mp} &= \int_0^{2\pi} \int_{-1}^{+1} -ph^m(\xi) \sin p\theta \left[\frac{\partial r}{\partial \xi} \frac{\partial z}{\partial \theta} - \frac{\partial z}{\partial \xi} \left(\frac{\partial r}{\partial \theta} - u_\theta \right) \right] d\xi d\theta
\end{aligned} \tag{3.62}$$

For a geometrically linear problem this reduces to the standard axisymmetric equivalent nodal loads as,

$$\begin{aligned}
F_r^{mp} &= \int_0^{2\pi} \int_{-1}^{+1} ph^m(\xi) G^p(\theta) \frac{\partial Z}{\partial \xi} d\xi R d\theta, & F_z^{mp} &= \int_0^{2\pi} \int_{-1}^{+1} ph^m(\xi) G^p(\theta) \frac{\partial R}{\partial \xi} d\xi R d\theta \\
F_\theta^{mp} &= 0.
\end{aligned} \tag{3.63}$$

Using linearization the load stiffness matrix is obtained as,

$$\begin{aligned}
-\begin{Bmatrix} dF_r^{mp} \\ dF_z^{mp} \\ dF_\theta^{mp} \end{Bmatrix} &= \begin{bmatrix} K_{rr}^{mpnq} & K_{rz}^{mpnq} & K_{r\theta}^{mpnq} \\ K_{zr}^{mpnq} & K_{zz}^{mpnq} & K_{z\theta}^{mpnq} \\ K_{\theta r}^{mpnq} & K_{\theta z}^{mpnq} & K_{\theta\theta}^{mpnq} \end{bmatrix} \begin{Bmatrix} du_r^{nq} \\ du_z^{nq} \\ du_\theta^{nq} \end{Bmatrix}, \text{ with} \\
K_{rr}^{mpnq} &= \int_0^{2\pi} \int_{-1}^{+1} ph^m(\xi) G^p(\theta) \frac{\partial z}{\partial \xi} h^n(\xi) G^q(\theta) d\xi d\theta \\
K_{zr}^{mpnq} &= \int_0^{2\pi} \int_{-1}^{+1} ph^m(\xi) G^p(\theta) \\
&\quad \left[-\frac{\partial r}{\partial \xi} h^n(\xi) G^q(\theta) - \left(r + \frac{\partial u_\theta}{\partial \theta} \right) \frac{\partial h^n}{\partial \xi} G^q(\theta) + \frac{\partial u_\theta}{\partial \xi} h^n(\xi) \frac{dG^q}{d\theta} \right] d\xi d\theta \\
K_{\theta r}^{mpnq} &= \int_0^{2\pi} \int_{-1}^{+1} ph^m(\xi) \sin p\theta \left[\frac{\partial z}{\partial \theta} \frac{\partial h^n}{\partial \xi} G^q(\theta) - \frac{\partial z}{\partial \xi} h^n(\xi) \frac{dG^q}{d\theta} \right] d\xi d\theta
\end{aligned}$$

$$K_{r_z}^{mpnq} = \int_0^{2\pi} \int_{-1}^{+1} p h^m(\xi) G^p(\theta) \left[\left(r + \frac{\partial u_\theta}{\partial \theta} \right) \frac{\partial h^n}{\partial \xi} G^q(\theta) - \frac{\partial u_\theta}{\partial \xi} h^n(\xi) \frac{dG^q}{d\theta} \right] d\xi d\theta$$

$$K_{z_z}^{mpnq} = 0$$

$$K_{\theta_z}^{mpnq} = \int_0^{2\pi} \int_{-1}^{+1} p h^m(\xi) \sin p\theta \left[\frac{\partial r}{\partial \xi} h^n(\xi) \frac{dG^q}{d\theta} - \left(\frac{\partial r}{\partial \theta} - u_\theta \right) \frac{\partial h^n}{\partial \xi} G^q(\theta) \right] d\xi d\theta$$

$$K_{r\theta}^{mpnq} = \int_0^{2\pi} \int_{-1}^{+1} p h^m(\xi) G^p(\theta) \left[q \frac{\partial z}{\partial \xi} h^n(\xi) \cos q\theta - \frac{\partial z}{\partial \theta} \frac{\partial h^n}{\partial \xi} \sin q\theta \right] d\xi d\theta$$

$$K_{z\theta}^{mpnq} = \int_0^{2\pi} \int_{-1}^{+1} p h^m(\xi) G^p(\theta) \left[-\frac{\partial u_\theta}{\partial \xi} h^n(\xi) \sin q\theta + \left(\frac{\partial r}{\partial \theta} - u_\theta \right) \frac{\partial h^n}{\partial \xi} \sin q\theta - q \frac{\partial r}{\partial \xi} h^n(\xi) \cos q\theta \right] d\xi d\theta$$

$$K_{\theta\theta}^{mpnq} = \int_0^{2\pi} \int_{-1}^{+1} p h^m(\xi) \sin p\theta \frac{\partial z}{\partial \xi} h^n(\xi) \sin q\theta d\xi d\theta \quad (3.64)$$

Since the hydrostatic pressure p is dependent on z , the additional terms that appear are readily obtained as:

$$\int_A p \mathbf{n} \cdot \delta \mathbf{u} dA = \int_0^{2\pi} \int_{-1}^{+1} -du_z \frac{dp}{dz} \left\{ \left[\frac{\partial z}{\partial \xi} \left(r + \frac{\partial u_\theta}{\partial \theta} \right) - \frac{\partial u_\theta}{\partial \xi} \frac{\partial z}{\partial \theta} \right] \delta u_r + \left[\frac{\partial u_\theta}{\partial \xi} \left(\frac{\partial r}{\partial \theta} - u_\theta \right) - \frac{\partial r}{\partial \xi} \left(r + \frac{\partial u_\theta}{\partial \theta} \right) \right] \delta u_z + \left[\frac{\partial r}{\partial \xi} \frac{\partial z}{\partial \theta} - \frac{\partial z}{\partial \xi} \left(\frac{\partial r}{\partial \theta} - u_\theta \right) \right] \delta u_\theta \right\} d\xi d\theta \quad (3.65)$$

With the use of the interpolation functions, the additional load stiffness contributions can be obtained as follows:

$$K_{r_z}^{mpnq} = \int_0^{2\pi} \int_{-1}^{+1} \frac{dp}{dz} h^m(\xi) G^p(\theta) \left[\frac{\partial z}{\partial \xi} \left(r + \frac{\partial u_\theta}{\partial \theta} \right) - \frac{\partial u_\theta}{\partial \xi} \frac{\partial z}{\partial \theta} \right] h^n(\xi) G^q(\theta) d\xi d\theta$$

$$K_{z_z}^{mpnq} = \int_0^{2\pi} \int_{-1}^{+1} \frac{dp}{dz} h^m(\xi) G^p(\theta) \left[\frac{\partial u_\theta}{\partial \xi} \left(\frac{\partial r}{\partial \theta} - u_\theta \right) - \frac{\partial r}{\partial \xi} \left(r + \frac{\partial u_\theta}{\partial \theta} \right) \right] h^n(\xi) G^q(\theta) d\xi d\theta$$

$$K_{\theta z}^{mpmq} = \int_0^{2\pi} \int_{-1}^{+1} \frac{dp}{dz} h^m(\xi) \sin p\theta \left[\frac{\partial r}{\partial \xi} \frac{dz}{\partial \theta} - \left(\frac{\partial r}{\partial \theta} - u_\theta \right) \right] h^n(\xi) G^q(\theta) d\xi d\theta \quad (3.66)$$

Pore Pressure Elements in Hybrid Formulation

For the hybrid formulation consisting of displacement degrees of freedom u and force degrees of freedom p , additional four noded pore pressure elements are used. In the hybrid formulation these degrees of freedom are internal to the element and represent the hydrostatic pressure in the material; these fluid elements are incompressible. In the pore pressure elements the degrees of freedom represent the hydrostatic pressure in the fluid as interpolated from the pressure variable at the external, user-defined nodes. Let the interpolation function for the (hydrostatic or pore) pressure in the r - z plane be denoted by $S^m(g,h)$. The interpolation functions are the same as for the regular axisymmetric hybrid and pore pressure elements, respectively.

Hence, the hydrostatic/pore pressure elements are chosen as

$$p(R, Z, \theta) = \sum_{m=1}^{m_1} S^m(g, h) \sum_{p=1}^P G^p(\theta) p^{mp} \quad (3.67)$$

Since higher-order terms are likely to lead to “locking” of the finite element mesh for nonaxisymmetric deformations (in the hybrid formulation), only the cosine terms as used in the interpolation function for p are used.

For a point in space in the pore pressure element, the pore pressure gradient calculation involves taking derivatives of the pore pressure with respect to the current position \mathbf{x} . This is calculated with respect to the original position \mathbf{X} , with the following transformation, viz.,

$$\frac{\partial p}{\partial \mathbf{x}} = \frac{\partial p}{\partial \mathbf{X}} \cdot \frac{\partial \mathbf{X}}{\partial \mathbf{x}} = \frac{\partial p}{\partial \mathbf{X}} \cdot \mathbf{F}^{-1} \quad (3.68)$$

where \mathbf{F} is the deformation gradient. The cylindrical components of the scalar gradient of the pore pressure with respect to \mathbf{X} are readily obtained from the following expressions, viz.,

$$\begin{aligned} \frac{\partial p}{\partial R} &= \sum_{m=1}^{m_1} \frac{\partial S^m}{\partial R} \sum_{p=1}^{P+1} G^p(\theta) p^{mp}, & \frac{\partial p}{\partial Z} &= \sum_{m=1}^{m_1} \frac{\partial S^m}{\partial Z} \sum_{p=1}^{P+1} G^p(\theta) p^{mp} \\ \frac{\partial p}{\partial \theta} &= \sum_{m=1}^{m_1} S^m \sum_{p=1}^{P+1} \frac{\partial G^p(\theta)}{\partial \theta} p^{mp} \end{aligned} \quad (3.69)$$

3.3.3. Plasticity Models in ABAQUS

Mechanical constitutive models provided in ABAQUS often consider elastic and inelastic response. The inelastic response is most commonly modeled with plasticity models. In the inelastic response models that are provided in ABAQUS, the elastic and inelastic responses are distinguished by separating the deformation into recoverable (elastic) and non-recoverable (inelastic) parts. This separation is based on the assumption that there is an additive relationship between strain rates:

$$\dot{\mathbf{E}} = \dot{\mathbf{E}}^{el} + \dot{\mathbf{E}}^{pl} \quad (3.70)$$

where $\dot{\mathbf{E}}$ is the total strain rate, $\dot{\mathbf{E}}^{el}$ is the rate of change of the elastic strain, and $\dot{\mathbf{E}}^{pl}$ is the rate of change of inelastic strain.

The total deformation, \mathbf{F} , is made up of inelastic deformation followed by purely elastic deformation (with rigid body rotation added in at any stage of the process):

$$\mathbf{F} = \mathbf{F}^{el} \cdot \mathbf{F}^{pl} \quad (3.71)$$

In considering addition of strain rate decompositions, the situation under which Equation (3.70) is a legitimate approximation to Equation (3.71) is given below. They are as follows:

1. The rate of deformation is given by the total strain rate Equation (3.70):

$$\dot{\boldsymbol{\epsilon}} = \text{sym}(\boldsymbol{L}) = \text{sym}(\dot{\boldsymbol{F}} \cdot \boldsymbol{F}^{-1}) = \text{sym}\left(\frac{\partial \boldsymbol{v}}{\partial \boldsymbol{x}}\right) \quad (3.72)$$

where \boldsymbol{v} is the velocity and \boldsymbol{x} is the current spatial position of the point under consideration:

2. When the elastic strains are small, then the approximation is consistent [Rice, 1975].

Equation (3.72) is used in all of the plasticity models that are implemented in ABAQUS. In practice the elastic strains, occurring in most of the materials, is small; this is true for the plasticity models provided for metals, soils, polymers, crushable foam, and concrete; and for each of these materials it is very unlikely that the elastic strain would be larger than a few percent (and even this would be quite unusual for metals). Thus the use of Equation (3.70) does not appear to be objectionable for the models in question, at least from a formal point of view. However, the user who needs to develop user subroutine UMAT or VUMAT for different material models in which the elastic strains and the inelastic strains may both be large should consider using Equation (3.71) directly.

The elastic part of the response is derived from an elastic strain energy density potential; the stress $\boldsymbol{\sigma}$ is defined by

$$\sigma = \frac{\partial U}{\partial \epsilon^{el}} \quad (3.73)$$

where U is the strain energy density potential. Since it is assumed that in the absence of plastic straining, the variation of elastic strain is the same as the variation in the rate of deformation, conjugacy arguments define the stress measure σ as the true (Cauchy) stress. All stress output in ABAQUS is given in this form.

The rate-independent plasticity models in ABAQUS and one of the rate-dependent models all have a region of pure elastic response. The yield function, f , defines the limit to this region of purely elastic response and is written so that

$$f(\sigma, T, H_\alpha) < 0 \quad (3.74)$$

for pure elastic response. Here T is the temperature, and H_α are a set of hardening parameters. The subscript α is introduced simply to indicate that there may be several hardening parameters, H_α ; the range of α is not specified until a particular plasticity model is defined. The hardening parameters are state variables that are introduced to allow the models to describe some of the complexity of inelastic response of real materials.

Stress states that cause the yield function to have a positive value cannot occur in rate-independent plasticity models, although this is possible in a rate-dependent model. Thus, in the rate-independent models the yield constraints are

$$f_i = 0 \quad (3.75)$$

during inelastic flow.

When the material is flowing inelastically the inelastic part of the deformation is defined by the flow rule, which can be written as

$$d\epsilon^{pl} = \sum_i d\lambda_i \frac{\partial g_i}{\partial \sigma} \quad (3.76)$$

where $g_i(\sigma, T, H_{i,\alpha})$ is the flow potential for the i th system, $d\lambda_i$ is the rate of change for time, dt , for a rate-dependent model or is a scalar measuring the amount of the plastic flow rate on the i th system. The summation is carried out over only the actively yielding systems: $d\lambda_i = 0$ for those systems for which $f_i < 0$.

For some rate-independent plasticity models the direction of flow is the same as the direction of the outward normal to the yield surface, viz.,

$$\frac{\partial g_i}{\partial \sigma} = c_i \frac{\partial f_i}{\partial \sigma} \quad (3.77)$$

where c_i is a scalar. Such a model is called an associative flow plasticity model. Materials in which dislocation motion provides the fundamental mechanisms of plastic flow, wherein there are no sudden changes in the direction of the plastic strain rate at a point (when the inelastic deformation is primarily caused by frictional mechanisms) the associative plasticity models do not give accurate representation of the behaviour. The metal plasticity models in ABAQUS (except cast iron) and the Cam clay soil model use associative flow. Cast iron, granular/polymer crushable foam, Mohr-Coulomb, Drucker-Prager/Cap, and jointed material models require non-associative flow with respect to volumetric straining and equivalent pressure stress.

The rate form of the flow rule is essential to incremental plasticity theory, because

it allows the history dependence of the response to be modeled. The final ingredient in plasticity models is the set of evolution equations for the hardening parameters. These equations can be written as

$$dH_{i,\alpha} = d\lambda_i h_{i,\alpha}(\sigma, \theta, H_{i,\beta}) \quad (3.78)$$

where $h_{i,\alpha}$ is the (rate form) hardening law for $H_{i,\alpha}$.

3.3.4. Process of Integration in Plasticity Models

The only rate equations involved in the process of integration are the evolutionary rule for hardening, the flow rule, and the strain rate decomposition. The simplest operator that provides unconditional stability for integration of rate equations is the backward Euler method; applying this method to the flow rule, given by Equation (3.76), leads to,

$$\Delta \epsilon^{pl} = \sum_i \Delta \lambda_i \frac{\partial g_i}{\partial \sigma} \quad (3.79)$$

and applying it to the hardening evolution equations given by Equation (3.78), gives

$$\Delta H_{i,\alpha} = \Delta \lambda_i h_{i,\alpha} \quad (3.80)$$

Throughout this section, any quantity not specifically associated with a time point is taken at the end of the increment (at time $t + \Delta t$). The strain rate decomposition, is integrated over a time increment as

$$\Delta \epsilon = \Delta \epsilon^{el} + \Delta \epsilon^{pl} \quad (3.81)$$

where $\Delta \epsilon$ is defined by the central difference operator:

$$\Delta \boldsymbol{\varepsilon} = \text{sym} \left[\frac{\partial \Delta \boldsymbol{x}}{\partial (\boldsymbol{x}_r + \frac{1}{2} \Delta \boldsymbol{x})} \right] \quad (3.82)$$

The total values of each strain is integrated as the sum of that strain value at the start of the increment, rotated to account for rigid body motion during the increment, and the strain increment. The rotation that accounts for rigid body motion during the increment is defined approximately using the algorithm of Hughes and Winget (1980). This allows the strain rate decomposition to be integrated into

$$\boldsymbol{\varepsilon} = \boldsymbol{\varepsilon}^{el} + \boldsymbol{\varepsilon}^{pl} \quad (3.83)$$

The problem is now algebraic from a computational viewpoint, i.e., the integrated equations of the constitutive model must be solved at the end of the increment. The algebraic problem are defined by the following set of equations, viz., (i) the strain decomposition, Equation (3.83); (ii) the elasticity, Equation (3.73); (iii) the integration flow rule, Equation (3.79); (iv) the integrated hardening law, Equation (3.80); and (v) for rate independent models, the yield constraints

$$f_i = 0$$

for active systems (systems in which $f_i < 0$ have $\Delta \lambda_i = 0$).

The flow surface is assumed to be sufficiently smooth so that its (second) derivatives with respect to stress and the hardening parameters are well defined. For rate independent models with a single yield system the algebraic problem is considered to be a problem in the components of $\Delta \boldsymbol{\varepsilon}^{pl}$. Once these components have been determined, the

elastic component together with the integrated strain rate decomposition gives the stress. The flow rule then defines $\Delta\lambda$ and the hardening laws define the increments in the hardening variables. Derivation of the equations using Newton method of solution for the case of rate independent plasticity with a single yield system is given below. The elasticity relationship and the integrated strain rate decomposition are satisfied exactly during solution, so that

$$\mathbf{c}_\sigma = -\mathbf{D}^{el} : \mathbf{c}_\epsilon \quad (3.84)$$

where \mathbf{c}_σ is the correction to the stress, \mathbf{c}_ϵ is the correction to the plastic strain increments, and

$$\mathbf{D}^{el} = \frac{\partial^2 U}{\partial \epsilon^{el} \partial \epsilon^{el}} \quad (3.85)$$

is the tangent elasticity matrix (as \mathbf{K}_0 and \mathbf{K}_a in Figure 3.4).

The hardening laws are also satisfied exactly so that

$$c_\alpha = h_\alpha c_\lambda + \Delta\lambda \left(\frac{\partial h_\alpha}{\partial \sigma} : \mathbf{c}_\sigma + \frac{\partial h_\alpha}{\partial H_\beta} c_\beta \right) \quad (3.86)$$

where c_α is the correction to ΔH_α and c_λ is the correction to $\Delta\lambda$.

$$\left[\mathbf{I} + \Delta\lambda \hat{\mathbf{N}} : \mathbf{D}^{el} \right] : \mathbf{c}_\epsilon - \hat{\mathbf{n}} c_\lambda = \Delta\lambda \frac{\partial g}{\partial \sigma} - \Delta\epsilon^{pl} \quad (3.89)$$

where

$$\hat{\mathbf{N}} = \frac{\partial^2 g}{\partial \sigma \partial \sigma} + \frac{\partial^2 g}{\partial \sigma \partial H_\alpha} \hat{\mathbf{w}}_\alpha$$

$$\hat{\mathbf{n}} = \frac{\partial g}{\partial \sigma} + \Delta\lambda \frac{\partial^2 g}{\partial \sigma \partial H_\alpha} \hat{H}_\alpha$$

The yield condition is not satisfied exactly during Newton iteration; hence

$$\frac{\partial f}{\partial \sigma} : \mathbf{c}_\sigma + \frac{\partial f}{\partial H_\alpha} c_\alpha = -f \quad (3.90)$$

Substitution of Equations (3.85) and (3.88) in the above equation gives

$$\hat{\mathbf{m}} : \mathbf{D}^{el} : \mathbf{c}_\epsilon - \frac{\partial f}{\partial H_\alpha} \hat{H}_\alpha c_\lambda = f \quad (3.91)$$

where

$$\hat{\mathbf{m}} = \frac{\partial f}{\partial \sigma} + \frac{\partial f}{\partial H_\alpha} \hat{\mathbf{w}}_\alpha$$

c_λ is eliminated between Equation (3.89) and Equation (3.91). By taking Equation (3.89)

along with $\hat{\mathbf{m}} : \mathbf{D}^{el}$ and using Equation (3.91) gives

$$c_\lambda = \frac{1}{d} \Delta\lambda \hat{\mathbf{m}} : \mathbf{D}^{el} : \hat{\mathbf{N}} : \mathbf{D}^{el} : \mathbf{c}_\epsilon - \frac{1}{d} \hat{\mathbf{m}} : \mathbf{D}^{el} : \left(\Delta\lambda \frac{\partial g}{\partial \sigma} - \Delta\epsilon^{pl} \right) + \frac{1}{d} f \quad (3.92)$$

where

$$d = \hat{\mathbf{m}} : \mathbf{D}^{el} : \hat{\mathbf{n}} - \frac{\partial f}{\partial H_\alpha} \hat{H}_\alpha$$

Use of this equation in Equation (3.89) gives

$$\left[\mathbf{I} + \Delta\lambda \mathbf{Z} : \hat{\mathbf{N}} : \mathbf{D}^{el} \right] : \mathbf{c}_\varepsilon = \mathbf{Z} : \left(\Delta\lambda \frac{\partial g}{\partial \sigma} - \Delta\varepsilon^{pl} \right) + \frac{1}{d} f \hat{\mathbf{n}} \quad (3.93)$$

where

$$\mathbf{Z} = \mathbf{I} - \frac{1}{d} \hat{\mathbf{n}} \hat{\mathbf{m}} : \mathbf{D}^{el}$$

which is a set of linear equations solved for \mathbf{c}_ε . The solution is then updated and the Newton's iteration continued until the flow equation and yield constraints are satisfied.

Tangent Matrix

The tangent matrix for the material, $\partial\sigma/\partial\varepsilon$, is required when ABAQUS/Standard is used for implicit time integration and Newton's method is used to solve the equilibrium equations (see Figure 3.3.4). The matrix is obtained directly by taking variations of the integral equations with respect to all solution parameters, and then solving for the relationship between σ and ε . The procedure closely follows the derivation used above for the Newton solution: the result is the tangent matrix

$$\sigma = \mathbf{D} : \varepsilon \quad (3.94)$$

where

$$\mathbf{D} = \left[\mathbf{I} + \Delta\lambda \mathbf{D}^{el} : \mathbf{Z} : \hat{\mathbf{N}} \right]^{-1} : \mathbf{D}^{el} : \mathbf{Z}$$

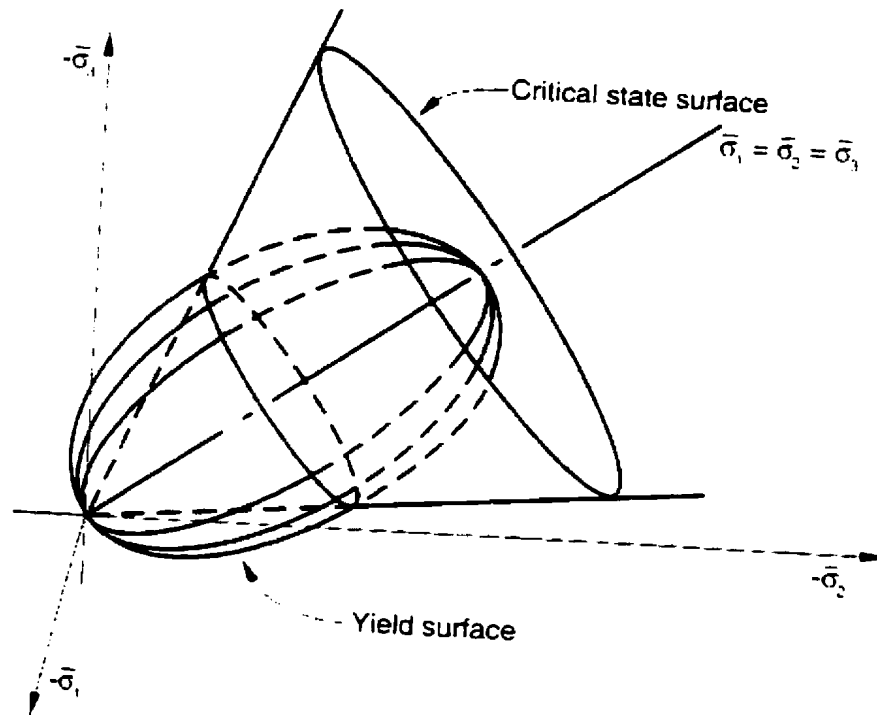


Figure 3.3.5 Cam-clay yield and critical state surfaces in principle stress space [HKS, 1998]

3.3.5. Critical State Models

ABAQUS/Standard provides an inelastic constitutive theory for modeling cohesionless (in the p-t plane – pressure vs deviatoric stress plane) material, based on the critical state plasticity theory developed by Roscoe and his colleagues at Cambridge (Schofield et al. 1968, and Parry 1972). The specific model implemented is based on an extension of the modified Cam-clay (Cambridge clay) theory. The model is entirely

implemented in terms of effective stress; the soil may be saturated with a permeating fluid that carries a pressure stress and is assumed to flow according to D'Arcy's law. The modified Cam-clay theory uses: (i) a strain rate decomposition in which the rate of mechanical deformation of the soil is decomposed into an elastic and a plastic part; (ii) an elasticity theory; (iii) yield surface; (iv) a flow rule; and (v) a hardening rule.

The Cam-clay model assumes that the combination of critical state line and elliptic surface defines a cam-clay yield surface (see Figure 3.3.5 to Figure 3.3.9), which is capable of simulating behaviour of soil on the dry side of critical state line where $t > M_p$; it is also capable of simulating behaviour of soil on the wet side of critical state line where $t < M_p$. The model has the following characteristics: (i) Uses elastic behaviour having either linear elasticity or the porous elasticity constitutive model, exhibiting an increasing bulk elastic stiffness as the material undergoes compression; and (ii) Inelastic behaviour giving a particular form of yield surface with associative flow and a hardening rule that allows the yield surface to grow or shrink.

The model displays a hardening/softening behaviour, where the locus of effective stress states with unrestricted, purely deviatoric, plastic flow of the soil skeleton occurs under constant effective stress. The critical state surface is a cone in the space of principal effective stress, whose vertex is the origin (zero effective stress) with the axis along the equivalent pressure stress, p . The transverse section of the surface in the π -plane (the plane of the principal stress orthogonal to the equivalent pressure stress axis) is circular (see Fig.3.3.5) in the original form of the critical state model; in ABAQUS this has been extended to the more general shape. The effective stress space is defined by the

equivalent pressure stress, p , and a measure of equivalent deviatoric stress, t ; the critical state surface appears as a straight line, passing through the origin, with slope M (see Figures 3.3.6 (a) and 3.3.7 (a)).

The size of the yield surface in effective stress space is controlled by the hardening/softening assumption. The hardening/softening depends only on the volumetric plastic strain component. When the volumetric plastic strain is compressive (that is, when the soil skeleton is compacted), the yield surface grows in size; and for an inelastic increase in the volume of the soil skeleton the yield surface shrinks. Consequently the choice of elliptical arc for the yield surface in the (p, t) plane, together with the associated flow assumption, causes softening of the material for yielding states where $t > Mp$ (to the left of the critical state line – see Figure 3.3.6 (b)), and hardening of the material for yielding states where $t < Mp$ (to the right of critical state line – see Figure 3.3.7 (b)).

Decomposition of Strain Rates in the Material

The volume change that occurs in the material is decomposed as

$$J = J^g \cdot J^{el} \cdot J^{pl} \quad . \quad (3.95)$$

where J is the ratio of current volume to original volume, J^g is the ratio of current to original volume of the soil grain particles, J^{el} is the elastic (recoverable) part of the ratio of current to original volume of soil, and J^{pl} is the plastic (nonrecoverable) part of the ratio of current to original volume of soil.

Volumetric strains are defined as

$$\begin{aligned}\varepsilon_{vol} &= \ln J \\ \varepsilon_{vol}^{el} &= \ln J^{el} \\ \varepsilon_{vol}^{pl} &= \ln J^{pl}\end{aligned}$$

These definitions and Equation (3.96) result in the usual additive strain rate decomposition for volumetric strain rates as

$$d\varepsilon_{vol} = d\varepsilon_{vol}^R + d\varepsilon_{vol}^{el} + d\varepsilon_{vol}^{pl} \quad (3.96)$$

The deviatoric strain rates are assumed to decompose in an additive manner, so that

$$d\varepsilon = d\varepsilon_{vol}^R \mathbf{I} + d\varepsilon^{el} + d\varepsilon^{pl}$$

where \mathbf{I} is a unit matrix.

Representation of Elastic Behaviour in Material

The elastic deformation occurring in material can be modeled as linear or by using a porous elasticity model, typically with zero tensile strength. The porous elastic model available in ABAQUS/Standard, is designed to be used in conjunction with a plasticity model that allows plastic volume changes. This is based on the experimental observation that in porous materials (during elastic straining), the change in the voids ratio, e , and the change in the logarithm of the equivalent pressure stress, p , given by

$$p = -\frac{1}{3} \text{trace } \boldsymbol{\sigma} = -\frac{1}{3} \boldsymbol{\sigma} : \mathbf{I}$$

are nearly related, so that in rate form,

$$de^{el} = -\kappa d(\ln(p + p_i^{el})) \quad (3.97)$$

which also includes the special case of zero tensile strength ($p_i^{el} = 0$). If the compressibility of the solid material is neglected, the volume change of a material sample is given by

$$J = \frac{1+e}{1+e_0} \quad (3.98)$$

where e_0 is the initial void ratio. The elastic void ratio can be defined from the elastic volume change according to the relationship

$$J^{el} = \frac{1+e^{el}}{1+e_0} \quad (3.99)$$

and the volumetric elasticity relationship is given by

$$\frac{\kappa}{1+e_0} \ln\left(\frac{p + p_i^{el}}{p_0 + p_i^{el}}\right) = 1 - J^{el} \quad (3.100)$$

where p_0 is the initial pressure stress, prescribed by initial conditions. This equation can be inverted to give

$$p = -p_i^{el} + (p_0 + p_i^{el}) \exp\left[\frac{1+e_0}{\kappa} (1 - \exp(\epsilon_{vol}^{el}))\right] \quad (3.101)$$

The deviatoric elastic behaviour is defined by choosing a constant shear modulus, G , and the deviatoric relationship is given by

NOTE TO USERS

Page(s) not included in the original manuscript are unavailable from the author or university. The manuscript was microfilmed as received.

100

This reproduction is the best copy available.

UMI[®]

$$p = -\frac{1}{3} \text{trace } \boldsymbol{\sigma} = -\frac{1}{3} \boldsymbol{\sigma} : \mathbf{I}$$

$$q = \sqrt{\frac{2}{3} \mathbf{S} : \mathbf{S}}$$

$$r^3 = \frac{9}{2} \mathbf{S} : \mathbf{S} : \mathbf{S}$$

and the yield surface is given as (Figure 3.3.8 and 3.3.9)

$$f(p, q, r) = \frac{1}{\beta^2} \left(\frac{p}{a} - 1 \right)^2 + \left(\frac{t}{Ma} \right)^2 - 1 = 0 \quad (3.103)$$

In this equation $\beta = \beta(\theta, f^\alpha)$ is a user-specified constant that can be a function of temperature θ and other predefined field variables $f^\alpha, \alpha = 1, 2, \dots$. This constant is used to modify the shape of the yield surface on the wet side of critical state, so that the elliptic arc on the wet side of critical state has a different curvature from the elliptic arc used on the dry side, viz., $\beta = 1$ on the dry side of critical state, and $\beta < 1$ in most cases on the wet side. $a(\theta, f^\alpha)$ defines the hardening of the plasticity model, and is the point on the p-axis at which the elliptic arcs of the yield surface intersect the critical state line. $M(\theta, f^\alpha)$ is the slope of the critical state line in the p-t plane, and $t = q/g$, where g is used to shape the yield surface in the π -plane, and is defined as

$$g = \frac{2K}{1 + K + (1 - K)(r/q)^3}$$

with $K = K(\theta, f^\alpha)$ as a user-defined constant. If $K=1$, the yield surface does not depend on the third stress invariant, and the π -plane section of the yield surface is a circle; this

choice gives the original form of the Cam-clay model. The effect of different values of K on the shape of the yield surface in the π -plane changes from circular at $K=1$ to curved tip triangle at $K=0.8$. In order to ensure convexity of the yield surface, $0.778 \leq K \leq 1.0$.

Modified Cam-clay plasticity model uses associative flow conditions. The size of the yield surface is defined by a ; the evolution of this variable, a , therefore, characterizes the hardening or softening of the material. Experimental observation shows that, during plastic deformation,

$$de = -\lambda d(\ln p)$$

where λ is a constant. Integrating this equation, and using Equations (3.96), (3.99), and (3.101), one obtains

$$a = a_0 \exp \left[(1 + e_0) \frac{1 - J^{pl}}{\lambda - \kappa J^{pl}} \right] \quad (3.104)$$

where a_0 defines the position of a at the beginning of the analysis. The value of a_0 can be given directly in the *CLAY PLASTICITY option or can be computed as

$$a_0 = \frac{1}{2} \exp \left(\frac{e_1 - e_0 - \kappa \ln p_0}{\lambda - \kappa} \right)$$

where p_0 is the initial value of the equivalent pressure stress, and e_1 is the intercept of the virgin consolidation line with the voids ratio axis in a plot of void ratio versus pressure stress.

ABAQUS checks that the initial effective stress state lays inside or on the initial yield surface. At any material point where the yield function is violated, α_0 is adjusted so that Equation (3.104) is satisfied exactly (and, hence, the initial stress state lies on yield surface).

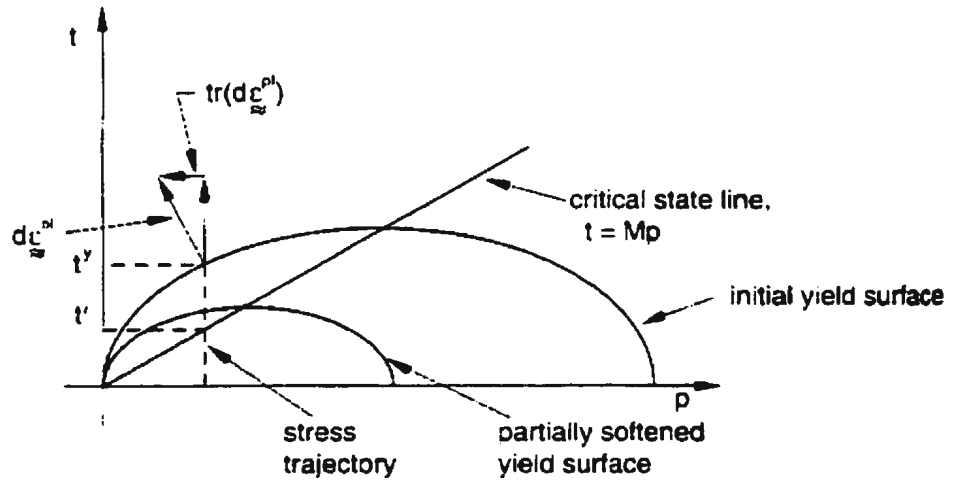


Figure 3.3.6a Shear test response on the dry side of critical state ($t > Mp$) [HKS, 1998]

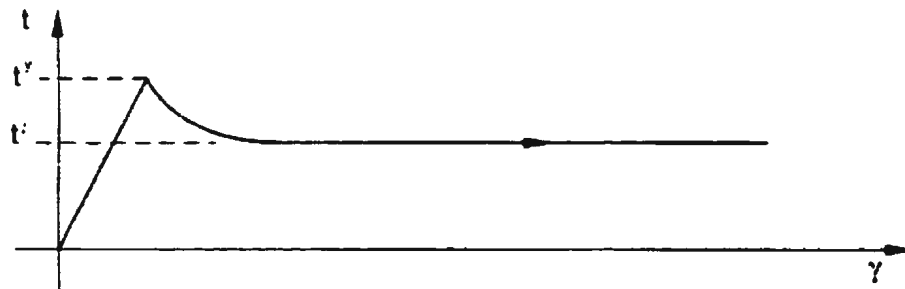


Figure 3.3.6b Shear test response on the dry side of critical state ($t > Mp$) [HKS, 1998]

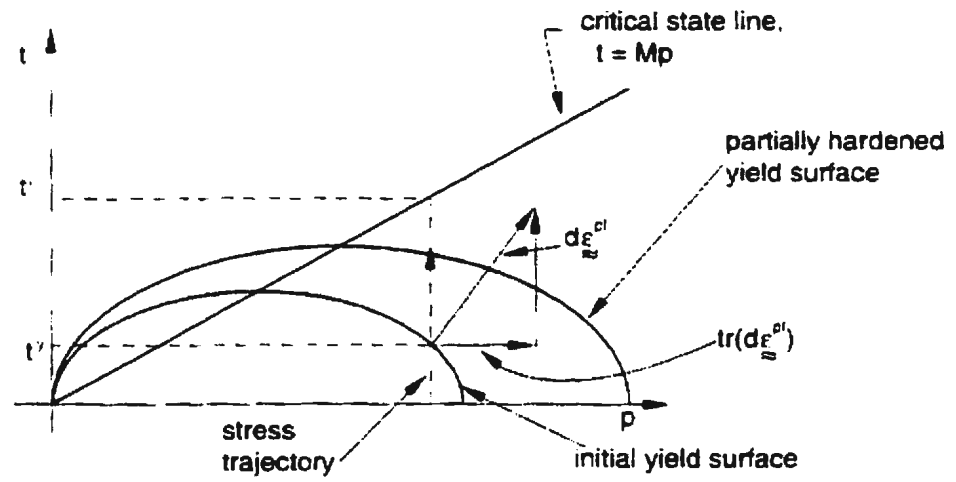


Figure 3.3.7a Shear test response on the wet side of critical state ($t < Mp$) [HKS, 1998]

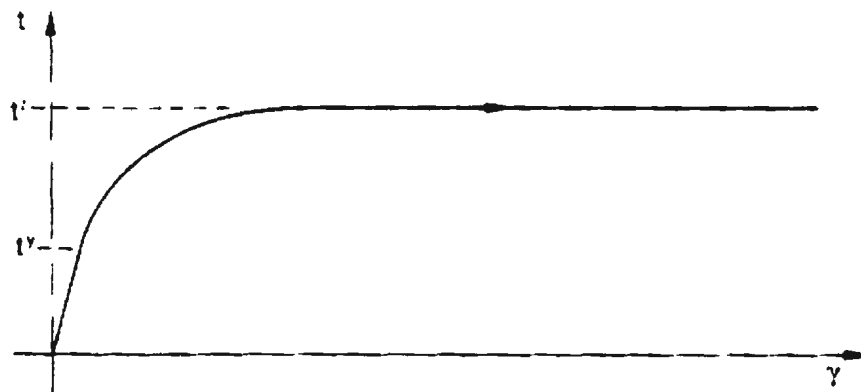


Figure 3.3.7b Shear test response on the wet side of critical state ($t < Mp$) [HKS, 1998]

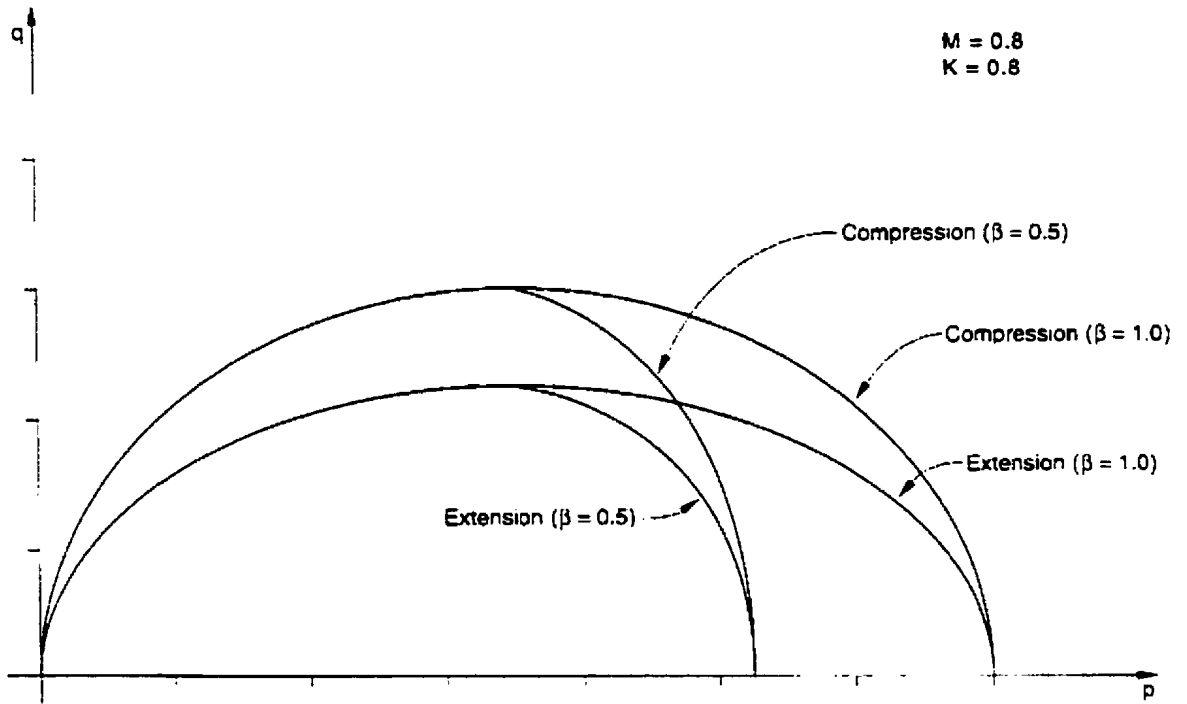


Figure 3.3.8 Cam-clay yield surface in p-q plane [HKS, 1998]

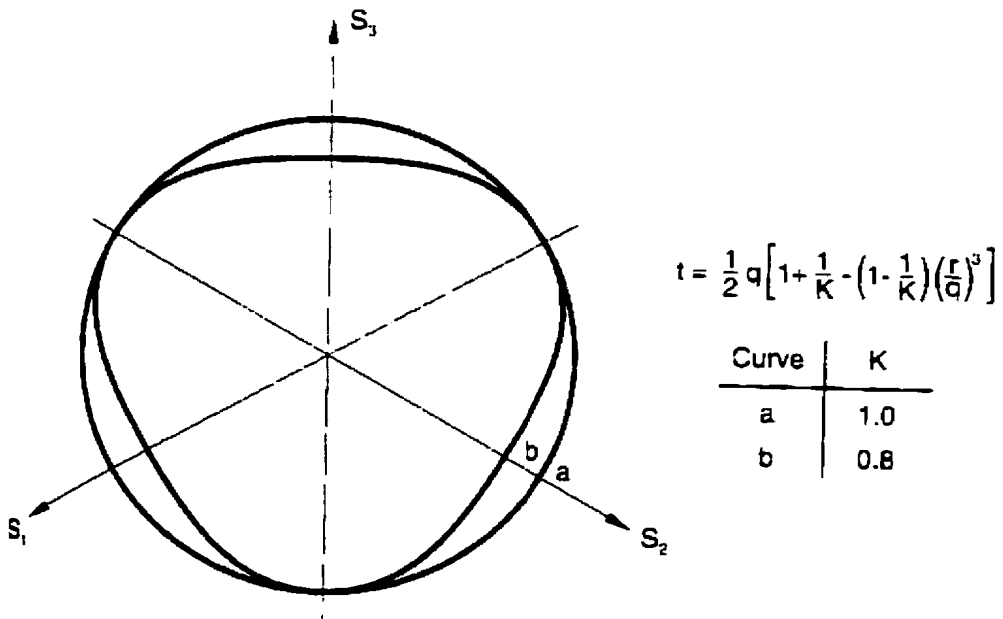


Figure 3.3.9 Cam-clay surfaces in the deviatoric plane [HKS, 1998]

3.4. Effect of Parameter β and K in Cam Clay Model

The application of soil parameters for Cam-clay model is based on soil parameters that are available from standard laboratory tests: λ , κ , and M. However, the other two parameters β and K are not obtainable from standard laboratory tests. Parameters β and K are used to calibrate the response behaviour of soil model to match with behaviour obtained from laboratory tests if applicable (i.e., triaxial, direct shear, and direct simple shear tests).

In order to examine the effect of these two parameters on the suction caisson foundation loads, one of the models (used in the study) is analysed by varying β and K values. Since, the mechanism of pullout test is equivalent to triaxial extension test and the stress state tends to stay in 'dry' side, the value of β should be equal to one (see Figure 3.4.6).

Model used to observe the effect of these parameters is the MIT test model, given in Figure 3.4.1. From the results of the analyses, the following statements could be made:

For $\beta = 1.0$, and two values of $K = 1.0$ and $K = 0.78$, it was found (see Figures 3.4.2 and 3.4.3):

- (i) With $\beta = 1.0$ and $K = 1.0$, maximum pullout capacity was 215.6 N.
- (ii) With $\beta = 1.0$ and $K = 0.78$, maximum pullout capacity was 216.0 N.

For $\beta = 0.8$ and 0.9 , and values of $K = 0.78$, it was found (see Figures 3.4.4 and 3.4.5):

- (i) With $\beta = 0.9$ and $K = 0.78$, maximum pullout capacity was 215.6 N.
- (ii) With $\beta = 0.8$ and $K = 0.78$, maximum pullout capacity was 217.2 N.

The difference in load-deformation behaviour is only marginal; hence it can be said that the effect of the K and β parameters is very small (see Figures 3.4.2 and 3.4.5) on the total pullout capacity of suction caisson foundations.

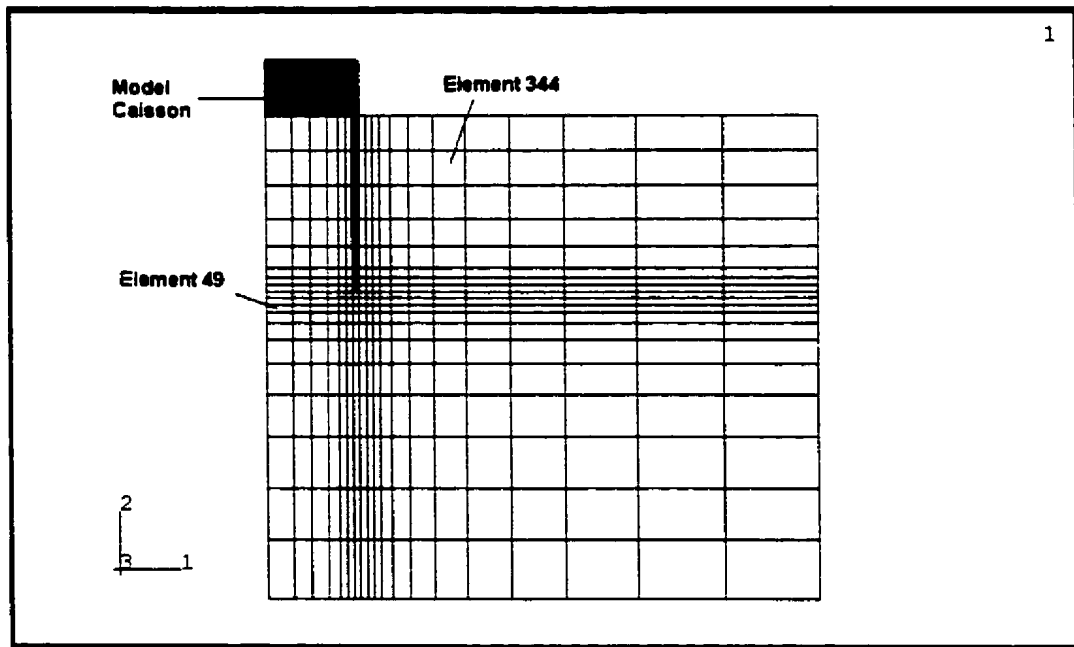


Figure 3.4.1 MIT suction caisson foundation model mesh.

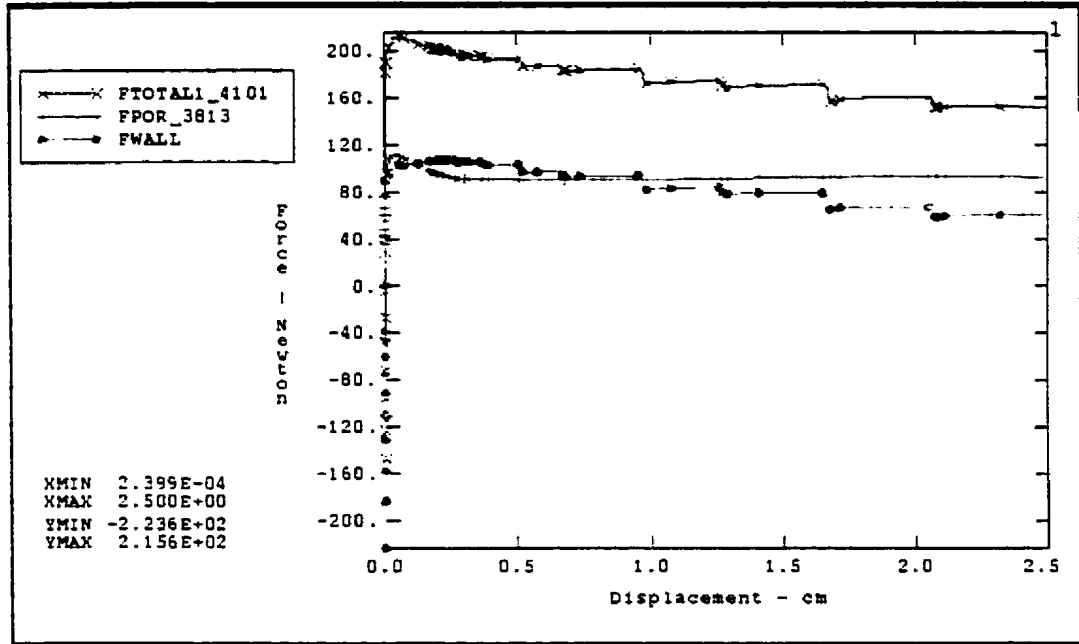


Figure 3.4.2 Force–displacement curve of MIT test model with $K = 1$ and $\beta = 1$

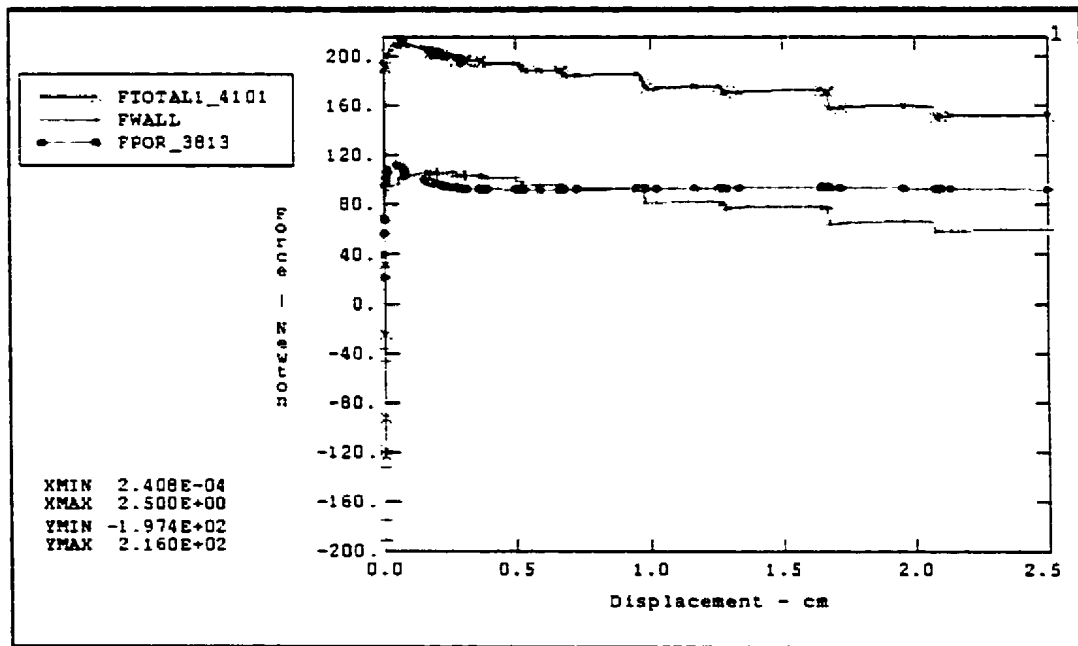


Figure 3.4.3 Force–displacement curve of MIT test model with $K = 0.78$ and $\beta = 1$

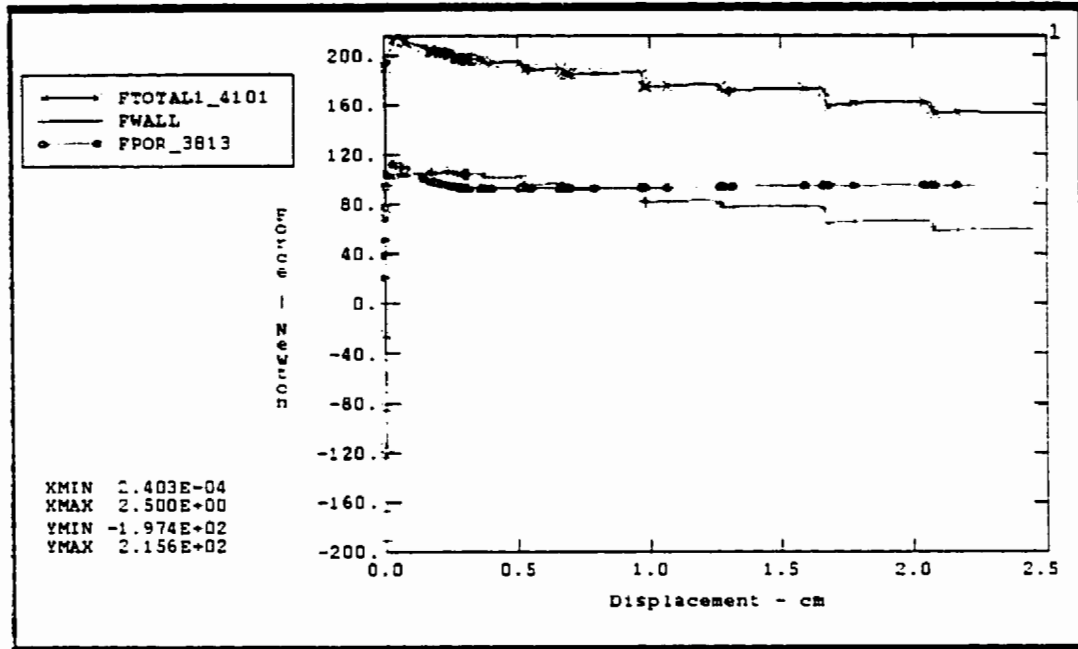


Figure 3.4.4 Force–displacement curve of MIT test model with $K = 0.78$ and $\beta = 0.9$

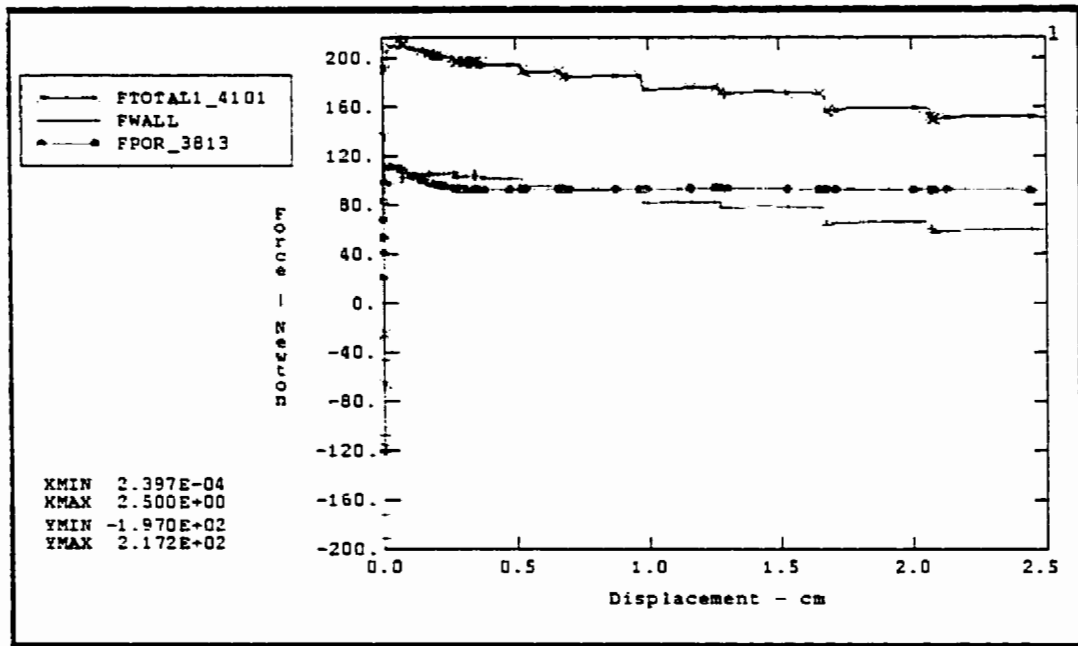


Figure 3.4.5 Force–displacement curve of MIT test model with $K = 0.78$ and $\beta = 0.8$

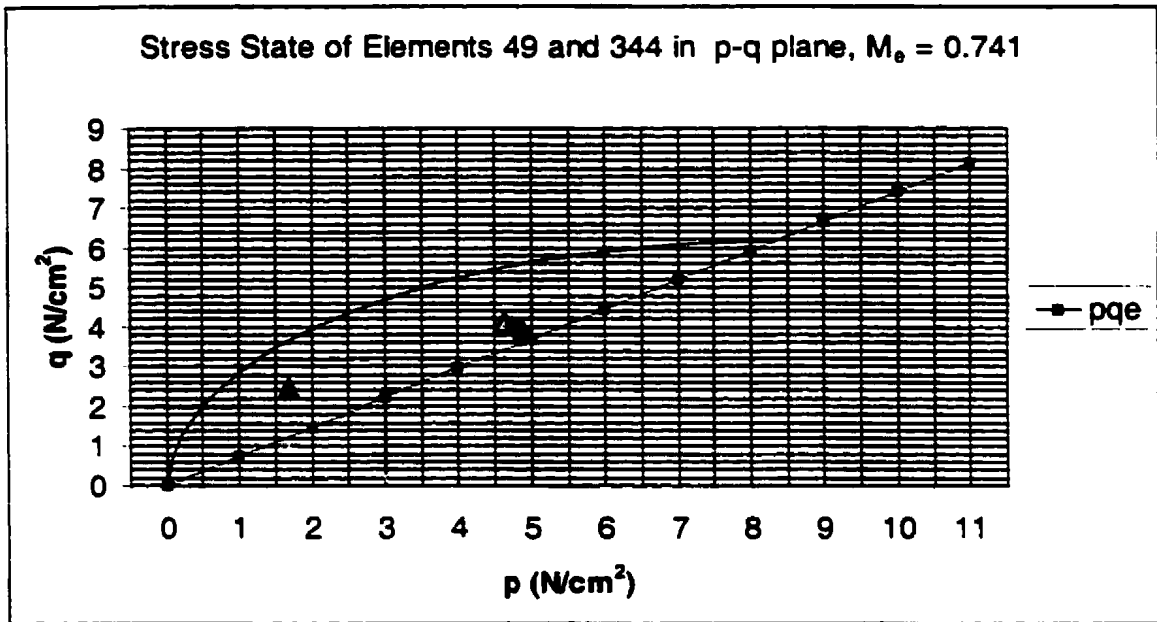


Figure 3.4.6 Stress state of element 49 and 344 in p-q plane

Note:

Stress path of element 344 is denoted by circles that start with circle having higher q value to circle having lower q value that resides on the pqe-line. Stress path of element 49 is indicated by triangles that start with triangle with higher p value to triangle that has lower value. Element 344 is located at middle height close to the outer wall, and element 49 is located at bottom centre below tip level. pqe-line is critical state line with slope $M_e = 0.741$ (value of M for extension).

3.5. Contact Surface

ABAQUS provides contact surface modeling that uses surface-based contact and element-based contact. Surface based contact model supports contact between two deformable bodies, rigid surface and deformable body, as well as small and finite sliding contact problems. On the other hand, contact elements are used especially when a model

uses CAXAn (Continuum Axisymmetric element with Asymmetric loading capability) and SAXAn (Shell Axisymmetric element with Asymmetric loading capability) elements. However, contact elements have a restriction on the amount of transversal displacement. In this study, a surface-based contact model is used in the axisymmetric model for suction foundation under vertical pullout, and a slide line contact element is used in asymmetric-axisymmetric model for the suction foundation under inclined pullout.

The contact surface model is defined by: (i) a pair of master and slave surfaces; and (ii) slide line element with nodes on master surface. The two types of modelling are shown in Figures 3.5.1 and 3.5.2. Contact surface model constitutive behaviour is based on Coulomb friction model that requires input of friction coefficient between surfaces with other optional parameters, such as “taumax” that represents maximum shear stress allowed to develop on contact surface during loading and “elastic slip” that represents maximum elastic displacement of contact surface before slip occurs, providing stability to the system. Elastic slip ranges in value between 0.01 and 0.00001 of the characteristic length of contact surface.

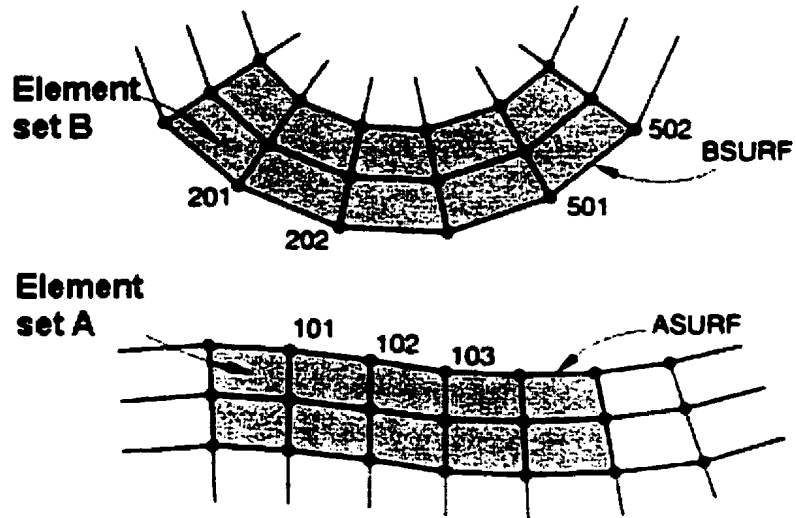


Figure 3.5.1 Contact Surface Model defined by a pair of Master surface (BSURF) and slave surface (ASURF) [HKS, 1998]

3.6. Suction Force Generation

A well-known issue in the use of suction foundation is the internal suction force generation due to soil separation inside the caisson during short-term tension loading. This contributes to an increase in the total suction foundation bearing capacity to tension loads. Since naturally occurring soils are porous in nature, fluid flow parameters affect the suction force generated within the suction caisson. Therefore, the coefficient of conductivity/permeability is a pertinent factor beside other mechanical properties.

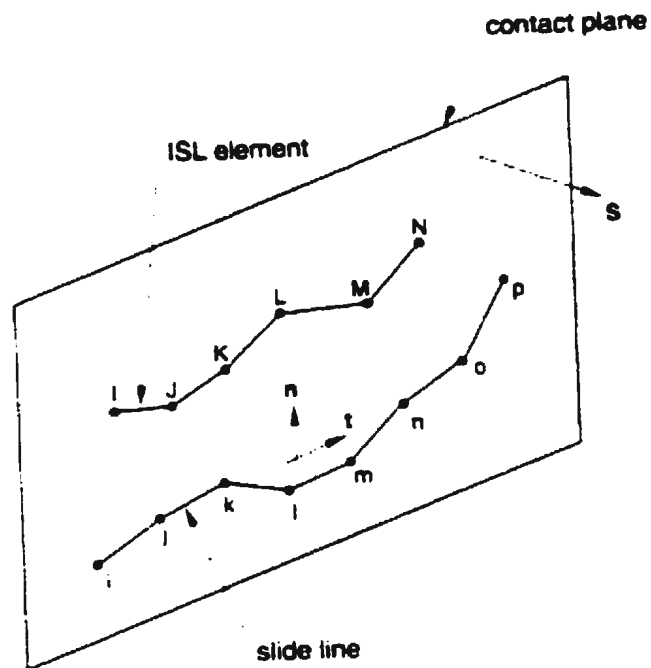


Figure 3.5.2 Contact Surface Model defined by a pair of Slide Line Element (ISL element) and Nodes at Master Surface (slide line) [HKS, 1998]

During tension loading, at a critical loading condition, the interior contact surface between foundation and soil body begins to slip, and an area of vacuum starts to be generated at the top, closed end portion of the suction foundation; in addition, fluid flow into this separated cross-section also occurs. The suction force generated may occur at a maximum of one atmosphere, and will get reduced due to fluid flow occurrence. Therefore, a certain formulation is needed to represent the suction force generated and the suction force applied on the interior of the suction foundation. This formulation should represent the development of suction force inside the caisson and carry the maximum suction force capable of being generated during analysis. A simple formulation is as given below:

$$F_s = p_p * A \quad (3.105)$$

where:

F_s = suction force generated

p_p = pore pressure generated inside the caisson top

A = area of the inside of suction caisson

The concepts that underlie the procedures for suction force generation are given below. Since ABAQUS does not handle such suction generation when a separation takes place between two different/or adjacent surfaces, this artificial phenomena needs to be incorporated into ABAQUS.

The idea is that when a separation (between surfaces) starts to take place, the suction force represents the force that acts on the suction foundation (inside) top and a negative pore pressure that acts on the porous soil medium. Therefore, a virtual distributed load needs to be applied to express the presence of suction at the top of suction foundation, and suction or negative pore pressure needs to be applied to the top of soil medium (inside the suction caisson) during finite element analysis (see Figure 3.6.1). During analysis some variables need to be monitored in order to make the connection between the loads applied to the inside of caisson top and the separating soil body. Those variables that need to be considered are the accumulated fluid volume, and the distance between two surfaces, viz., soil body and foundation body. Suction force at the inside of suction foundation top is applied as soon as a negative pore pressure is generated at the

interface of the finite element model and the body is allowed to develop a gap in between soil medium and suction foundation (inside) top. A fluid flow is assumed to occur as soon as a gap or separation starts to take place. This fluid flow velocity formulation follows D'Arcy's law of seepage flow in porous medium, and is treated as an input for analysis in finite element model. D'Arcy's equation is given as follows:

$$v = k i \quad (3.106)$$

where: k = permeability of soil;

i = hydraulic gradient.

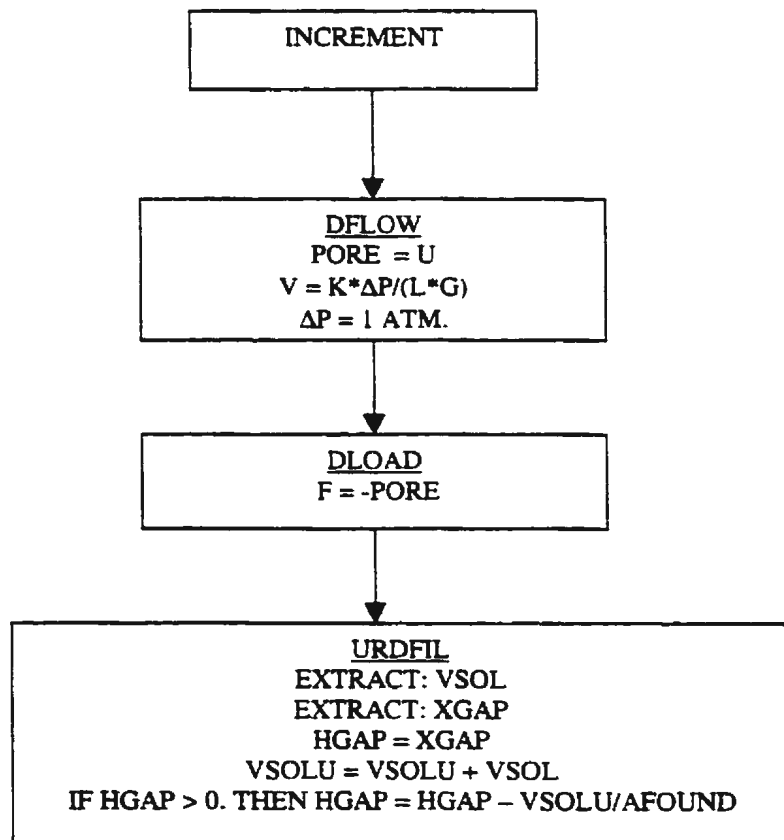


Figure 3.6.1 Flowchart of Suction Force Generation

Where:

DFLOW, DLOAD, URDFIL: ABAQUS build-in user subroutine.

U, PORE: pore pressure.

VSOL, VSOLU: volume of solution passed at referenced increment, viz., water accumulation.

XGAP, HGAP: gap developed.

K, L, G: permeability, path length, and gravity, respectively.

AFOUND: internal diameter cross-section area of suction foundation.

Figure 3.6.1 Flowchart of Suction Force Generation (Cont'd)

The detail of subroutines used in the suction force generation are given in Appendix A1.

3.7. Failure Mode Identification

Failure mode identification is necessary since general finite element analysis like ABAQUS does not consider separation to take place in the soil body during analysis. For suction foundation pullout tests, the failure and loading characteristics are equivalent to combination of triaxial extension test and direct simple shear test. Therefore, a numerical simulation attempt for this test should use soil sample strength properties obtained from triaxial extension tests. Identifying the failure mode may be traced by monitoring changes

of stress, strain, and stress ratio contours of every single iteration in the finite element analysis. For separation or failure identification in the soil body, one may use plastic strain generation in the soil body as long as the finite element formulation considers non-linear and large deformation problems. Also a condition of the first principal stress becoming positive or developing tensile stresses can be used to identify possible tensile failure in the soil body. This check would also apply to the second and third principal stresses for the overall direction of separation or failure. Another approach is to use the ratios of soil shear strength characteristics obtained from triaxial extension tests. This ratio gives the ratio of shear strength of soil sample to applied vertical compression stress under extension load conditions. This ratio is applied to determine the absolute ratio of shear stress to shear strength magnitude developed that will give an idea of the location where shear failure occurs during pullout. After a certain number of iterations the limiting contour of stress ratio and principal strain or stress are found to occur; hence, one can conclude that this pattern of failure or mode of failure occurs before failure takes place in the suction caisson. A similar idea also applies to ratio of soil shear strength characteristics obtained from direct simple shear test.

In the finite element analysis, principal strain, the ratio of shear stress to ultimate shear strength become pertinent parameters that assist in tracing the failure modes.

3.8. Model to Prototype Relationships

In design practice, model simulation has become a standard approach to examine

the behaviour of a structural design. In order to represent similar conditions for both physical properties and loading characteristics, the scaling of these parameters should follow the general similitude relationships that exist between prototype and model. In geotechnical modelling, there are two types of modelling approaches, based on the gravitational environment used for the test: 1g and ng models.

3.8.1. 1g Model to Prototype Relationships

The idea of an 1g model is to use standard laboratory environment with proper scaling of geometry of structure and loading condition to achieve a relatively similar behaviour between the model structure and prototype. In order to obtain the proper scaling for 1g model, basic variables should be scaled and follow general similitude rules.

In this case, basic variables are length dimension (L), gravity (g), submerged unit weight (γ'), permeability (k), velocity (V), stress (σ), and force (F). Since the same environment and material are used in the prototype and model, $\lambda_g = 1$ ($= g_m/g_p$), and $\lambda_{\gamma'} = 1$ ($= \gamma'_m/\gamma'_p$). From similitude analysis, the following relationships were obtained (by choosing L, g and σ as main parameters), viz.,

$$\lambda_k = (\lambda_L * \lambda_g)^{1/2}; \quad \lambda_v = (\lambda_L * \lambda_g)^{1/2}; \quad \lambda_\sigma = (\lambda_L * \lambda_{\gamma'}); \quad \lambda_F = \lambda_L^2 * \lambda_\sigma \quad (3.107)$$

In order to represent almost the same stress state of the prototype in the model, the applied average stress in the model is kept the same as overburden stress value of the mid-height of the prototype. This situation gives the following relationships using results from similitude analysis in Equation (3.107).

$$\lambda_\sigma = \lambda_L * \lambda_{\gamma'}; \quad \bar{\gamma}_m = (\sigma_T + \sigma_B)/(H_m); \quad \lambda_{\tau'} = \bar{\gamma}_m / \bar{\gamma}_p; \quad \bar{\sigma}_m = (\sigma_T + \sigma_B)/2 \quad (3.108)$$

$$\lambda_{\sigma} = \bar{\sigma}_m / \bar{\sigma}_p . \quad (3.109)$$

By implementing Equation (3.108) relationship to Equation (3.109), one can obtain,

$$\bar{\sigma}_p = l_p / l_n * H_m / 2 * \bar{\gamma}_p = \lambda_L^{-1} * H_m / 2 * \bar{\gamma}_p$$

where: m, p : denote model and prototype, respectively. H_m : height of the model.

T, B : denote top and bottom level in the model, respectively.

λ_v : scaling ratio of model to prototype of velocity.

3.8.2. ng Model to Prototype Relationships

The idea of the ng model is to represent the characteristic stress state in the model the same as that of prototype. This model is simulated by generating an artificial gravity environment to n times the normal gravity environment. The artificial gravitational field is created by spinning a hinged rigid box attached to a horizontal arm at an angular speed such that the centrifugal acceleration at the specified location of the model (in rigid box) is ng, where g is the acceleration due to gravity and n is the scale of the model.

Typical scaling relationships for an ng model are given in Table 3.8.1.

Table 3.8.1 Scaling relations [Scott, 1979]

Quantity	Full scale	Ng model
Linear dimension, Displacement	1	1/n
Area	1	1/n ²
Volume	1	1/n ³
Stress	1	1
Strain	1	1
Force	1	1/n ²
Acceleration	1	n
Velocity	1	1
Time – In dynamic Terms	1	1/n
Time – In Diffusion Terms	1	1/n ²
Frequency in Dynamic Problems	1	n

3.9. Skempton's Soil Strength Criterion

In order to simulate correctly the soil sample stress in the model to represent the site sampled average stress characteristics (in numerical analysis) of the prototype in the 1g model, it becomes essential to use Skempton's soil strength correlation formula; this equation gives the equivalent overburden pressure that need to be applied on the top of soil as initial stress condition for numerical analysis.

Soil strength parameter that is commonly referred as an important parameter in the design of foundation is undrained cohesion, c_u . For a normally consolidated clay deposit, the magnitude of c_u increases almost linearly with the increase of effective

overburden pressure, p . Skempton (1957) correlated the values of c_u and p for normally consolidated clay, and found a relationships as follows:

$$\frac{c_u}{p} = 0.11 + 0.0037(PI) \quad (3.110)$$

where PI = plasticity index of soil in percent.

This equation was utilized later on to compute the overburden pressure that is to be applied on the soil surface to obtain the undrained cohesion of soil in the 1g model.

In laboratory tests, there are two possible methods to prepare a soil sample: (i) by obtaining the sample core from an equivalent site having similar soil characteristics necessary for test; or (ii) by simulating the sedimentation process using commonly available commercial type of soil material (i.e. kaolin clay), and adjusting the strength characteristics to meet the required strength conditions. Both of these procedures have been used in the experimental investigations considered in this study (in Chapter 4) for numerical simulation and verification.

3.10. Summary

In order to carry out finite element analyses of suction foundations experiencing large deformations pullout loads, several aspects of finite element modeling, data interpretation between laboratory and field behaviour, and model characterization have to be considered. These aspects can be summarized as follows:

- An axisymmetric model combined with the cam clay plasticity model provide simple

and reliable simulation of the suction foundation behaviour under pullout loads in clay.

- **An asymmetric (loading) - axisymmetric (geometry of caisson) model capable of simulating transverse loading of suction foundations (due to inclined loads) using Fourier series representation to model the applied load is required.**
- **Porous medium idealization enables the simulation of pore pressure generation during soil structure interaction.**
- **Cam clay is one of the plasticity models capable of simulating clay soil behaviour under load.**
- **Contact surface is used to simulate the possible slip occurring between soil and suction foundation.**
- **Pullout mechanism of the suction foundation exhibits combination of triaxial extension and direct simple shear mechanisms in soil body with stress state lying on the 'dry' side.**
- **Modelling of suction force generation becomes essential in computing the maximum resistance offered by suction foundations to pullout loads.**
- **Failure modes identification have been carried out and verified while comparing the theoretical prediction with experimental measurements.**
- **Scaling of I_g and n_g models becomes necessary in comparing the experimental results with those predicted for the prototype structure.**

Chapter 4 Comparison Of Numerical Results With Experimental Data from 1g Models

4.1. Introduction

Ideally, a numerical approach requires verification from a wide range of data gathered from small and large-scale tests with detailed available soil properties. However, available data regarding suction foundation tests in the public domain are very much limited. Some available data used for verification of results of the numerical approach reported herein are from small laboratory tests carried out at a number of locations, viz., (i) Massachusetts Institute of Technology (MIT), Cambridge, Boston, USA [Cauble, 1997], (ii) University of Texas at Austin, USA [El-Gharbawy, 1998], (iii) Indian Institute of Technology, Madras, India [Prasad, 1992], and (iv) Indian Institute of Technology, Madras, India [Rao et al, 1997].

4.2. Massachusetts Institute of Technology Tests [Cauble, 1997]

The reference document is a PhD thesis of D.F. Cauble at Department of Civil and Environmental Engineering, Massachusetts Institute of Technology (MIT), Cambridge, Boston, USA [Cauble, 1997]. The study was on a small size model aimed to model suction caisson behaviour during installation and its pullout capacity with different loading environments for a suction caisson with length to diameter (L/D) ratio equal to

one. The soil media used was a Resedimented Boston Blue Clay (RBBC) sample that was used in a series of tests to determine its index and physical properties, implementing a new method to reproduce Boston Blue Clay properties and using a new apparatus to deal with the tests reported in that study.

4.2.1. Test Geometry and Instrumentation

The model caisson and clay sample geometry were similar for all tests. Fourteen small size tests were carried out under this investigation. The caisson was a two component cylindrical model, comprising of an outer caisson wall and an inner caisson cap. The wall was blunt-tipped with an outside diameter of $D = 0.0508$ m and a wall thickness of $t_w = 0.00145$ m to give a diameter to thickness ratio of $D/t_w = 35$ (see Figure 2.2). The caisson for each pullout test had penetrated 0.0508 m into the clay strata to give an embedment to diameter ratio of $L/D = 1$. The clay media, into which the caisson penetrated during earlier penetration study, had a diameter of 0.305 m (the size of the test enclosure) and a pre-installation sample height that ranged from $H_c = 0.121$ to 0.143 m with an average $H_c = 0.132$ m.

The instrumentation package for each test included between 12 and 15 transducers. All tests included the five primary transducers, which measured the caisson wall and cap force (F_w and F_c) and displacement (δ_w and δ_c , respectively) and consolidation chamber air pressure (P_a). Other transducers measured cap pore pressure, clay pore pressures in three locations, and clay surface displacements at four different locations.

4.2.2. Test Loading Schedule

The load history for each test was divided into a series of driving, equilibrium, and tensile loading stages. In each test the clay media (in the cylindrical tank) was consolidated into the virgin compression range to a consolidated stress of $\sigma'_{vc} = 73.5$ kPa, with the caisson wall upper end flush with the caisson cap at the surface of the clay.

Following the penetration phase in all tests, the caisson was allowed to attain equilibrium for at least 18 hours prior to tensile loading. During the equilibrium phase, a constant total force of $F_{tot} = 149$ N was maintained on the caisson, allowing no relative displacement between the cap and wall. After the first equilibrium phase, a variety of tensile loading schemes were applied. These can be classified into two categories: monotonic pullout to failure and sustained loading. Six caisson specimens were pulled monotonically to failure (Caisson Element Test 3 to Caisson Element Test 8 or CET3 to CET8), while six others were subjected to a sustained load following the first equilibrium phase, and pullout (CET1 and CET2 were not considered in the analyses since the results were not reliable) (see Table 4.2.2.).

In three tests (CET3, 4, 8) the caisson was withdrawn at a rate of 0.0003 m/min beyond peak tensile load and then was pulled at a rate of 0.003 m/min until complete extraction. In tests CET5, 6, and 7, the caisson was pulled at 0.0003 m/min. until just after peak load, whereupon the caisson was allowed to attain equilibrium (the second time) in the clay with a compressive force of $F_{tot} = 149$ N for more than a day. After re-consolidation in these tests, the caisson was then pulled again at a rate of 0.0003 m/min.

Loading schedules of selected tests are given in the following Table 4.2.1.

Table 4.2.1. Tests loading schedule of MIT laboratory tests

Test ID	Conso lid. at 73.5 kPa	Suction Driving	Equil. I and sus-tained loading 149 N	Monotonic Pullout I m/min.	Equil. II and sus-tained loading 149 N	Monotonic Pullout II m/min.
CET3	24 hr.	L = 0.051 m; 0.003 m/min.	24 hr.	0.0003 m/min to L=0.003 m; 0.003 m/min to extraction	-	-
CET4	28 hr.	L = 0.051 m; 0.003 m/min.	18 hr.	0.0003 m/min to L=0.003 m; 0.003 m/min to extraction	-	-
CET5	48 hr.	L = 0.051 m; 0.003 m/min.	24 hr.	0.0003 m/min to L=0.003 m	67 hr.	0.0003 m/min to L=0.003 m
CET6	25.5 hr.	L = 0.0105 m; 0.0001 m/min.; L = 0.0405 m; 0.003 m/min.	30 hr.	0.0003 m/min to L=0.003 m	66.6 hr.	0.0003 m/min to L=0.004 m
CET7	24.9 hr.	L = 0.051 m; 0.003 m/min.	25.6 hr.	0.0003 m/min to L=0.003 m	24.1 hr.	0.0003 m/min to L=0.003 m; 0.003 m/min to extraction
CET8	25.8 hr.	L = 0.051 m; 0.003 m/min.	33.3 hr.	0.0003 m/min to L=0.003 m; 0.003 m/min to extraction		

L = length of suction driving or pullout.

4.2.3. Test Quality

Test quality aimed to clarify certain perturbations in the results that were due to control or instrumentation errors. Table 4.2.2 lists the ratings given for the control and instrumentation for each phase in first eight tests, using a scale from 1 (good) to 4 (unusable). In terms of test control, the grade represented how well the automatic feedback control was able to maintain the target force or displacement for that particular test phase. Most of the data for test phases and instrumentation that received ratings of 1, 2, and 3 were included in the results and analyses that were presented [Cauble, 1997]. Data that received a rating of 4 were considered unusable and were not presented.

Table 4.2.2 Quality assessment for individual test control and instrumentation [Cauble, 1997]

CET Test #	1	2	3	4	5	6	7	8
Installation	4	4	3	2	3	3	3	1
Equilibrium 1	4	-	1	3	3	2	2	2
Monotonic Pullout 1	4	-	3	3	2	1	1	1
Sustained Loading	-	-	-	-	-	-	-	-
Equilibrium 2	-	-	-	-	-	-	-	-
Monotonic Pullout 2	-	-	-	-	-	-	3	3

Key: 1: good; 2: fair; 3:poor; 4:unusable

From given test results, CET3, CET4, CET5, CET6, CET7, and CET8 were chosen to be used in finite element analysis.

4.2.4. Soil Properties

The soil used was Resedimented Boston Blue Clay (RBBC). Natural Boston Blue Clay (BBC) was deposited in the Boston basin area about 12,000 to 14,000 years ago

following the Wisconsin glacial period (Kenney, 1964). A large number of tests had been carried out earlier on BBC, to assess its index and physical properties [Bailey, 1961; Jackson, 1963; Varallyay, 1964; Ladd 1965; Preston, 1965; Braaten, 1966; Dickey, 1967; Kinner, 1970; Ladd, 1971; Bensari, 1984; O'Neil, 1985; Seah, 1991; Sheahan, 1991; Santagata, 1994].

Index Properties

Data from sieve analysis showed that the soil had fine fraction (% passing the #200 sieve) greater than 98%. The average clay fraction (% less than 2 μm) was $58 \pm 1.2\%$. Data from Atterberg limit tests showed that average plastic limit (PI) was $w_p = 23.5 \pm 1.1\%$, the average liquid limit (LL) was $w_l = 46.1 \pm 0.9\%$, and the average plasticity index (PI) was $I_p = 22.7 \pm 1.2\%$. These data confirmed that the material was a low plasticity (CL) clay. Measurement of specific gravity for Series IV RBBC tests, yielded an average value of $G_s = 2.81$, which was higher than previous research, but was still within the expected range for illitic clays ($G_s = 2.60$ to 2.84 for illite clay; Lambe and Whitman, 1968). At water content of 46.26 % and 100 % saturation, it gives a submerged unit weight of 7.72 kN/m^3 .

Compression, Consolidation, and Flow Properties

Compression, consolidation and flow properties were obtained from consolidometer tests in CET program. Under the consolidometer tests in CET program, the RBBC was consolidated using a rigid top cap. In all tests the slurry was loaded

incrementally with a load increment ratio of $LIR = 1$ to a maximum stress of $\sigma'_v = 49$ kPa. In four tests (RBBC 401, 404-406), the clay was unloaded in two increments to a stress of $\sigma'_v = 12.25$ kPa. There was a little scatter in the compression indices; in the stress range from $12.25 < \sigma'_v < 24.5$ kPa the compression index was $C_c = 0.588 \pm 0.046$, while for $24.5 < \sigma'_v < 49$ kPa the index was lower at $C_c = 0.525 \pm 0.033$. The swelling index calculated for two stress intervals, $12.25 < \sigma'_v < 24.5$ kPa and $24.5 < \sigma'_v < 49$ kPa, averaged $C_s = 0.022$ and 0.010 , respectively. The vertical coefficient of consolidation c_v for 5 stress levels from $\sigma'_v = 3.0674$ to 49 kPa were as follows: at lowest levels of $\sigma'_v = 3.0674$ kPa, the average value was $c_v = (3.27 \pm 0.59) \times 10^{-8}$ m²/sec.; at $\sigma'_v = 6.125$ kPa, the average value was $c_v = (4.18 \pm 1.07) \times 10^{-8}$ m²/sec.; at $\sigma'_v = 12.25$ kPa, the average value was $c_v = (6.51 \pm 2.28) \times 10^{-8}$ m²/sec.; at $\sigma'_v = 24.5$ kPa, the average value was $c_v = (8.80 \pm 2.85) \times 10^{-8}$ m²/sec.; and at $\sigma'_v = 49$ kPa, the average value was $c_v = (10.59 \pm 1.94) \times 10^{-8}$ m²/sec.

The vertical hydraulic conductivity decreased with increasing consolidation stress as the data suggested. From $\sigma'_v = 6.125$ to 12.25 kPa, the computed hydraulic conductivity averaged $k_v = 47.4 \times 10^{-10}$ m/sec; and decreased to $k_v = 41.6 \times 10^{-10}$ m/sec for the stress interval from $\sigma'_v = 12.25$ to 24.5 kPa; and dropped further to $k_v = 23.7 \times 10^{-10}$ m/sec for the stress interval from $\sigma'_v = 24.5$ to 49 kPa.

Undrained Triaxial Compression

Typical behavior for normally consolidated RBBC during undrained triaxial compression was obtained from two tests (CTX-11, 13) conducted by Sheahan (1991).

The test specimens were trimmed from Series III RBBC tests, with K_o – consolidation to $\sigma'_{vc} = 274.4$ kPa, and sheared in triaxial compression at the standard rate of $\dot{\epsilon}_a = 0.5\%/hr$. The average lateral earth pressure coefficient ($K_o = \sigma'_h/\sigma'_v$) during consolidation beyond a vertical stress of $\sigma'_v = 58.8$ kPa, was $K_o = 0.47$. The undrained shear strength ratio of the normally consolidated RBBC in compression averaged $s_{uTC}/\sigma'_{vc} = 0.32$, which was mobilized at an average axial strain of $\epsilon_a = 0.15\%$. The friction angle at peak shear stress and maximum obliquity averaged $\phi'_p = 25.0^\circ$ and $\phi'_{mo} = 33.4^\circ$, respectively. Gradual post-peak strain softening was evident, as the mobilized shear strain resistance at $\epsilon_a = 10\%$ strain was $q_{10\%}/\sigma'_{vc} = 0.25$, which was nearly 80% of the peak strength ($q_{10\%}/s_{uTC} = 0.78$). Measurement of the shear stiffness at very small strains ($\epsilon_a < 0.01\%$) was hampered by the lack of on-the-specimen strain measurement equipment. The average normalized secant shear modulus measured at $\epsilon_a = 0.01\%$ strain was $G_{sec}/\sigma'_{vc} = 457$.

Undrained Triaxial Extension

Sheahan (1991) also conducted two standard undrained triaxial extension tests (CTX-9, 50), wherein the specimen was K_o -consolidated to an average stress of $\sigma'_{vc} = 274.4$ kPa and sheared at the standard rate of $\dot{\epsilon}_a = 0.5\%/hr$. As for the compression test, the lateral earth pressure coefficient during consolidation beyond $\sigma'_v = 58.8$ kPa was $K_o = 0.47$. An average peak normalized strength of $s_{uTE}/\sigma'_{vc} = 0.13$ (60% lower than in compression) was reached at an average strain of $\epsilon_a = 12.2\%$ (much higher than in compression) and at a friction angle of $\phi'_p = 35.0^\circ$. The friction angle at maximum

obliquity was $\phi'_{mo} = 35.3^\circ$. At an axial strain of $\epsilon_a = 0.01\%$, the normalized secant shear modulus was $G_{sec}/\sigma'_{vc} = 551$, which was about 20% higher than in compression.

Direct Simple Shear

Three K_o -normally consolidated undrained direct simple shear tests (DSS-222, 228, 233) were performed on Series III RBBC tests by Ortega (1992). The DSS specimens were consolidated to a stress of $\sigma'_{vc} = 784$ kPa, prior to shearing at an average rate of $\dot{\gamma}_a = 3.8$ %/hr. The measured undrained shear strength, $s_{uDSS}/\sigma'_{vc} = 0.20 \pm 0.01$ ($s_{uDSS} = \tau_{max}$), was mobilized at an average strain of $\gamma = 5.53 \pm 0.65$ %. Note that the peak normalized strength in DSS was only 62.5% of the strength measured in triaxial compression ($s_{uDSS}/s_{uTC} = 0.625$), but was 54% higher than the strength found in triaxial extension ($s_{uDSS}/s_{uTE} = 1.54$). At peak shear stress in the DSS tests, the angle of shear stress obliquity averaged at $\psi = (20.1 \pm 1.2)^\circ$ [$\psi = \tan^{-1}(\tau/\sigma'_v)$]. At large strains ($\gamma = 25\%$), the normalized shear stress had dropped to an average of $\tau/\sigma'_{vc} = 0.12 \pm 0.02$, which was 60% of the peak. Measurement of initial shear stiffness was not possible due to large system compliance.

4.2.5. Monotonic Pullout Test Results

From the chosen tests for numerical analysis, the tests results reported in the following table (Table 4.2.3) were obtained.

Table 4.2.3 Test results from MIT laboratory tests

Monotonic Pullout I: 0.0003 m/min.				
CET Test #	Values at Peak Force			
	Wall Displacement at Top (m)	Wall Force (N)	Cap Force (N)	Total Force (N)
3	0.00172	124.56	64.53	189.09
4	0.00227	140.25	82.48	222.73
5	0.00235	149.08	85.82	234.90
6	0.00300	107.89	110.83	218.72
7	0.00187	69.05	103.96	173.01
8	0.00234	132.41	87.29	219.70

All of the above tests indicated that the failure was in tension mode.

4.3. Tests at University of Texas at Austin [El-Gharbawy, 1998]

The reference document is the PhD thesis of S.L. El-Gharbawy completed at the Department of Civil Engineering, University of Texas at Austin [El-Gharbawy, 1998]. The study was on a number of small sized caisson models aimed to model suction caisson behaviour and its pullout strength under static and cyclic loading environment. The loads on caissons simulated the loads exerted on suction caisson foundations of a Tension Leg Platform (TLP) type of structure with length to diameter (L/D) ratios ≥ 2 . The soil media used was a kaolin clay sample that was produced from dry soil through mixing and consolidation processes.

4.3.1. Test Geometry and Instrumentation

Four model caissons with L/D ratios of 2, 4, 6, and 12 having an outer diameter of 0.1016 m for the first three models, and 0.0508 m for the last model were tested. Each of the model caissons was made of a tube with a wall thickness-to-diameter ratio (t/D) = 0.03125 and fitted to a caisson cap. Material for first three models was acrylic and for the last model was stainless steel. The soil sample was accommodated in a tank of approximately 0.762 m height and 0.762 m diameter.

Caissons 2, 4, and 6 (L/D ratios) were instrumented with 0.003175 m diameter piezometric tubes to obtain the pore pressure distribution both inside and outside the caisson. Three flexible Teflon piezometric tubes were mounted on the inner walls opening at different elevations and two rigid brass tubes were fitted to the caisson cap to obtain pore pressures at the top of soil plug. Another two Teflon tubes were mounted on the outside wall to measure pore pressure on outside wall. The caisson with an L/D ratio equal to 12 was not instrumented with pore pressure transducers due to lack of space on the cap and workability of steel material.

4.3.2. Test Loading Schedule

Two major groups of tests were carried out: (i) Short term pullout (undrained loading); and (ii) Long term pullout (drained loading). The details of selected tests loading scenario are given in the following tables (Tables 4.3.1 and 4.3.2).

Table 4.3.1 Short-term pullout (undrained loading)

Test ID	L/D ratio	Pullout speed (m/sec)
STCC2	2	0.0508
STCC4	4	0.0254 – 0.0508
STCC6	6	0.0254 – 0.0508
STCC12	12	0.0254 – 0.0508

Table 4.3.2 Long-term pullout (drained loading)

Test ID	L/D ratio	Loading/Treatment
STCC2	2	11.12 N increment, wait 3 hr. for drainage
STCC4	4	22.24 N increment, wait 30 min. for drainage
STCC4a	4	22.24 N increment, wait 2.5 hr. for drainage, maintained load 133.44 N
STCC4b	4	22.24 N increment, wait 3 hr. for drainage, loading history: 111.2, 133.44, 137.89 N
STCC4c	4	22.24 N increment, wait 2.5 - 3 hr. for drainage, loading history: 111.2, 124.54 N
STCC6	6	22.24 N increment, 3 hr. for drainage
STCC12	12	22.24 N Increment, wait 3 hr. for drainage

4.3.3. Soil Properties

The type of soil used was Kaolinite clay. The preparation process includes mixing process and consolidation processes. The mixing process involved complex programmed mixing tasks. The consolidation process included application of a vacuum pressure of

6.90 MPa (14 in Hg) at the bottom and maintaining freestanding water surface on top of the sample. Application of suction was considered to accelerate the consolidation process. It was observed that a period of 15 days of loading indicated sufficiency of steady state downward seepage condition to be established.

Specific gravity of the soil ranged between 2.59 and 2.63, and particle sizes smaller than 0.005 mm in diameter were 98% of the soil used in the study. At water content of 84.3 % and 100 % saturation, it gives a submerged unit weight of 4.93 kN/m³. From consolidation tests the following record, given in Table 4.3.3, was obtained.

Table 4.3.3. Consolidation and shearing stress parameters of test soil [El-Gharbawy, 1998]

Date of Test	Normal Stress (Pa)	Max Shear Stress (Pa)	Displacement at Failure (m)	Time to Failure (Min.)	Coefficient of Consolidation (m ² /day)	Final Water Content (%)
11/11/96	191.52	238.44	0.0035306	65	0.033444	93.5
11/8/96	406.98	317.92	0.0065024	95	0.040876	92.1
10/28/96	622.44	505.61	0.003175	140	0.007432	91.0
11/11/96	837.9	566.42	0.0032512	165	0.004645	90.1
11/18/96	1053.36	709.58	0.0026924	165	0.002787	86.3
11/22/96	1268.82	807.73	0.0034544	220	0.003716	86.3
11/4/96	1599.19	969.09	0.0031496	315	0.002787	84.3

4.3.4. Monotonic Pullout Test Results

Results of selected test scenarios, used in this study, are given as in Table 4.3.4 and Table 4.3.5.

Table 4.3.4. Short-term pullout (undrained loading) test results

Test ID	Failure Mode	Note	Suction Pressure at top cap (Pa)	Max. Pullout Capacity (N)	Displacement at maximum load (m)
STCC2	General Shear	With soil plug + 0.0032 m soil cover	-	164.576	0.014732
STCC4	General Shear	With soil plug + 0.0032 m soil cover	20684.271	382.528	0.024638
STCC6	General Shear	With soil plug + 0.0032 m soil cover	20684.271	596.032	0.02159
STCC12	General Shear	With soil plug + 0.0032 m soil cover	-	177.92	0.03048

- = not available.

Table 4.3.5. Long-term pullout (drained loading) test results

Test ID	Failure Mode	Note	Max. Pullout Capacity (N)	Displacement at maximum load (m)
STCC2	Tension Failure	With soil plug	88.96	0.003302
STCC4	Shear Failure	With soil plug, partial drainage	311.36	-
STCC4a	Tension Failure	No soil plug, Full drainage	151.232	0.022352
STCC4b	Tension Failure	With soil plug, partial drainage	137.888	-
STCC4c	Tension Failure	With soil plug, partial drainage	124.544	0.02921
STCC6	Shear Failure	No soil plug, Full drainage	177.92	0.00381
STCC12	-	Full drainage	88.96	0.000762

- = not available.

4.4. Indian Institute of Technology (I I T), Madras (India) Tests [Prasad, 1992]

The reference document is a PhD thesis of Y.V.S.N. Prasad at the Ocean Engineering Centre, Indian Institute of Technology, Madras, India [Prasad, 1992]. The selected laboratory tests data were part of three types of anchor tests: screw anchor, plate anchor, and pile anchor. This part of the tests was used for verification of pile group capacity to single pile capacity. Soil type used was typical marine clay present in the coastal areas along the Eastern coasts of India.

4.4.1. Test Geometry and Instrumentation

Selected tests from the program of IIT (Madras) Tests [Prasad, 1992] were on single piles considered as friction piles without any soil plug inside the pile. Test set-up was arranged by placing the pile model with the pile tip touching the base of the test tank and soil was laid layer by layer.

Test geometry of the single friction pile consisted of two different diameters and wall thicknesses: 0.0138 m diameter with 0.0015 m thickness, and 0.018 m diameter with 0.002 m thickness. Each diameter with three different L/D ratios of 15, 25 and 40 gave a total of 6 models to test. The material of the model was stainless steel tube.

4.4.2. Test Loading Schedule

The test load was applied through the use of strain controlled static pullout equipment. The pullout load was applied on an anchor at a constant rate of 0.004 m per

minute using a hydraulic jack. In this test phase, each test was continued beyond a peak failure load until well-noticed failure behaviour was obtained.

4.4.3. Soil Properties

The soil used for tests was from the coastal deposits in the east coast of India. Two types of soil samples were used in the tests, and designated as soil 1 and soil 2. The soil sample was considered as soft marine clay. From reference material [Prasad, 1992], SPT value, N for the soil sample was 2, which gives unit weight in wet condition between 11 to 16 kN/m^3 [Bowles, 1996]. It was chosen to use 16 kN/m^3 for the soil sample. The prepared soil sample had an undrained compressive strength, C_u , of 5 kPa. The index properties of the soil samples obtained in the tests are given as in the following Table 4.4.1.

Table 4.4.1. Index properties of soil sample

Soil ID	C_u (kPa)	Liquid Limit (LL) (%)	Plastic Limit (PL) (%)	Plasticity Index (PI) (%)	Grain Size Distribution		
					Clay (%)	Silt (%)	Sand (%)
Soil 1	5	82	32	50	40	50	10
Soil 2	5	75	25	50	62	20	15

4.4.4. Monotonic Pullout Test Results

Results of the chosen single friction pile tests are given in the following table (Table 4.4.2), with full load-displacement behaviour shown in Figures 4.4.1 and 4.4.2.

Table 4.4.2 Test results of single friction pile

Test ID	Diameter (m)	L/D ratio	Max Pullout Capacity (N)	Displacement at maximum load (m)
1	0.0138	15	52	0.0005
2	0.0138	25	71	0.0004
3	0.0138	40	90	0.00075
4	0.018	15	80	0.0004
5	0.018	25	110	0.0004
6	0.018	40	130	0.00025

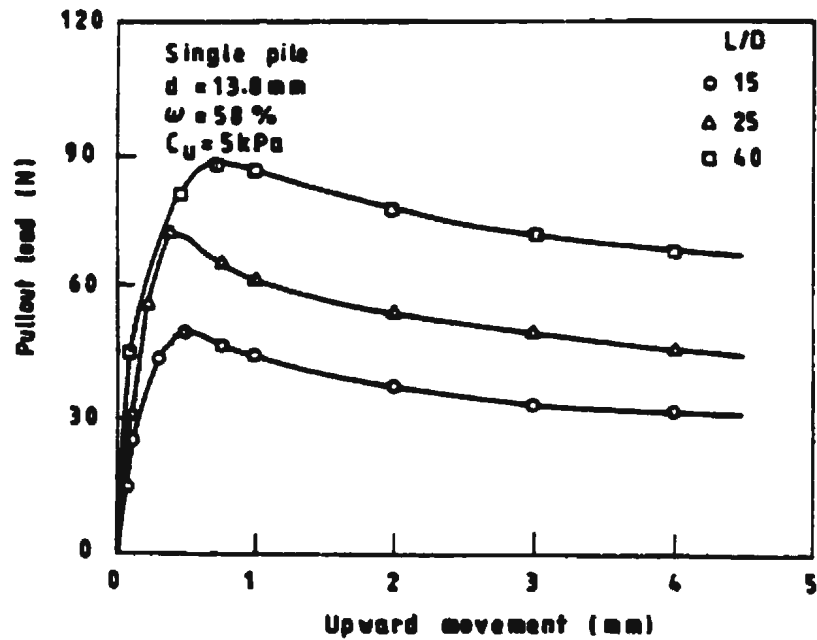


Figure 4.4.1. Pullout tests of single pile, dia. = 13.8 mm, IIT Madras [Prasad, 1992]

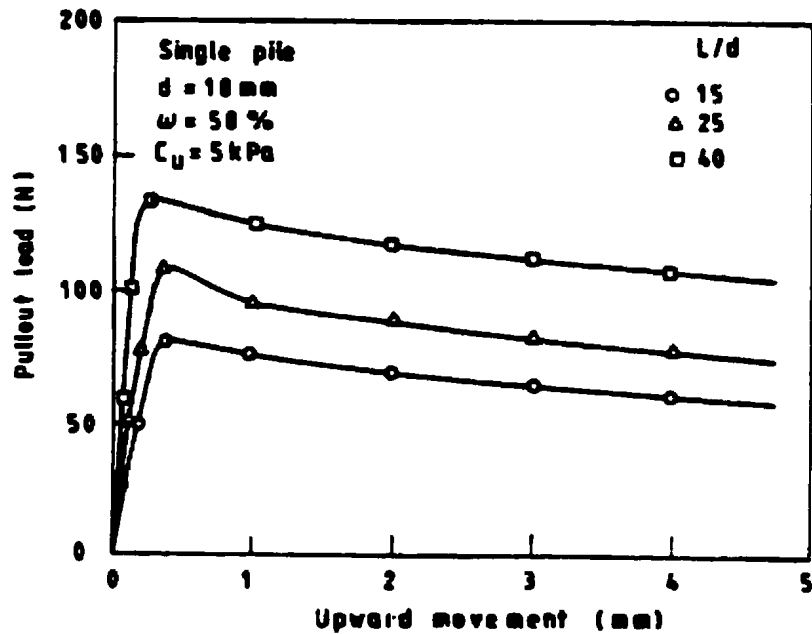


Figure 4.4.2. Pullout tests of single pile, dia. = 18.0 mm, IIT Madras [Prasad, 1992]

4.5. IIT Madras (India) Tests [Rao et al., 1997]

4.5.1. Test Geometry and Instrumentation

The test geometry of the model anchor was 0.075 m diameter and 0.003 m wall thickness. The model represented a 1:100 scale model of prototype size anchor used for the Snorre TLP. The variation of length to diameter ratio (L/D) was determined to be 1.0, 1.5, and 2.0.

The tests were conducted in a cylindrical test tank of 0.75 m diameter and 0.9 m height. There were three different major setup of tests: (i) Anchor with open top; (ii) Surface suction anchor; and (iii) Buried suction anchor. In this study the results of only

anchors with surface suction anchor was used. Three soil types were chosen for investigation to take into account the different consistency of the soil used, giving a total of 9 analyses to be carried out for this study.

4.5.2. Test Loading Schedule

A flexible wire rope was connected to the centre of the anchor top and then passed over a pulley arrangement in the loading frame. For static loading, the pullout load was applied in increments by placing weights on the load hanger attached to the other end of the wire rope.

4.5.3. Soil Properties

Soil type used was typical marine clay obtained from a coastal deposit on the east coast of India. Soil properties obtained from tests that were conducted are given in Table 4.5.1.

Table 4.5.1. Properties of soil sample [Rao et al., 1997]

Soil ID	Liquid Limit (LL) (%)	Plastic Limit (PL) (%)	Liquidity Index (LI)	c_u (kPa)	γ (kN/m ³)	S_r (%)
1	82	32	0.8	1.8	16.4	0.97
2	82	32	0.6	3.6	16.45	0.96
3	82	32	0.4	5.8	16.71	0.95

4.5.4. Monotonic Pullout Test Results

Some results presented in the source reference [Rao et al., 1997] were used as reference for verification of the numerical analyses results. From one of the tests group, it was found that three distinct phases were identified. Phase I at initial stage of deformation up to 0.002 m showed a steep rise in the pullout resistance. It was followed by phase II, where a gradual and slow increase in the pullout resistance with consequent large deformation was obtained. In phase III, there was a sudden increase in pullout resistance, which was followed by a sudden pullout of the anchor. It was also noticed that in all tests the soil remained intact inside the anchor. Results given in the source reference are shown in the following figures, Fig. 4.5.1 to 4.5.4.

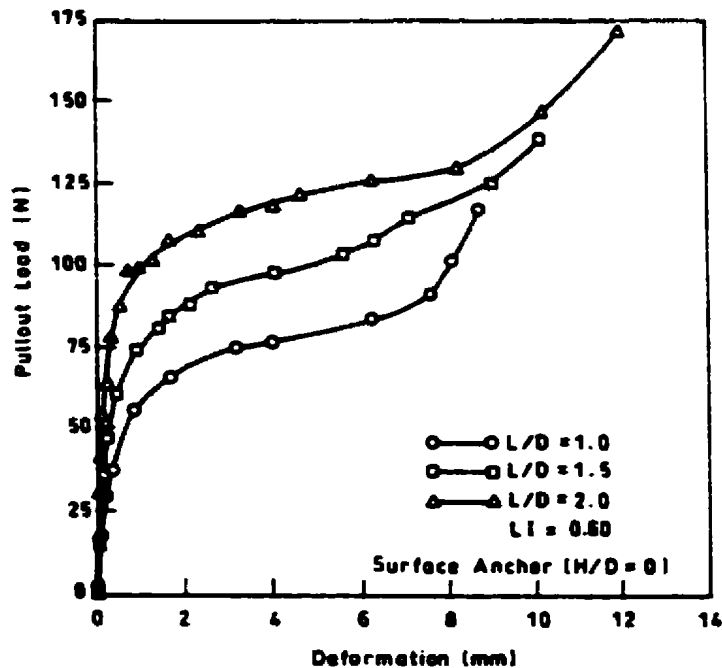


Figure 4.5.1. Pullout load – displacement curve of suction anchor, LI = 0.6 [Rao et al., 1997]

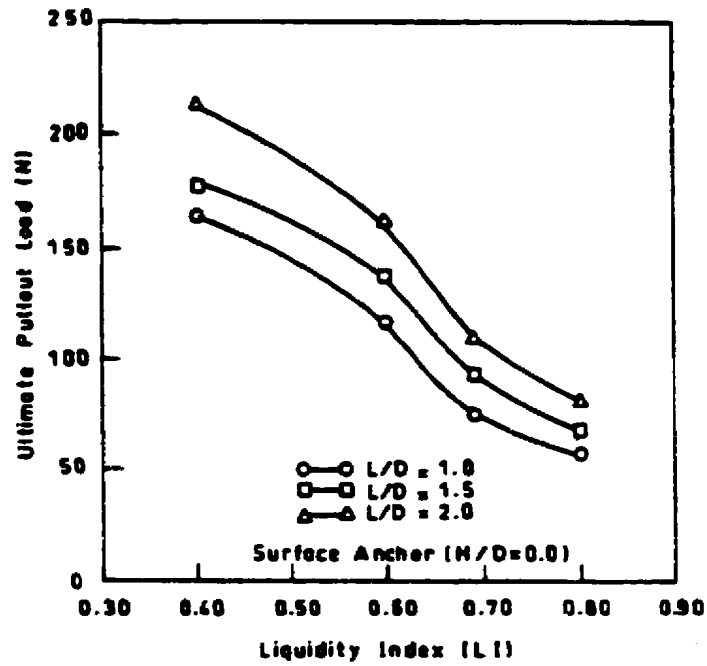


Figure 4.5.2. Variation of ultimate pullout load with Liquidity index (LI) [Rao et al., 1997]

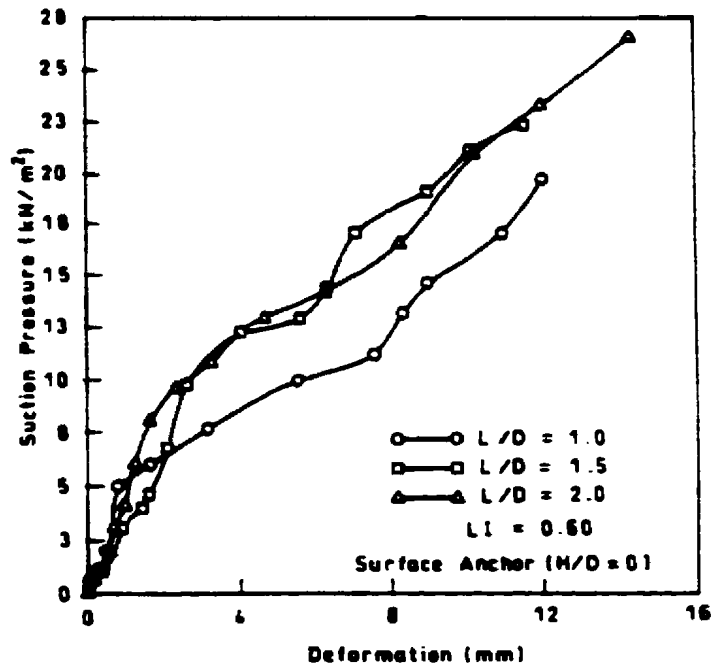


Figure 4.5.3. Variation of suction pressure with deformation for different L/D ratio [Rao et al., 1997]

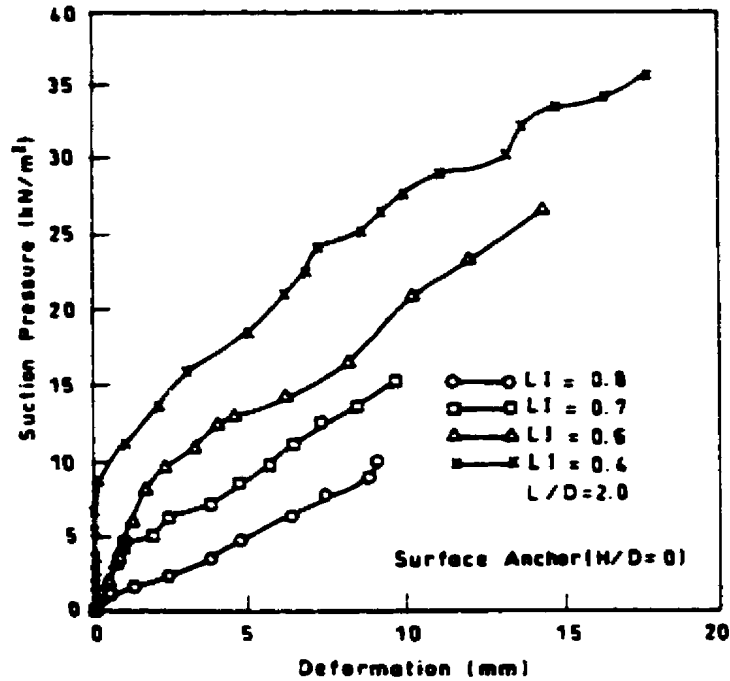


Figure 4.5.4. Influence of soil consistency on suction pressure, $L/D = 2$ [Rao et al., 1997].

4.6. Results from Finite Element Analyses

All soil tests referred in this study were on different types of clay; therefore, it was chosen to use the Camclay model (available in ABAQUS computer program) to simulate its behaviour during finite element analyses. Idealization and treatment of loadings were carried out to be as close as possible to those applied during laboratory tests. Also, a consistent approach was used to model the loading and displacement effect during the preparation of soil sample.

4.6.1. Results of MIT Model Tests

From the source reference for MIT tests [Cauble, 1997], the parameters required for finite element analysis were as follows:

Average size of soil sample: 0.14 m height and 0.305 m diameter. Suction foundation model size: 0.051 m height, 0.051 m diameter, and 0.0015 m wall thickness.

Caisson model Material Properties: Brass Shelby tube

Young Modulus, E : 109 GPa

Poisson's ratio, ν : 0.3

Soil Properties: RBBC

Slope of virgin consolidation line in $e:\log p'$ diagram, λ : 0.22826

Slope of swelling line in $e:\log p'$ diagram, κ : 0.00435

Shear modulus, G : 404.985 kPa.

Water content, w_c : 46.26 %

Permeability, k : 2.37×10^{-9} m/s

K_0 : 0.47

Friction coefficient, f : 0.466

Specific gravity, G_s : 2.81

Critical State ratio, M_c : 0.74

Taumax : 9.633 kPa

Finite element analysis used an axisymmetric element mesh to model the system using quadrilateral eight-noded elements with pore pressure degrees of freedom. The finite element analysis also utilised contact surface idealization to simulate contact between soil body and foundation. The finite element mesh model used 368 axisymmetric elements with contact surface idealization as shown in Fig.4.6.1. An idealization of suction force generation was used to simulate its behaviour during tests in this analysis,

the details of which are given in Chapter 3. A distributed load of 73.5 kPa was also applied in the same manner as in the laboratory tests. This distributed load was used to bring the soil sample to its virgin compression range and kept it as a normally consolidated sample [Cauble, 1997]. The different loading treatment in laboratory test environment is implemented through initially by geostatic process followed by consolidation process. This is to ensure that equilibrium of geostatic stress field with applied load and boundary conditions is achieved initially and to ensure that there is no excess pore pressure before loading process. Pullout loading is treated by implementing pullout rate at the same amount as applied in laboratory test to a certain pullout length. Suspend step is treated as consolidation process at certain stage between pullout loadings where consolidation analysis implemented during certain period the same period as treated in laboratory test for respected model. Results obtained from the finite element analyses are given in Table 4.6.1.

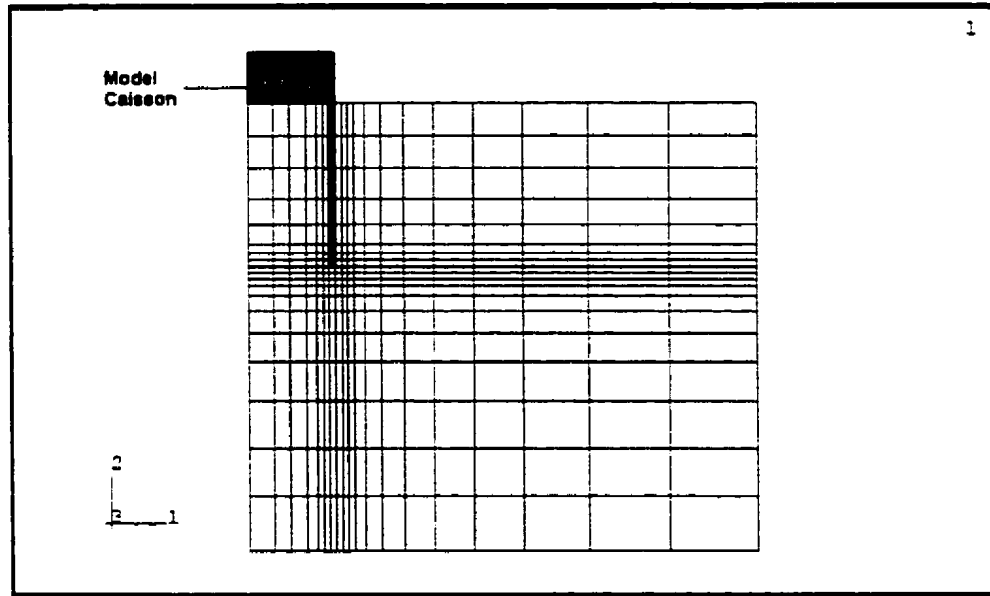


Figure 4.6.1 MIT suction caisson foundation model mesh.

The results from all finite element analyses gave results for different scenarios as given in Table 4.2.1. Referring to Table 4.6.1, some the numerical results were very close to the experimental values, whereas others were not. This difference from the laboratory test results may be attributed to different constraints that apply for the set-up of each test; however, in the finite element analysis these different constraints could not be included since it was not quantified exactly in the experimental results. It is also seen from Table 4.6.1 that the finite element results gave a stiffer response. Even though the displacements at peak loads did not agree very well with the experimental results, the theoretical load–displacement curves showed an excellent agreement with the experimental load–displacement curves as seen in Figures 4.6.2 to 4.6.4. Results of analysis from one test are given in the Figures 4.6.2 to 4.6.4, and all the other results are given in Appendix A2.

Table 4.6.1 Finite element analysis results of MIT model tests.

Monotonic Pullout I: 0.0003 m/min.; Values at Peak Total Force				
Results given in brackets indicate the results obtained from laboratory tests.				
CET Test no.	Wall displacement at top (m)	Wall Force (N)	Cap Force (N)	Total Force (N)
3	6.5502E-04 (0.00172)	107.20 (124.56)	109.55 (64.53)	216.75 (189.09)
4	4.4514E-04 (0.00227)	105.14 (140.25)	111.22 (82.48)	216.36 (222.73)
5	6.4695E-04 (0.00235)	109.65 (149.08)	110.44 (85.82)	220.09 (234.90)
6	4.4514E-04 (0.00300)	105.14 (107.89)	111.22 (110.83)	216.36 (218.72)
7	4.4514E-04 (0.00187)	105.14 (69.05)	111.22 (103.96)	216.36 (173.01)
8	4.4514E-04 (0.00234)	105.14 (132.41)	111.22 (87.29)	216.36 (219.70)

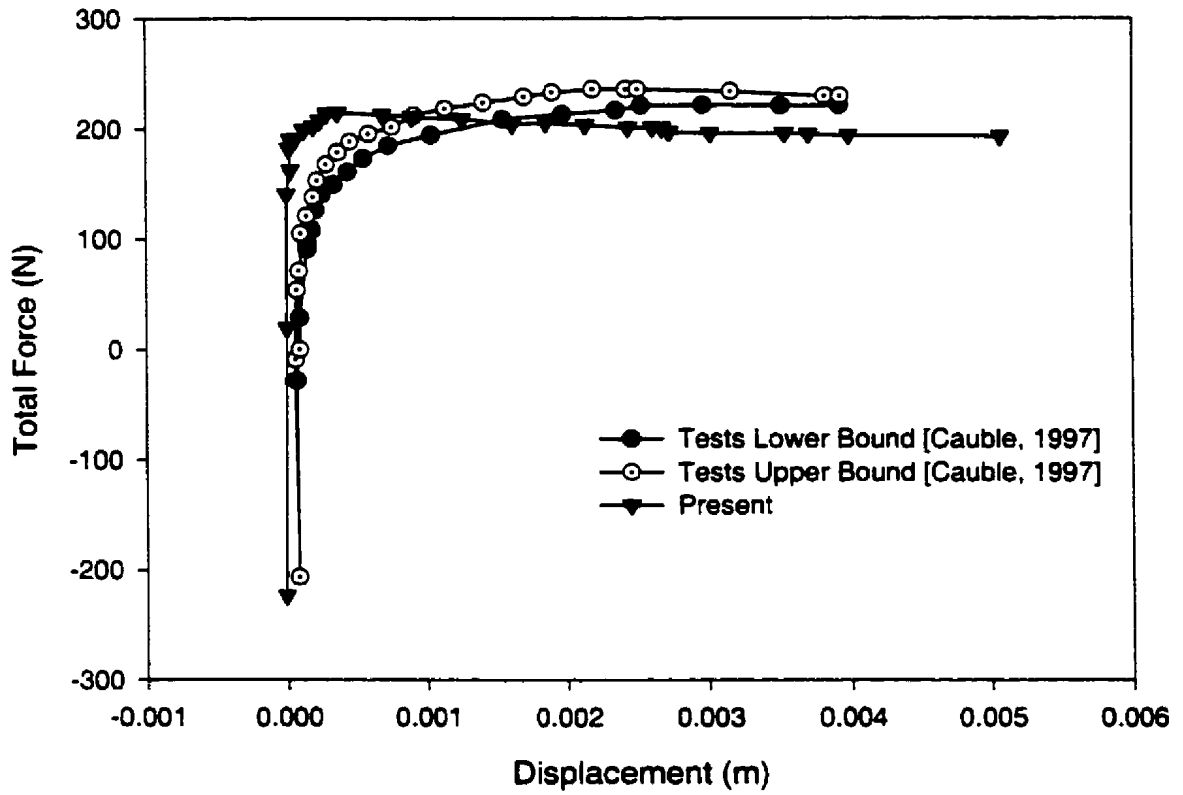


Figure 4.6.2. Total force-displacement curves of laboratory test results (CET3) and FEM analysis results.

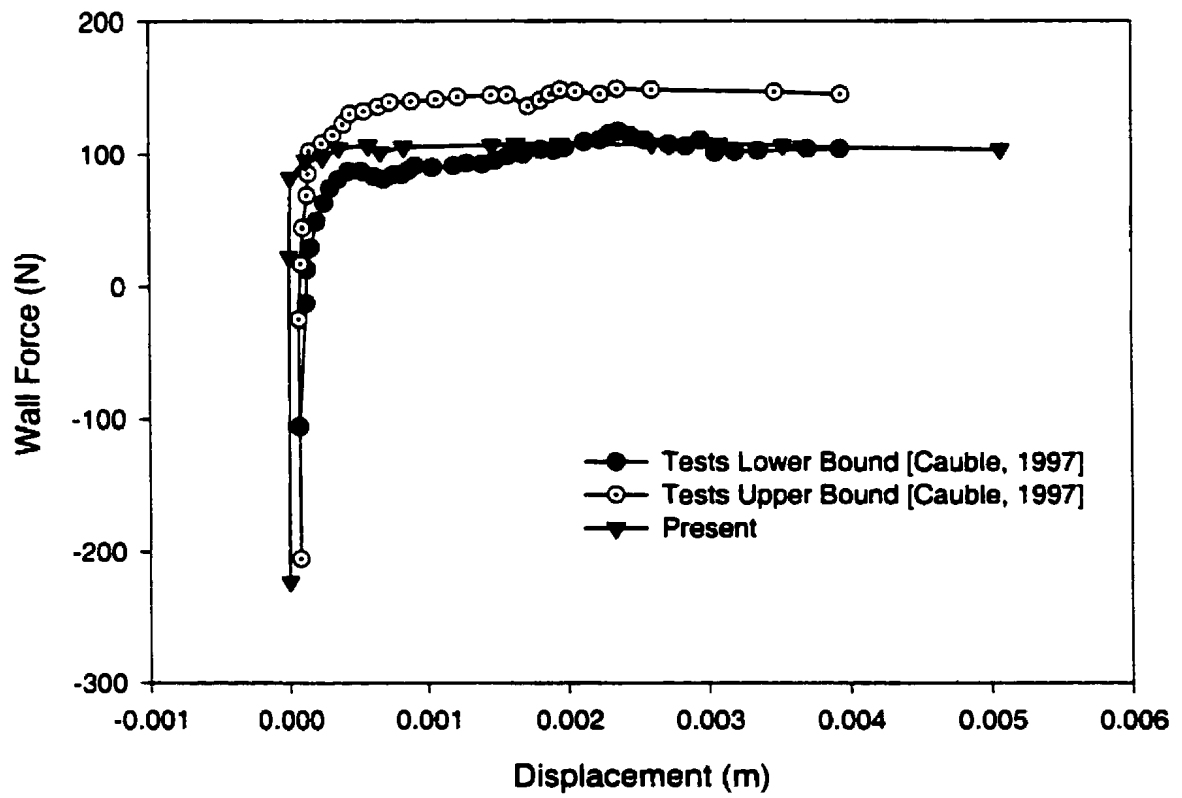


Figure 4.6.3. Wall force-displacement curves of laboratory test results (CET3) and FEM analysis results.

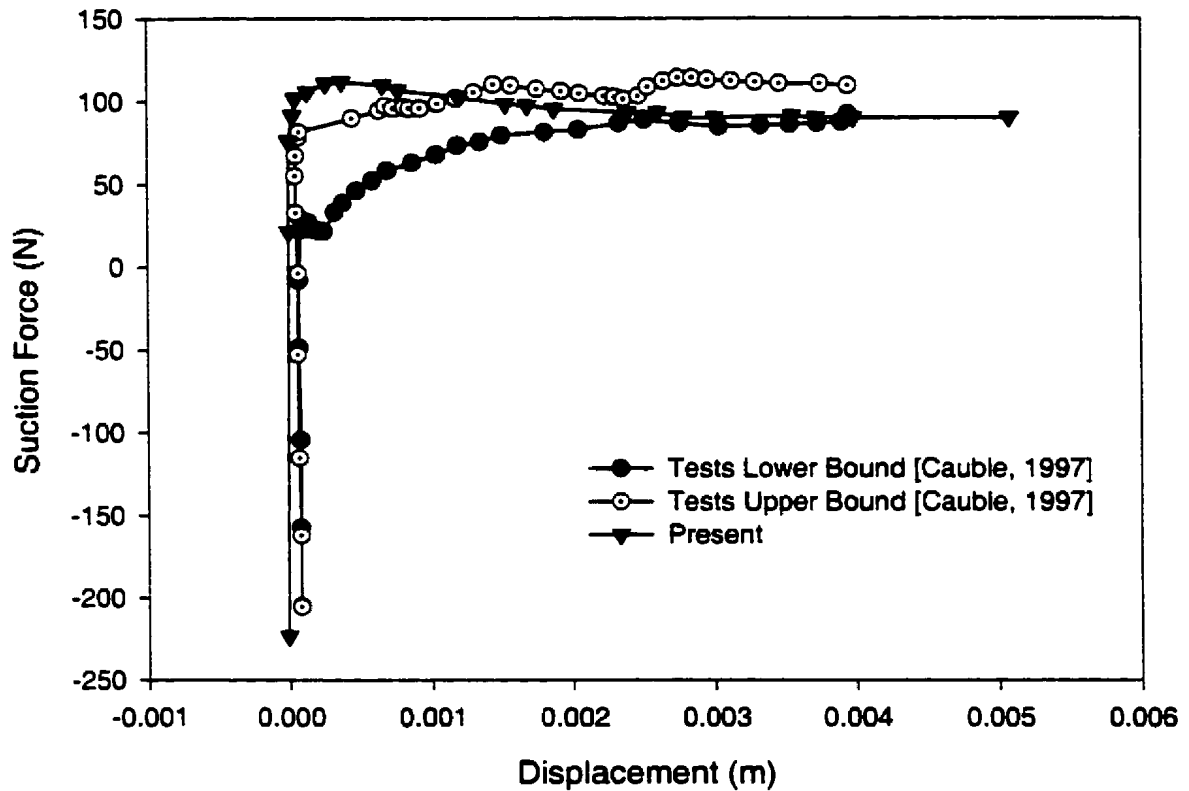


Figure 4.6.4. Suction force-displacement curves of laboratory test results (CET3) and FEM analysis results.

Analytical Approximations using Christensen’s Formulation

From various formulations given in Chapter 2, the Christensen’s formulation [Christensen et al., 1991] (given in section 2.5.1) was simplified to apply it to the MIT tests and analysis results of analysis were obtained as follows:

Shear Failure:

$$F = F_u^{int} + T_c + T_i$$

Tension Failure:

$$F = T_c + W_s + F_t$$

In this case $F_t = A_i * (-P_{up})$

General Shear Failure:

$$F = T_c + W_s + N * c_u * A_e - q_{tip} * A_e$$

where:

$$F_{uint} = A_i * P_{top} \quad W_s = \gamma' * V_s \quad N = \min(9, 6.2 * (1 + 0.35 * a_2 / D_e))$$

$$T_c = P_e * C_u * \alpha * a_1 = T_i$$

In order to use the above formulations, the following information was required to complete the failure modes calculations.

$$\begin{aligned} A_e &= 0.002043 \text{m}^2 & \alpha &= 1 \\ A_i &= 0.00181 \text{m}^2 & a_1 = a_2 &= 0.051 \text{m} \\ P_e &= 0.160221 \text{m} \\ T_i = T_e &= 192.1886 \text{N} \end{aligned}$$

$$\begin{aligned} c_u &= 23520 \text{Pa} & V_s &= 0.0001042 \text{m}^3 \\ D_e &= 0.051 \text{M} & \gamma' &= 7720 \text{N/m}^3 \\ q_{tip} = \sigma_{at} &= 393.72 \text{Pa} & W_s &= 0.8042993 \text{N} \end{aligned}$$

Table 4.6.2 Components in Christensen's equation for test data

Test	CET3	CET4	CET5	CET6	CET7	CET8
$-P_{tip}$ (Pa)	68600.000	68600.000	68600.000	68600.000	68600.000	68600.000
$-P'_{tip}$ (Pa)	15000.000	15000.000	15000.000	15000.000	15000.000	15000.000
$-P_{top}$ (Pa)	35626.519	45534.807	47375.691	61182.320	57392.265	48187.845
$T_i = T_e$ (N)	192.189	192.189	192.189	192.189	192.189	192.189
N	8.370	8.370	8.370	8.370	8.370	8.370
W_s (N)	0.804	0.804	0.804	0.804	0.804	0.804
F_t (N)	124.136	124.136	124.136	124.136	124.136	124.136
F'_t (N)	27.143	27.143	27.143	27.143	27.143	27.143
F_u^{int} (N)	64.468	82.398	85.729	110.713	103.855	87.199
$N \cdot c_u \cdot A_p$ (N)	402.155	402.155	402.155	402.155	402.155	402.155
$q_{tip} \cdot A_p$ (N)	0.804	0.804	0.804	0.804	0.804	0.804
FSH (N)	448.845	466.775	470.106	495.090	488.232	471.576
FTS (N)	317.128	317.128	317.128	317.128	317.128	317.128
FTS' (N)	220.136	220.136	220.136	220.136	220.136	220.136
FGS (N)	594.343	594.343	594.343	594.343	594.343	594.343
Hypothesis	tensionf	tensionf	tensionf	tensionf	tensionf	tensionf

Table 4.6.3 Components in Christensen's equation for analysis data

Analysis	CET3	CET4	CET5	CET6	CET7	CET8
$-P_{tip}$ (Pa)	14700.000	14210.000	14700.000	14210.000	14210.000	14308.000
$-P_{top}$ (Pa)	60478.453	61398.895	60965.746	61398.895	61398.895	61398.895
$T_i = T_e$ (N)	192.189	192.189	192.189	192.189	192.189	192.189
N	8.370	8.370	8.370	8.370	8.370	8.370
W_s (N)	0.804	0.804	0.804	0.804	0.804	0.804
F_t (N)	26.600	25.714	26.600	25.714	25.714	25.891
F_u^{int} (N)	109.439	111.105	110.321	111.105	111.105	111.105
$N \cdot c_u \cdot A_p$ (N)	402.155	402.155	402.155	402.155	402.155	402.155
$q_{tip} \cdot A_p$ (N)	0.804	0.804	0.804	0.804	0.804	0.804
FSH (N)	493.816	495.482	494.698	495.482	495.482	495.482
FTS (N)	219.593	218.707	219.593	218.707	218.707	218.884
FGS (N)	594.343	594.343	594.343	594.343	594.343	594.343
Hypothesis	tensionf	tensionf	tensionf	tensionf	tensionf	tensionf

where:

FSH = Ultimate load for Shear Failure,

FTS = Ultimate load for Tension Failure,

FGS = Ultimate load for General Shear Failure,

FTS' = Modified ultimate load for tension failure.

Using data from laboratory tests, the values given in Table 4.6.2 were obtained. Table 4.6.2 gives the values obtained for the three modes of failures (FSH, FTS or FTS' and FGS) expected for suction caisson foundations. From the results of Table 4.6.2, it can be seen that the caisson failed in tension (FTS or FTS'), as reported in experiment. It is observed that P_{tip} from laboratory tests (given in second row of Table 4.6.2) gave unrealistic values; therefore, it was changed to P'_{tip} (an approximate value obtained from the results of analysis and average value of laboratory test results margin) to give a better correlation and to match with the total capacity obtained from laboratory tests (FTS').

Using data from finite element analyses, the values given in Table 4.6.3 were obtained. Table 4.6.3 gives the loads obtained for the three modes of failure expected for suction caissons. It is seen that the caisson fails in tension as reported in the experiment. Table 4.6.4 gives the ratios between the experimentally computed values and analytically computed values of various terms in Christensen's equation. From the calculations shown in Table 4.6.4, it can be seen that the results obtained using finite element data match very well with the load for failure modes obtained from laboratory tests (using modified P'_{tip} and FTS'). T/A in Figure 4.6.4 refers to the ratio of test result by analysis result.

Table 4.6.4 Ratio of components in Christensen's equation between laboratory tests and finite element analyses results

Ratio = T/A	CET3	CET4	CET5	CET6	CET7	CET8
$-P_{tip}$	4.667	4.828	4.667	4.828	4.828	4.795
$-P'_{tip}$	1.020	1.056	1.020	1.056	1.056	1.048
$-P_{top}$	0.589	0.742	0.777	0.996	0.935	0.785
$T_i = T_e$	1.000	1.000	1.000	1.000	1.000	1.000
W_s	1.000	1.000	1.000	1.000	1.000	1.000
F_t	4.667	4.828	4.667	4.828	4.828	4.795
F'_t	1.020	1.056	1.020	1.056	1.056	1.048
F_u^{int}	0.589	0.742	0.777	0.996	0.935	0.785
$N \cdot C_u \cdot A_e$	1.000	1.000	1.000	1.000	1.000	1.000
$Q_{tip} \cdot A_e$	1.000	1.000	1.000	1.000	1.000	1.000
FSH	0.909	0.942	0.950	0.999	0.985	0.952
FTS	1.444	1.450	1.444	1.450	1.450	1.449
FTS'	1.002	1.007	1.002	1.007	1.007	1.006
FGS	1.000	1.000	1.000	1.000	1.000	1.000

4.6.2. Results of University of Texas at Austin Model Tests

From the source reference used for tests carried out at the University of Texas at Austin [El-Gharbawy, 1998], the following parameters required for finite element analysis were obtained.

Average soil sample size: 0.762 m height and 0.762 m diameter. Suction foundation model size: 0.106 m diameter with various length to diameter ratios (L/D ratios, of 2, 4, and 6) were used. Also another model with a diameter of 0.0508 m and L/D ratio equal to 12 was used. The tests used one soil sample with properties as given below.

Caisson model Material Properties: Acrylic

Young Modulus, E : 3 GPa

Poisson's ratio, ν : 0.35

Soil Properties: Kaolinite

Slope of virgin consolidation line in $e:\log p'$ diagram, λ : 0.22583

Slope of swelling line in $e:\log p'$ diagram, κ : 0.04853

Poisson's ratio, ν : 0.3

K_0 : 0.56

Permeability, k : 2.72288×10^{-8} m/s

Friction coefficient, f : 0.466

Specific gravity, G_s : 2.61

Water content, w_c : 84.3 %

Critical State ratio, M_c : 0.75

Ta_{max} : 0.5984 kPa; 0.8273 kPa; 1.6545 kPa for model with $L/D = 2, 4, (6 \text{ and } 12)$ respectively.

The finite element analysis used the axisymmetric element mesh to model the system using quadrilateral eight-noded elements with pore pressure degrees of freedom. The finite element analysis also utilised contact surface idealization to simulate contact between soil body and foundation. Finite element mesh used 596 to 615 elements with contact surface idealization; a typical mesh detail for the specimen STCC6 is shown in Fig.4.6.5. An idealization of suction force generation was used to simulate its behaviour during tests, as given in chapter 3. An equivalent distributed load of 51.08 kPa was applied to the soil surface for each finite element analysis to simulate soil strength characteristics due to suction pressure applied at the bottom (to bring it to the required

value of consolidation stress required for the test) during preparation of the soil sample. The magnitude of the distributed load, applied on top of the soil body, was found by using an equivalent energy approach of stress and displacement obtained due to suction pressure application. Results from finite element analyses are given in Tables 4.6.2 and 4.6.3.

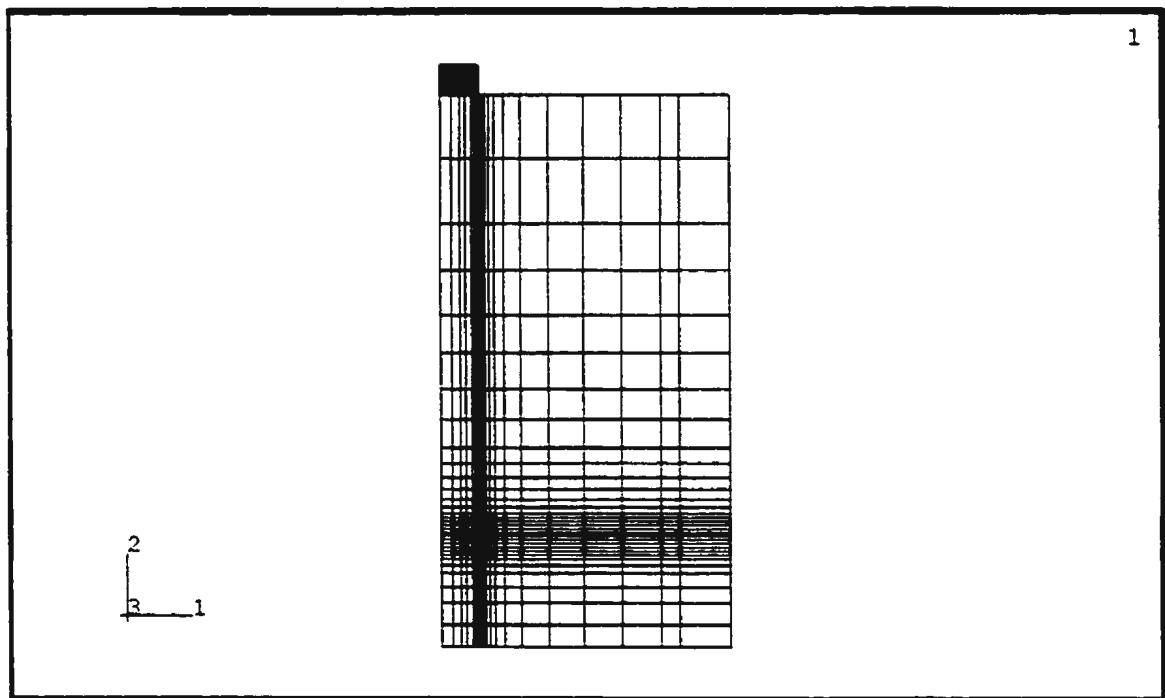


Figure 4.6.5 University of Texas suction foundation model mesh for $L/D = 6$.

Table 4.6.5 Short term pullout (undrained loading) analysis results

Test ID	Suction Pressure at top cap (kPa)	Maximum Pullout Capacity (N)	Displacement at maximum load (m)
STCC2	14.48 (-)	163.24 (164.57)	0.0026 (0.0030)
STCC4	18.61 (20.68)	349.17 (382.53)	0.0040 (0.0246)
STCC6	16.54 (20.68)	663.19 (596.03)	0.0067 (0.0216)
STCC12	16.54 (-)	246.86 (177.92)	0.0017 (0.0305)

Results given in brackets indicate the results obtained from laboratory tests.
 - = not available.

Table 4.6.6 Long-term pullout (drained loading) analysis results

Test ID	Maximum Pullout Capacity (N)	Displacement at maximum load (m)
STCC2	77.84 (88.96)	0.0016 (0.0033)
STCC4	200.16 (151.23, 60.13)	0.0017 (-)
STCC6	200.16 (177.92)	0.0023 (0.0038)
STCC12	200.16 (88.96,129)	0.0009 (0.0007)

Results given in brackets indicate the results obtained from laboratory tests.
 - = not available.

From finite element analyses, it was found that the responses of the model were stiffer than the behaviour found in laboratory tests results. It was also observed that the maximum pullout capacity forces of the FEA (finite element analysis) were close to the experimental ones, except in the case of STCC12 for drained loading. It was observed from the load applied on top of the soil body that it was equal to a soil height of 10.35 m,

which gave a model to prototype ratio of 101. This closely simulates the results of an L/D ratio equal to 2, where an excellent agreement has been obtained between load-displacement behaviour (Table 4.6.5). For other L/D ratios, the load to be applied on the top had to be different to obtain values closer to experimental values. Hence it is observed that the suction pressure applied at the bottom in the University of Texas tests should have been different for different L/D ratios to give a better fit with the analytical results.

Test results of the force–displacement relationship for an undrained test (STCC2) are given in Figure 4.6.6 showing a good match with the results from laboratory tests. Figure 4.6.7 gives results from an undrained test simulation of STCC2 where the model was pulled at a load increment of 11.12 N with a waiting time (for drainage to take place) of 3 hours. From the figure it is seen that there were 7 load increments applied during simulation starting at 11.12 N and giving a total load of 77.84 N, which is close to 88.94 N obtained in laboratory test. Also, all the finite element analysis results are given in Appendix A3.

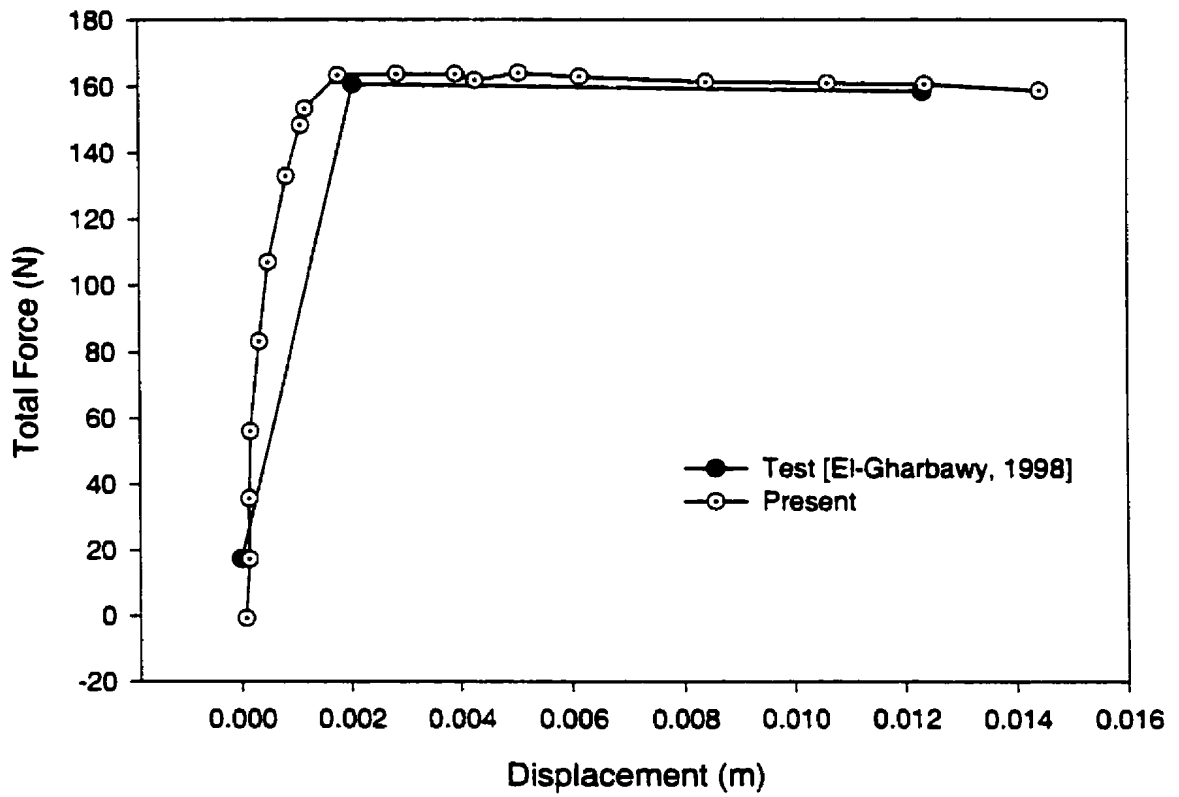


Figure 4.6.6. Force-displacement curve of STCC2 for undrained loading

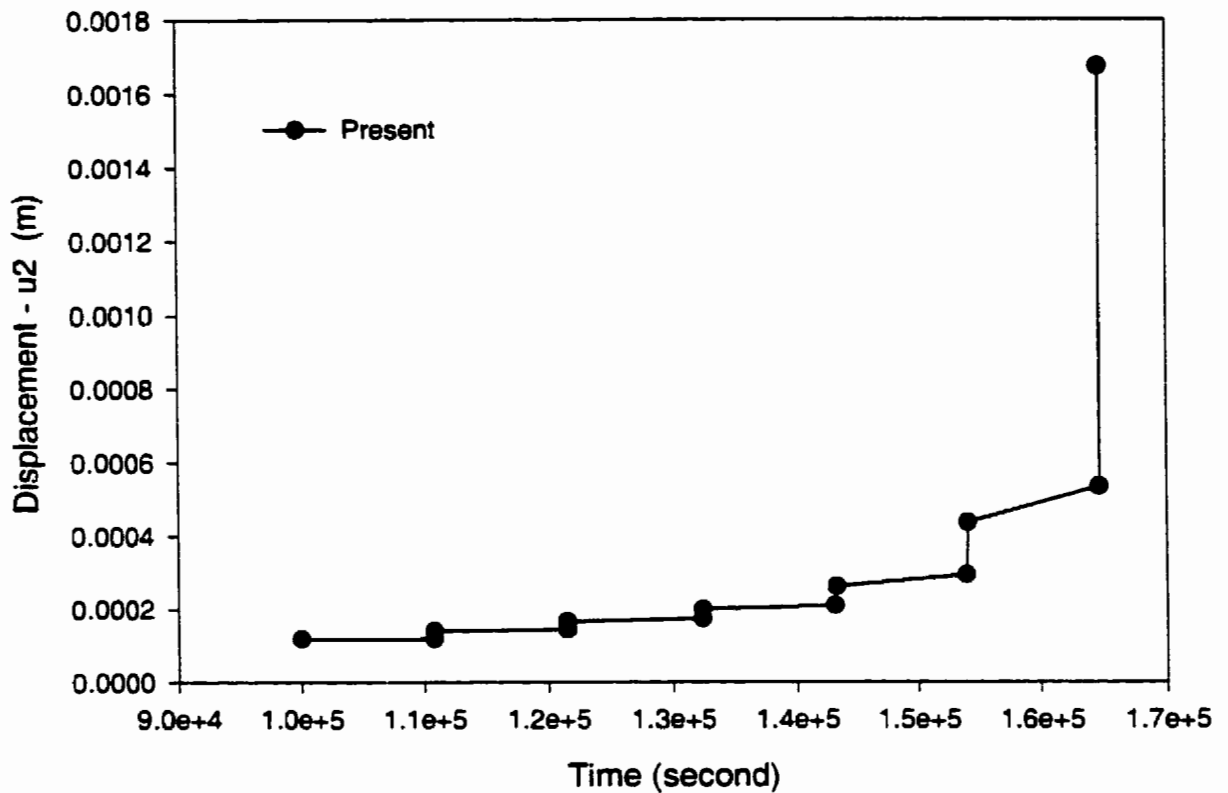


Figure 4.6.7. Displacement-time curve of STCC2 for drained loading (at caisson head top center)

Analytical Approximations using Christensen's Formulation

From formulations given in Chapter 2, the Christensen formulation (given in section 2.5.1) was simplified to apply it to the undrained Texas tests and analysis results were obtained similar to the MIT tests given in section 4.6.1.

In order to use Christensen's formulations, the following information was required to complete the failure modes calculations.

$$\begin{array}{llll}
 A_{e1} = 0.008107\text{m}^2 & A_{e2} = 0.002027\text{m}^2 & \text{gamma}' = 4931.949\text{N/m}^3 & \text{alpha} = 1 \\
 A_{i1} = 0.007126\text{m}^2 & A_{i2} = 0.001781\text{m}^2 & D_{e1} = 0.1016\text{m} & \\
 P_{e1} = 0.319186\text{m} & P_{e2} = 0.159592\text{m} & D_{e2} = 0.0508\text{m} &
 \end{array}$$

P_{e1} , A_{e1} , A_{i1} and D_{e1} are for models with $L/D = 2, 4,$ and 6 ; P_{e2} , A_{e2} , A_{i2} and D_{e2} for $L/D = 12$.

Table 4.6.7 Components in Christensen's equation for undrained tests data

Test	STCC2	STCC4	STCC4a	STCC6	STCC12
$-P_{top}$ (Pa)	-	27579.000	15513.188	24131.625	-
$-P_{top}$ (Pa)	-	20684.250	20684.250	20684.250	-
c_v (Pa)	-	827.370	827.370	1654.740	-
A_1 (m)	-	0.406	0.406	0.610	-
$q_{top} = \sigma_{at}$ (Pa)	-	2004.344	2004.344	3006.516	-
N	-	9.000	9.000	9.000	-
$T_e = T_i$ (N)	-	107.324	107.324	321.972	-
W_s (N)	-	14.282	14.282	21.423	-
F_i (N)	-	196.516	110.540	171.952	-
$N \cdot c_v \cdot A_e$ (N)	-	60.370	60.370	120.740	-
$q_{top} \cdot A_e$ (N)	-	16.250	16.250	24.375	-
F_u^{int} (N)	-	147.387	147.387	147.387	-
FSH (N)	-	362.035	362.035	791.331	-
FTS (N)	-	318.122	232.147	515.347	-
FGS (N)	-	151.444	151.444	418.337	-
Hypothesis	-	generalf	generalf	generalf	-

Table 4.6.8 Components in Christensen's equation for undrained analyses data

Analysis	STCC2	STCC4	STCC6	STCC12
$-P_{tip}$ (Pa)	10342.125	15513.188	30888.480	28613.213
$-P_{top}$ (Pa)	14478.975	18615.825	16547.400	16547.400
c_u (Pa)	598.464	827.370	1654.740	1654.740
A_1 (m)	0.203	0.406	0.610	0.610
$q_{tip} = \sigma_{mat}$ (Pa)	1002.172	2004.344	3006.516	3006.516
N	9.000	9.000	9.000	9.000
$T_e = T_i$ (N)	38.816	107.324	321.972	160.985
W_s (N)	7.141	14.282	21.423	21.423
F_i (N)	73.694	110.540	220.098	203.886
$N \cdot c_u \cdot A_e$ (N)	43.667	60.370	120.740	120.740
$q_{tip} \cdot A_e$ (N)	8.125	16.250	24.375	24.375
F_u^{int} (N)	103.171	132.648	117.910	117.910
FSH (N)	180.802	347.297	761.854	439.880
FTS (N)	119.650	232.147	563.493	386.294
FGS (N)	74.358	151.444	418.337	257.350
Hypothesis	generalf	Generalf	generalf	Generalf

Table 4.6.9 Ratio of components in Christensen's equation between laboratory tests and finite element analysis results for undrained loading

Ratio = T/A	STCC2	STCC4	STCC6	STCC12
$-P_{tip}$	-	1.778	0.781	-
$-P_{top}$	-	1.111	1.250	-
c_u	-	1.000	1.000	-
A_1	-	1.000	1.000	-
q_{tip}	-	1.000	1.000	-
$T_e = T_i$	-	1.000	1.000	-
W_s	-	1.000	1.000	-
F_i	-	1.778	0.781	-
$N \cdot c_u \cdot A_e$	-	1.000	1.000	-
$q_{tip} \cdot A_e$	-	1.000	1.000	-
F_u^{int}	-	1.111	1.250	-
FSH	-	1.042	1.039	-
FTS	-	1.370	0.915	-
FGS	-	1.000	1.000	-

where:

FSH = Ultimate load for Shear Failure,

FTS = Ultimate load for Tension Failure,

FGS = Ultimate load for General Shear Failure.

Using data from laboratory tests, the values given in Table 4.6.7 were obtained. Table 4.6.7 gives the values obtained for the three modes of failures expected for suction caisson behaviour. It can be seen that the caissons failed in general shear, as reported in experimental results.

The laboratory test results were not complete for STCC2 and STCC12, consequently they could not be calculated as seen in Tables 4.6.7. Using data from finite element analysis, the values given in Table 4.6.8 were obtained. Table 4.6.8 gives the loads obtained for the three modes of failures expected for suction caissons. It is seen that the caisson fails in general shear as reported in the experiment. Table 4.6.9 gives the ratio between the experimentally computed and analytically computed values. The results given in Table 4.6.9 show that there is no proper correlation between the experimental and analytical values, except in the case of FSH (ultimate force for shear strength failure) and FGS (ultimate force for general shear failure) for STTC4 and STCC6 tests. The probable reason may be that the test techniques were not similar between University of Texas and other tests that show good correlation between Christensen's formulation and test results (i.e. MIT tests).

4.6.3. Results of IIT Madras Model Tests [Prasad, 1992]

Soil properties obtained for soil sample of IIT Madras Tests are as given earlier in Tables 4.4.1. From the literature, it was obtained that, for normally consolidated clays [Skempton, 1957]:

$$c_u/p = 0.11 + 0.0037(PI) \quad (3.110)$$

where: c_u = undrained shear strength of soil

p = effective vertical stress

PI = plasticity index in percent

Internal friction angle of this soil with $c_u = 5$ kPa is in the range of 19° to 24° [Senneset and Janbu, 1985], which gives $K_0 = 0.6$ and $f = 0.345$. From another study by Pots and Martins (1982), it was found that the ratio of $\tan(\text{friction angle of wall-soil contact})$ to $\tan(\text{internal friction angle})$ was around 0.9. This could be used to determine friction angle for soil to wall contact. Permeability, k used was 2.7×10^{-8} m/s, and critical state ratio, M_c was 0.74.

Also, in order to obtain approximate values of coefficient of consolidation and coefficient of swelling, the following equations were used:

$$\text{a) } C_c = 0.2343 (LL/100) G_s \quad \text{Nagaraj \& Murty (1985)} \quad (3.111)$$

$$\text{b) } C_c = 0.5 G_s (PI/100) \quad \text{Wroth \& Wood (1978)} \quad (3.112)$$

and $C_s = 1/5$ to $1/4 C_c$ (used value was: $C_s = 0.225 C_c$)

Poisson's ratio = 0.3

From the above relationships, the values given below required for application of cam-clay model were obtained:

Table 4.6.10 Bulk and swelling moduli coefficients

Soil ID	Bulk Modulus, λ (a)	Swelling Modulus, κ (a)	Bulk Modulus, λ (b)	Swelling Modulus, κ (b)
Soil 1	0.223868	0.050370	0.186434	0.041947
Soil 2	0.204757	0.046070	0.145652	0.032771

a, b refer to the two different equations cited above; also $C_c/\lambda = 2.3$; $C_s/\kappa = 2.3$

Finite element meshes used consisted of 680 ($L/D = 15$), 1140 ($L/D = 25$), and 1840 ($L/D = 40$) quadrilateral eight-noded axisymmetric elements with pore pressure degrees of freedom for the three different models used. A typical mesh for $L/D = 25$ is shown in Fig.4.6.8. Contact surface idealization was also used to simulate contact between soil body and foundation. Also in the numerical analysis, a virtual distributed load of 16.95 kPa was also applied to the top of soil-surface to simulate the average soil strength characteristics of soil samples. Typical results (obtained from finite element analysis) are given in Table 4.6.11. The analytical results obtained are slightly lower than the experimental values for lower L/D ratios and higher for higher L/D ratios. Also the correlation between experiment and analysis seems to be better for the L/D ratio equal to 25. From the given c_u value of 5 kPa, the soil data given simulated very closely the analytical results for $L/D = 25$.

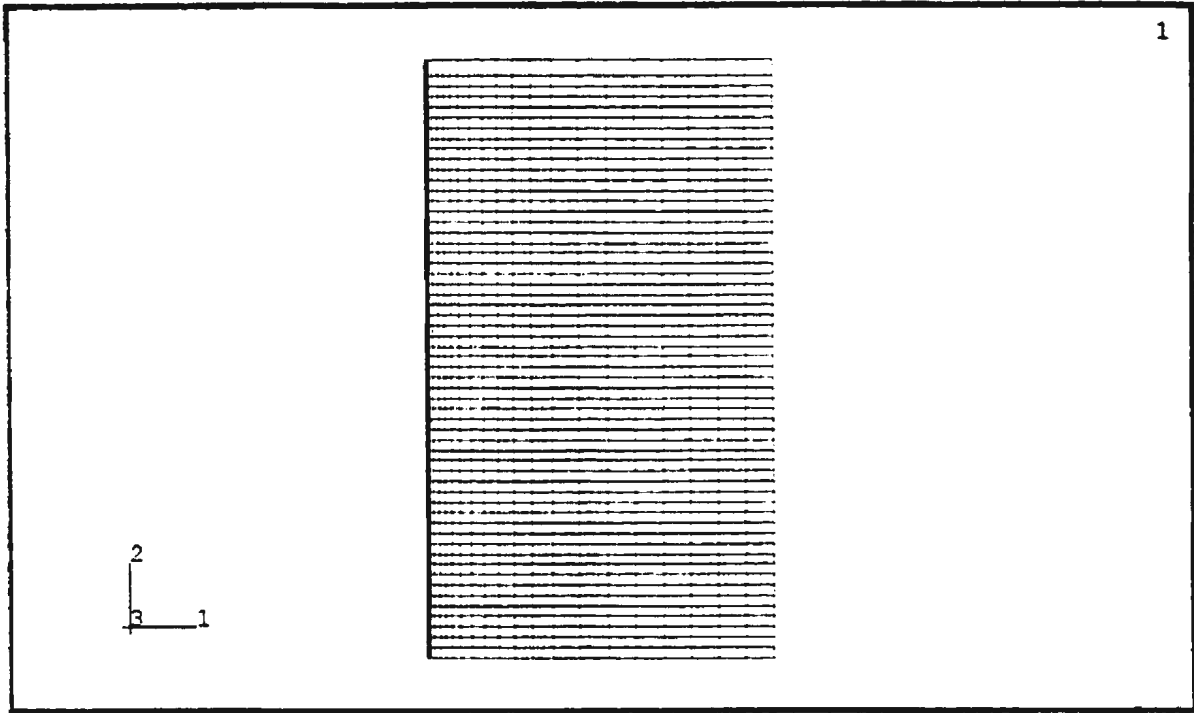


Figure 4.6.8 IIT suction foundation model mesh for $L/D = 25$, $D = 13.8$ mm.

Table 4.6.11 Results from finite element analysis (Laboratory test values)

Test ID	Diameter (mm)	L/D	Max Pullout Capacity (N)	At Displacement (mm)
1	13.8	15	43 (52)	0.35 (0.50)
2	13.8	25	72 (71)	0.34 (0.40)
3	13.8	40	117 (90)	0.49 (0.75)
4	18	15	72 (80)	0.36 (0.40)
5	18	25	123 (110)	0.36 (0.40)
6	18	40	200 (130)	0.14 (0.25)

Results given in brackets indicate the results obtained from laboratory tests.

Figures showing force-displacement curves are given in Figures 4.6.9 and 4.6.10.

All results from finite element analyses along with respective experimental values are given in Appendix A4.

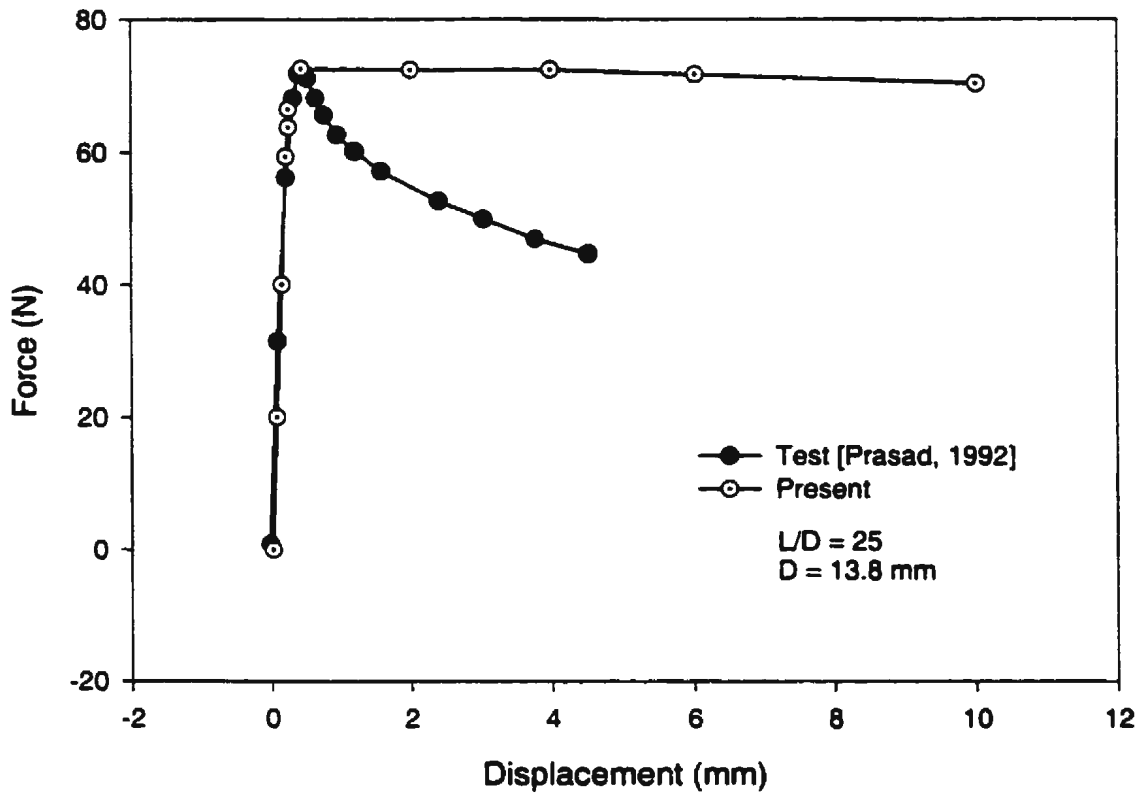


Figure 4.6.9 Force-displacement curve of single pile pullout test, Dia.: 13.8 mm, L/D = 25, IIT Madras model.

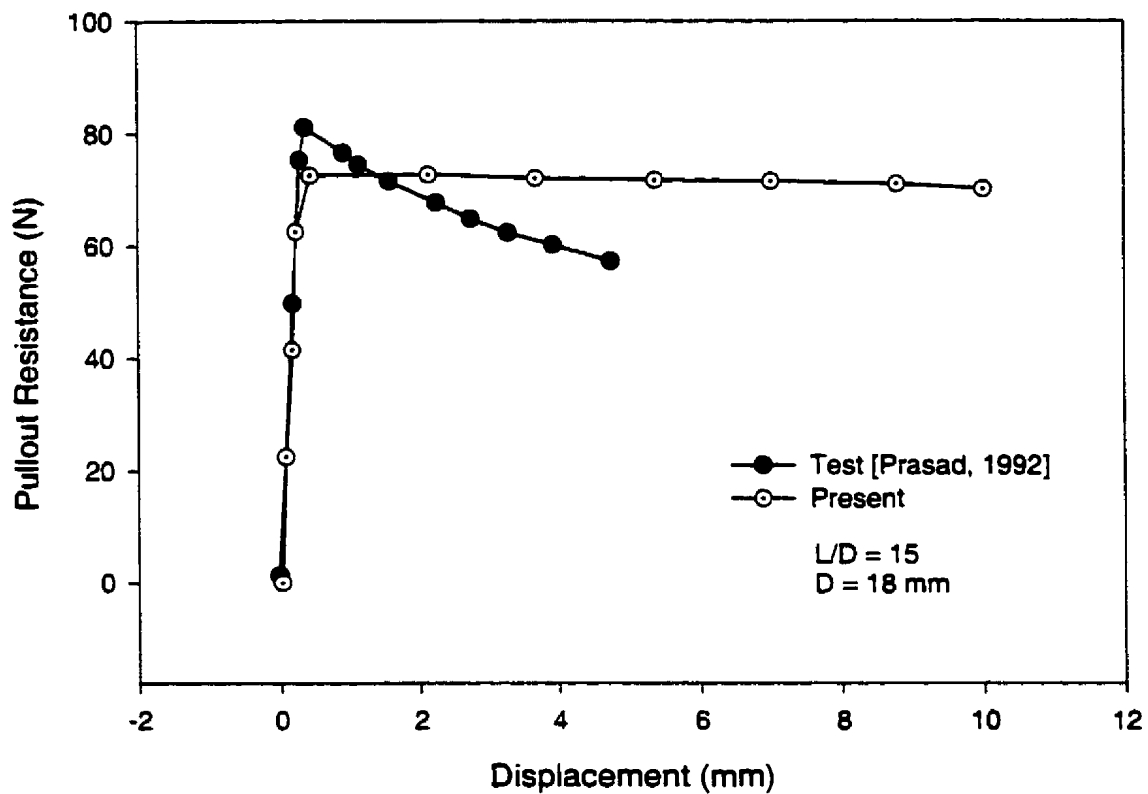


Figure 4.6.10 Force-displacement curve of single pile pullout test, Dia.: 18.0 mm, $L/D = 15$, IIT Madras model.

The difference in force-displacement curves between laboratory test and finite element analysis results could be attributed to constitutive equation of both contact surface and soil plasticity. However, the major factor seems to come from contact constitutive equation that needs to be improved to get better results.

4.6.4. Results of IIT Madras Model Tests [Rao et al., 1997]

An approach similar to that given in Section 4.6.4 was used to determine soil parameters for the finite element analysis. From the formulations given in section 4.6.4 and soil properties obtained from source reference [Rao et al., 1997], as given earlier in Section 4.5.4, the following coefficients needed for cam-clay model were obtained (see Table 4.6.12). The values in Table 4.6.12 are the same for the three soil due to the value of liquid limit, LL and plasticity index, PI (see Table 4.5.1) that are used to define C_c by equations (3.111) and (3.112) are the same. Other properties used the same value as IIT Madras test by Prasad (1992).

Table 4.6.12 Bulk and swelling moduli coefficients

Soil ID	Bulk Modulus, λ (a)	Swelling Modulus, κ (a)	Bulk Modulus, λ (b)	Swelling Modulus, κ (b)
Soil 1	0.223868	0.050370	0.186434	0.041947
Soil 2	0.223868	0.050370	0.186434	0.041947
Soil 3	0.223868	0.050370	0.186434	0.041947

a, b refer to the two different equations cited in earlier in section 4.6.4; also $C_c/\lambda = 2.3$;

$$C_s/\kappa = 2.3$$

Finite element meshes consisted of 2688 eight-noded quadrilateral axisymmetric elements with pore pressure degrees of freedom (see Figure 4.6.11) (the finite element model represents the actual test situation carried out). Contact surface idealization was also used to simulate contact between soil body and foundation. Also, in numerical analyses, virtual distributed loads of 6.1017, 12.20339, and 19.66102 kPa, for the three

different c_u values of 1.8, 3.6, and 5.8 kPa, respectively, were also applied on the top of soil-surface to simulate the average soil strength characteristics of soil samples. Results from finite element analyses are given in the following Table 4.6.13 along with experimental values that were extracted from previous Figures 4.5.1 to 4.5.4 in Section 4.5. It is observed from the results given in Table 4.6.13 that $L/D = 1$ very closely simulates the analysis and test results. Some results from finite element analyses obtained are given in the following Figures 4.6.12 to 4.6.14. All results from finite element analyses are given in Appendix A5.

Table 4.6.13 Results from finite element analysis (laboratory test values)

Test Models	Ultimate Pullout Capacity of Suction Caisson Model (N)		
	LI = 0.8	LI = 0.6	LI = 0.4
$L/D = 1$	52 (56.11)	98 (115.55)	150 (162.78)
$L/D = 1.5$	168 (56.67)	221 (136.36)	289 (176.67)
$L/D = 2$	84 (83.33)	136 (170.45)	N/A (210)

Results given in brackets indicate the results obtained from laboratory tests.

N/A = not available

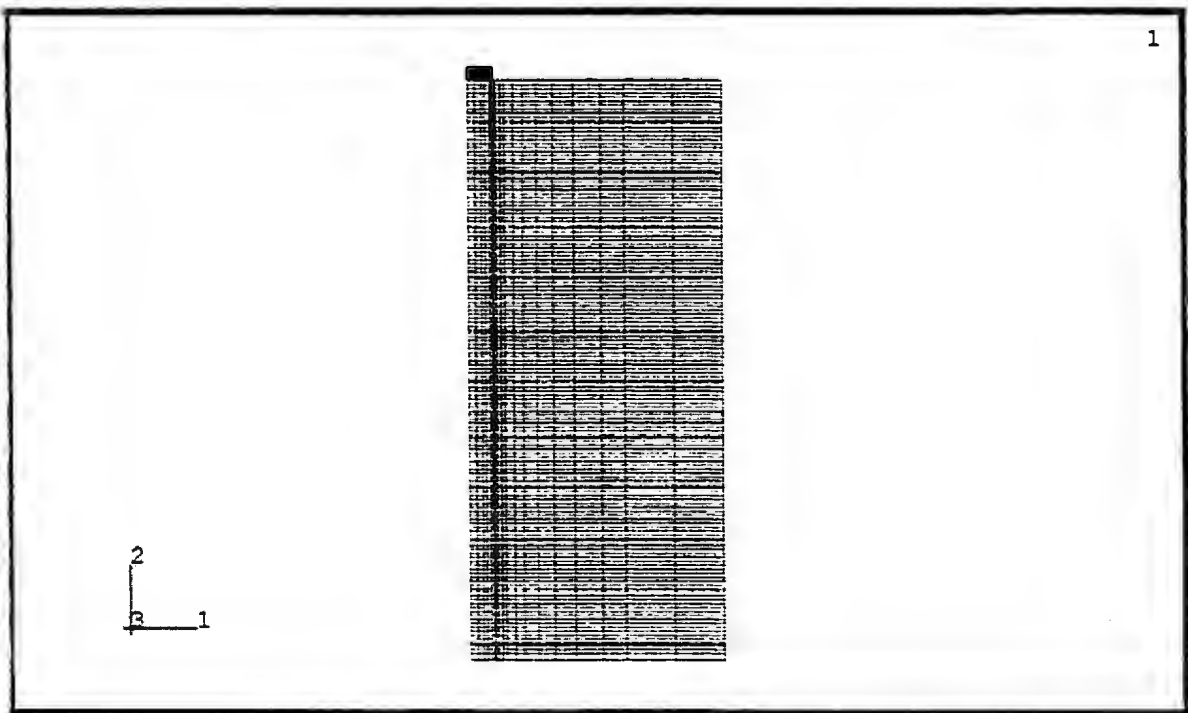


Figure 4.6.11 IIT suction foundation model mesh for $L/D = 1$, $D = 75$ mm.

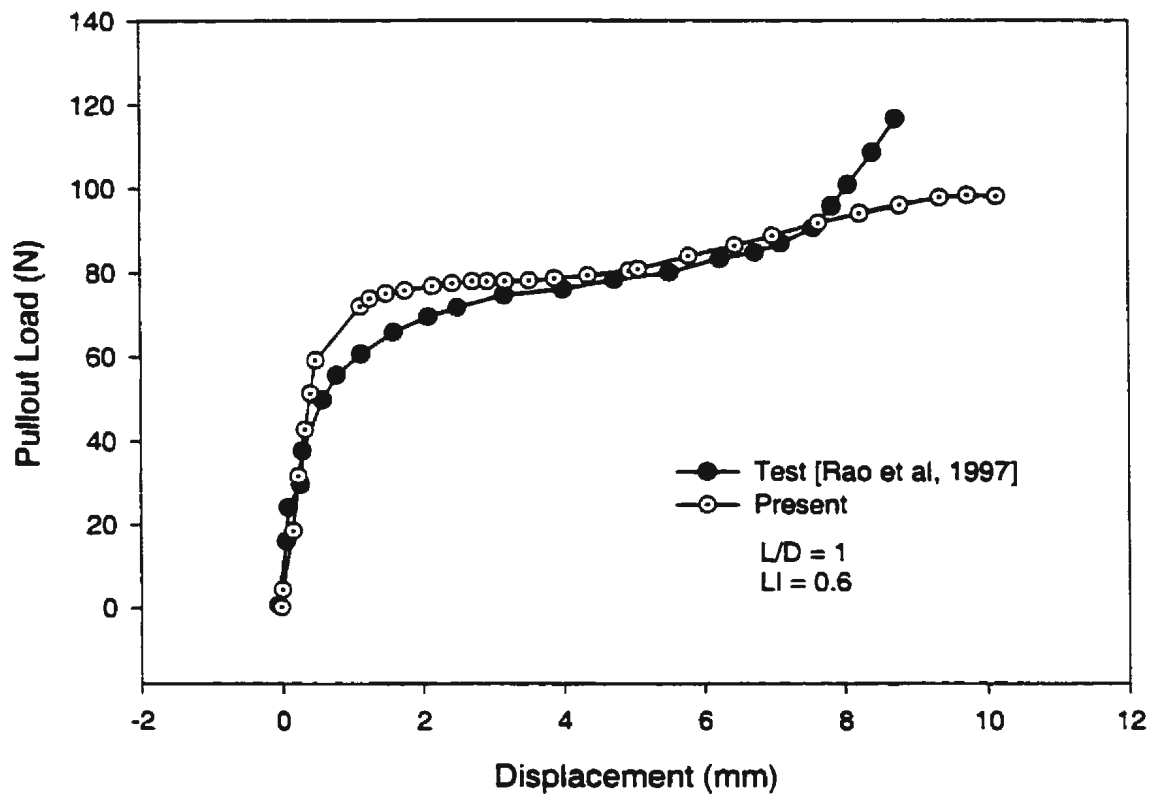


Figure 4.6.12 Pullout load–displacement curve, for $L/D = 1$, $LI = 0.6$

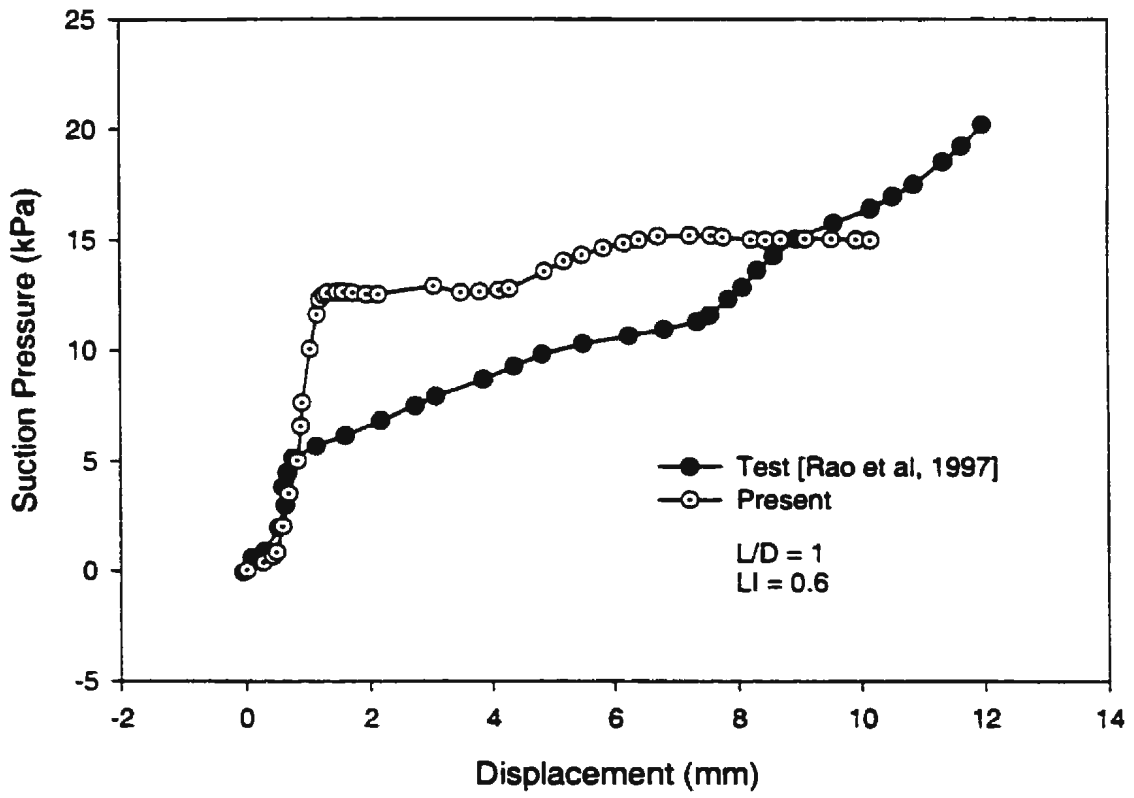


Figure 4.6.13 Suction pressure–displacement curve, for $L/D = 1$, $LI = 0.6$

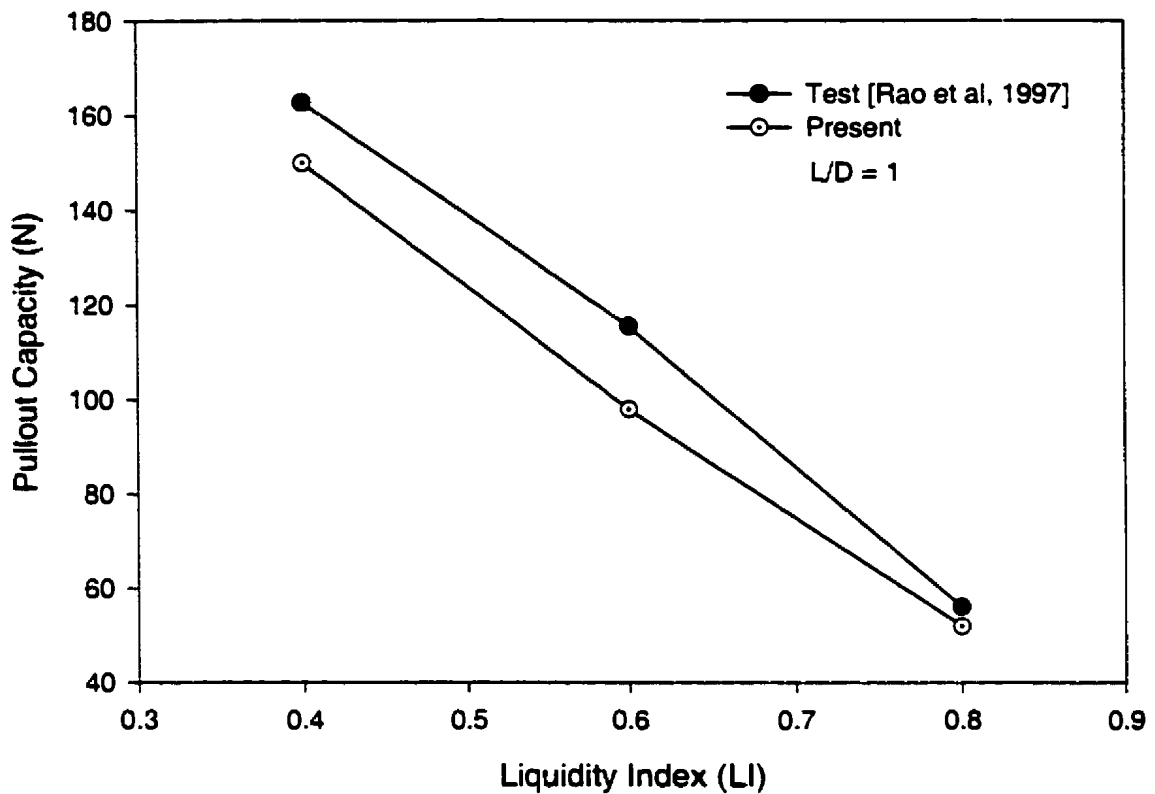


Figure 4.6.14 Pullout capacity–liquidity index (LI) curve, for $L/D = 1$

Analytical Approximations using Christensen’s Formulation

From the formulations given in Chapter 2, the Christensen’s formulation (given in section 2.5.1) was simplified to apply it to these tests; analysis results were obtained similar to that reported earlier for MIT tests in section 4.6.1. The following calculation of failure modes using Christensen’s formulation is carried out for the model with $L/D = 1$ only. In order to use the formulations, the following information was required to complete failure mode calculations: $\gamma = 16400 \text{ N/m}^3$, $\alpha = 1$.

Table 4.6.14 Components in Christensen's equation for tests data

Test	#1	#2	#3
A_i (m ²)	0.004	0.004	0.004
A_o (m ²)	0.004	0.004	0.004
P_o (m)	0.236	0.236	0.236
$-P_{top}$ (Pa)	0.000	0.000	0.000
Sigmat (Pa)	1230.000	1230.000	1230.000
$-P_{top}$ (Pa)	20000.000	20000.000	20000.000
c_u (Pa)	1800.000	3600.000	5800.000
$A_1=a_2$ (m)	0.075	0.075	0.075
q_{tip} (Pa)	1230.000	1230.000	1230.000
N	8.370	8.370	8.370
$T_o = T_i$ (N)	31.809	63.617	102.494
W_s (N)	5.434	5.434	5.434
F_i (N)	5.434	5.434	5.434
$N \cdot c_u \cdot A_o$ (N)	66.560	133.119	214.470
$q_{tip} \cdot A_o$ (N)	5.434	5.434	5.434
F_u^{int} (N)	88.357	88.357	88.357
FSH (N)	151.975	215.592	293.346
FTS (N)	42.677	74.485	113.362
FGS (N)	92.934	191.302	311.530
Hypothesis	Tensionf	tensionf	tensionf

Table 4.6.15 Components in Christensen's equation for analyses data

Analysis	#1	#2	#3
A_i (m ²)	0.004	0.004	0.004
A_e (m ²)	0.004	0.004	0.004
P_e (m)	0.236	0.236	0.236
$-P_{tip}$ (Pa)	1185.000	2338.000	3639.000
Sigmat (Pa)	1230.000	1230.000	1230.000
$-P_{top}$ (Pa)	15000.000	15000.000	15000.000
c_u (Pa)	1800.000	3600.000	5800.000
$A_1=a_2$ (m)	0.075	0.075	0.075
q_{tip} (Pa)	1230.000	1230.000	1230.000
N	8.370	8.370	8.370
$T_e = T_i$ (N)	31.809	63.617	102.494
W_s (N)	5.434	5.434	5.434
F_t (N)	5.235	5.434	5.434
$N \cdot c_u \cdot A_e$ (N)	66.560	133.119	214.470
$q_{tip} \cdot A_e$ (N)	5.434	5.434	5.434
F_u^{int} (N)	66.268	66.268	66.268
FSH (N)	129.885	193.502	271.257
FTS (N)	42.478	74.485	113.362
FGS (N)	92.934	191.302	311.530
Hypothesis	Tensionf	tensionf	tensionf

Table 4.6.16 Ratio of components in Christensen's equation between laboratory tests and finite element analysis results

Ratio =T/A	#1	#2	#3
$-P_{tip}$	0.000	0.000	0.000
$-P_{top}$	1.333	1.333	1.333
c_u	1.000	1.000	1.000
A_1	1.000	1.000	1.000
q_{tip}	1.000	1.000	1.000
$T_e = T_i$	1.000	1.000	1.000
W_s	1.000	1.000	1.000
F_t	1.038	1.000	1.000
$N \cdot c_u \cdot A_e$	1.000	1.000	1.000
$q_{tip} \cdot A_e$	1.000	1.000	1.000
F_u^{int}	1.333	1.333	1.333
FSH	1.170	1.114	1.081
FTS	1.005	1.000	1.000
FGS	1.000	1.000	1.000

Using data from laboratory tests, the values given in Table 4.6.14 were obtained. Table 4.6.14 gives the values obtained for the three types of failures expected for suction caisson behaviour. It appears that the caisson failed in tension, not as reported in experiment (which was claimed as general shear failure).

Using data from finite element analysis, the values given in Table 4.6.15 were obtained. Table 4.6.15 gives the loads obtained for the three types of failure expected for suction caissons. It is seen that the caisson fails in tension, not as reported in the experiment (which was claimed as general shear failure).

In Table 4.6.16, it shows good correlation between results from tests data and results from analysis data. The difference arises from different value of P_{top} between test results and analysis results.

4.7. Summary

From the comparison of finite element results with laboratory test results, it can be summarized that:

Finite element analysis results gave results close to 1g model test forces, when the model tests simulated closely the average soil pressures exerted on the prototype specimens [these tests were MIT tests with $L/D = 1$, University of Texas test for $L/D = 2$, and IIT Madras test (Rao et al., 1997) for $L/D = 1$].

The suction force model very closely approximated the suction pressures generated in 1g laboratory model tests during test simulations of the suction foundation

under pullout loads in some cases, viz., MIT model tests, and Texas model tests; however it did not properly simulate suction pressures for IIT model tests for $D = 0.076$ mm with $L/D = 1.5$ and 2 (see Appendix A5).

Christensen's formulation very closely approximates the failure modes and ultimate loads of the suction foundation for MIT test cases; however, it does not accurately predict ultimate pullout capacity for both Texas and IIT Madras tests. Christensen's formulation also would require input of actual suction pressures developed inside the caisson to get good correlation with test results.

Chapter 5 Scale Models and Failure Mode Analysis

5.1. Introduction

The testing of scaled models is necessary to explore the behaviour of a structural system in a laboratory environment before it is built to its actual size and usage. In geotechnical engineering, two different scaling model approaches are usually carried out in a laboratory in terms of its gravitational environment. The first model is a simple and inexpensive model that is tested in the normal or 1g environment. The second model is tested in an artificially generated ng environment. 1g model does not truly represent the actual soil stress state characteristics over the model; however it gives the required force displacement relationships that are required from tests carried out in a standard and simple laboratory environment. An ng model is capable of simulating the actual stress state characteristics of soil; however, some problems are encountered in the centrifuge model, due to scaling difficulties. The best known of these problems is that of conflicting time scales encountered when generation and dissipation of pore pressures take place as a result of dynamic excitation. Whereas the time scale for dynamic effect in the model is n times the prototype time, the model time is n^2 times prototype time for the fluid diffusion process. Thus the rate of pore pressure dissipation in seismically excited saturated sand exceeds the rate of generation [Scott, 1994]. In the scale model analyses reported in this chapter, a consistent scale is applied to the MIT suction caisson form to analyze 1g, ng and prototype model test results and examine the consistency of these results.

In the design of suction foundations, it is known that three types of failure modes occur in actual practice, viz., shear, tension, and general shear failures. It is also known that the general shear failure mode has the highest pullout resistance (or strength) capacity. Therefore, failure mode of a designed suction foundation is a significant information that could be used to explore better and optimal geometrical design of suction foundations. In the failure mode analyses, the MIT suction caisson form is used to examine the feasibility of obtaining different failure modes for the same soil environment (having the same properties). In this analysis the procedures for identifying different failure mode scenarios of suction foundations under pullout loads are examined.

5.2. Scale Model Analysis

In the scale model analysis, the typical MIT suction caisson form, shown in Figure 5.2.1, is used for analysing the model at 1g scale. Then all the geometric (as well as velocity) parameters are scaled up to the prototype dimensions as shown in Figure 5.2.2, and analysis is carried out for the prototype at 1g scale. It should be noted that the prototype is exactly the same finite element mesh as that used in Figure 5.2.1 with the exception that the mesh size is much larger. The reduced finite element model for ng tests will be the same as that shown in Figure 5.2.1. Additionally, all the necessary parameters are scaled down for the ng model and analysis carried out for the ng model. The results obtained from all the three models are correlated to examine the differences that exist between the results obtained from these three models.

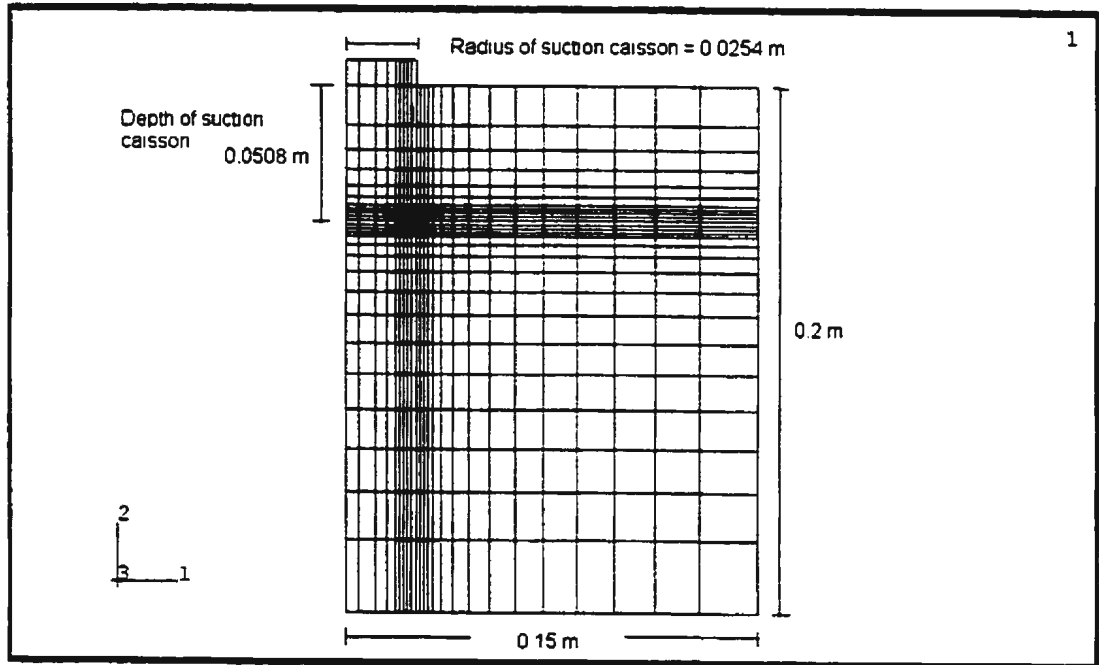


Figure 5.2.1 1g Model Finite Element Mesh

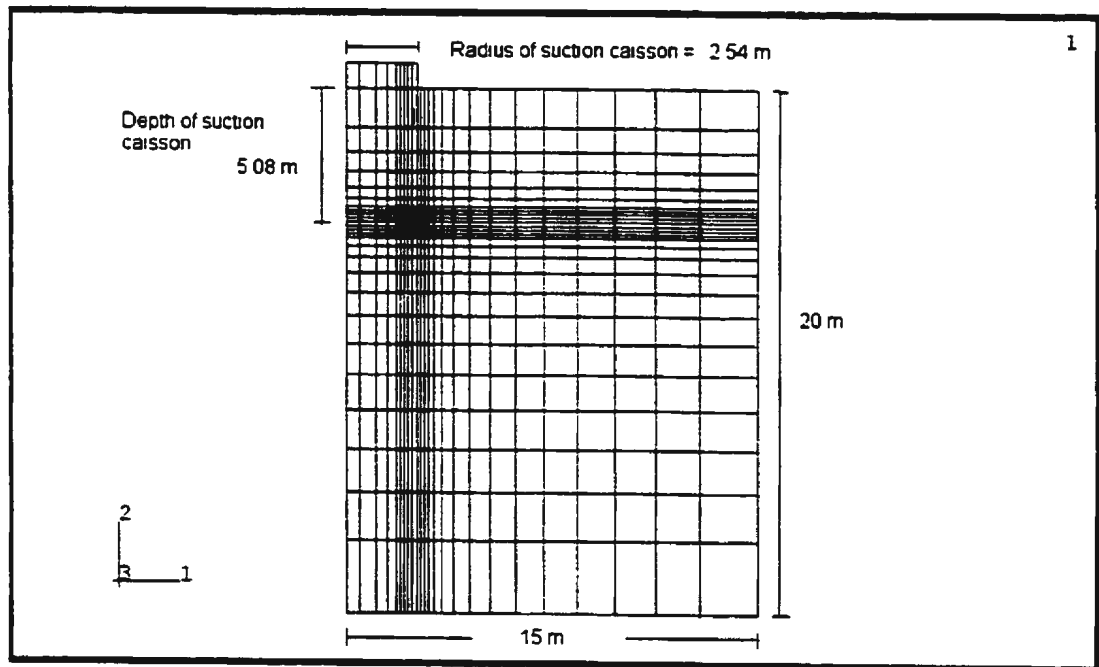


Figure 5.2.2 Prototype Finite Element Mesh

5.2.1. 1g Model Analysis

A 1g-model analysis is carried out for the model shown in Figure 5.2.1 having the same soil properties as the MIT test soil sample reported in section 4.2. The salient system properties are given in Table 5.2.1. In this model, a distributed load is applied on top of soil surface to simulate the average lateral soil stress state (as exists in the prototype caisson): this magnitude ($p = 19.33$ kPa) is equivalent to the overburden pressure of soil that exists at the depth of half foundation height of 2.5 m for a model to prototype scale of 1:100 (see Figure 5.2.3). Then the pullout analysis on this model is carried out at the same pullout rates as the original MIT 1g model tests.

Table 5.2.1 Salient system properties for 1g small model

Parameter	Value
Coefficient of elastic bulk modulus, κ	0.00435
Coefficient of hardening bulk modulus, λ	0.22826
Submerged unit weight of soil, γ'	7.735 kN/m ³
Permeability of soil, k	2.37×10^{-9} m/s
First pullout rate, V_1	0.0003 m/min.
Second pullout rate, V_2	0.003 m/min.
Fluid flow velocity, V_f	1.748×10^{-7} m/s
Average lateral soil stress, $p = 19.33$ kPa	7.732 kPa

The finite element model used for this study is shown in Figure 5.2.1. From the pullout test simulation of this 1g model, results obtained for the force-displacement relationships are shown in Figure 5.2.4. The initial at rest horizontal soil stress distribution obtained for the model is given in Figure 5.2.3, both on the inside and outside of the caisson. From the results given in Figure 5.2.4, a maximum pullout force capacity (F_{TOTAL}) of 37.7 N is obtained. This total force is made up of two components, viz., a maximum suction force (F_{POR}) of 21.5 N and a corresponding wall friction force (F_{WALL}) of 16.2 N. The soil shear stress state during the maximum pullout force is shown in Figure 5.2.5 along with the pore pressure developments in Figure 5.2.6.

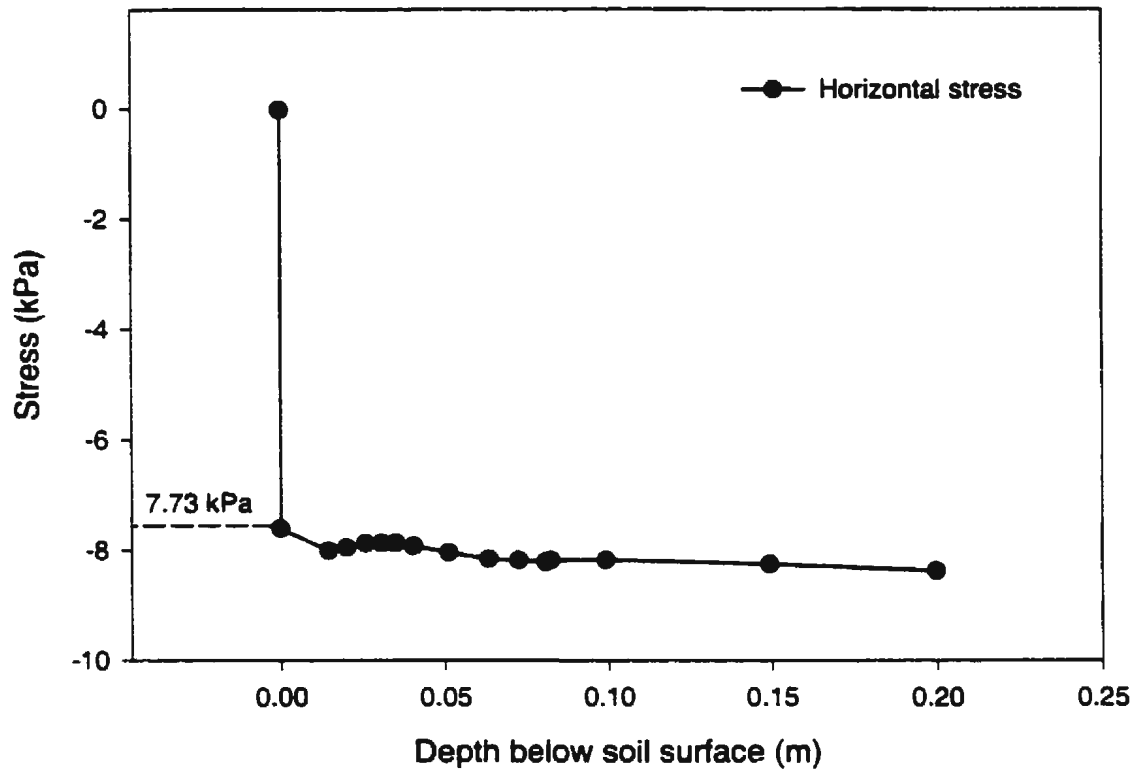


Figure 5.2.3 Initial “at rest” horizontal stress state acting on the walls of 1g model

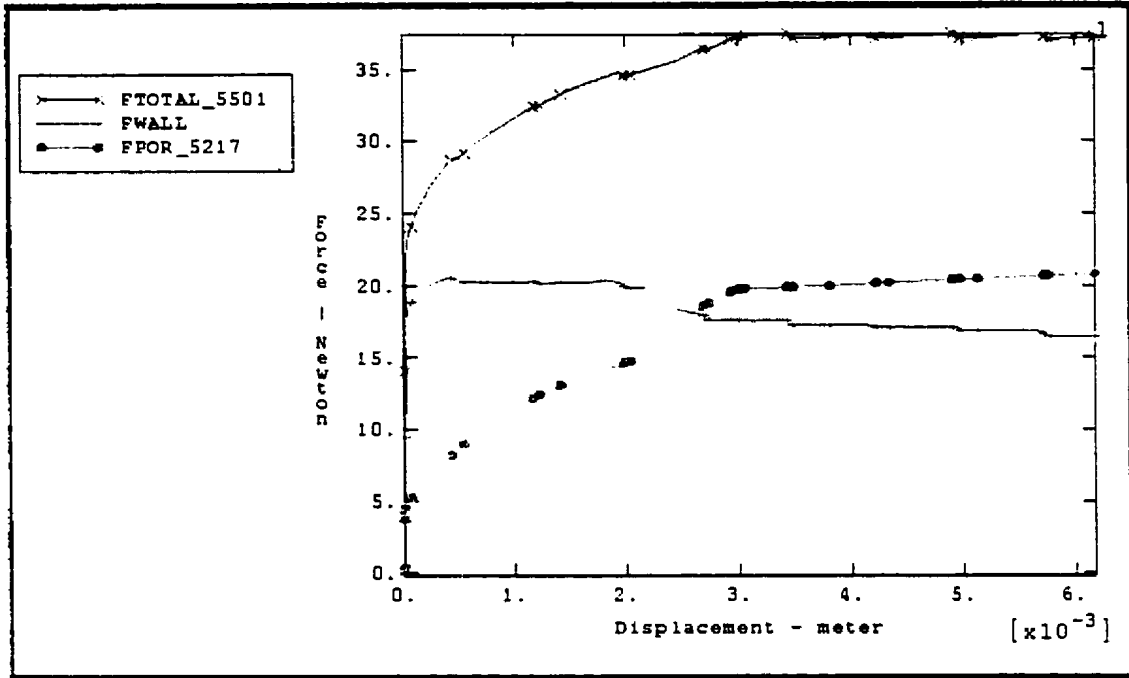


Figure 5.2.4 Pullout Forces of 1g model.

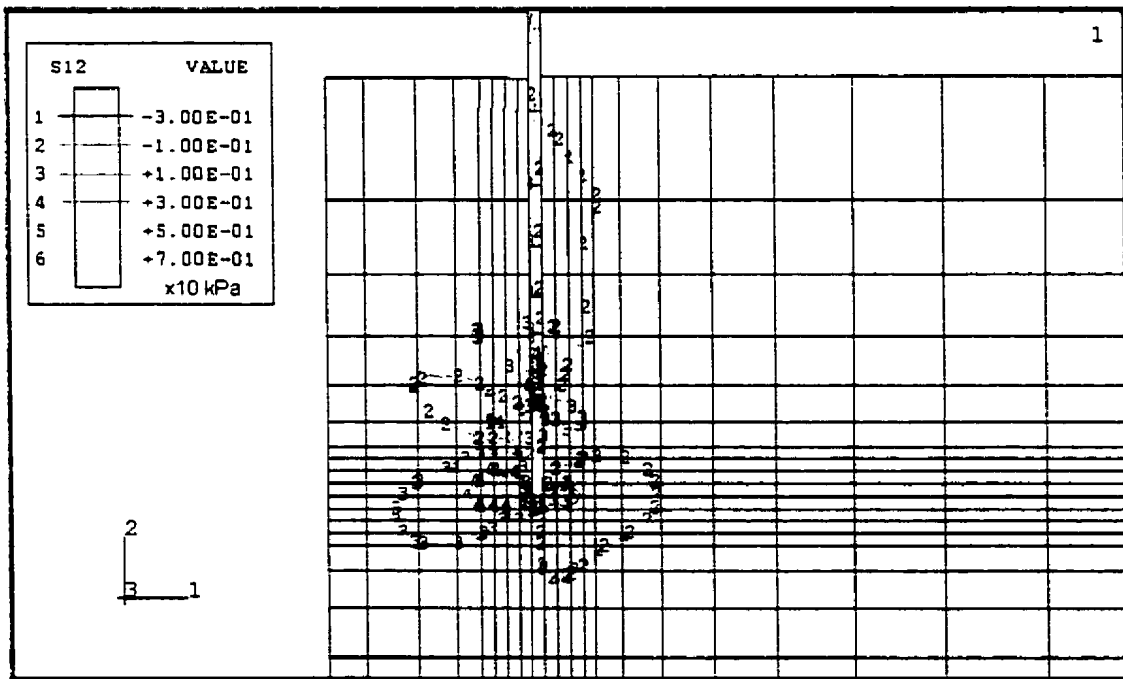


Figure 5.2.5 Contour of shear stress state at maximum pullout capacity of 1g model

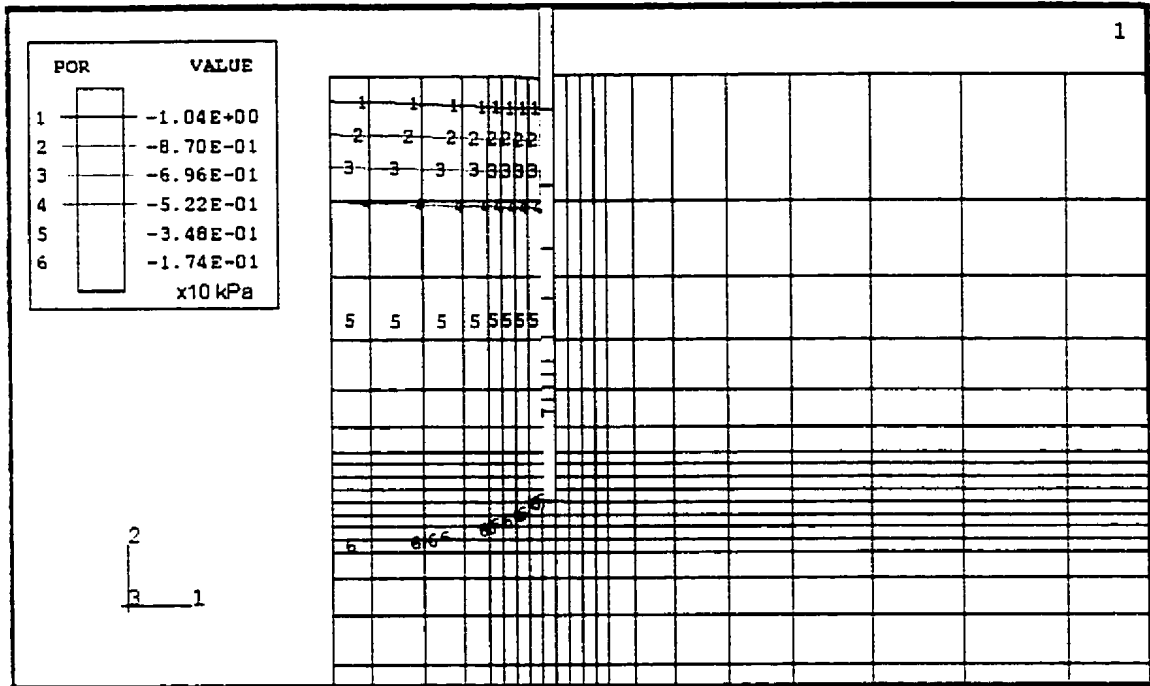


Figure 5.2.6 Contour of pore pressure distribution at maximum pullout capacity of 1g model

5.2.2. Prototype Analysis

In the prototype analysis, relevant soil and geometry parameters are scaled from the 1g model environment to the prototype condition by using the relationships given in Chapter 3 section 3.8. These values are given in Table 5.2.2. The salient system properties used are given in Table 5.2.3.

Table 5.2.2 Scale values from 1g small model to prototype

Parameter	1g	Prototype
Length	1	100
Force	1	10000
Velocity	1	10

In this prototype, no distributed load was applied on top of the soil surface as shown in Figure 5.2.7, which represents the initial “at rest” horizontal stress distributions. By using the data given in Table 5.2.3 and carrying out pullout analysis for the prototype, the results given below were obtained. The finite element model for this prototype is shown in Figure 5.2.2. The results obtained from this prototype finite element model are given in Figures 5.2.8 and 5.2.11. The soil shear stress state during the maximum pullout force and the corresponding pore pressure developments are given in Figures 5.2.9, 5.2.10, 5.2.12, and 5.2.13.

Table 5.2.3 Salient system properties for prototype

Parameter	Value
Coefficient of elastic bulk modulus, κ	0.00435
Coefficient of hardening bulk modulus, λ	0.22826
Submerged unit weight of soil, γ'	7.735 kN/m ³
Permeability of soil, k	2.37 x 10 ⁻⁸ m/s
First pullout rate, V_1	0.003 m/min.
Second pullout rate, V_2	0.03 m/min.
Fluid flow velocity, V_f	1.748 x 10 ⁻⁶ m/s

First set of results, given in Figures 5.2.8 to 5.2.10, were obtained considering no decay in fluid velocity. This caused the suction on the wall to keep on increasing. Since this is not possible in a prototype situation, an exponential decay was built in into the

fluid velocities computed. Figures 5.2.11 to 5.2.13 show the results obtained for this assumption within the suction caisson. The results show that there is not much of difference between both conditions; however, the model with decayed fluid flow velocity indicated a decrease of pullout capacity after 0.5 m displacement, whereas the model with no fluid velocity decay gave increasing trend of pullout capacity.

From Figure 5.2.8, a maximum pullout (resistance) ($F_{TOTAL_}$) of 460 kN was obtained with components as: suction force ($F_{POR_}$) of 229 kN and wall friction force (F_{WALL}) of 231 kN. With a decay in fluid velocity (inside the suction caisson) these forces become 215 kN ($F_{POR_}$) and 235 kN (F_{WALL}). The expected values for the prototype from the model values are given in Table 5.2.4. It is observed that the suction force development within the prototype structure is nearly 10.41 % lower (of the modelled magnitude) whereas the wall friction forces of the prototype are 48.73 % higher (of modelled magnitude). It is seen the suction force developed within the prototype is better modelled by the 1g model; the reason for this closeness should be found in the model-prototype relationship used in modelling the fluid flow within the soil. The consistent dynamic process modelling seems to give better results (than diffusion process modelling). The probable reason for such a large difference in the wall friction force is due to the large suction pressures built-up inside the model caisson that reduce the effective stress of soil on the inside of caisson walls. Comparing Figure 5.2.5 with 5.2.9 and Figure 5.2.6 with 5.2.10, it is seen that the shear stress inside the model caisson is much less than the prototype caisson; moreover, the suction pressures on the inside are higher in the model than the prototype.

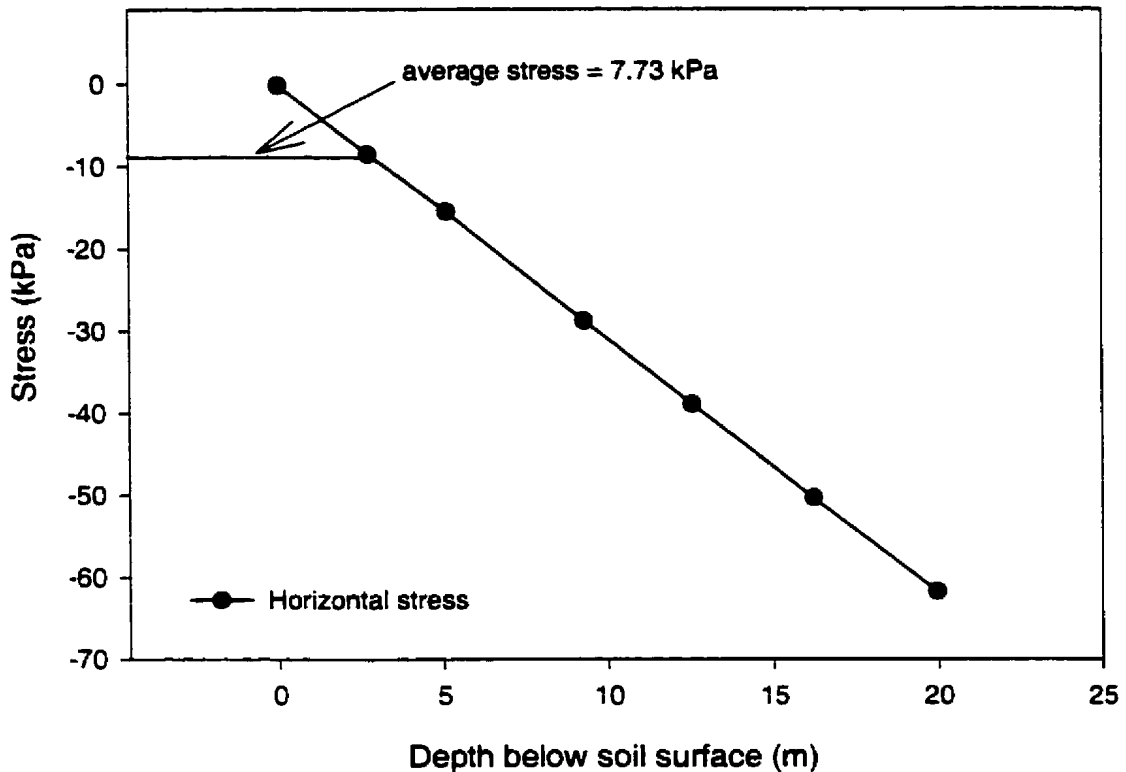


Figure 5.2.7 Initial "at rest" horizontal stress state of prototype structure

Table 5.2.4 Expected and actual force values obtained for the prototype

Forces	Value Expected (kN) (using 1g model results)	Value Computed (with fluid velocity decay) (kN)	% Difference
Total maximum force (FTOTAL_)	377	450	+19.36
Wall force (FWALL)	158	235	+48.73
Suction Force (FPOR_)	240	215	-10.41

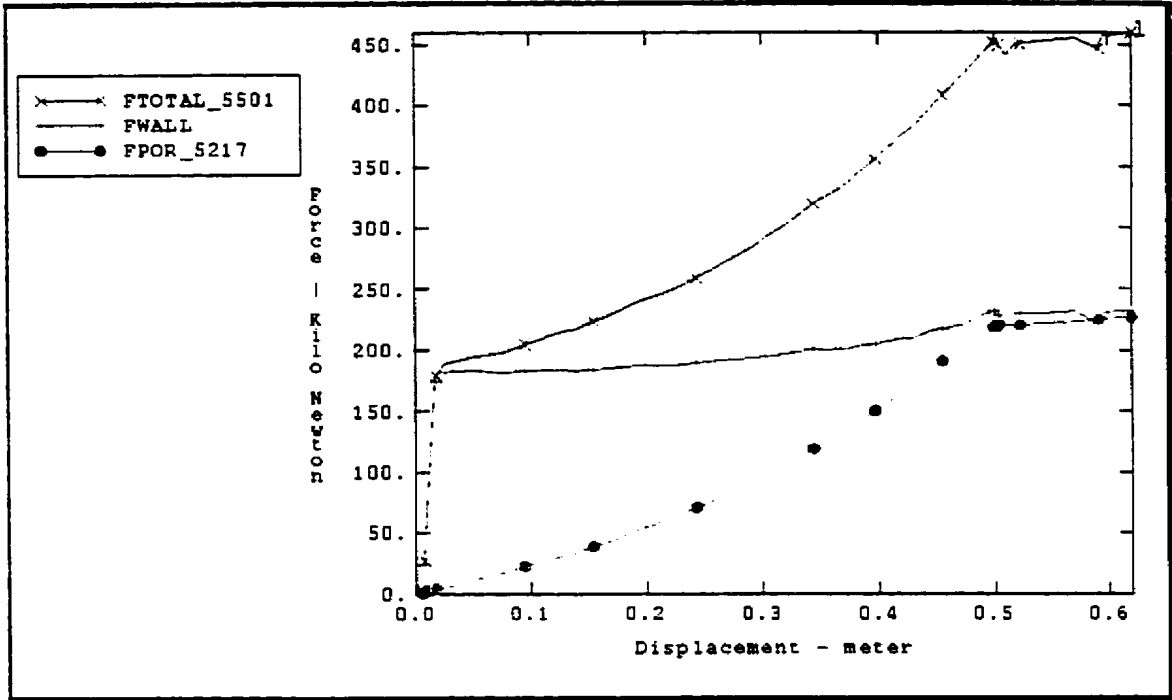


Figure 5.2.8 Pullout forces of prototype with no decay in fluid flow rate

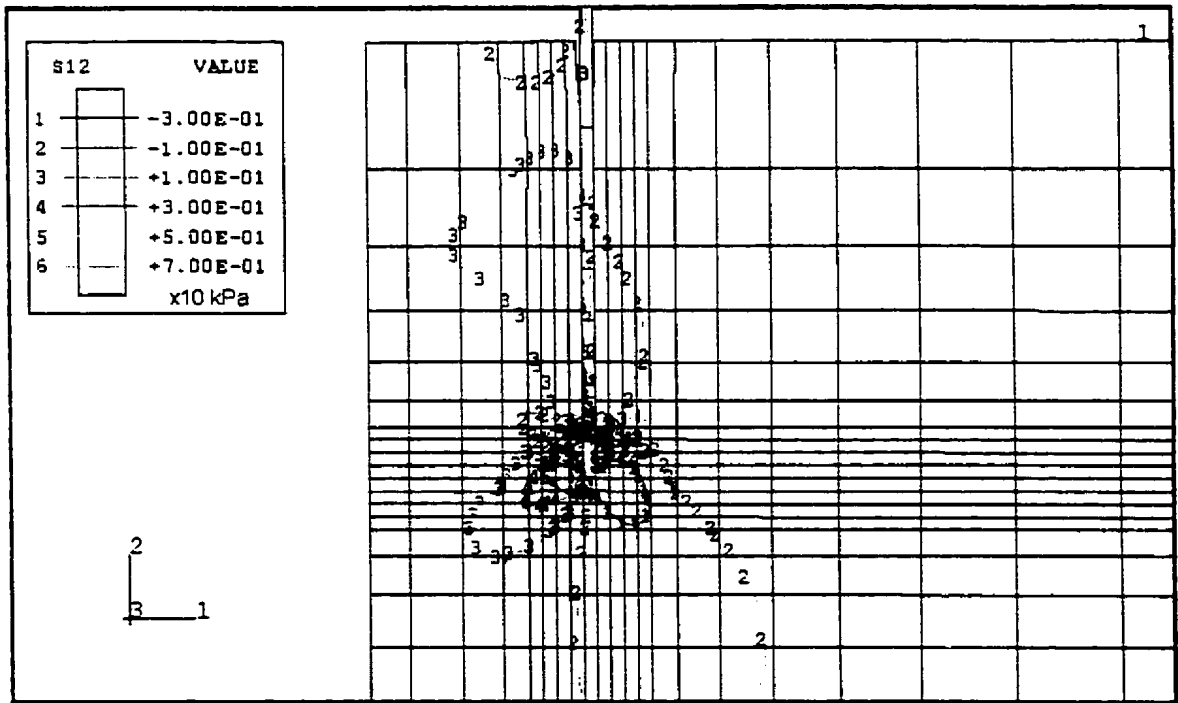


Figure 5.2.9 Contour of shear stress state at maximum pullout capacity of prototype with no decay in fluid flow rate

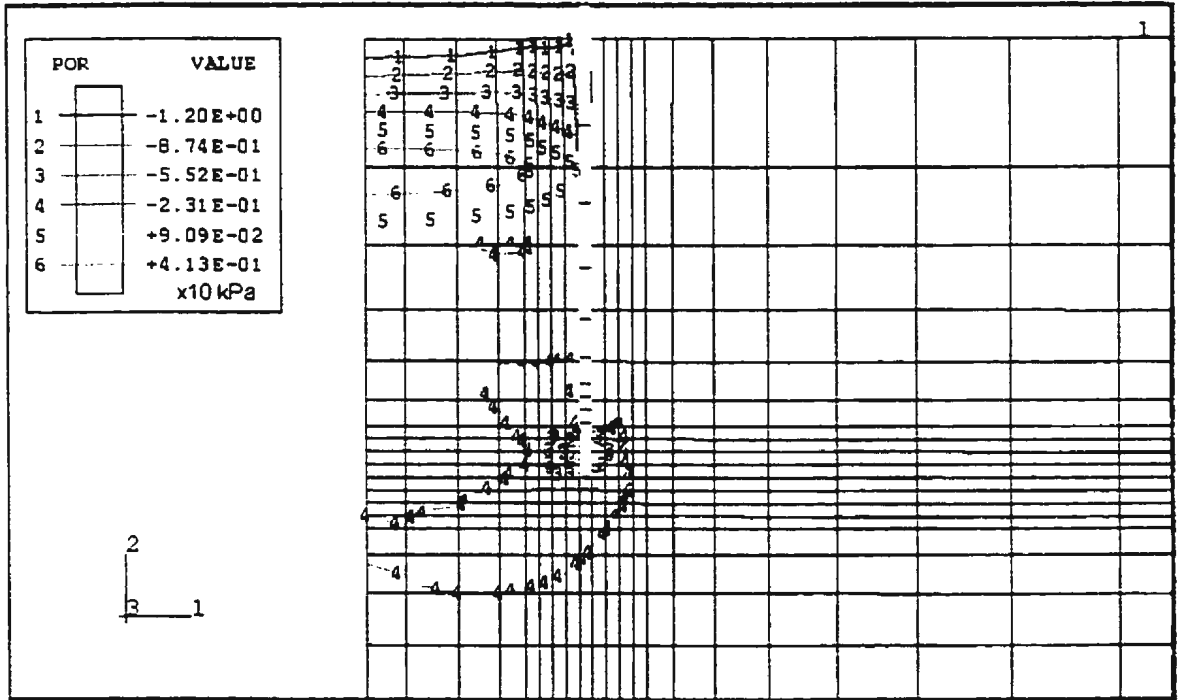


Figure 5.2.10 Contour of pore pressure distribution at maximum pullout capacity of prototype with no decay in fluid flow rate

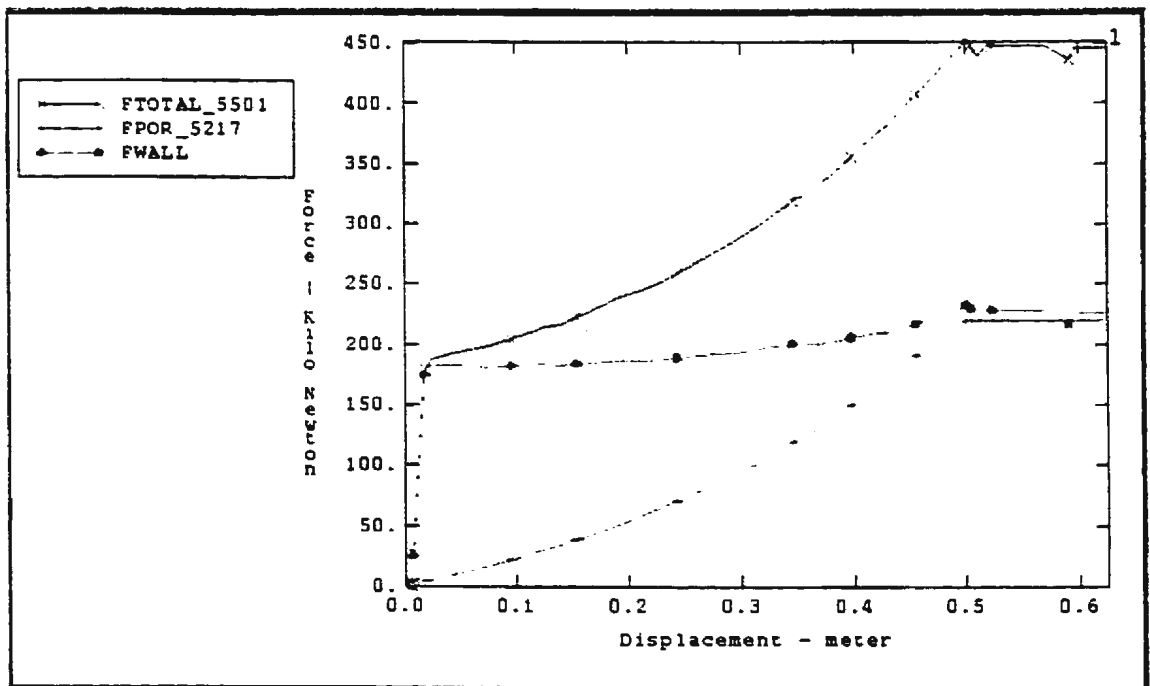


Figure 5.2.11 Pullout forces of prototype with decay in fluid flow rate

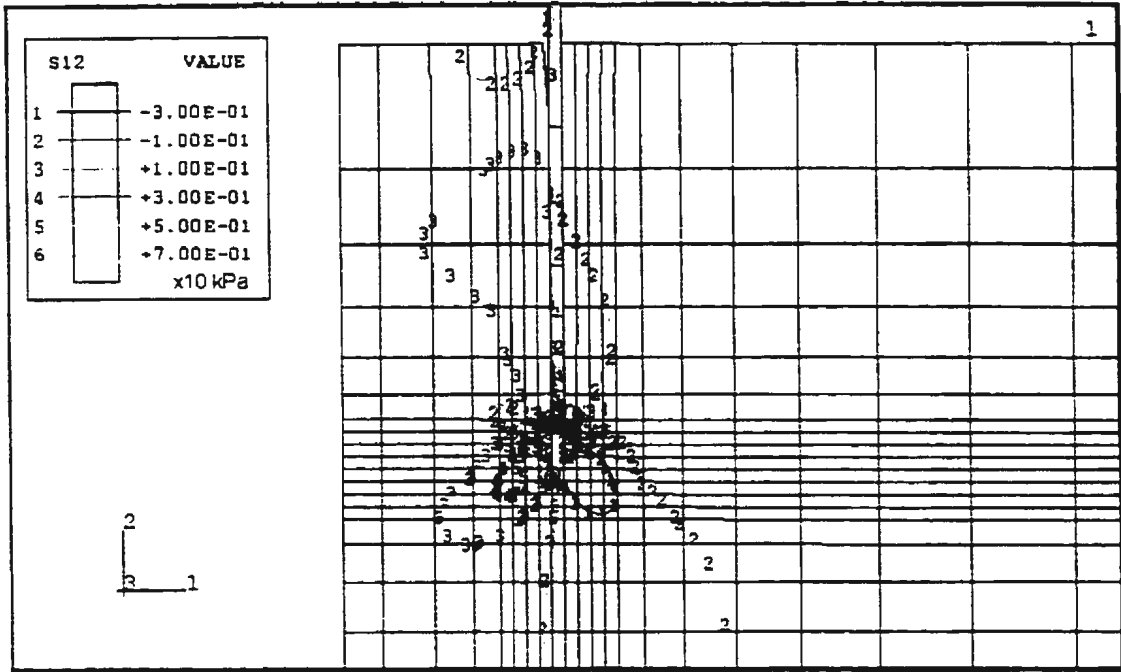


Figure 5.2.12 Contour of shear stress state at maximum pullout capacity of prototype with decay in fluid flow rate

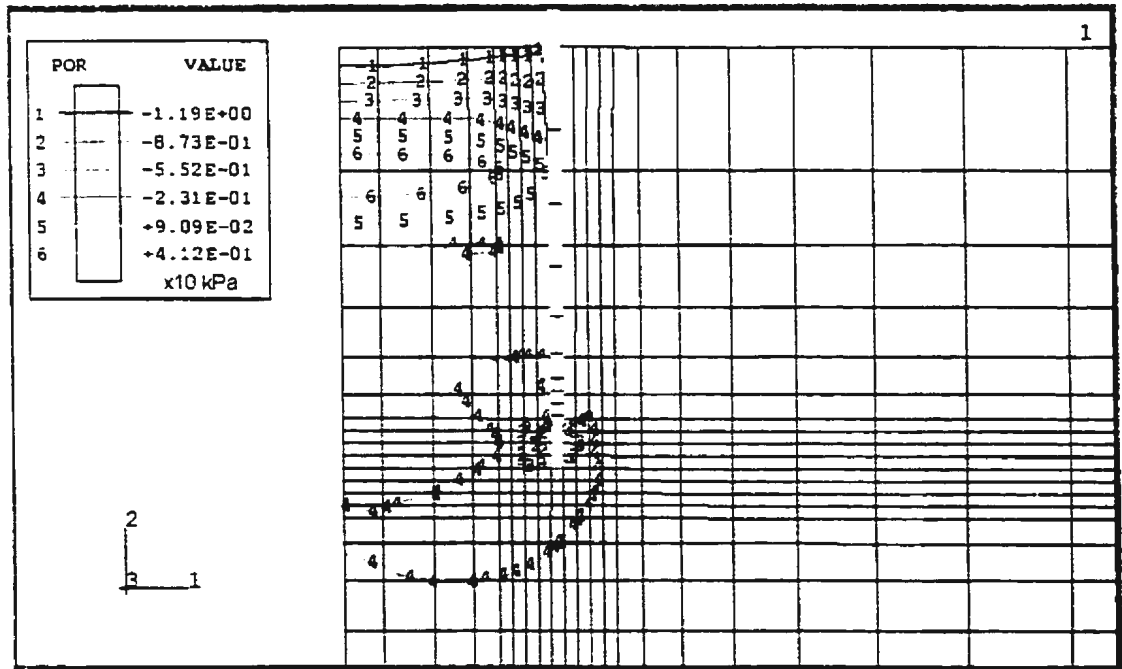


Figure 5.2.13 Contour of pore pressure distribution at maximum pullout capacity of prototype with decay in fluid flow rate

5.2.3. ng Model Analysis

In the ng-model analysis of the suction caisson form shown in Figure 5.2.1, soil and geometry parameters used for analysis are given in Table 5.2.5. In this ng model, no distributed load was applied on top of soil surface. The finite element discretization is the same as that given in Figure 5.2.1.

The initial “at rest” horizontal stress distributions obtained for the ng model is given in Figure 5.2.14. Figure 5.2.15 gives the force-displacement relationships obtained. The soil shear stress state during the maximum pullout force and the corresponding pore pressure developments are given in Figure 5.2.16 and 5.2.17. It is also seen from Figures 5.2.3, 5.2.7 and 5.2.14, that the average “at rest” soil stress states are the same in lg, prototype, and ng tests.

Comparing Figures 5.2.12 and 5.2.16 it is seen that the soil stress states (with decay) are close to one another, whereas the pore pressure states, as seen in Figures 5.2.13 and 5.2.17, are not very close to one another.

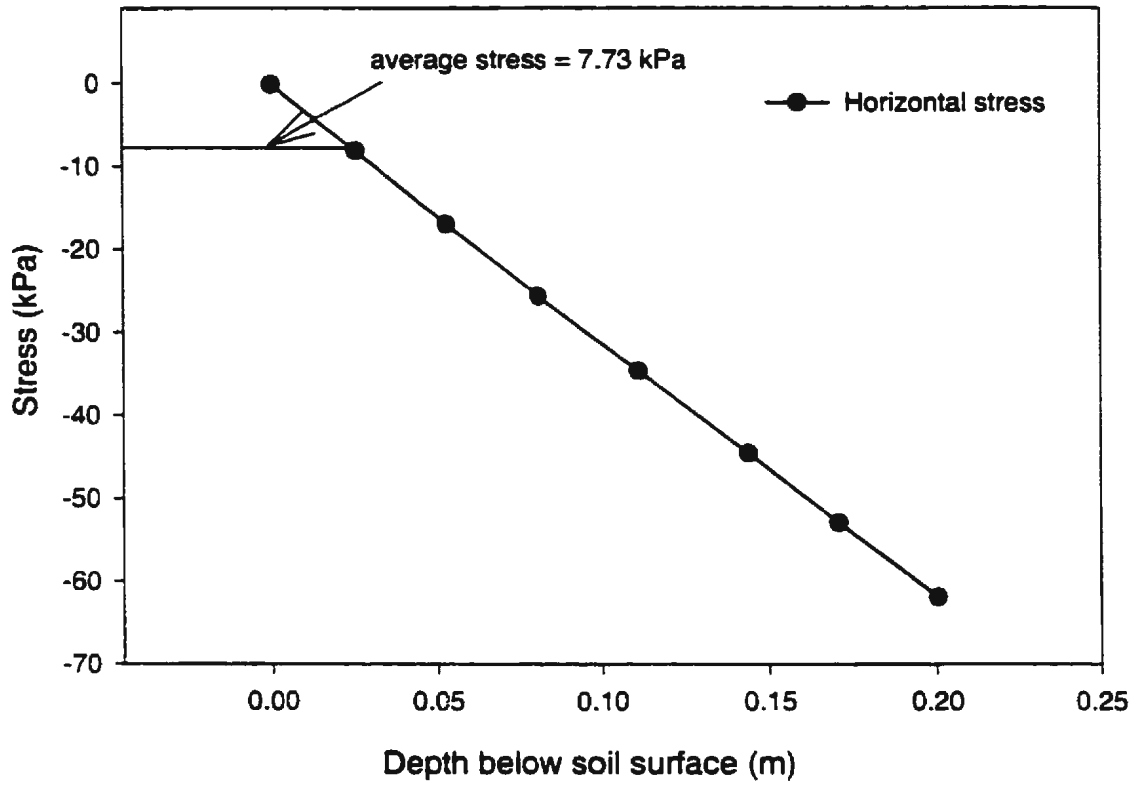


Figure 5.2.14 Initial "at rest" horizontal stress state of ng model

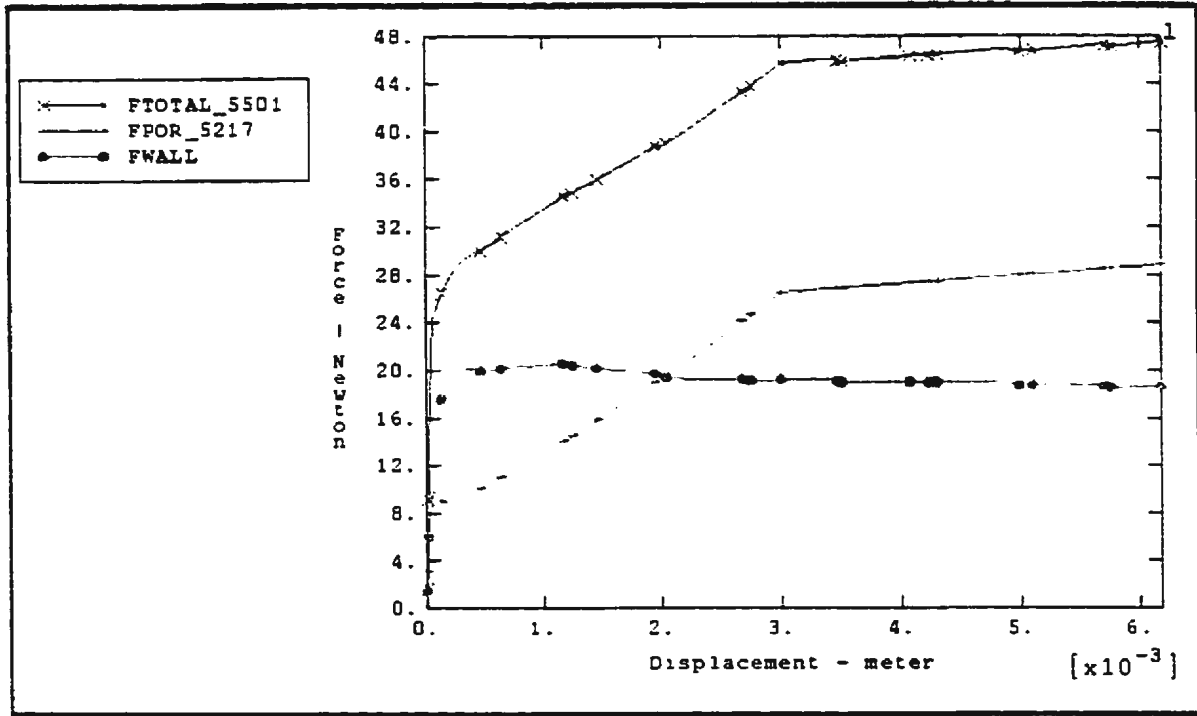


Figure 5.2.15 Pullout forces of ng model

Table 5.2.5 Salient system properties for ng scale model

Parameter	Value
Coefficient of elastic bulk modulus, κ	0.00435
Coefficient of hardening bulk modulus, λ	0.22826
Submerged unit weight of soil, γ'	773.5 kN/m ³
Permeability of soil, k	2.37 x 10 ⁻⁸ m/s
First pullout rate, V_1	0.3 m/min.
Second pullout rate, V_2	3 m/min.
Fluid flow velocity, V_f	1.748 x 10 ⁻⁴ m/s

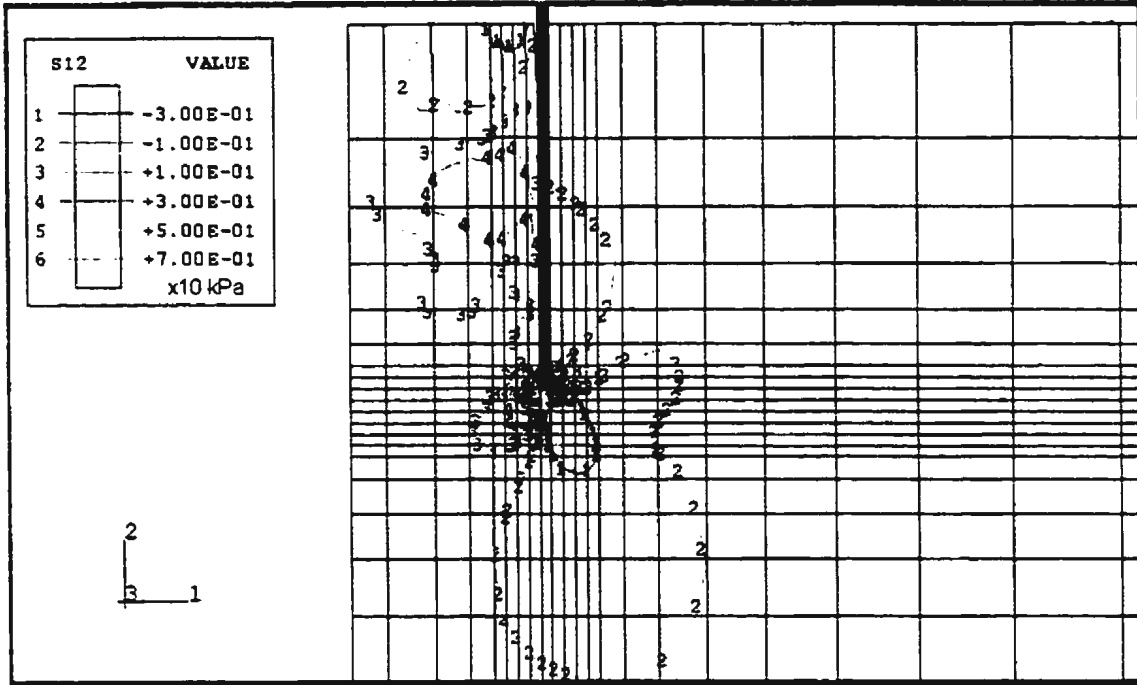


Figure 5.2.16 Contour of shear stress state at maximum pullout capacity of ng model

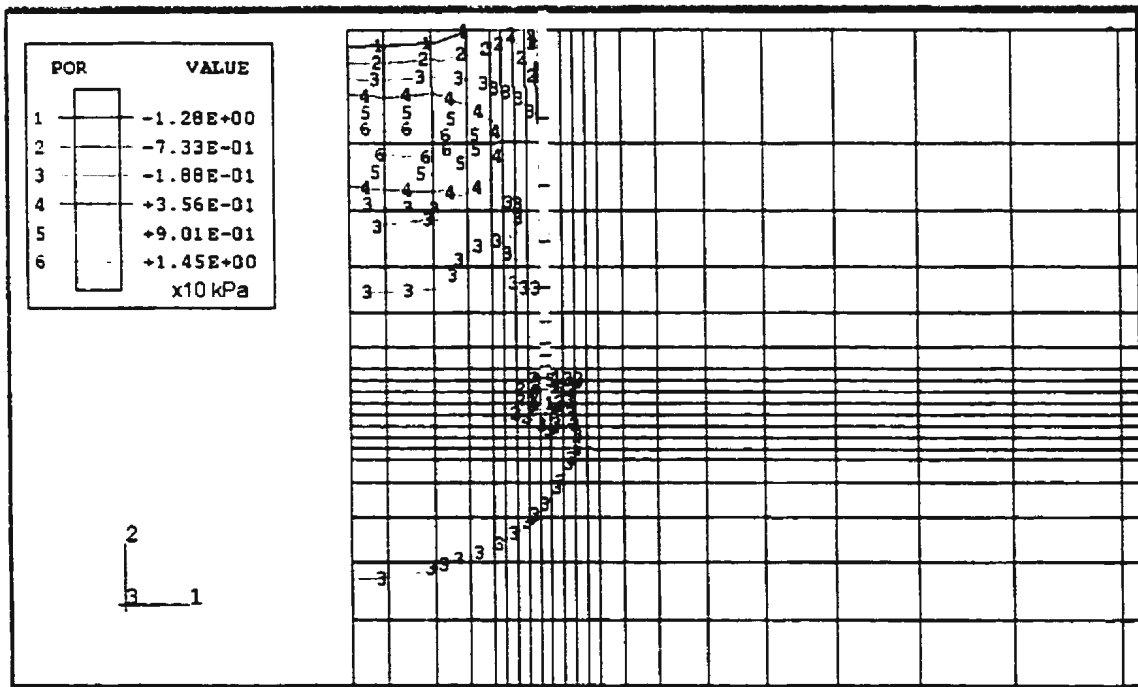


Figure 5.2.17 Contour of pore pressure distribution at maximum pullout capacity of ng model

From Figure 5.2.15, a maximum force capacity ($F_{TOTAL_}$) of 47.4 N is obtained, and its components are: suction force ($F_{POR_}$) of 29 N and wall friction force (F_{WALL}) 18.4 N at a displacement analogous to the prototype (at 0.6177 m in the prototype and 0.006177 m in the ng model). The expected values for the prototype from these values are given in Table 5.2.6. Comparing the values given in Table 5.2.6, it is observed that the total maximum force development within the prototype is 5.33% lower than that obtained for the modelled value from the ng model results. It is also observed that the suction force keeps on increasing; as such, the difference of +34.88% is rather a behaviour observed at a pre-specified displacement; it tends to keep on increasing until failure occurs by any one of the failure modes. The wall friction force in the prototype is observed to be 21.70% higher than that obtained for the value from ng model results.

Thus the ng model gives a better representation of the prototype behaviour for the soil friction force exerted on the wall of the suction caisson during pullout. It is also observed that it fails to give proper suction force values developed within the caisson; the problem may lie in the model-prototype relationships used in modelling the fluid flow within the soil.

Comparing Figure 5.2.5, 5.2.12, and 5.2.16, it is observed that the soil shear stress contours (on the outside wall) of three models are closer to one another. It is also observed that the soil shear stress contours on caisson walls, within the 1g and ng models seem to agree well; this agreement is not good between the prototype and the 1g and ng models. The pore pressure development (within the caisson walls) given in Figure 5.2.6, 5.2.13, and 5.2.17 also compare well; while the suction pore pressures at the top of soil

NOTE TO USERS

Page(s) not included in the original manuscript are unavailable from the author or university. The manuscript was microfilmed as received.

199

This reproduction is the best copy available.

UMI[®]

1.0, and 2.1, respectively, were considered in the analyses. The procedure for identifying the failure pattern has been presented earlier in section 3.9. The details have been condensed and given in Table 5.3.1.

The identification of the three modes of failure is based on: (i) whether shear stress conditions have been developed for direct shear stress failure (for overall shear failure) on both sides of the caisson: (ii) whether direct shear stress condition has been developed on the outside of the caisson and extension shear failure conditions at the base of the caisson (for overall tension failure); or (iii) whether extension shear failure conditions have been developed away from the caisson in the body of soil (for overall general shear failure).

Application of the shear stress to shear strength ratio to determine the three failure scenarios is defined as follows:

- i. In the shear failure region, close to the caisson foundation wall, both on the inside and outside, the ratio of shear stress to shear strength is determined using the value of shear strength to vertical compressive stress ratio obtained from direct simple shear tests, as the limiting factor. When this ratio exceeds one, failure is deemed to have occurred in shear.
- ii. When the shear failure occurs only on the outside of the caisson and then the failure zone proceeds to the soil body at the base of the caisson, then the possibility of tension failure at the base of the foundation is examined. For this case, the shear failure region near the bottom of caisson foundation is examined for extensional failure in shear. In this case the ratio of shear stress to shear

strength values is examined using a value of shear strength to vertical compressive stress ratio obtained from triaxial extension tests. When this ratio becomes greater than or equal to one, the foundation is deemed to have failed in tension.

- iii. When both the shear stress failure condition (around the caisson wall) and tensile stress failure condition (at the base of caisson foundation) do not occur, then the condition for the occurrence of general shear failure condition is examined in the region away from the caisson walls and base. In this case the failure in soil body is considered to satisfy the condition of extensional shear strength failure conditions used for tensile failure.

These failure criteria have been applied to the various cases considered in this section and the salient aspects discussed.

Table 5.3.1 Procedure for identifying failure modes

Failure Mode	Identification
Shear Failure	<p><u>Shear stress to shear strength ratio:</u></p> <p>Development of shear stress to shear strength ratio up to a magnitude of greater than or equal to one should occur in the vicinity of wall. This should occur on both the inside and outside wall area of the soil body. The shear strength parameter is obtained from a direct simple shear test of the soil.</p> <p><u>Shear strain:</u></p> <p>Significant shear strain magnitude is developed around the inside and outside wall area up to 10 to 15%.</p>
Tension Failure	<p><u>Shear stress to shear strength ratio:</u></p> <ul style="list-style-type: none"> i) Development of shear stress to shear strength ratio (based on triaxial extension test) up to a magnitude of greater than or equal to one occurs on most of the cross sectional area of soil body near the base of suction caisson causing the soil to fail in tension along the caisson base. This follows the occurrence of shear stress to shear strength ratio (based on direct simple shear test) contours greater than one along most of the outside wall area in the soil body. ii) Alternatively, tension failure condition can also first occur followed by shear failure along the outside wall area in the soil body, as described above. <p><u>Tension strain:</u></p> <p>A significant tensile strain magnitude is developed around the base of caisson.</p> <p><u>Tension stress:</u></p> <p>A positive axial stress, or a positive first principal stress occurs at the base of caisson.</p>
General Shear Failure	<p><u>Shear stress to shear strength ratio:</u></p> <p>This failure condition is identified by the occurrence of shear failure and tension failure in soil near but away from the outside wall area and below the base of suction foundation at around the same time.</p> <p><u>Shear strain:</u></p> <p>Contours of significant shear strain values occur (based on triaxial extension test) in soil body surrounding the suction caisson.</p>

From Figures 5.3.1 to 5.3.5, it is seen that the model with $L/D = 0.4$ has the following failure characteristics:

- i. The failure condition occurs after peak load capacity (in the load-displacement curve Figure 5.3.5).
- ii. From Figure 5.3.3, it is seen that a unit value and above for shear stress to shear strength contour ratio (based on DSS test) occurs near the inside wall region, which represents shear failure at inside wall of foundation. The same condition is not observed on the outside wall. In Figure 5.3.4, it appears as if the failure in extensional shear occurs in the soil body adjacent to the suction caisson outside wall. This suggests that the failure on the outside occurs rather due to general shear failure than shear failure. It is also observed from Figure 5.3.3, that at some points along the outside wall failure has occurred due to direct shear. Hence the failure states due to pure shear and general shear must be occurring closer to one another. This condition explains the fact that shear failure occurs on the inside wall, and slow extensional shear failure occurs on the outside wall. Hence, the failure is characterized as closer to shear failure than general shear failure.

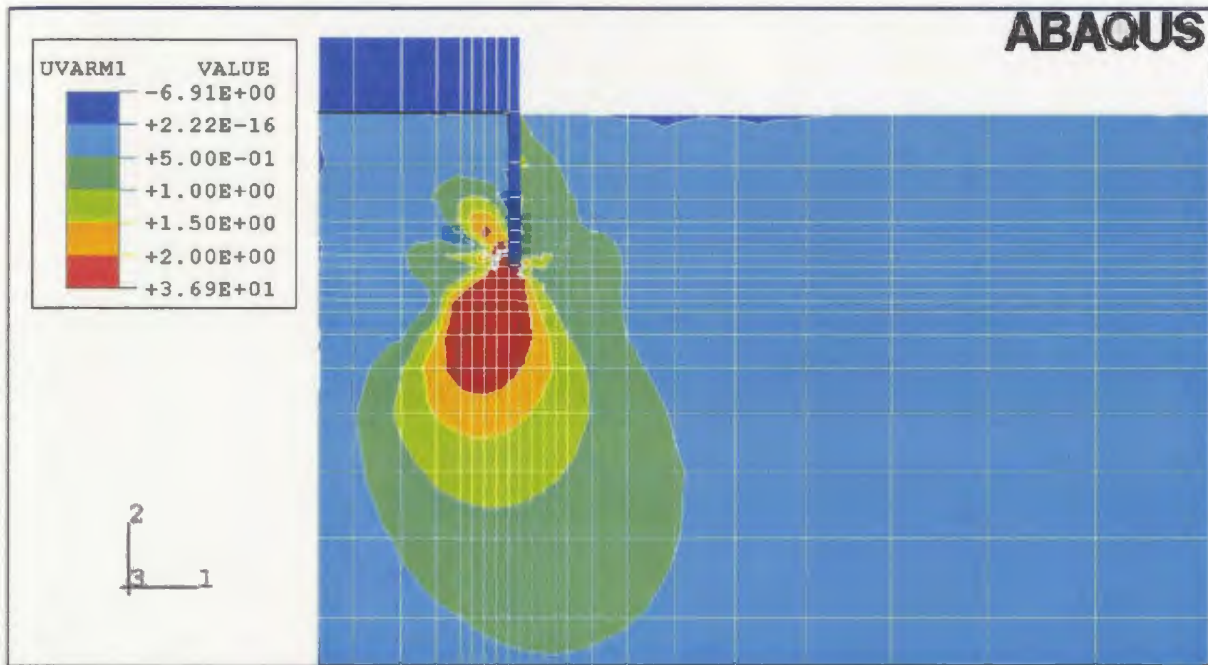


Figure 5.3.1 Contours of shear stress to shear strength ratio based on direct simple shear tests of the model with $L/D = 0.4$ at peak pullout capacity (step = 3, increment = 25). Failure between the wall and soil has begun to occur on the inside wall of caisson, but has not occurred on the outside wall.

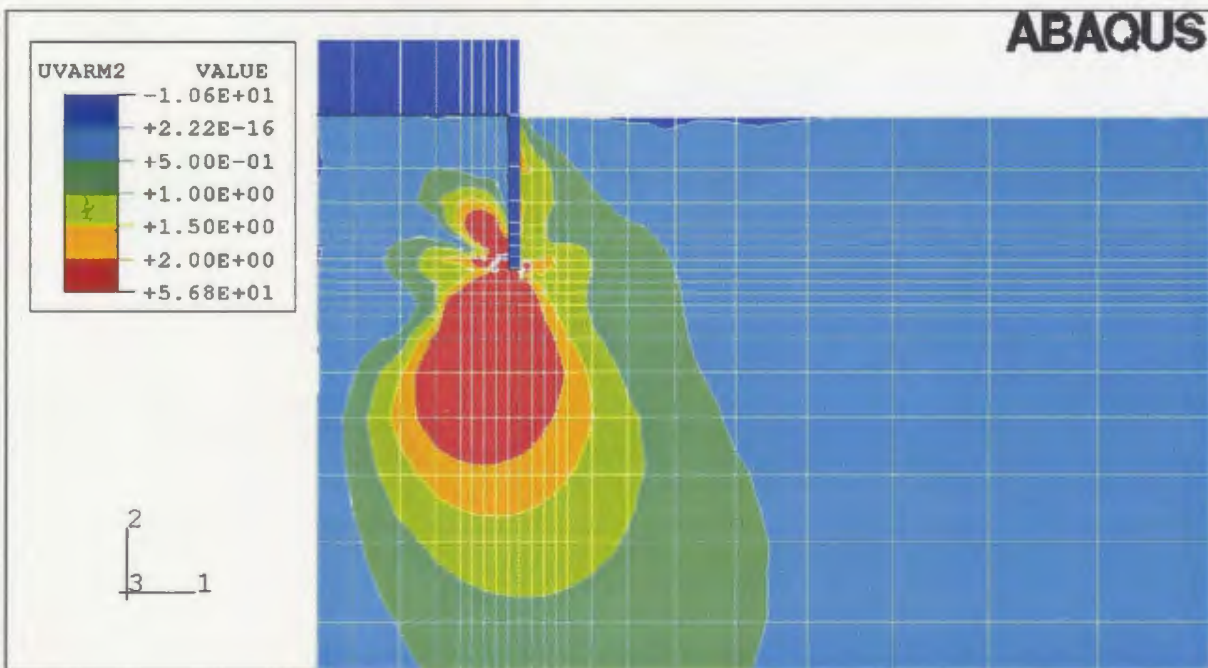


Figure 5.3.2 Contours of shear stress to shear strength ratio based on triaxial tests of the model with $L/D = 0.4$ at peak pullout capacity (step = 3, increment = 25). Conditions favourable to extensional shear failure occurs on the outside of suction caisson wall, but not on the inside.

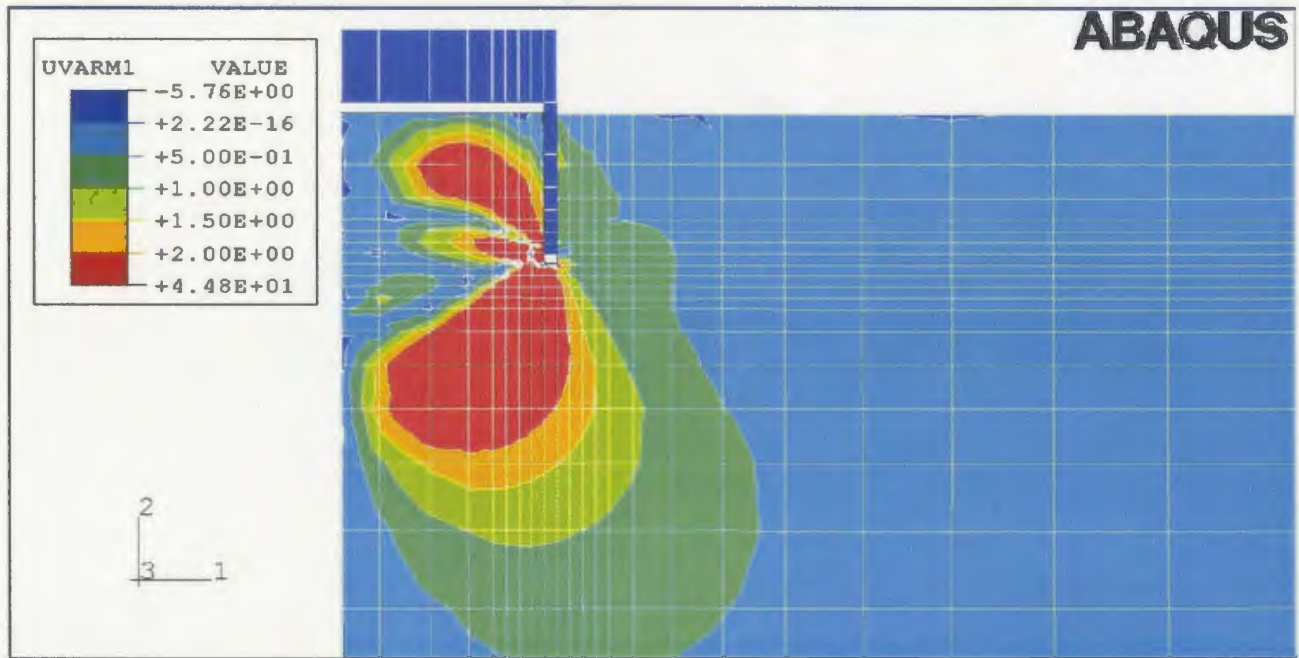


Figure 5.3.3 Contours of shear stress to shear strength ratio based on direct simple shear tests of the model with $L/D = 0.4$ at failure (step = 3, increment = 57). Failure has not occurred between the outside wall of caisson and the soil (except at some local points). It is almost at the final failure stage due to direct shear on the inside wall of caisson.

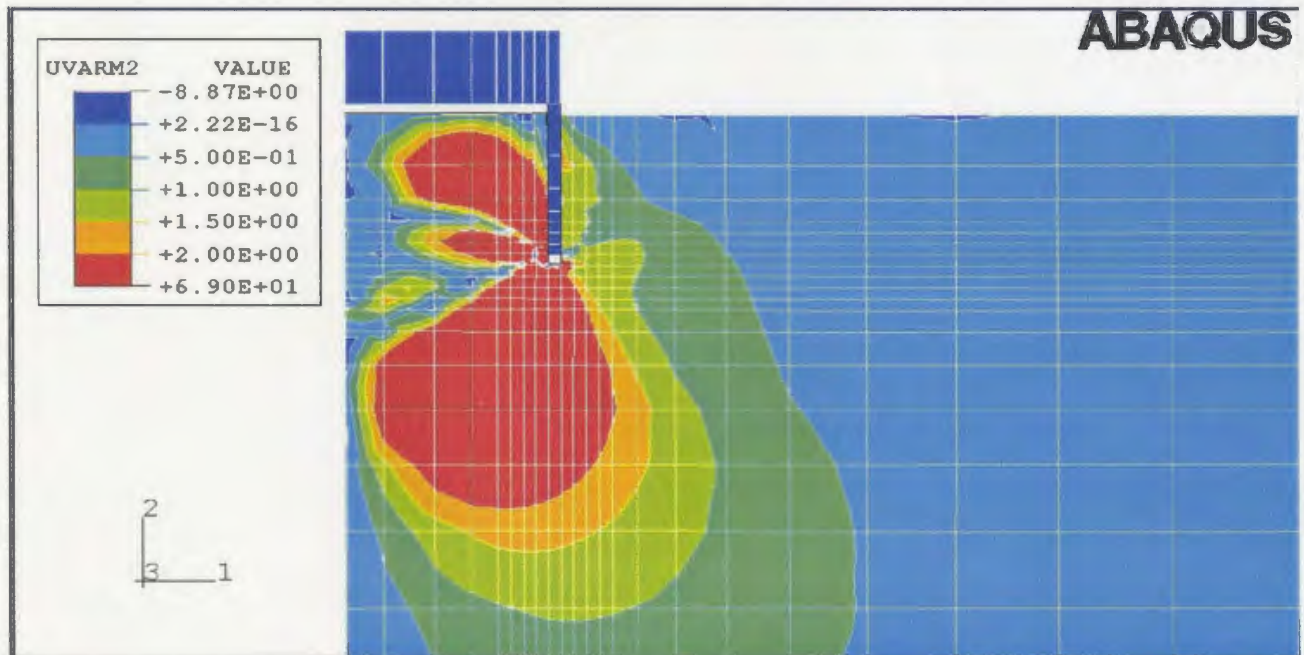


Figure 5.3.4 Contours of shear stress to shear strength ratio based on triaxial tests of the model with $L/D = 0.4$ at failure (step = 3, increment = 57). Conditions favourable to extensional shear failure occur over the outside and inside of caisson walls; possible tensile failure also occurs at the caisson bottom soon after the occurrence of above shear failure.

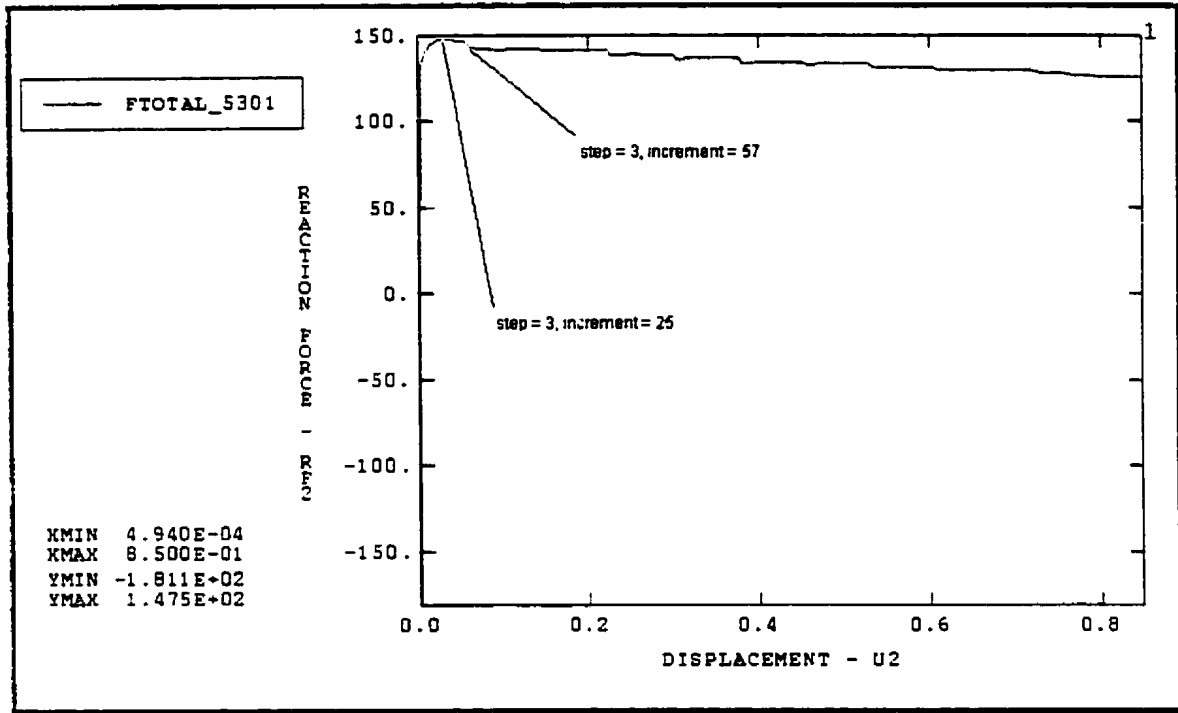


Figure 5.3.5 Load-displacement curve of $L/D = 0.4$ model. Units: Force (N), Displacement (cm).

From Figures 5.3.6 to 5.3.10, it is seen that the model with $L/D = 1$ has the following failure characteristics:

- i. The failure condition occurs after peak load capacity (observed from load-displacement curve shown in Figure 5.3.10).
- ii. Figure 5.3.8 shows no high value contour of shear stress to shear strength ratio (based on DSS test) at the inside wall region. From Figure 5.3.9, it is seen that a unit value of shear stress to shear strength contour ratio, based on triaxial extension test, occurs at the base of the foundation; this shows that tension failure has occurred at the base of suction caisson. It is also seen from Figure

5.3.9, that extensional failure has occurred in the soil body adjacent to the suction caisson outside wall indicating a general shear failure. Hence the foundation seems to be failing under a tension failure at the base and general shear failure around the outside caisson wall.

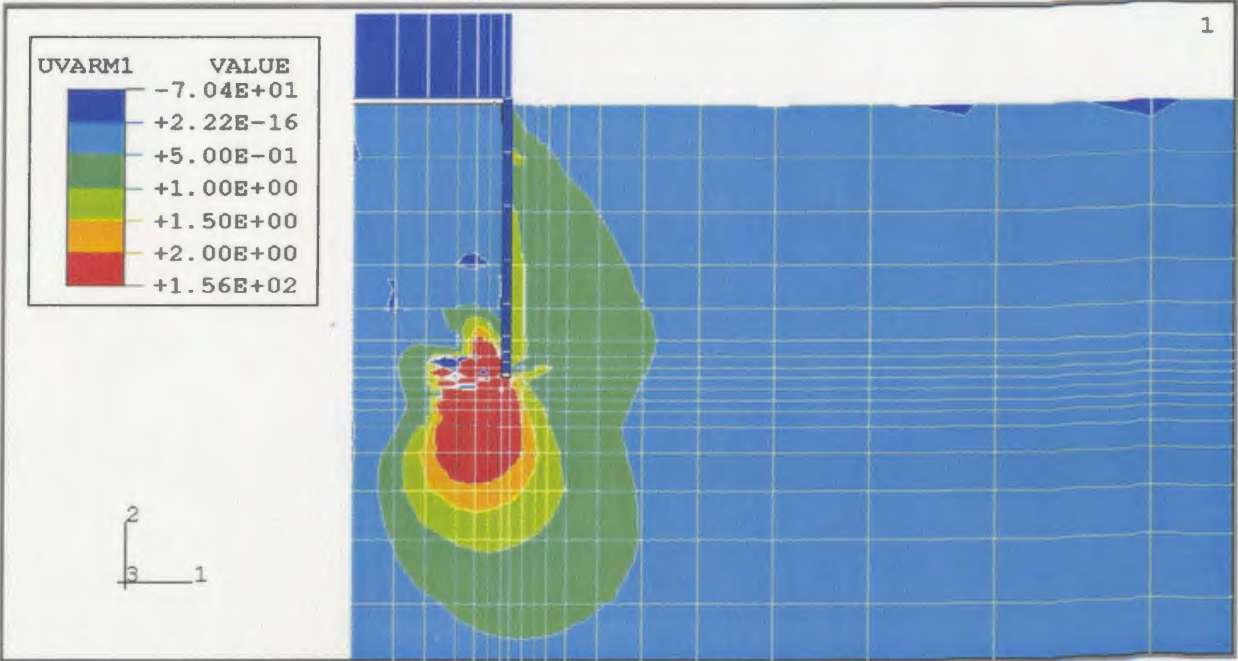


Figure 5.3.6 Contours of shear stress to shear strength ratio based on direct simple shear tests of the model with $L/D = 1$, at peak pullout capacity (step = 3, increment = 45). Direct shear failure is progressing along the outside caisson wall, but it is not developing on the inside wall at all.

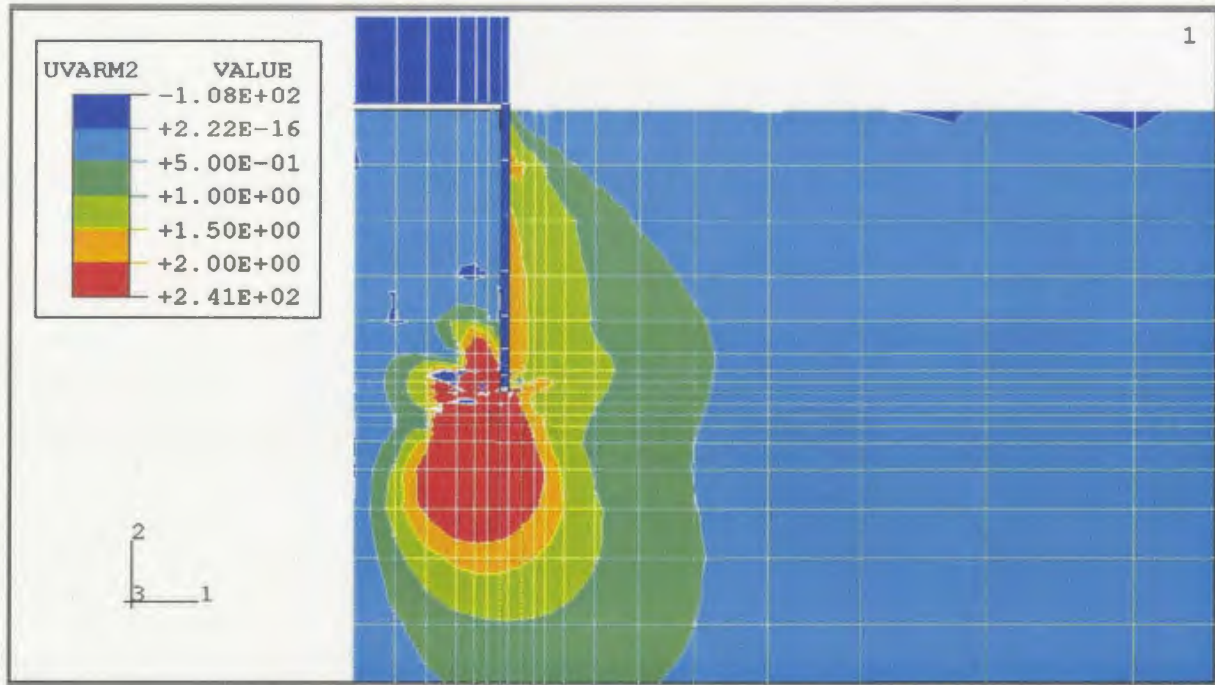


Figure 5.3.7 Contours of shear stress to shear strength ratio based on triaxial tests of the model with $L/D = 1$, at peak pullout capacity (step = 3, increment = 48). Extensional shear failure conditions have developed almost over the whole length of outside caisson wall, but have not developed at all on the inside or at the base.

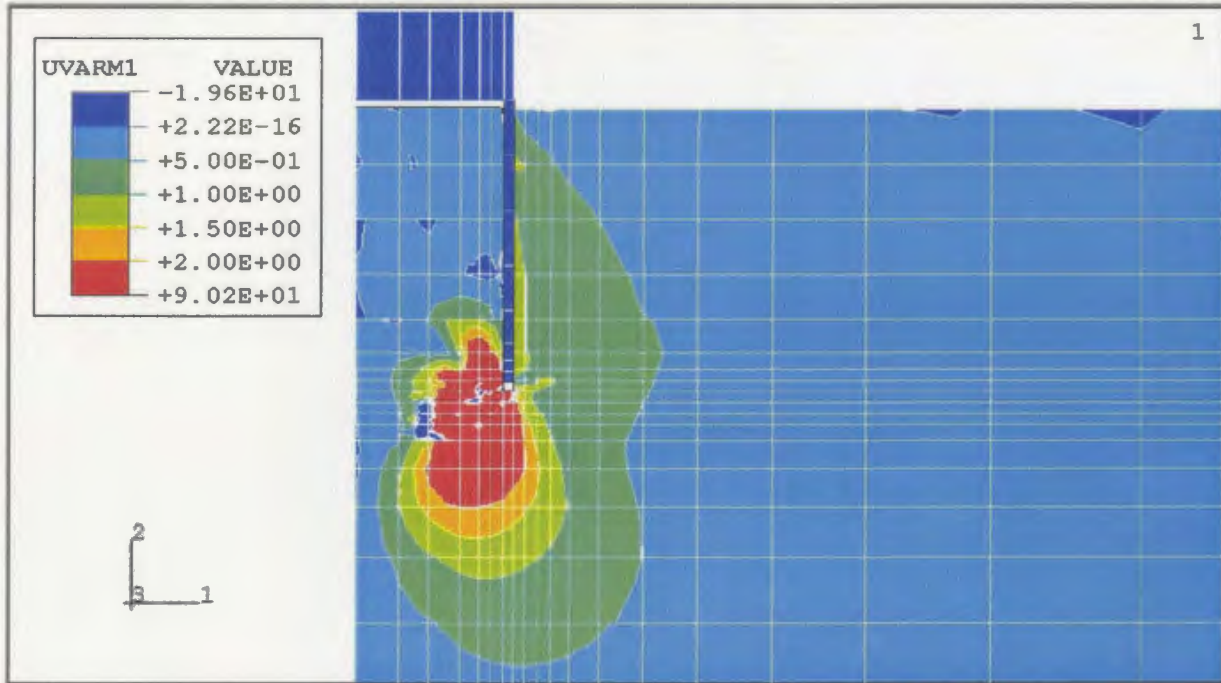


Figure 5.3.8 Contours of shear stress to shear strength ratio based on direct simple shear tests of the model with $L/D = 1$, at failure (step = 3, increment = 48). Direct simple shear failure conditions have developed almost along the whole length of the caisson outside wall, but have not developed at all on the inside.

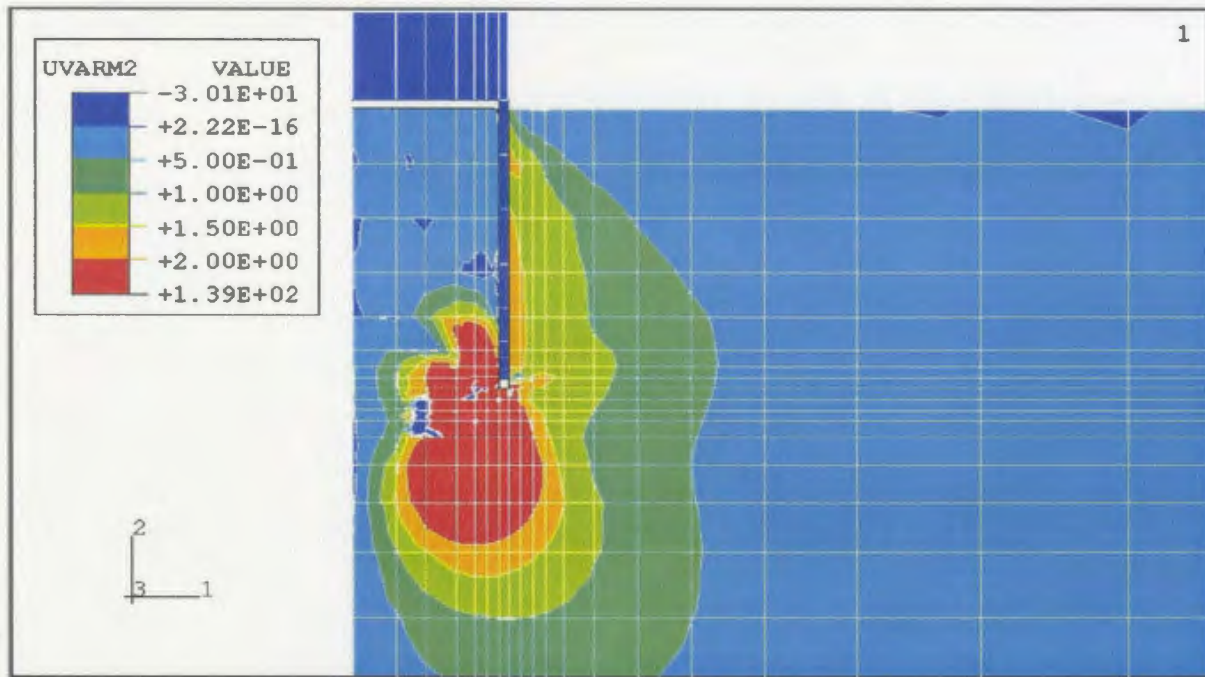


Figure 5.3.9 Contours of shear stress to shear strength ratio based on triaxial tests of the model with $L/D = 1$, at failure (step = 3, increment = 48). Extensional shear failure conditions occur almost along the whole cross sectional area of suction caisson at its base, along with general shear failure conditions on the outside wall.

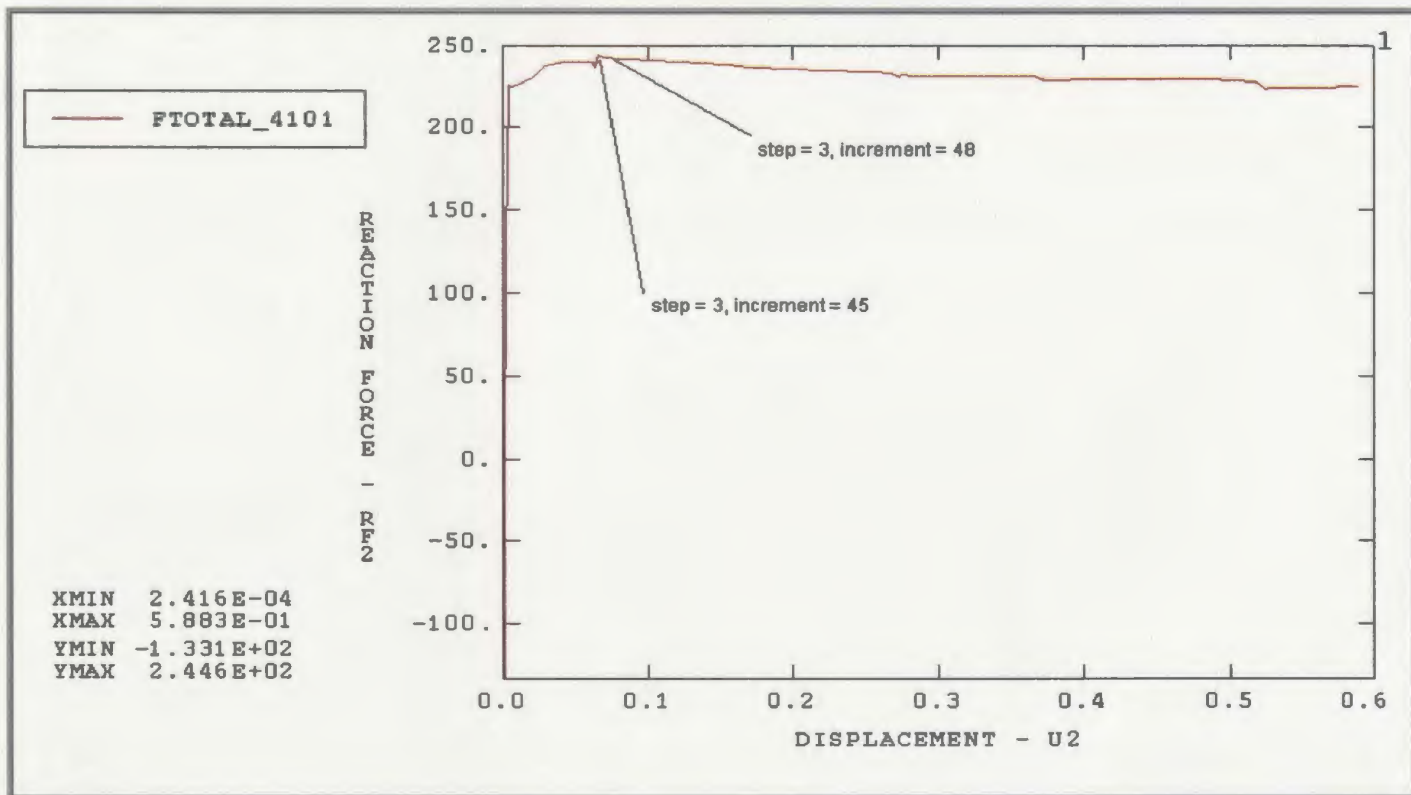


Figure 5.3.10 Load-displacement curve of $L/D = 1.0$ model. Unit: Force (N), Displacement (cm).

From Figures 5.3.11 to 5.3.15, it shows that model with $L/D = 2.1$ has the following failure characteristics:

- i. A partial tensile failure condition occurs at the base of caisson wall before peak load capacity (shown in the load-displacement curve Figure 5.3.15), identified by full coverage of shear stress to shear strength ratio, based on triaxial test, in Figure 5.3.12. Even results based on direct shear tests, show the same in Figure 5.3.11.
- ii. Figure 5.3.13 does not show a unit value shear stress to shear strength contour ratio based on DSS test at around the inside wall region. Therefore, it can be concluded that this model is failing in tension mode. Whereas Figure 5.3.14 shows that general shear failure has occurred on the soil around the caisson outside wall; and as well the soil has also failed in extensional and direct shear conditions along the base of the caisson. The failure is characterized by tension failure at the caisson base followed by general shear failure in soil body around the caisson outside wall.

Hence it should be stated that failure of suction caissons are not clear cut into shear failure, tensile failure or general shear failure scenarios as outlined by Christensen [Christensen et al, 1991]. A mixture of failure conditions occurs, initiated primarily by a direct shear, tensile or general shear failure condition. More analytical investigation needs to be carried out to exactly determine the applicability of Christensen's equations and the consequent modifications required.

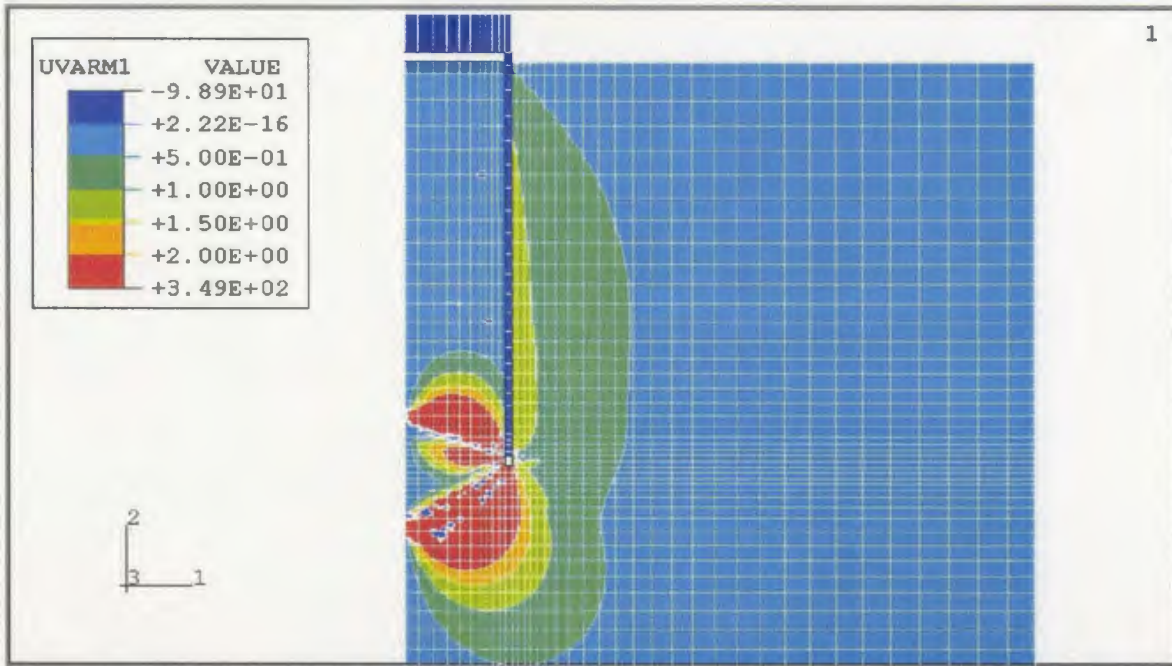


Figure 5.3.11 Contours of shear stress to shear strength ratio based on direct simple shear tests of the model with $L/D = 2.1$ at peak pullout capacity (step = 3, increment = 253). Conditions favourable to direct simple shear failure occur over almost the whole length of caisson outside wall, but do not occur on the inside. Also failure occurs resulting from direct shear stresses at the base of the caisson foundation.

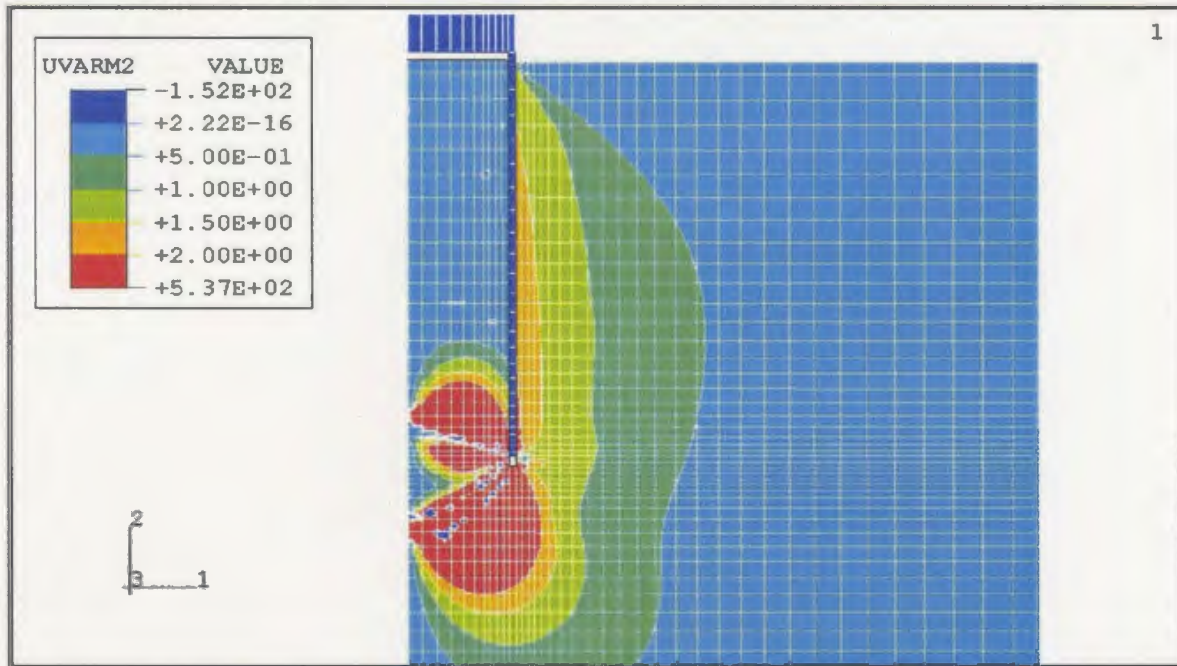


Figure 5.3.12 Contours of shear stress to shear strength ratio based on triaxial tests of the model with $L/D = 2.1$, at peak pullout capacity (step = 3, increment = 253). Conditions favourable to extensional shear failure occur along the base of suction caisson showing that tensile failure has occurred at the base. In addition, extensional shear failure seems to be occurring in the soil surrounding the suction caisson outside wall.

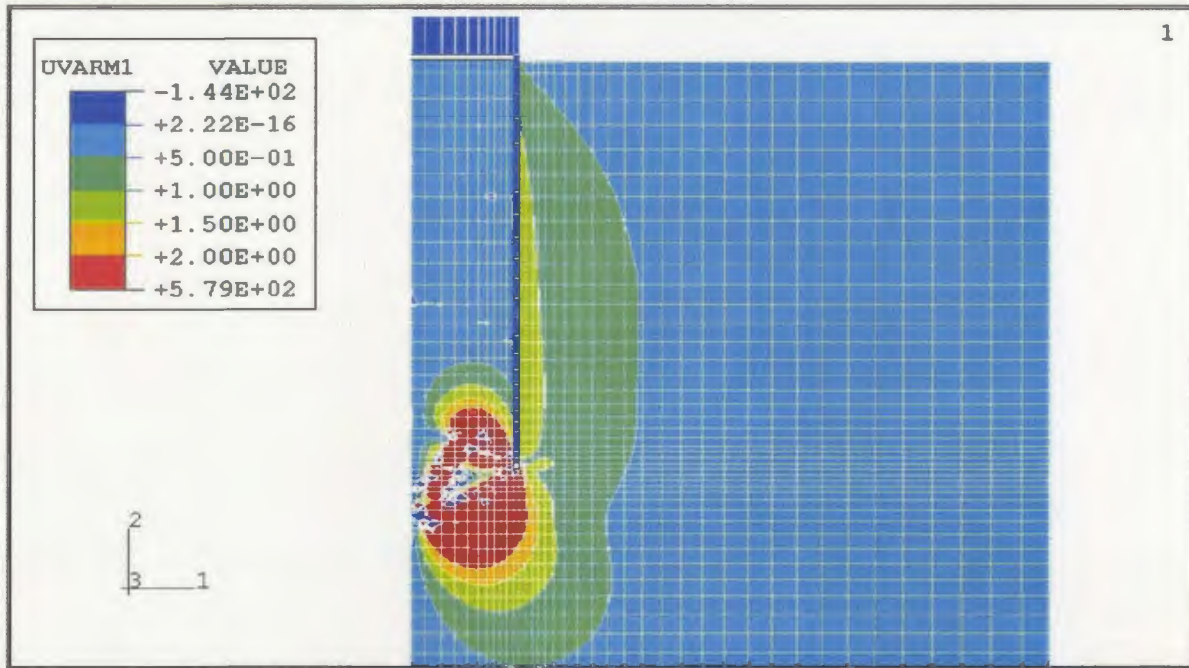


Figure 5.3.13 Contours of shear stress to shear strength ratio based on direct simple shear tests of the model with $L/D = 2.1$, at failure (step = 3, increment = 97). Conditions favourable to direct simple shear failure occur along most of the outside wall; not along the inside wall. Also the shear stress contour has become greater than one along the base of the foundation showing tension failure resulting from shear.

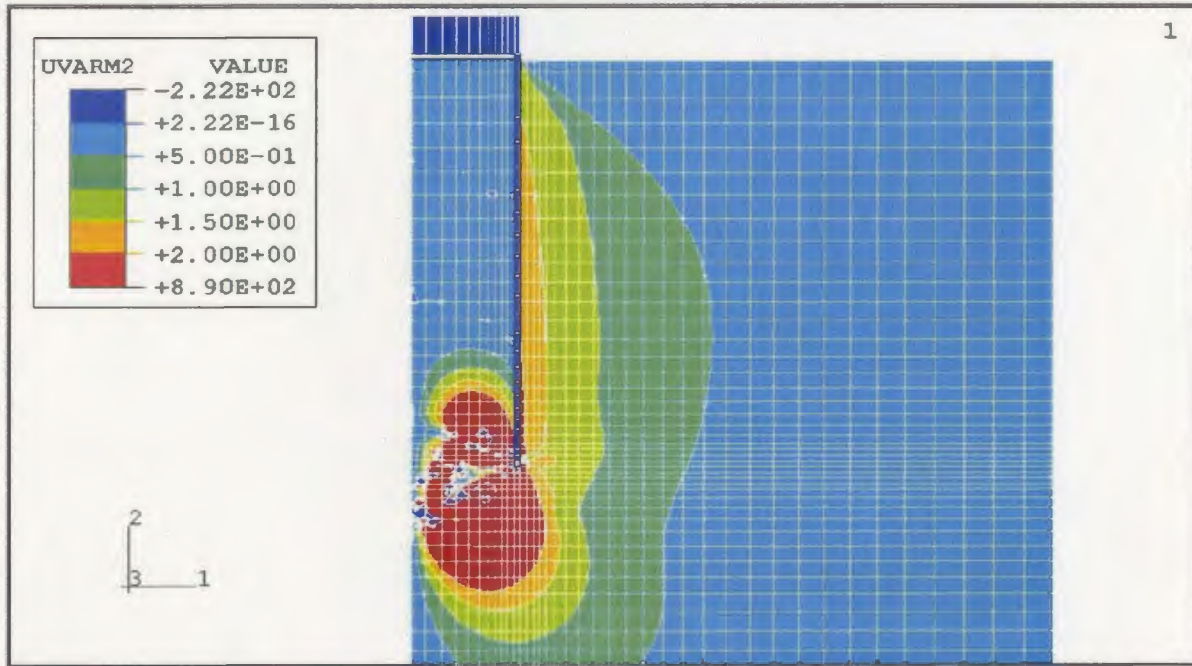


Figure 5.3.14 Contour of shear stress to shear strength ratio based on triaxial tests of the model with $L/D = 2.1$, at failure (step = 3, increment = 97). Conditions favourable to extensional shear failure occur in the soil body at the base of suction caisson and around the caisson wall. Hence it is a combination of tension and general shear failure scenarios.

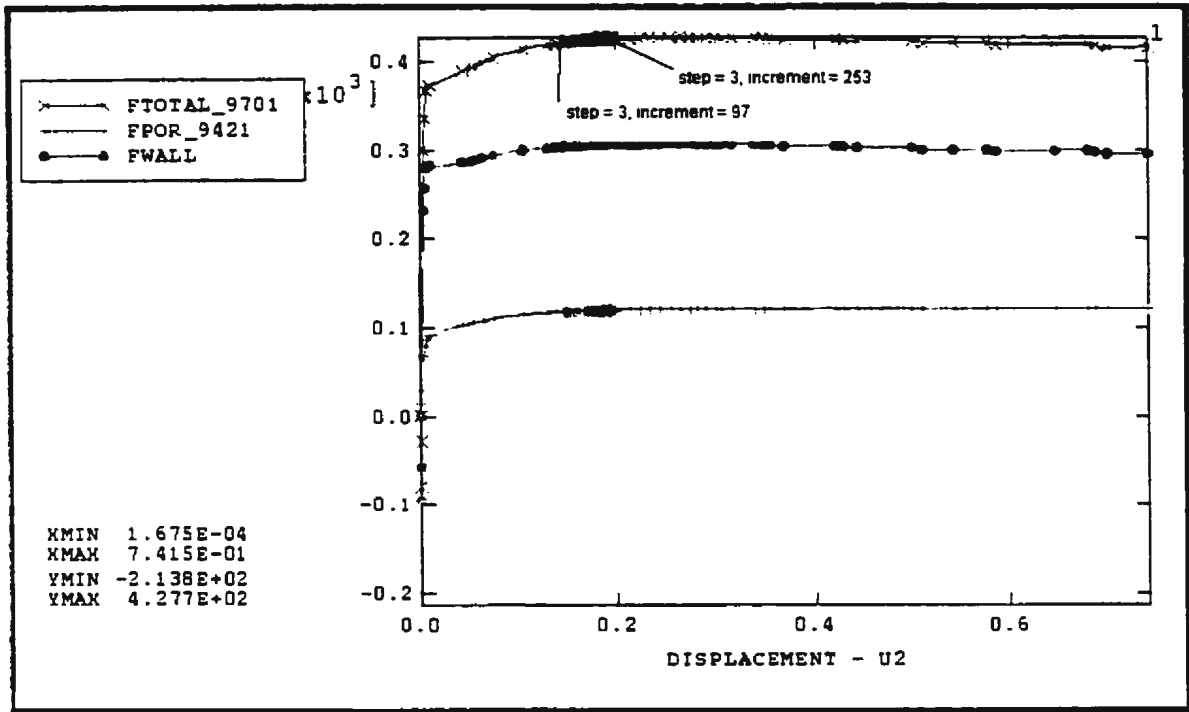


Figure 5.3.15 Load-displacement curve of L/D = 2.1 model. Unit: Force (N), Displacement (cm).

5.4. Summary

Based on the results of analyses given in the previous sections in this chapter, it can be stated that:

- From scale model analysis, it is seen that the 1g model can approximately simulate prototype force–displacement behaviour by applying a distributed load having a magnitude equal to the overburden stress of soil at half the height of suction foundation.
- From the analysis of the results of various models, it is seen that the soil stress state is properly modelled by an ng model rather than 1g model. The error

observed in this study is within 35% attributed to suction force generation, as the maximum error of the force component considered.

- The suction pressure developed inside during pullout is approximately modelled by the procedure developed in this thesis, giving results within 35 % of the expected value. It appears that 1g model tests give better suction representation than ng model tests, primarily due to the conflict that arises in ng models between dynamic scaling and diffusion scaling criteria.
- Overall the 1g model gives results which can be used to predict the actual component prototype values within an error of $\pm 50\%$. In hindsight, perhaps a finer mesh, used in prototype analysis, would have given a lesser wall force giving values closer to the expected values in 1g and ng models. Thus the margin of error would have been much less.
- Failure mode analyses show that identification of failure modes is possible using finite element analysis using soil properties obtained from laboratory tests. The conventional failure classification boundaries, presented by Christensen et al (1991) and others [Steensen-Bach, 1992], into direct shear, tension, and general shear failure seems to be rather too narrow to be justified by the results of analyses. A combination of failure conditions occurs before the suction caisson is pulled out of its location.

Chapter 6 Suction Caisson Subjected to Inclined Pullout Loading using Two-Dimensional and Three-Dimensional Analyses

6.1. Introduction

As previously stated in Chapter 1, some advantages of suction caissons are: (i) smaller associated costs compared to piles or drag anchor; and (ii) ease of application compared to other foundation systems. In addition to the benefit derived from additional suction resistance generated (due to suction pressure development under the cap), the suction caisson also has applicability for anchor systems requiring inclined pullout loading, i.e., for semisubmersibles, tankers, and guyed towers. For these applications, suction caissons are more economical, in terms of chain length requirement, and preferred due to ease of application.

In this chapter, numerical analyses are carried out to examine the behaviour of suction caissons subjected to inclined loads and to observe particular differences between 2D and 3D analyses using finite element procedure. The two dimensional (2D) finite element analysis carried out for this purpose, uses axisymmetric elements having asymmetric loading provision with pore pressure degrees of freedom on corner nodes; these are combined with a contact element to simulate contact behaviour along wall surface. The three-dimensional finite element analysis uses three-dimensional elements with pore pressure degrees of freedom on corner nodes combined with contact surface

model to simulate contact behaviour along the wall surface. The behaviour of the soil material is modelled using the Cam-clay plasticity model.

6.2. Comparison of Results from Axisymmetric (with Asymmetric Loading) and Three-Dimensional Finite Element Models

In finite element analysis, different idealizations could affect the results in different ways. The purpose of this section is to assess the significance of the difference in results, between the two chosen idealizations, and outline the merits and demerits of the simplified 2-D modelling procedure. The physical model of the caisson used in the study is based on MIT test model, described earlier in Section 4.2.

The axisymmetric finite element model used 8-noded quadrilateral axisymmetric elements, with pore pressure degree of freedom on the corner nodes for soil, and no pore pressure degree of freedom for the caisson. The mesh consisted of 437 elements including slide-line elements that were used to define contact interaction between the soil and caisson foundation. The three-dimensional finite element model used 20-noded solid cubic elements, with pore pressure degrees of freedom on their corner nodes for soil, and no pore pressure degree of freedom for caisson. The mesh consisted of 6964 elements, plus contact surface definition to simulate contact between the soil and caisson foundation. The applied loading was a pullout load, applied at an anchor point on a side of the caisson at the soil surface level, at a rate of 0.0003 m/min and at an angle of

inclination 6° from the vertical axis (towards positive 1 and 2 axes for axisymmetric model, and towards positive 1 and 3 axes in three-dimension model).

From the results (see Figures 6.2.1 and 6.2.2), it is seen that there is a difference between the two idealizations used, with regard to various force components, viz., the frictional force developed on the wall, and the suction force generated under the cap. Figures 6.2.1 and 6.2.2 show that the axisymmetric caisson model behaved as a very flexible system during the earlier part of the pullout loading, with a large suction pressure development; whereas, the 3D model behaved as a stiffer system during the earlier part of its pullout loading with very small suction force development. Otherwise total forces developed are nearly the same. This difference is probably due to the improper finite element modelling of cylindrical surface and the critical stress zone (at the bottom of suction caisson), in the 3-D model, and the smaller number of Fourier components used in the axisymmetric model (with asymmetric loading capabilities). Table 6.2.1 gives the comparison between the axisymmetric models with 2 and 4 Fourier components; the two components are made of the zeroeth (static axisymmetric force component) and the first and second harmonic terms of the Fourier series, whereas the four components are made up of the zeroeth (static axisymmetric force component) and the first four harmonic terms of the Fourier series. It is seen that the inclusion of a larger number of Fourier components tends to increase the wall loads and decrease the suction pressure loads. Since suction force development will be governed by the presence of relevant rigid body caisson movement, the presence of smaller displacements in the 3-D model (during its initial stage of force development) tends to decrease the early suction pressure

development. Moreover, the critical stress zone developed at the bottom of the suction caisson could not be properly modelled in the 3D model. Hence the suction forces obtained in the 3D would only be a lower bound. Since ABAQUS provides only a maximum of 4 Fourier components for axisymmetric-asymmetric analysis, a point load would require more Fourier components to represent it properly.

The use of larger number of Fourier components in analysis would require greater amount of time and memory than that used at present. For the present axisymmetric analysis (with asymmetric loading capabilities) it took more than 15.81 hours of CPU time to finish the applied pullout scenario, and the 3D analysis required more than 70.59 hours of CPU time. If ABAQUS had allowed more than four Fourier components (say 5 or 6), then the results will be much more closer to the 3D analysis results; the time consumed could be doubled or more instead of the present 15.81 hours. Hence the axisymmetric model saves quite a lot of computational time, giving almost the same accuracy.

The three-dimensional physical model used contact surface definition that considers both first and second direction contact interaction; whereas the axisymmetric-asymmetric physical model used this type of contact only at the nodal points of the Fourier components (hence may be getting a lower contribution from the wall). As a consequence, different amounts of wall force resistances are generated between the two models. If more Fourier components had been used in the axisymmetric-asymmetric model, the wall force would have been much larger; and if more elements were used in the 3D finite element model the wall force would have been less than the present one.

From the contours of shear stress to shear strength ratios, based on Direct Simple Shear (DSS) and Triaxial Extension (TE) tests, and by comparing these figures, set by set (Figures 6.2.4 and 6.2.5 with 6.2.6 and 6.2.7), it is observed that the failure patterns are similar irrespective of the failure conditions used (whether based on DSS or TE tests). Hence the axisymmetric analysis, with asymmetric load application, gives results closer to the 3D analysis. The correctness of the modelling procedure can be established only by comparing them with experimental results. Pore pressure contours from both models gave approximately the same trend with a different magnitude and distribution (see Figures 6.2.8 to 6.2.9). However, the suction pressure magnitudes were very small in the three-dimensional model.

Table 6.2.1 Force components comparison between two and four Fourier components of axisymmetric models, and 3D-model

Model	Ftotal (N)	Fwall (N)	Fpor (N)	Peak Fpor (N)
Axisymmetric model with 2 Fourier components	286.747	240.1928	45.20483	87.71085
Axisymmetric model with 4 Fourier components	392.1686	317.1084	75.52238	85.37313
Results from 3D-model	394.8	386.4865	9.9617	21.9157

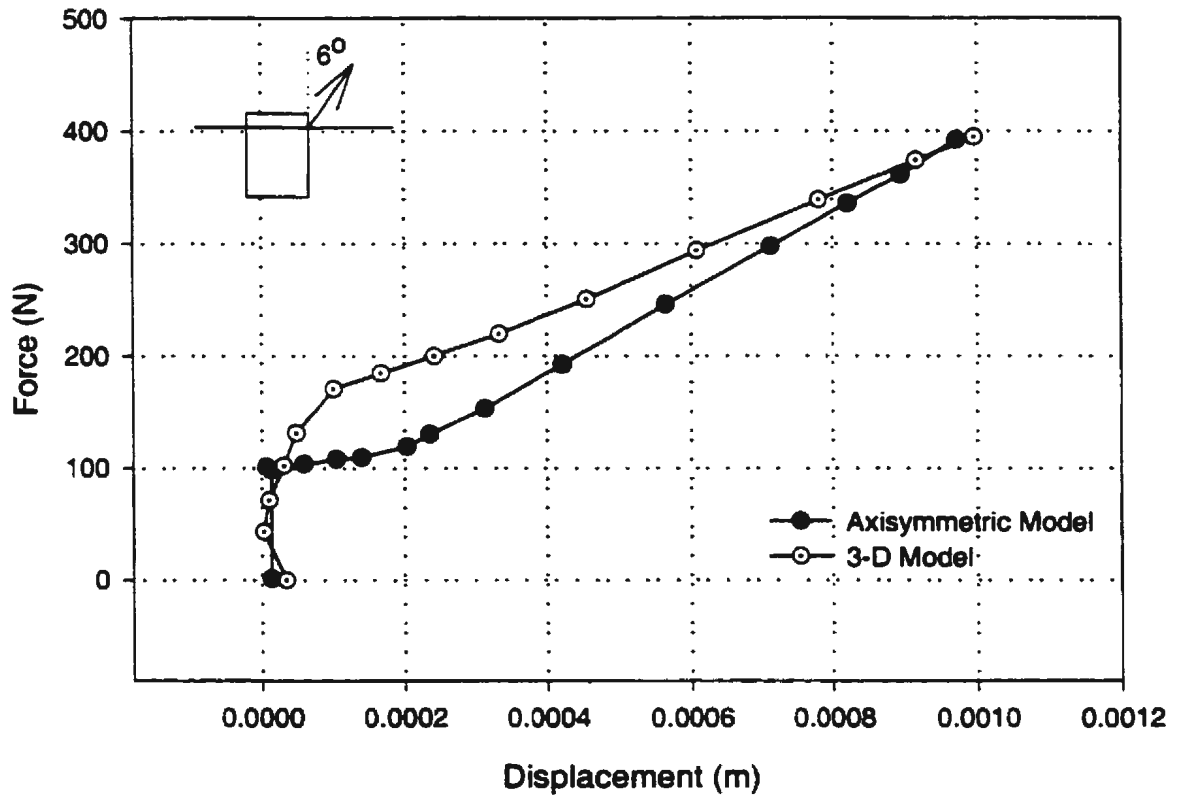


Figure 6.2.1 Force-displacement curve of total forces component from axisymmetric and 3-D model

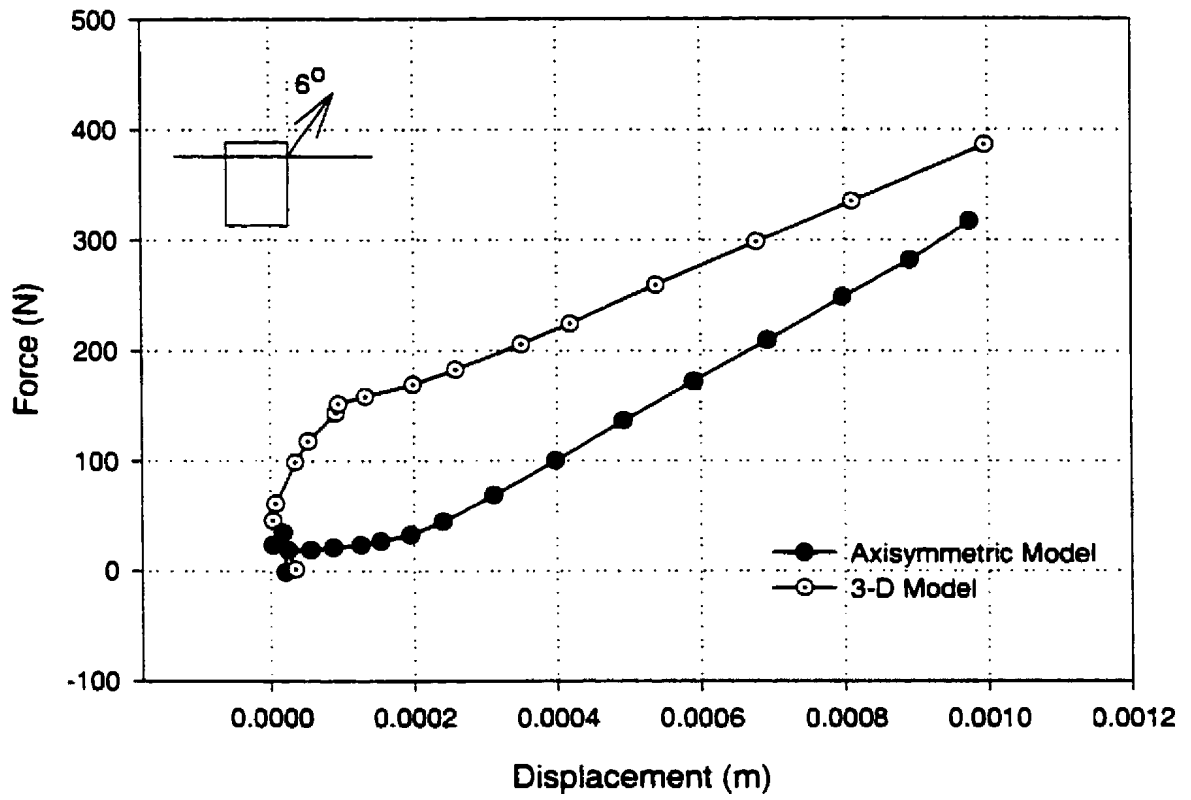


Figure 6.2.2 Force-displacement curve of wall force component from axisymmetric and 3-D model

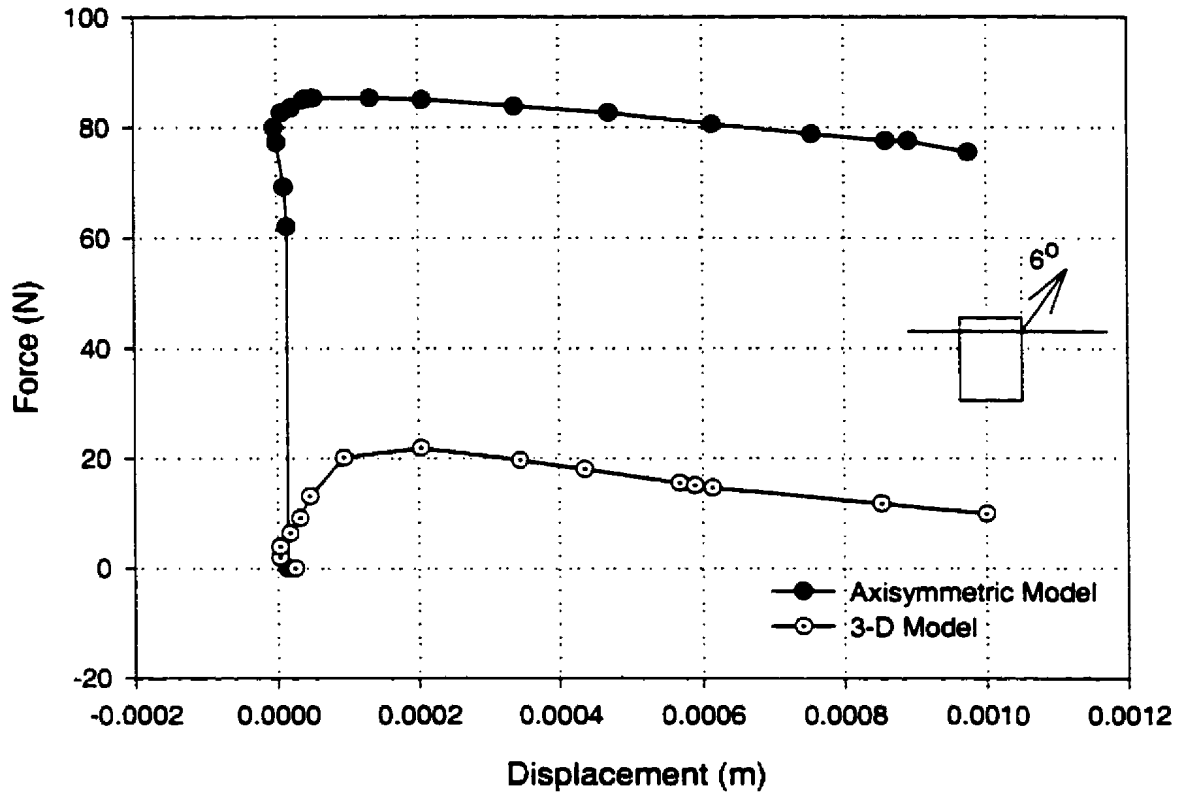


Figure 6.2.3 Force-displacement curve of suction force component from axisymmetric and 3-D model

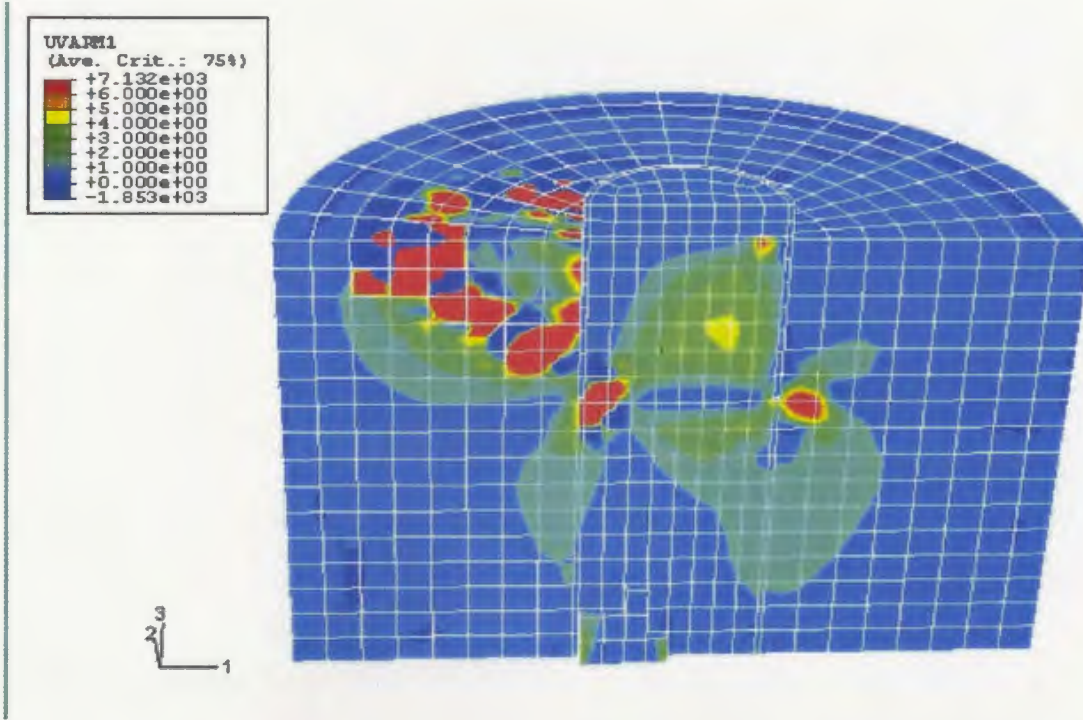


Figure 6.2.4 Shear stress to shear strength ratio contour based on DSS test, cross section of three-dimensional model

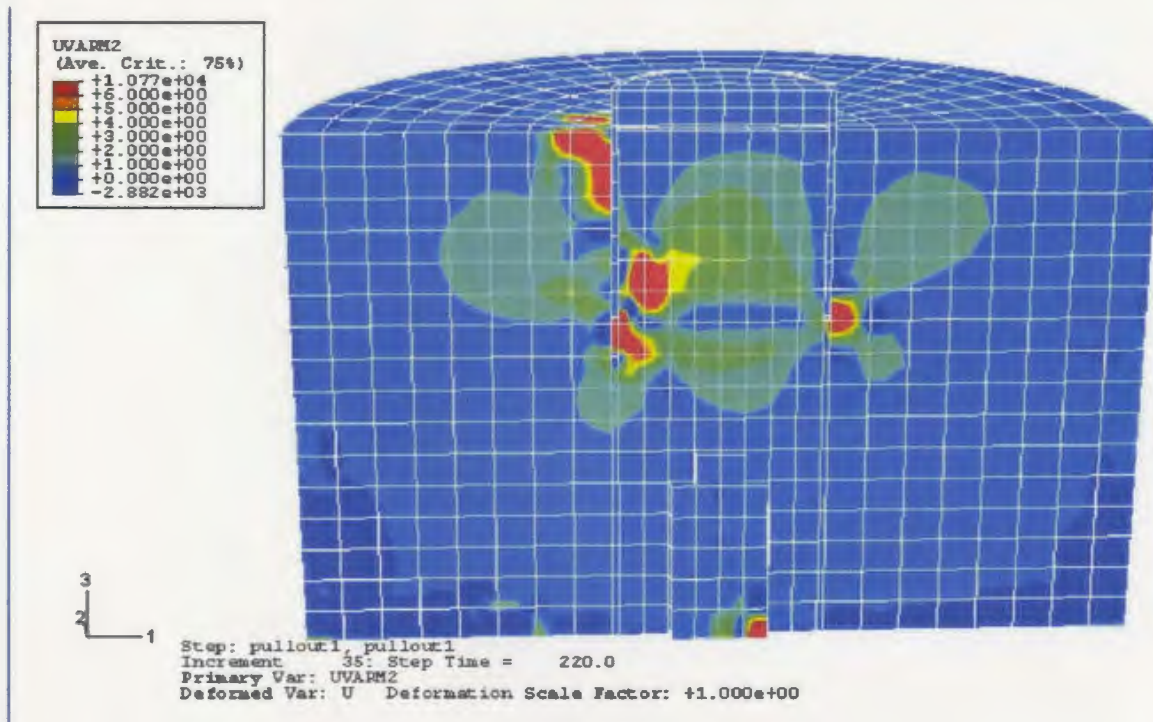


Figure 6.2.5 Shear stress to shear strength ratio contour based on TE test, cross section of three-dimensional model

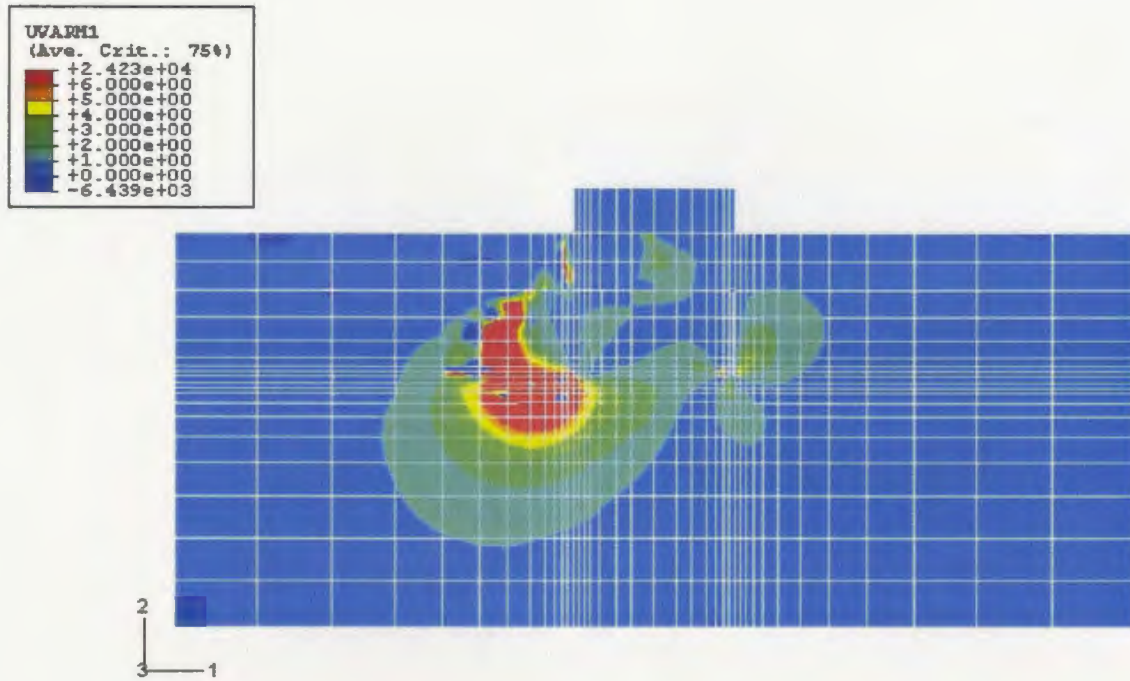


Figure 6.2.6 Shear stress to shear strength ratio contour based on DSS test, cross section of axisymmetric model

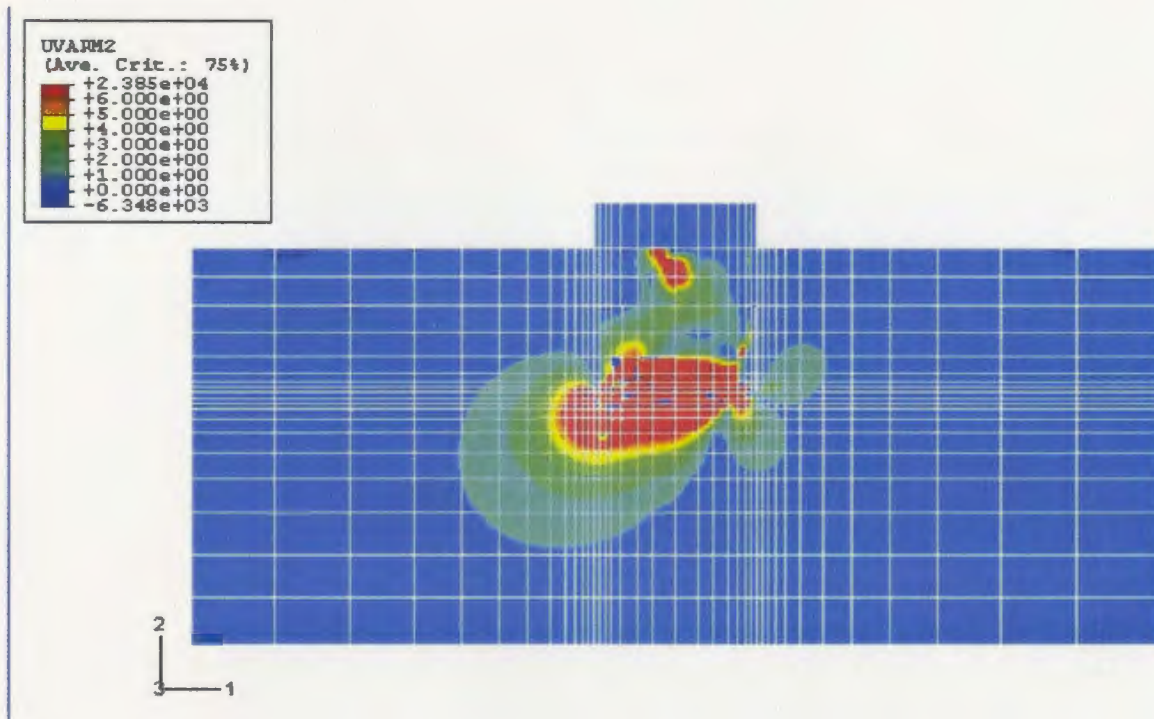


Figure 6.2.7 Shear stress to shear strength ratio contour based on TE test, cross section of axisymmetric model

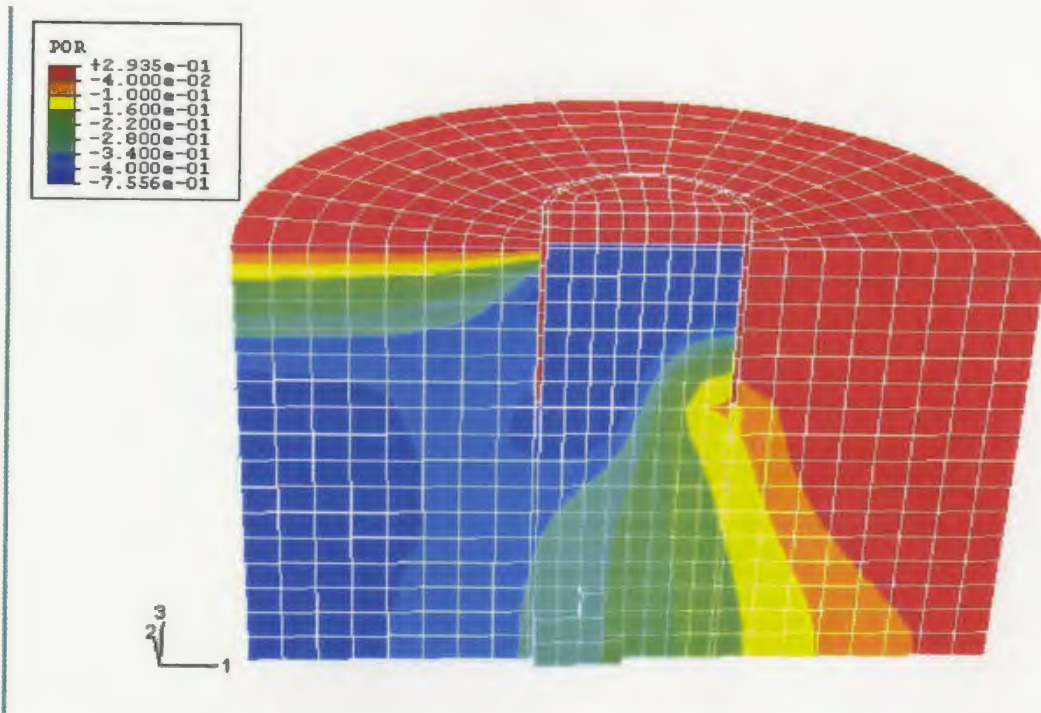


Figure 6.2.8 Pore pressure contour, cross section view of three-dimensional model

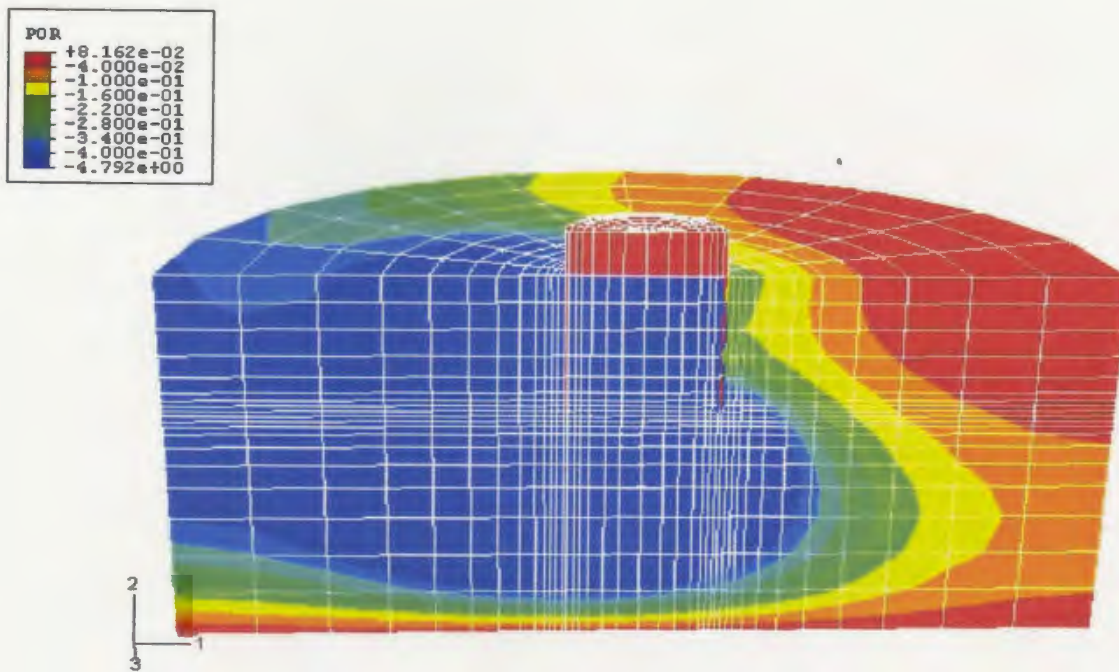


Figure 6.2.9 Pore pressure contour, cross section of axisymmetric model

6.3. Summary

From the analyses of results presented in this chapter, it can be concluded as:

- i) The 3D model, which is capable of representing the unsymmetric response behaviour of the model produce a higher resistance than the axisymmetric model. This higher value was due to the fact that the isoparametric second order elements did not represent the true cylindrical nature of the caisson surface; it was also due to the improper finite element meshing at the bottom of the caisson, where the critically stressed zones occurred, resulting in a stiffer response.
- ii) The results from 3D model gave a smaller suction force than the results of axisymmetric model and the wall force from the 3D model was larger than the wall force generated by the axisymmetric model. This condition was caused by the stiffer wall resistance generated in the 3D models which restricted the slip occurring during pullout; hence 3D model gave less suction force. However, the axisymmetric model showed a flexible wall resistance, which allowed greater slip to occur during pullout; hence it gave a higher suction force. This could have been avoided by using more harmonics during the Fourier series analysis in ABAQUS.
- iii) The axisymmetric-asymmetric model took nearly 4.7 times less CPU time for the analysis than the 3D model. Even if more Fourier harmonics were taken in the axisymmetric model, the time taken would have been nearly 2 to 3 times

less than the 3D model. Consequently the use of an axisymmetric-asymmetric analytical model for the suction caisson saves a large amount of computational time.

- iv) Overall, the axisymmetric-asymmetric model behaviour was close to the 3D model. Hence in the subsequent studies only the axisymmetric-asymmetric model is used for further analyses.

Chapter 7 Suction Caisson Under Inclined Pullout Load: Effect of Pullout Anchor Inclination and Location

7.1. Introduction

In this chapter, numerical analyses are carried out to examine the behaviour of suction caissons under inclined loads, considering the effect of anchor point location and load inclination on bearing resistance. The finite element analysis carried out for this purpose uses axisymmetric elements, having an asymmetric loading provision, with pore pressure degrees of freedom on corner nodes; it is combined with the use of contact elements to simulate contact behaviour along the wall surface. The behaviour of soil material is modelled using the Cam-clay plasticity model.

7.2. Axisymmetric Model

7.2.1. Model Definition

Model geometry and material properties are taken from MIT test data (see section 4.2). The suction caisson model has a 0.051 m diameter and 0.051 m length with a wall thickness of 0.0015 m. The material for the soil is Resedimented Boston Blue Clay (RBBC) with properties as given in Table 7.2.1. This is the same material that was used in suction foundation model tests for the MIT series, given in section 4.2.2.

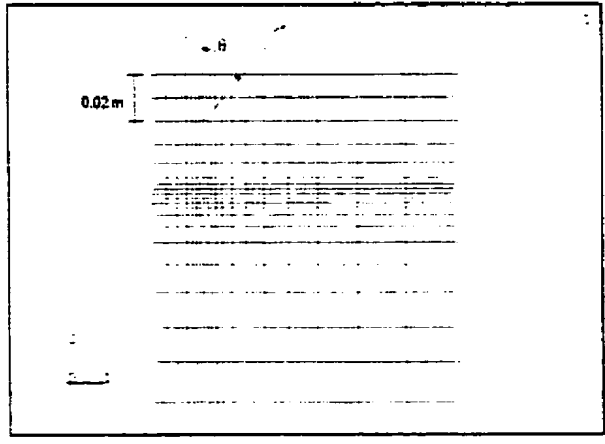
Table 7.2.1 Salient soil properties for RBBC

Parameter	Value
Coefficient of elastic bulk modulus, κ	0.00435
Coefficient of hardening bulk modulus, λ	0.22826
Submerged unit weight of soil, γ'	7.735 kN/m ³
Permeability of soil, k	2.37 x 10 ⁻⁹ m/s

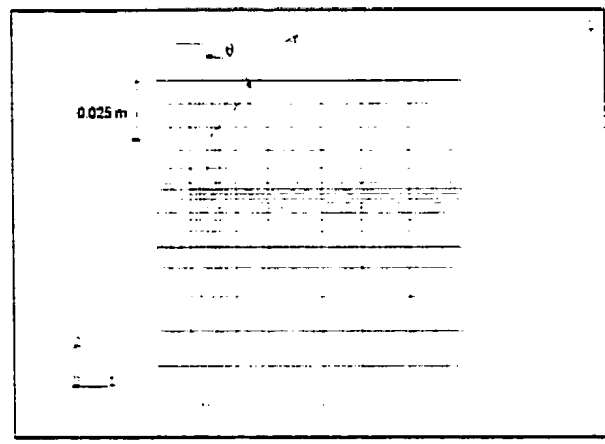
In the original laboratory set-up of the MIT tests, a distributed load of 73.5 kPa was applied on top of soil surface to bring the stress state at virgin loading; this load is kept the constant. This load eventually simulates the average soil stress exerted over the prototype caisson wall. Hence it must be remembered that the pullout loads and suction pressures obtained would represent the soil behaviour only in an approximate average sense.

7.2.2. Pullout Scenarios

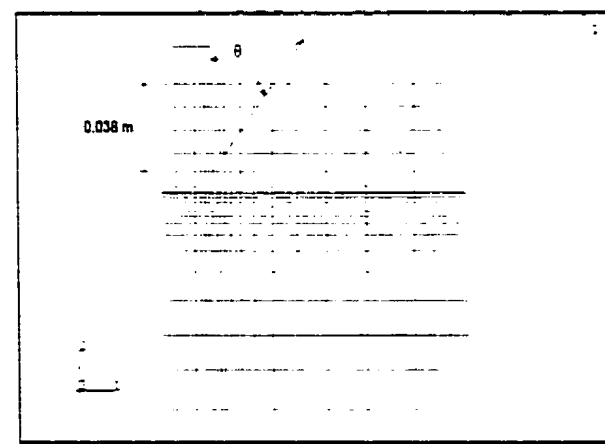
Pullout scenarios consisted of different pullout angles and anchor point locations. Pullout angles consisted of: (i) three to four different angles, θ , of pullout; viz., 5°, 20°, 60° and 90° (from vertical axis), and (ii) three different anchor point locations; viz., at 0.02 m, 0.025 m, and 0.038 m below the soil surface level. The pullout rate was 0.0003 m/min, at the node where the anchor point is located, as shown in Figures 7.2.1.



(a)



(b)



(c)

Figure 7.2.1 Mesh and pullout scenario for the three different anchor points location

7.2.3. Presentation and Discussion of Results

Force-displacement curves obtained from finite element analyses are shown in Figures 7.2.2 to 7.2.10. It is seen from the results (Figures 7.2.2 to 7.2.10) that trends of force-displacement curves show that for a higher pullout angle of inclination, the caisson-soil system behaves in a stiffer manner. This behaviour is similar for the three different anchor point locations examined.

Compared with results from vertical pull out analysis (see section 4.2), it is seen that the pullout resistance of (central) vertical pullout (maximum is around 218 N) is much less than pullout resistance obtained from non-central inclined pullout loads (see Figures 7.2.2 to 7.2.4). This is due to the fact that transverse soil resistance is marshalled by the suction caisson during the various stages of inclined pullout. From Figure 7.2.2 to 7.2.4 it appears that the maximum total force on the caisson increases when the pullout anchor point is closer to the centre of caisson height. Moreover, suction forces generated during inclined pullout analyses were mostly smaller than suction forces generated during the vertical pullout analysis (see Figures 7.2.8 to 7.2.10 and compare with Figure 4.6.4). This difference is due to the increased shear deformation of the suction caisson that occurs for the case of inclined pullout loads; this reduces the displacement response of the suction caisson before first slip occurrence, resulting in reduced suction pressure development at the top of caisson. Therefore, the greater the inclination of applied load, the lesser the suction force generated.

Since there is no available reference data to compare the present results obtained for inclined pullout loads, a basic formulation was used to verify the results. The basic formulation chosen was that used for the ultimate load design of an anchor (Das, 1995).

Influence factor was defined as ratio of embedment depth, H , to anchor vertical length, h ($= H/h$) (see Figure 7.2.11). According to Das, the critical value of this ratio was defined as:

$$(H/h)_{cr} = 4.7 + 2.9 \times 10^{-3} c \leq 7 \quad ; \text{ for a square anchor.} \quad (7.1)$$

where:

c = cohesion in lb/ft^2 .

Empirical ultimate resistance relationship for $H/h \leq (H/h)_{cr}$ was given as:

$$[(H/h)/(H/h)_{cr}] = [(P_u/cBh)/(7.425 + 1.575(h/B))] A \quad (7.2)$$

where:

A = $0.41 + 0.59 (H/h)/(H/h)_{cr}$

P_u = ultimate design load

c = cohesion

B = anchor foundation width

h = anchor foundation vertical length

From MIT studies data, the ratio of undrained shear strength to compression stress from undrained triaxial compression was 0.32 at 0.6 kgf/cm^2 compression stress. From the above formula, P_u was found to be 177.7 N at a compression stress of 73.5 kPa (0.75 kgf/cm^2), for a test environment.

Another verification formulation was from Brom's formula for a rigid pile in cohesive soil (Tomlinson, 1994). The idea of the formula is simple: it is assumed that an evenly distributed reaction on soil at a value of $9.c.B$ per unit height was applied during ultimate loading. Therefore, the total ultimate capacity, $H_u = 9.c.B.h$, can be easily calculated, and it gives a value of 551.1 N. However, this formula seems to be for deeper foundations since the original formulation does not seem to include length to depth of embedment ratio equal to one. Therefore, the result is higher than the actual ultimate capacity.

The actual values from numerical analysis for 60° and 90° pullout inclination varied between 370 to 490 N with a mean value of 430 N. This value is in between 177.5 N and 551.1 N. This would confirm that the results obtained from finite element analyses are in the right ballpark range.

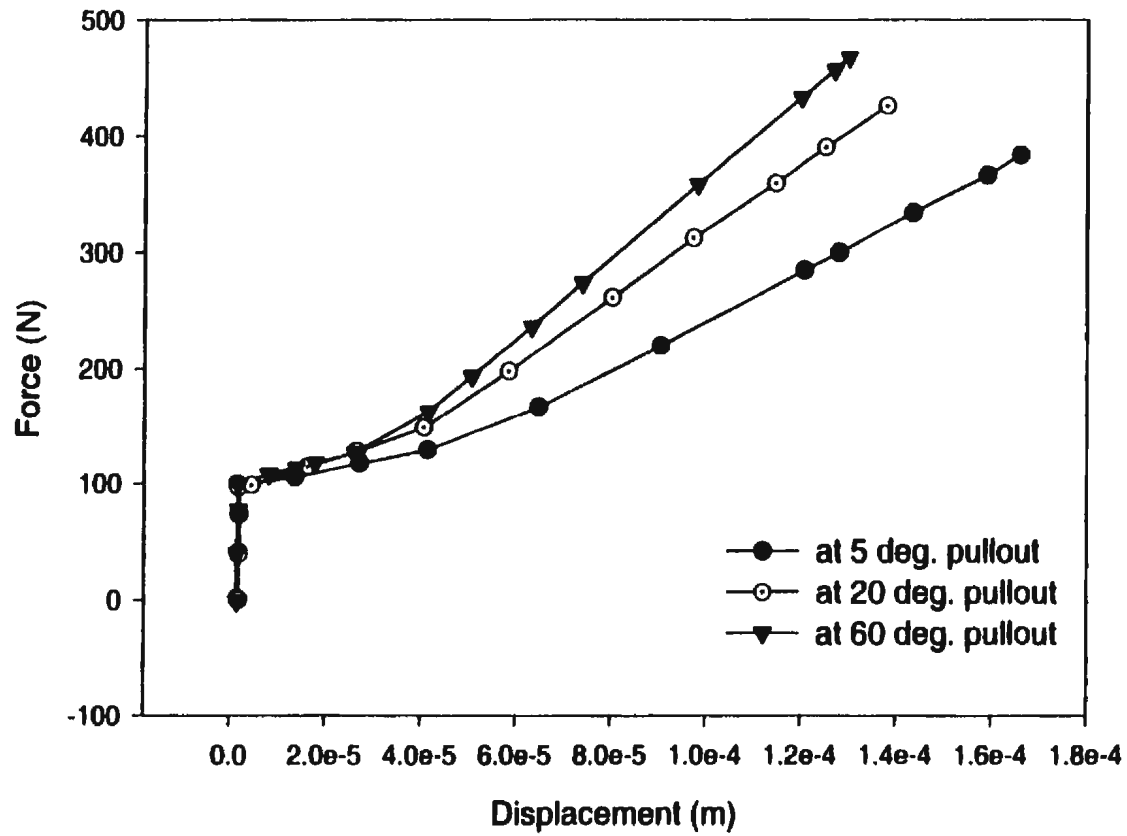


Figure 7.2.2 Total resistance force-displacement curve at 0.02 m anchor point below the soil surface.

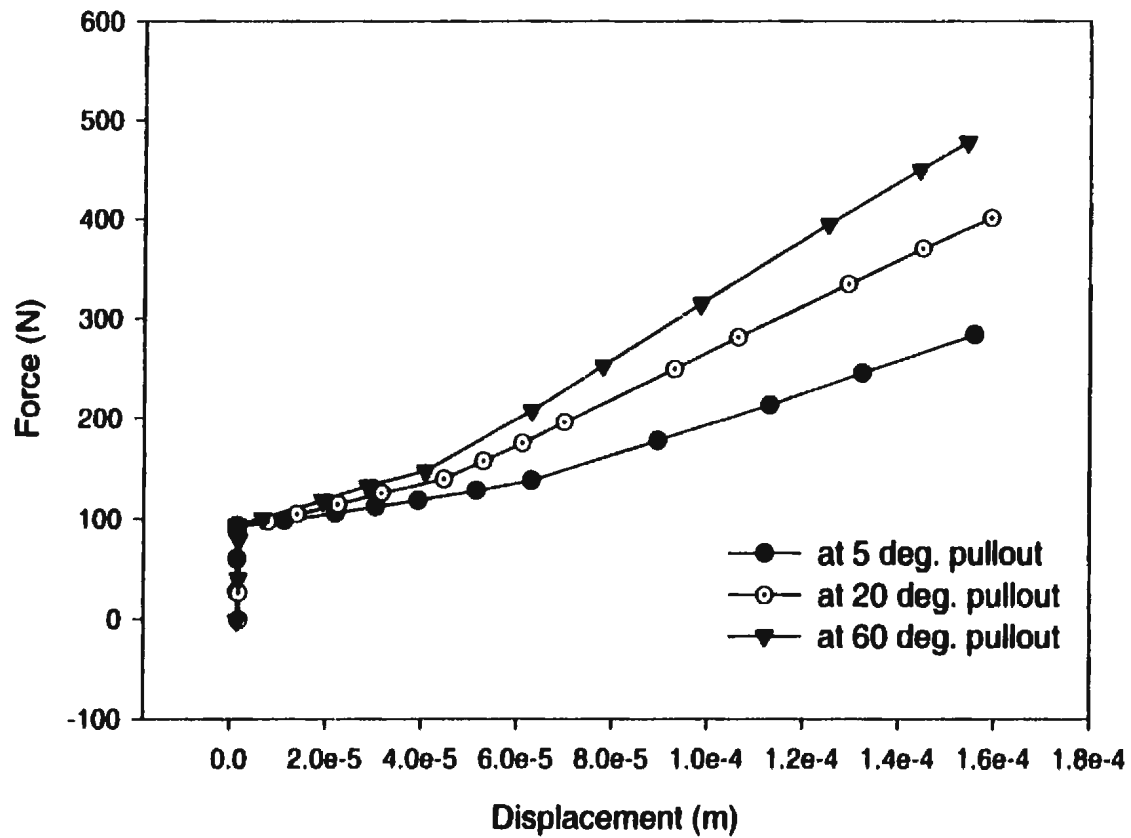


Figure 7.2.3 Total resistance force-displacement curve at 0.025 m anchor point below the soil surface.

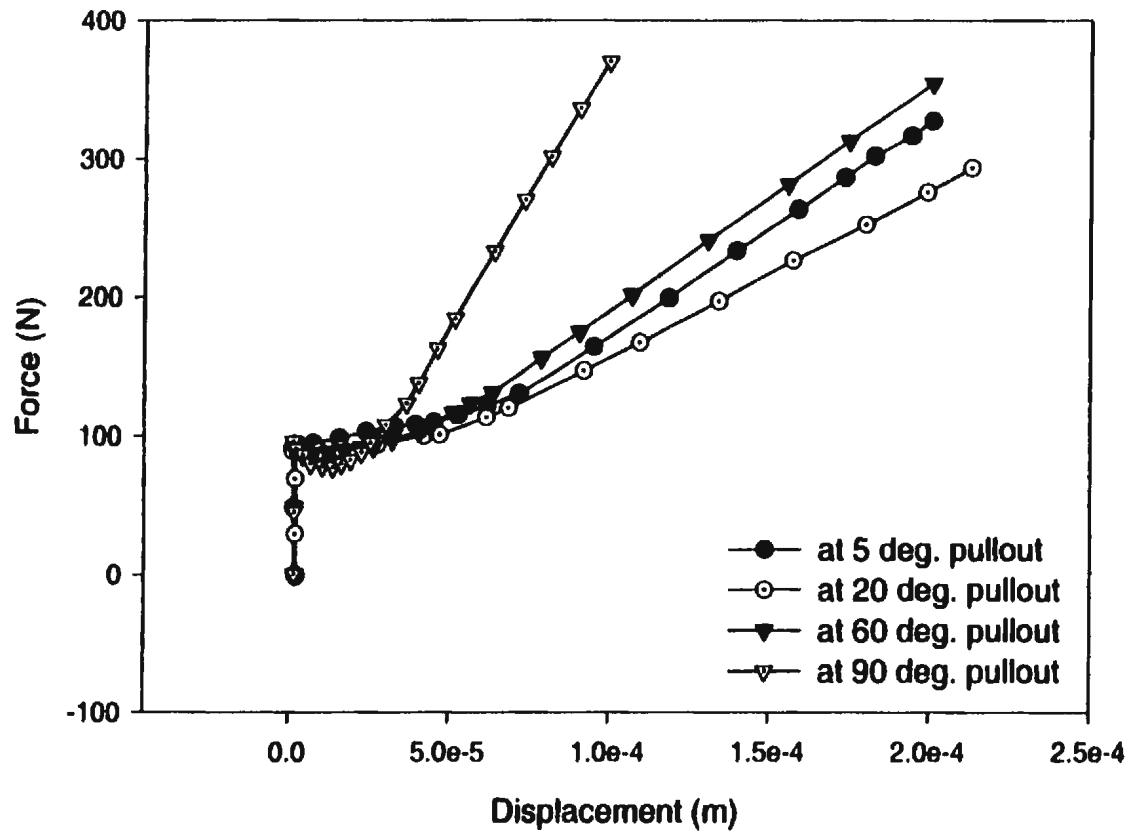


Figure 7.2.4 Total resistance force-displacement curve at 0.038 m anchor point below the soil surface.

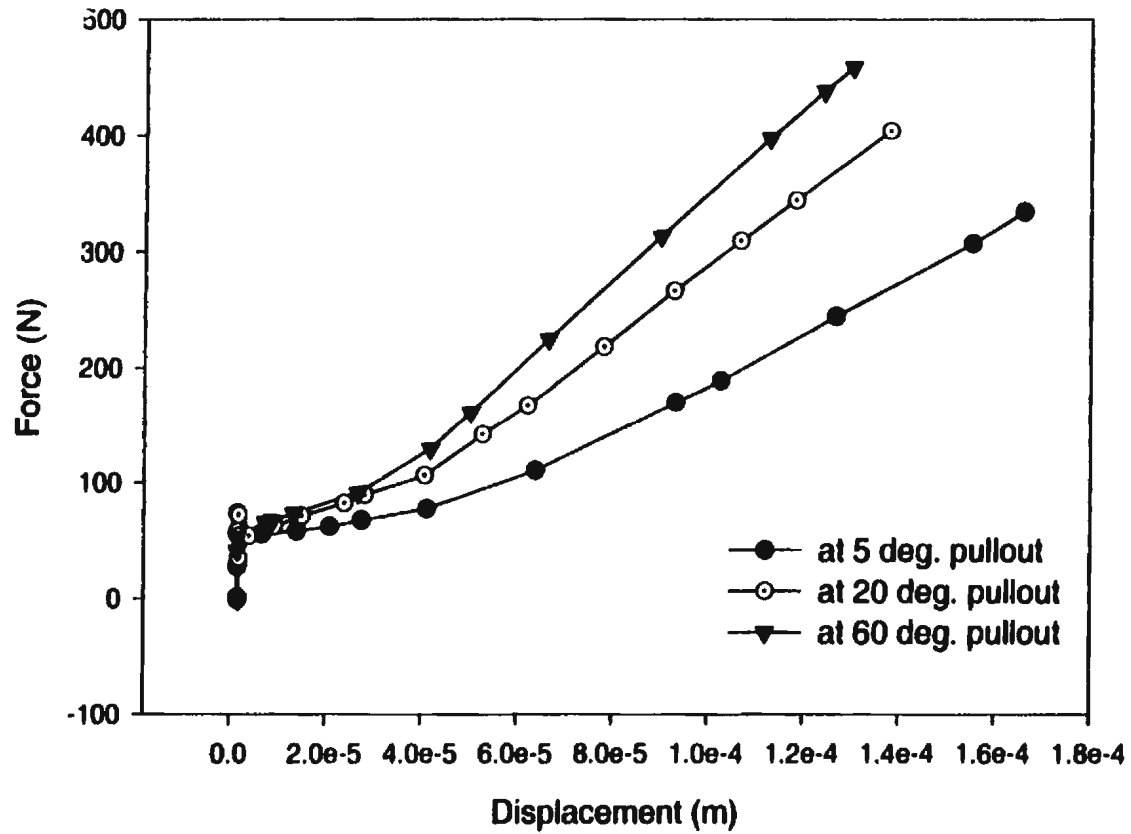


Figure 7.2.5 Wall resistance force-displacement curve at 0.02 m anchor point below the soil surface.

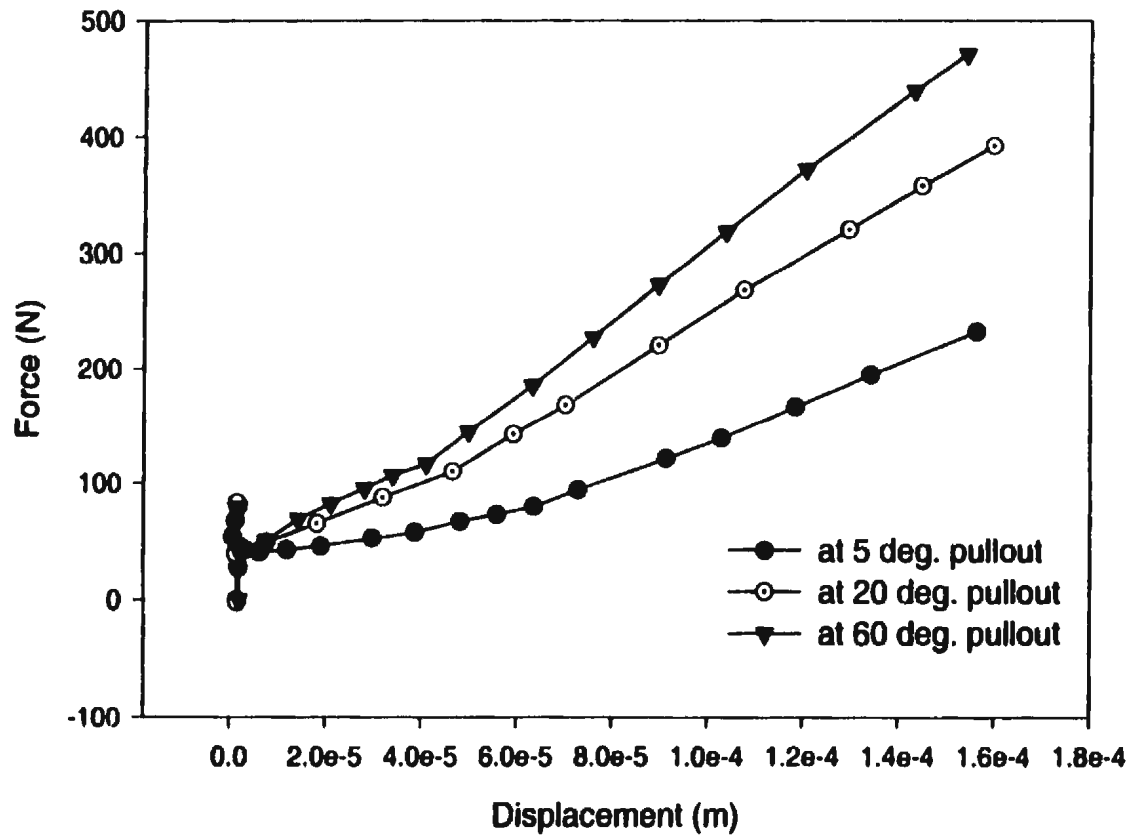


Figure 7.2.6 Wall resistance force-displacement curve at 0.025 m anchor point below the soil surface.

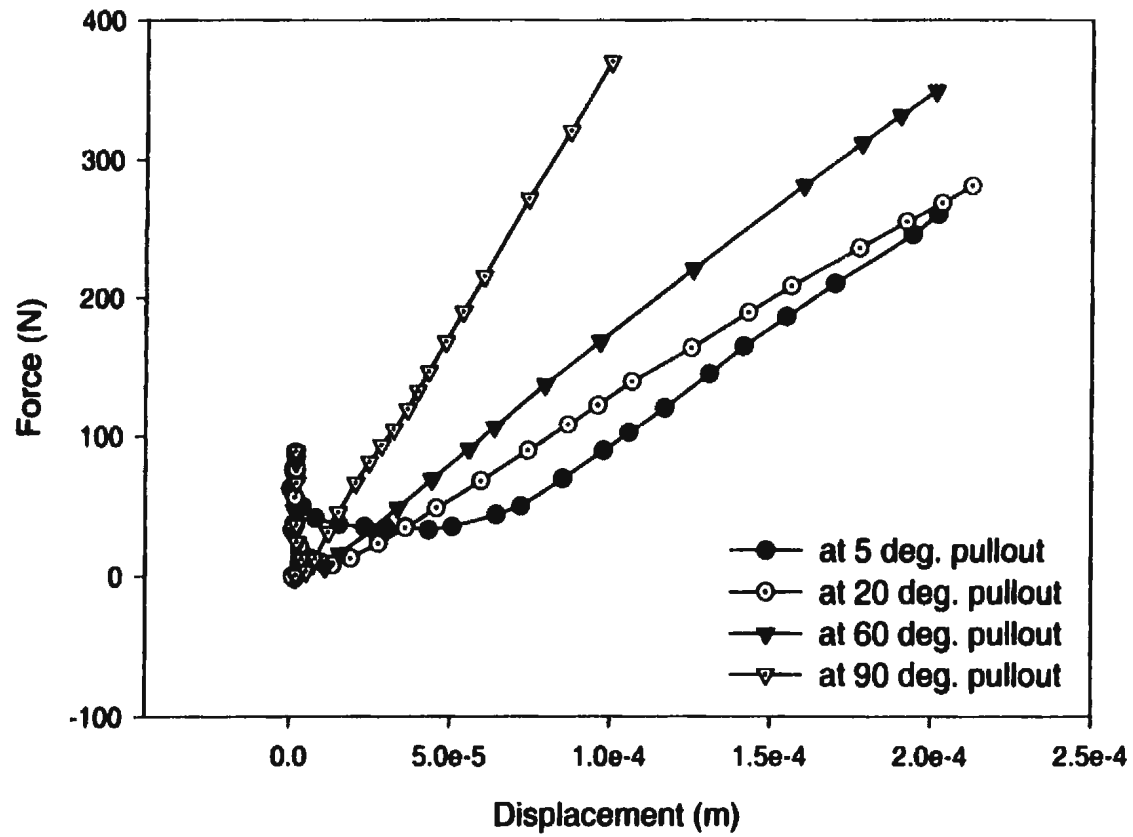


Figure 7.2.7 Wall resistance force-displacement curve at 0.038 m anchor point below the soil surface.

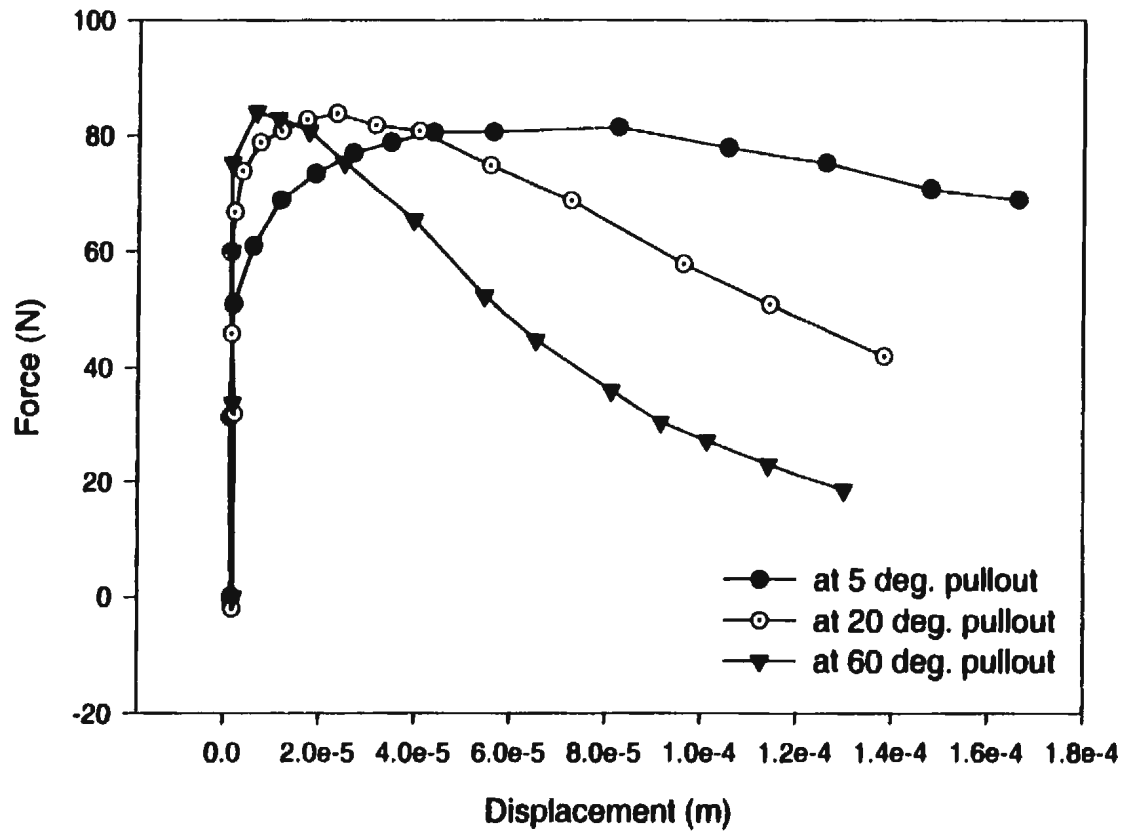


Figure 7.2.8 Suction resistance force-displacement curve at 0.02 m anchor point below the soil surface.

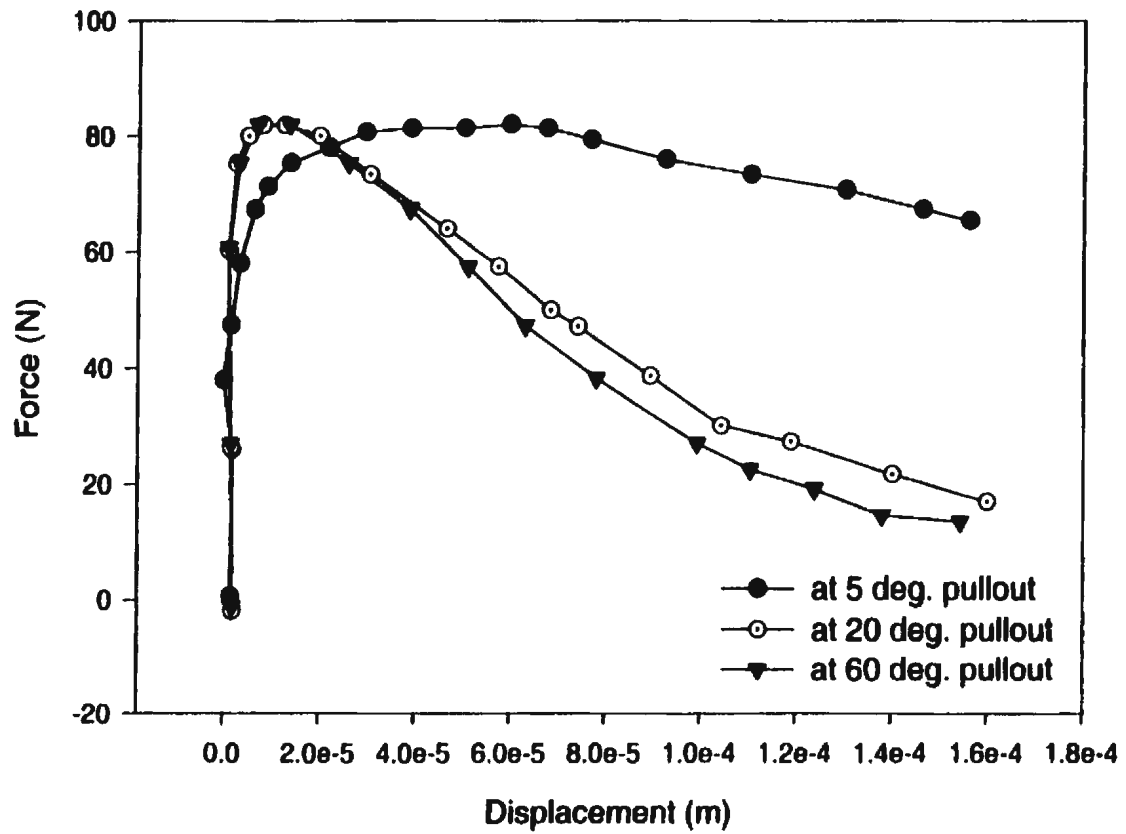


Figure 7.2.9 Suction resistance force-displacement curve at 0.025 m anchor point below the soil surface.

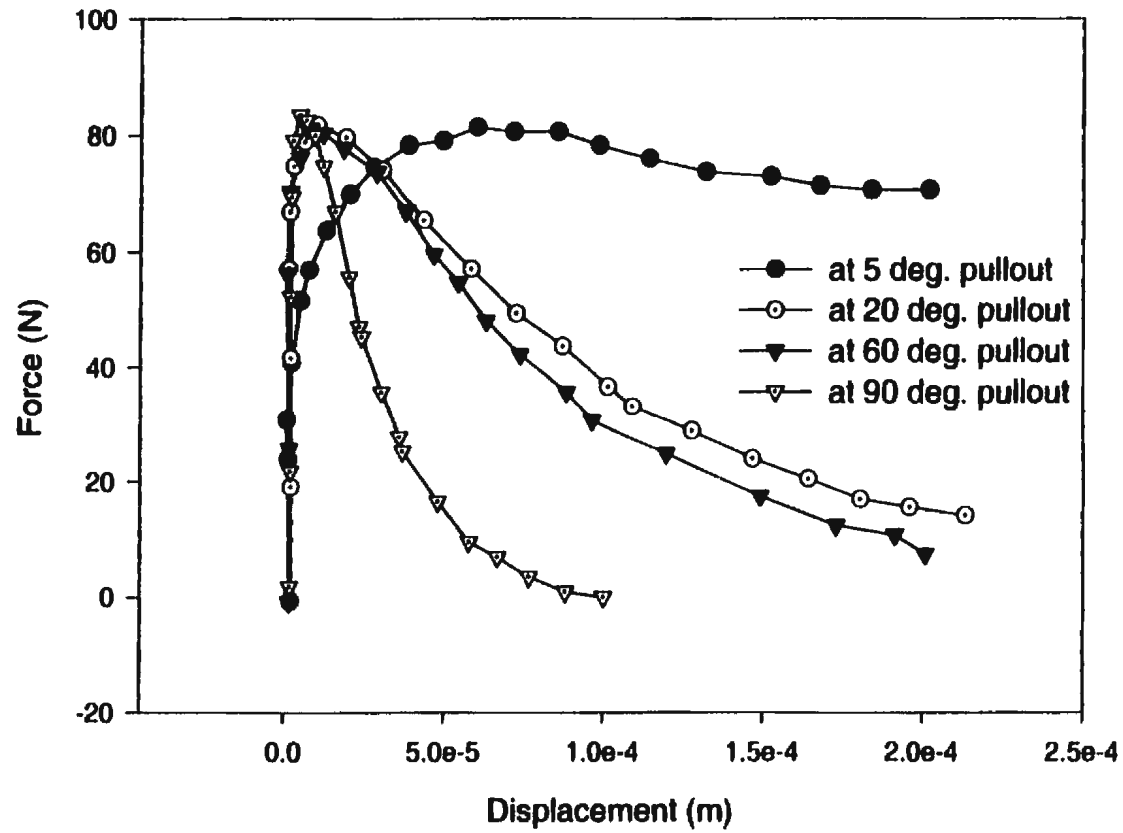


Figure 7.2.10 Suction resistance force-displacement curve at 0.038 m anchor point below the soil surface.

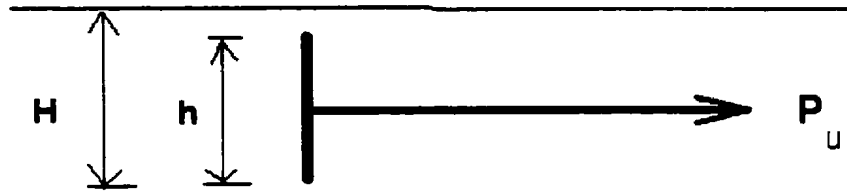


Figure 7.2.11 Plate anchor in clay

7.3. Failure Behaviour of Suction Caisson System under Inclined Pullout Loads based on Shear Stress to Shear Strength ratios

From contours of results obtained during the earlier analyses, some interesting behaviour characteristics of suction caissons under inclined pullout loads can be observed. The interesting characteristics are related to possible patterns of failure surfaces, and factors that affect the bearing resistance of caisson foundations.

From Figures 7.3.1 to 7.3.20, it is seen that the contours of shear stress to shear strength ratios, based on DSS (Direct Simple Shear) and TE (Triaxial Extension) tests, give some salient characteristic behaviour of suction foundations, under inclined loads. The behaviour has to be interpreted by combining the contours of these failure characterizations; DSS tests are based on the shear failure of clays, while TE tests are based on tensile failure of clays.

For the sake of clarity, only Figures 7.3.5, 7.3.6, 7.3.11, 7.3.12, 7.3.17, 7.3.18, 7.3.19 and 7.3.20 are considered in detail. Figures 7.3.5 and 7.3.6 shows that the soil foundation rather failed in shear due to the reverse slope stability of the soil on the toe of suction foundation. At the bottom of the caisson the soil seems to have failed primarily in tension rather than shear. Bearing failure does not seem to have taken place in front of the suction caisson.

Considering Figures 7.3.11 and 7.3.12 whose the load is applied almost at the level of the centroid of suction caisson, the failure is dominated by reverse slope stability, at the back of caisson, and by tensile failure at the bottom of suction caisson. No bearing failure has been observed in front of the caisson. A similar failure pattern is observed from Figure 7.3.19 and 7.3.20. The stress levels, at failure, seem to be almost the same in all the above-mentioned three cases (see Figures 7.3.5, 7.3.11, & 7.3.17, and 7.3.6, 7.3.12 & 7.3.18).

Also when the contour of shear stress to shear strength ratio based on direct shear and triaxial extension tests results are combined, i.e., in Figures 7.3.1 and 7.3.2, it will give approximately a similar surface as that failure surface obtained for the Snorre suction caisson model test carried out by the Norwegian Geotechnical Institute (see Figure 7.3.21).

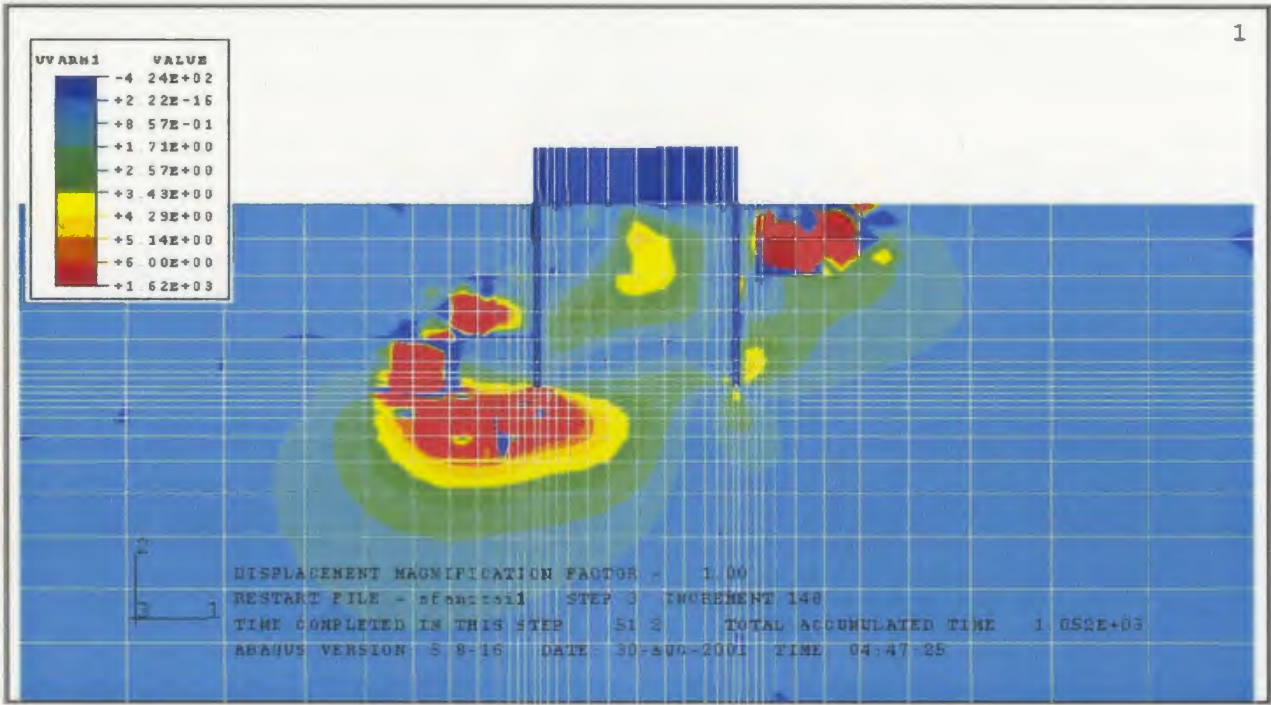


Figure 7.3.1 Contour of ratio of shear stress to shear strength based on DSS test of pullout with inclined angle of 5° and anchor point at 0.02 m below the soil surface.

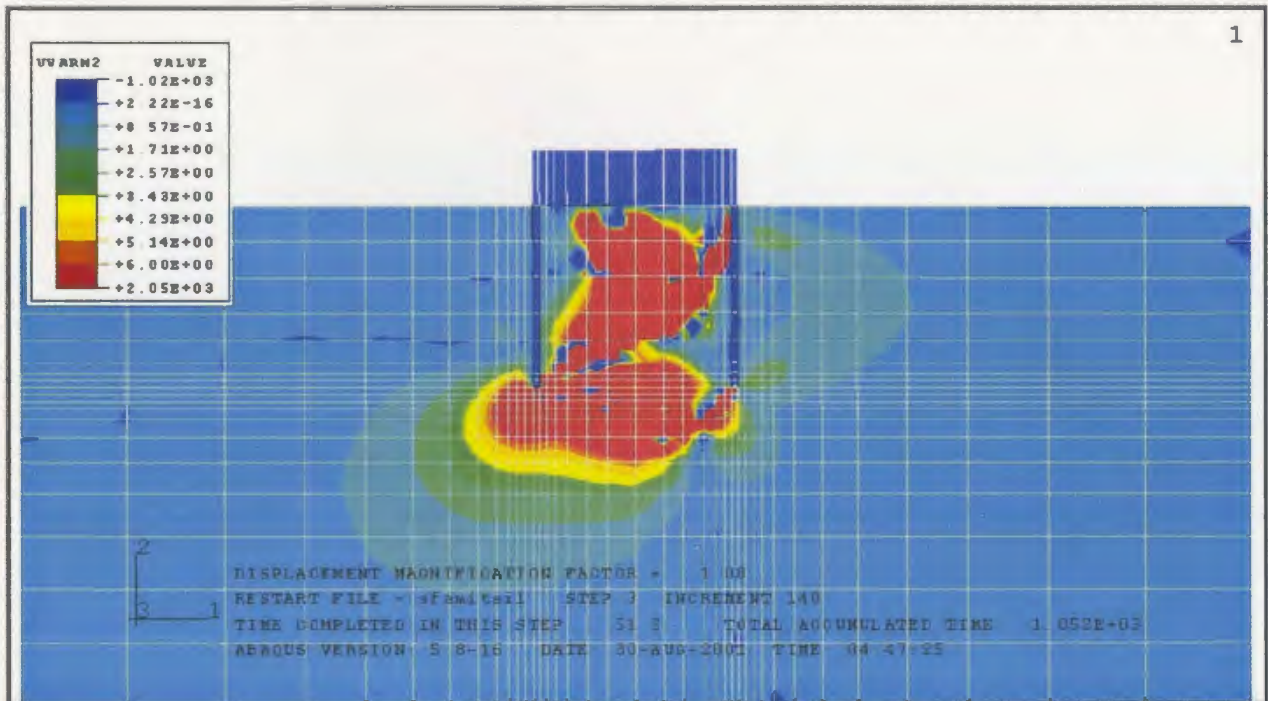


Figure 7.3.2 Contour of ratio of shear stress to shear strength based on TE test of pullout with inclined angle of 5° and anchor point at 0.02 m below the soil surface.

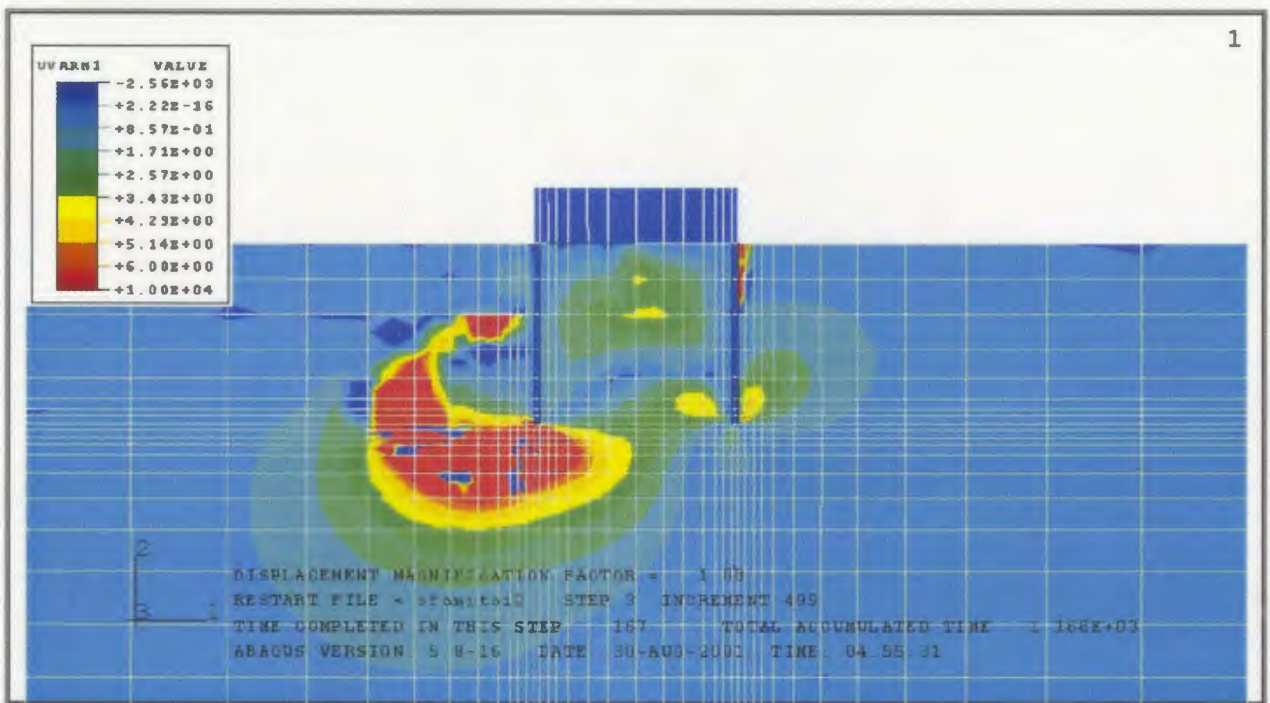


Figure 7.3.3 Contour of ratio of shear stress to shear strength based on DSS test of pullout with inclined angle of 20° and anchor point at 0.02 m below the soil surface.

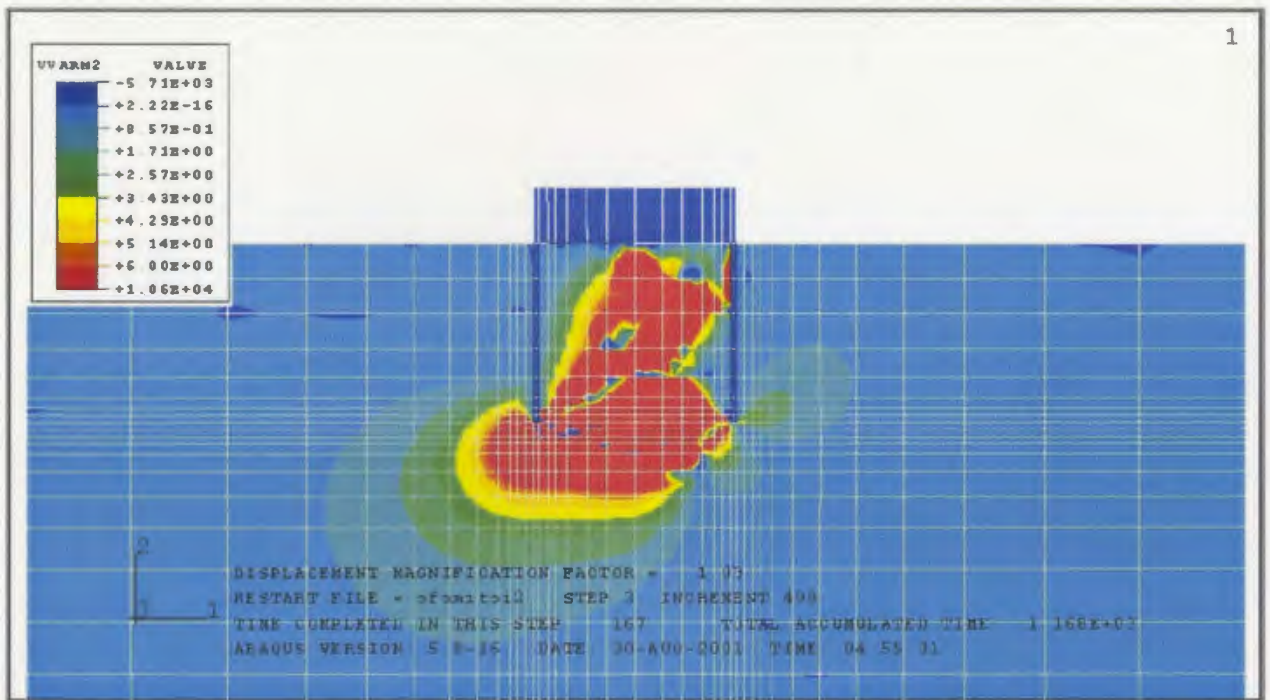


Figure 7.3.4 Contour of ratio of shear stress to shear strength based on TE test of pullout with inclined angle of 20° and anchor point at 0.02 m below the soil surface.

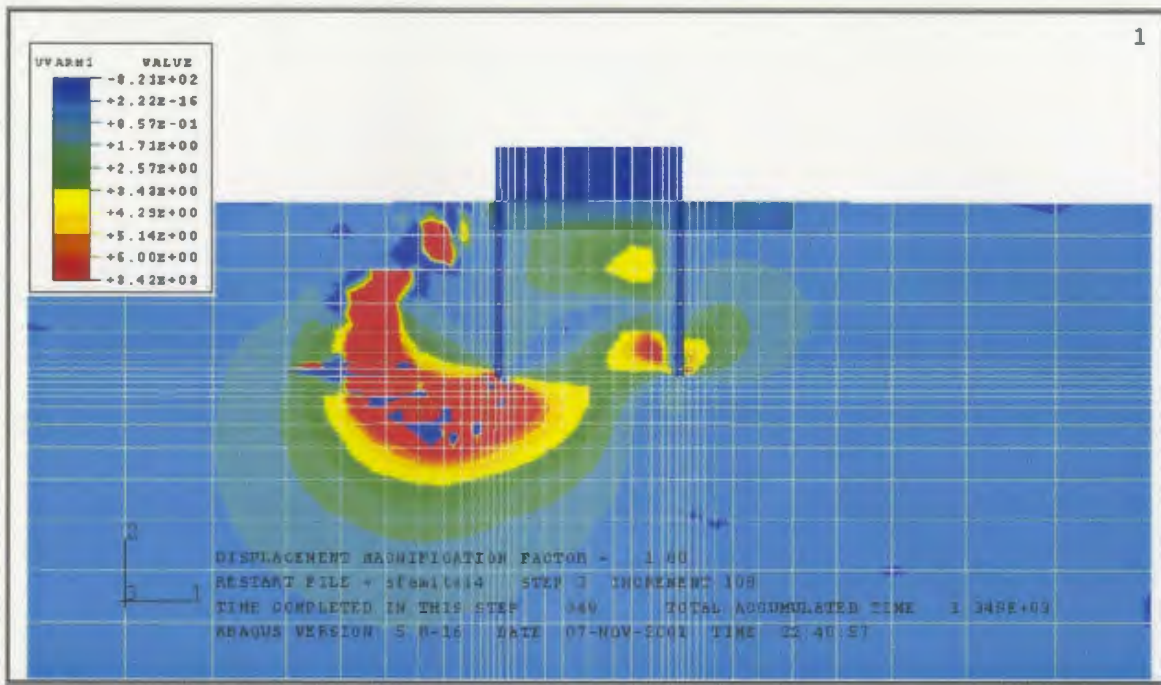


Figure 7.3.5 Contour of ratio of shear stress to shear strength based on DSS test of pullout with inclined angle of 60° and anchor point at 0.02 m below the soil surface.

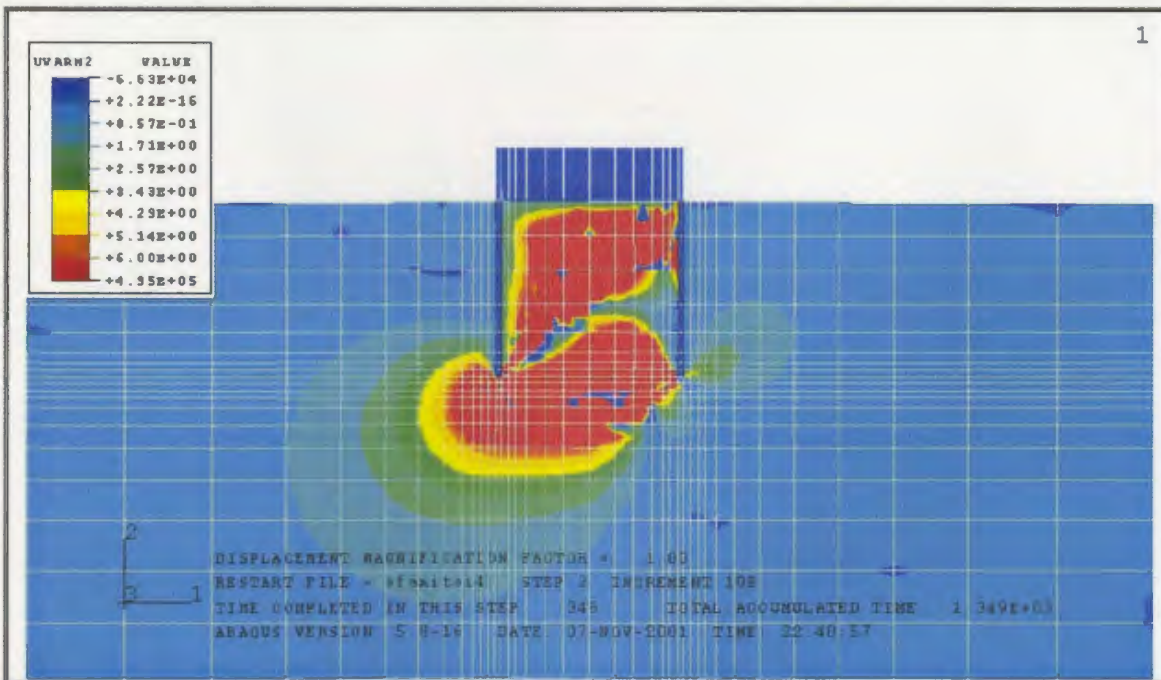


Figure 7.3.6 Contour of ratio of shear stress to shear strength based on TE test of pullout with inclined angle of 60° and anchor point at 0.02 m below the soil surface.

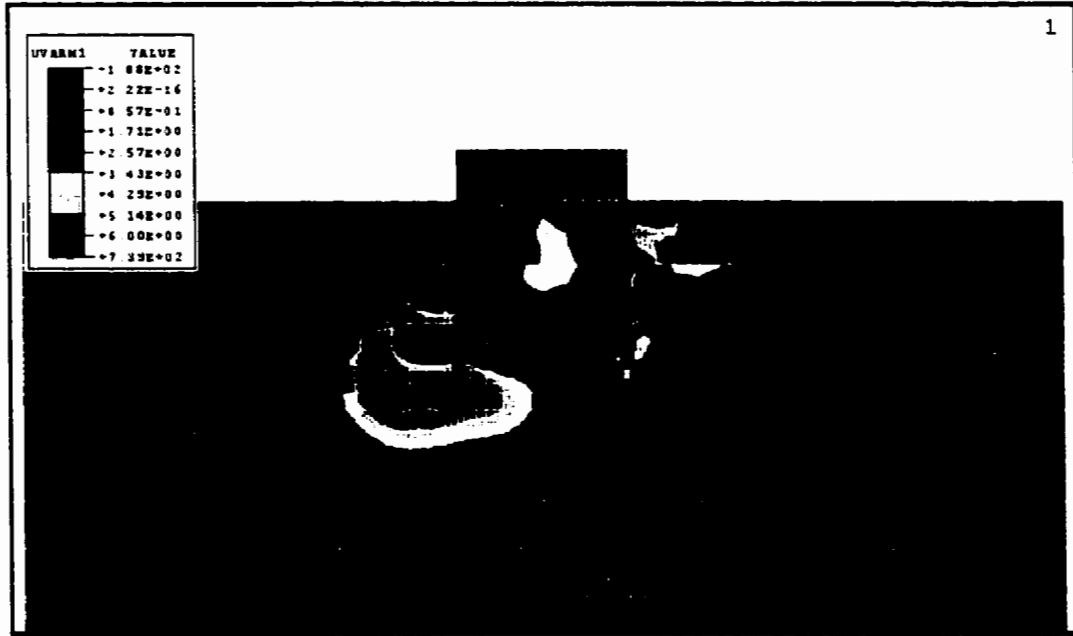


Figure 7.3.7 Contour of ratio of shear stress to shear strength based on DSS test of pullout with inclined angle of 5° and anchor point at 0.025 m below the soil surface.

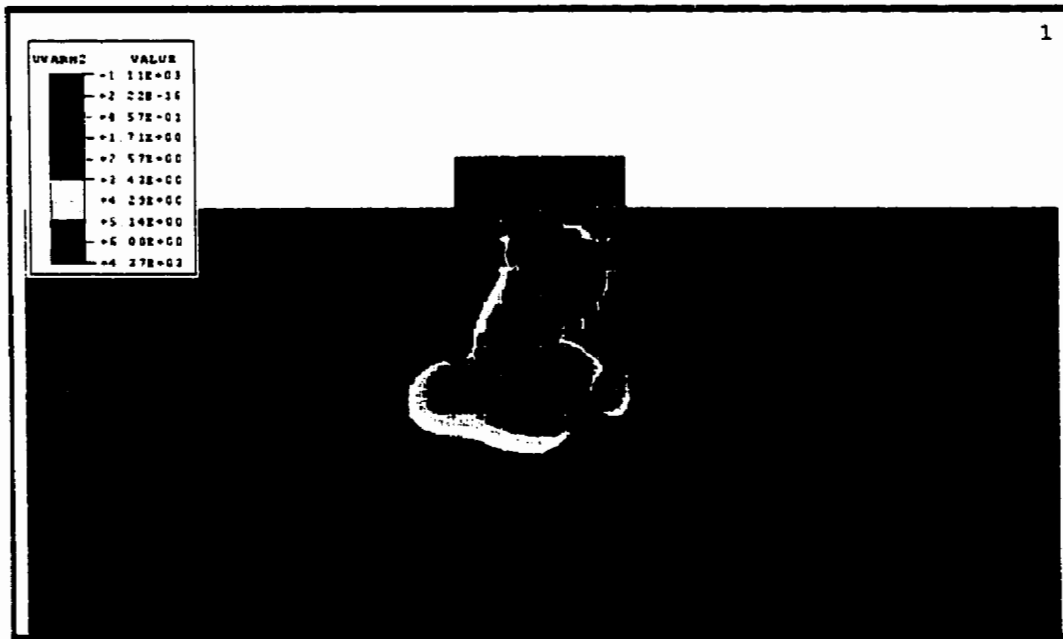


Figure 7.3.8 Contour of ratio of shear stress to shear strength based on TE test of pullout with inclined angle of 5° and anchor point at 0.025 m below the soil surface.

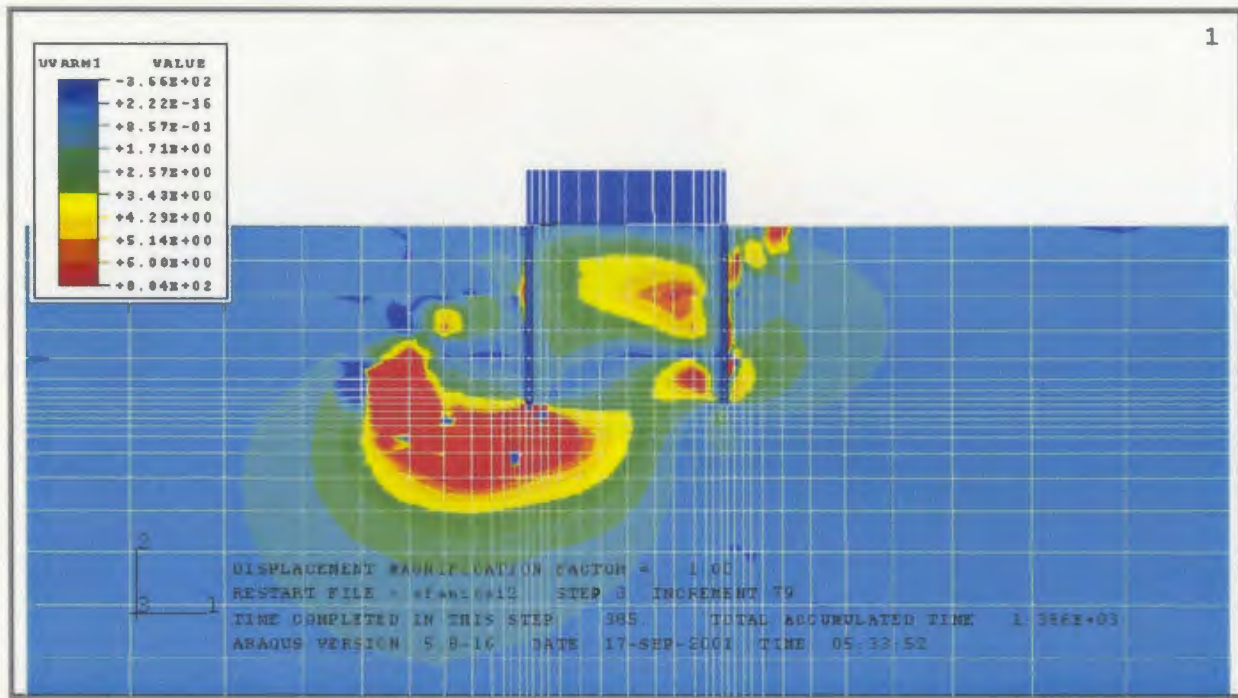


Figure 7.3.9 Contour of ratio of shear stress to shear strength based on DSS test of pullout with inclined angle of 20° and anchor point at 0.025 m below the soil surface.

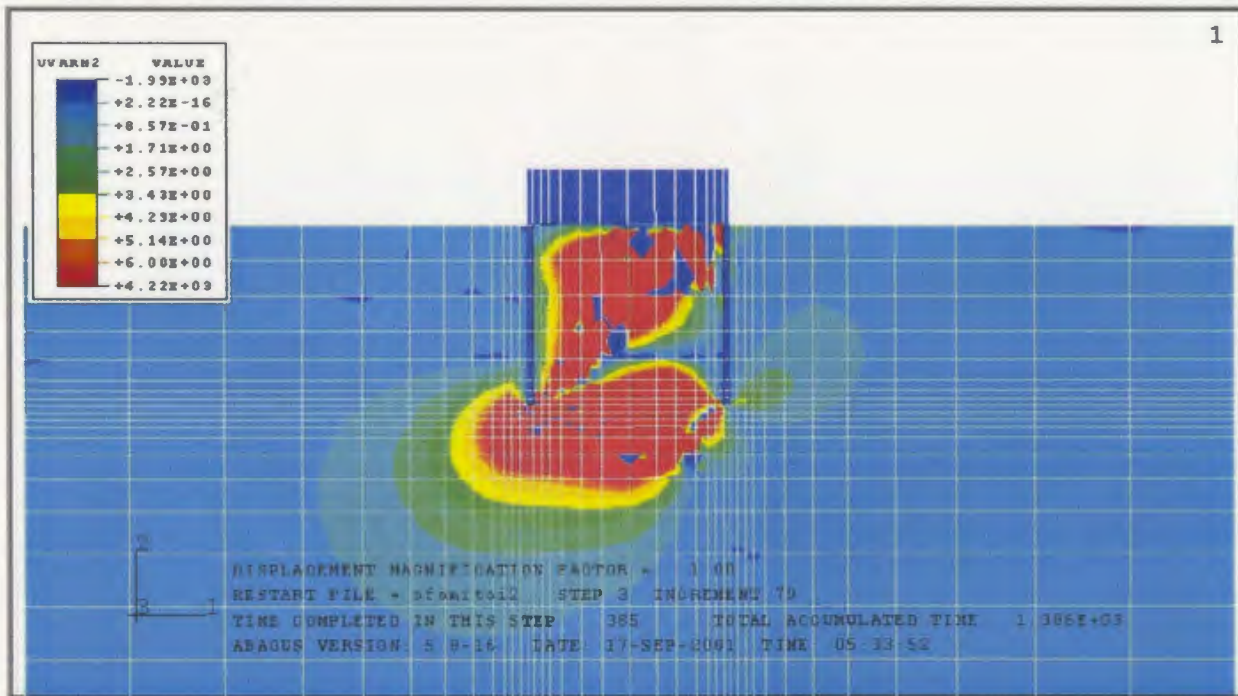


Figure 7.3.10 Contour of ratio of shear stress to shear strength based on TE test of pullout with inclined angle of 20° and anchor point at 0.025 m below the soil surface.

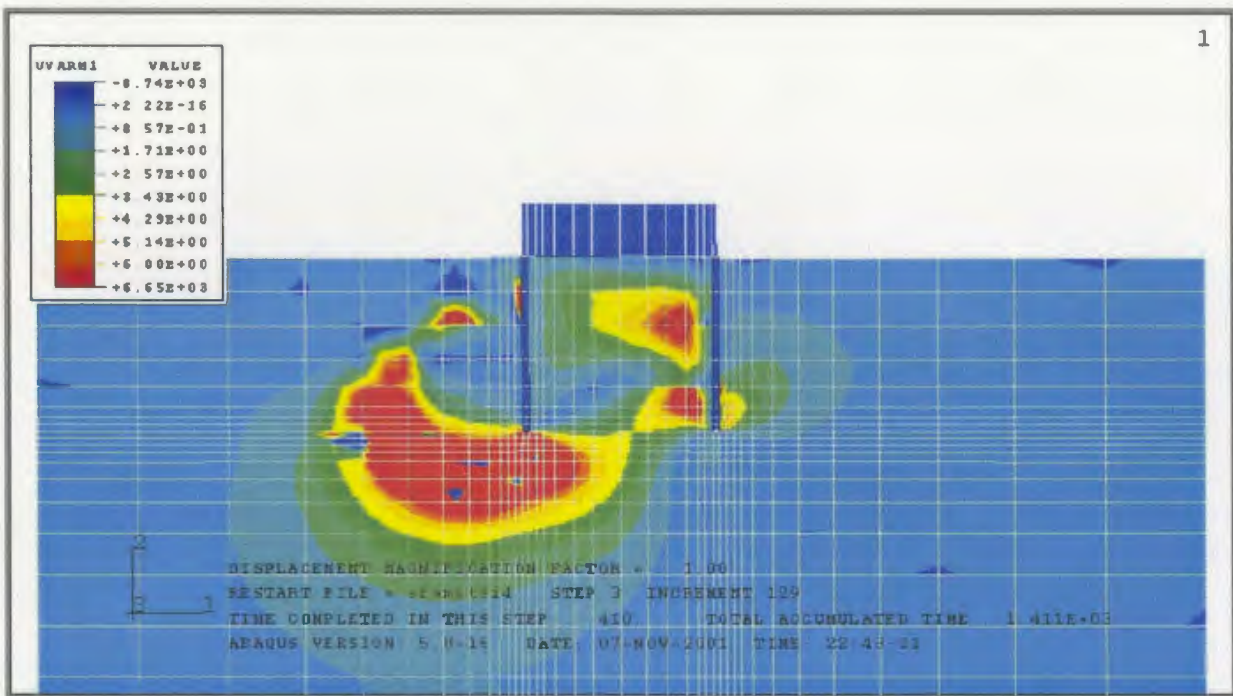


Figure 7.3.11 Contour of ratio of shear stress to shear strength based on DSS test of pullout with inclined angle of 60° and anchor point at 0.025 m below the soil surface.

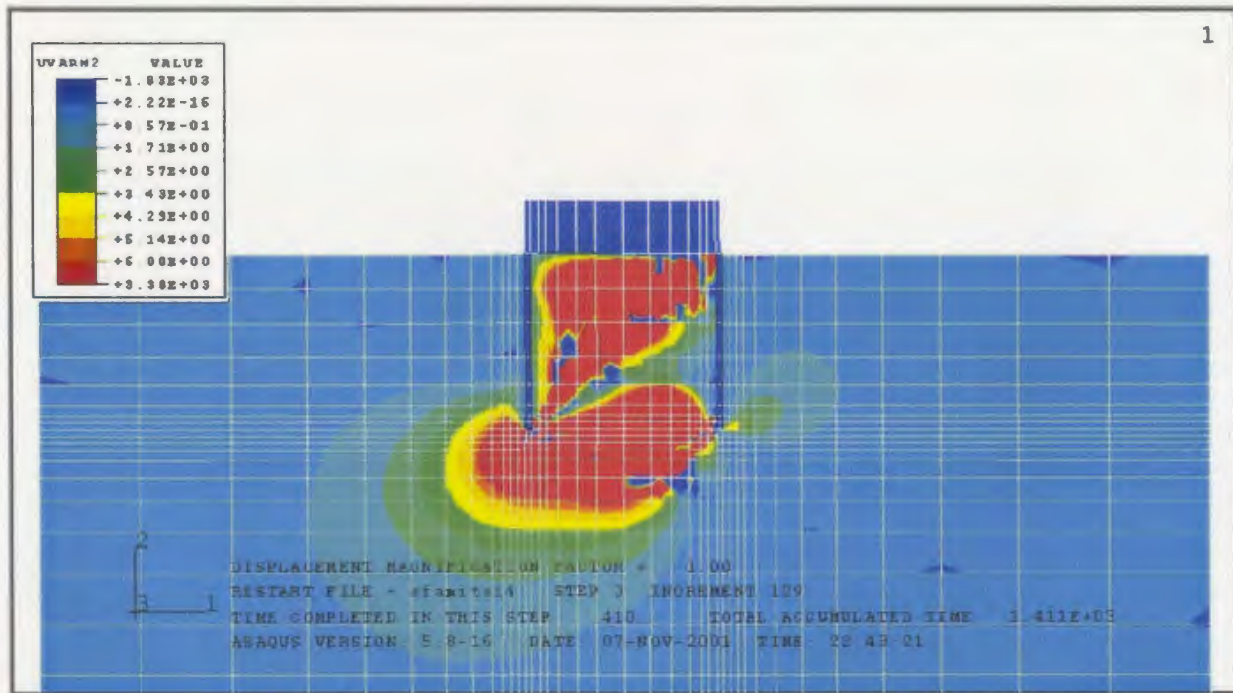


Figure 7.3.12 Contour of ratio of shear stress to shear strength based on TE test of pullout with inclined angle of 60° and anchor point at 0.025 m below the soil surface.

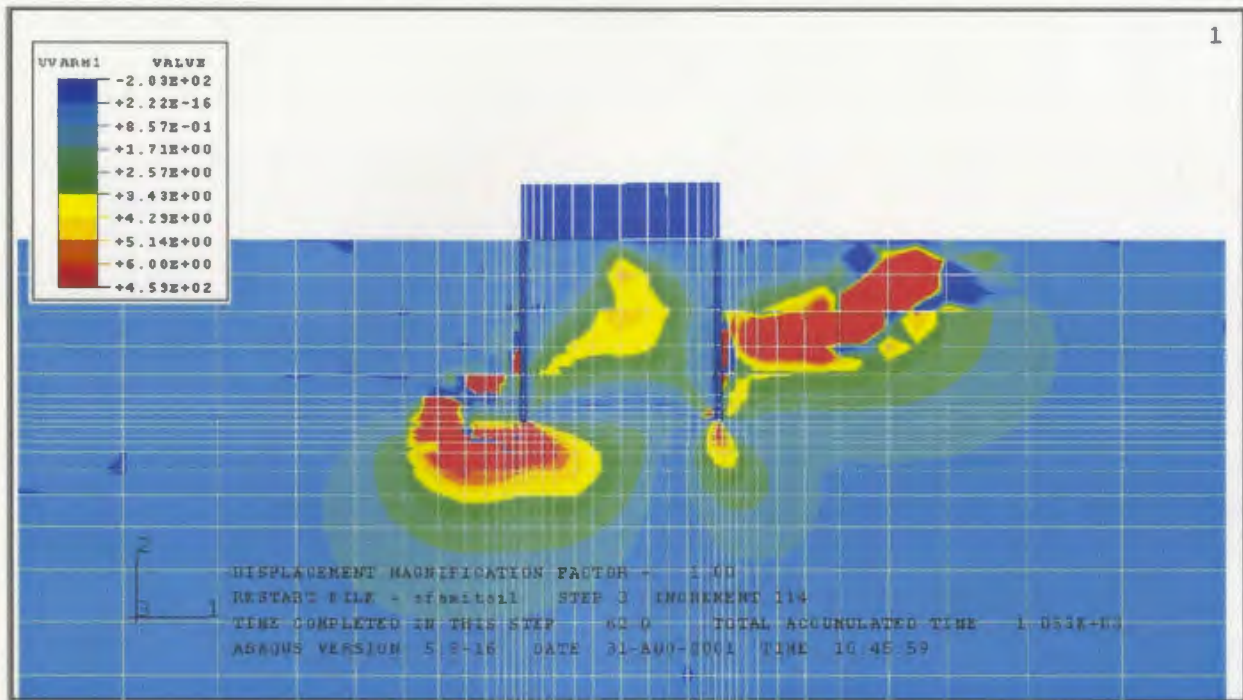


Figure 7.3.13 Contour of ratio of shear stress to shear strength based on DSS test of pullout with inclined angle of 5° and anchor point at 0.038 m below the soil surface.

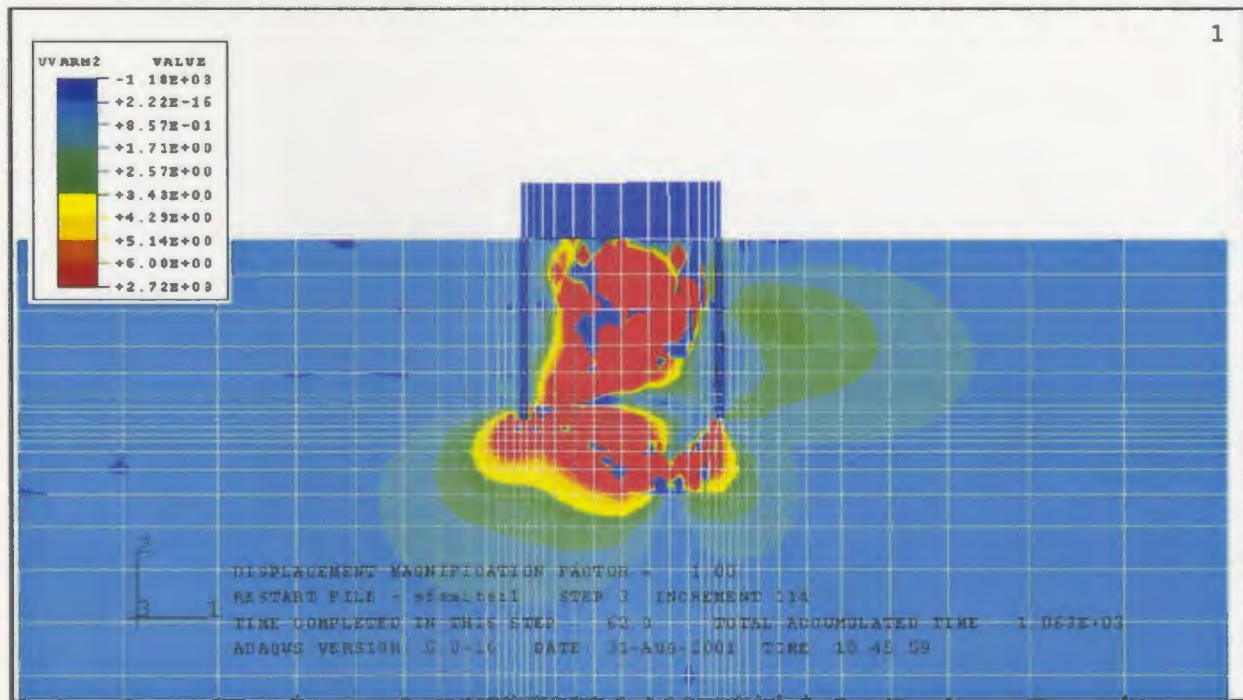


Figure 7.3.14 Contour of ratio of shear stress to shear strength based on TE test of pullout with inclined angle of 5° and anchor point at 0.038 m below the soil surface.

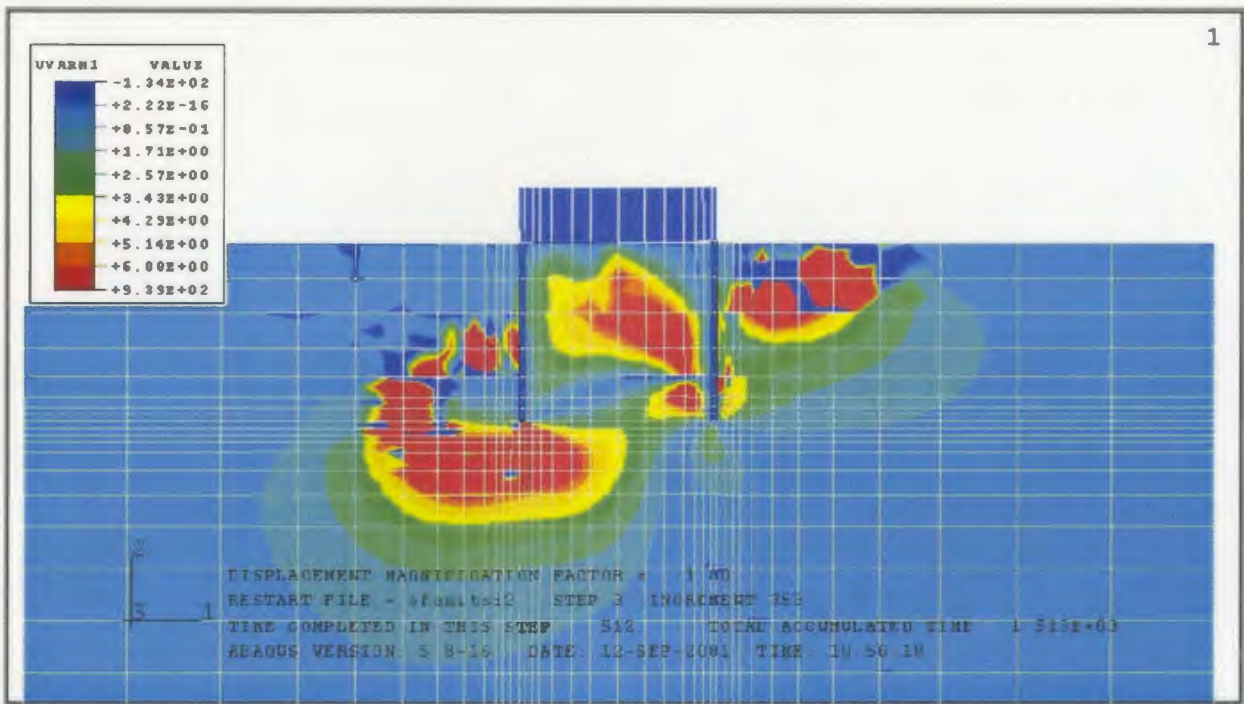


Figure 7.3.15 Contour of ratio of shear stress to shear strength based on DSS test of pullout with inclined angle of 20° and anchor point at 0.038 m below the soil surface.

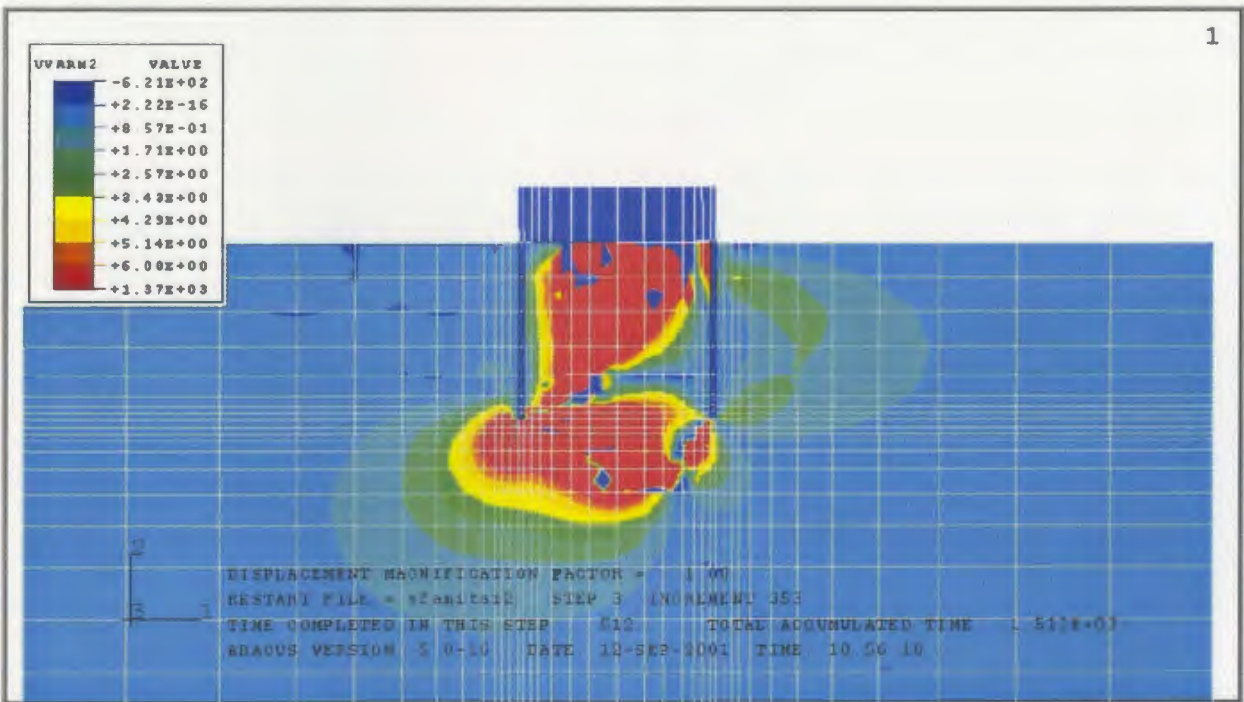


Figure 7.3.16 Contour of ratio of shear stress to shear strength based on TE test of pullout with inclined angle of 20° and anchor point at 0.038 m below the soil surface.

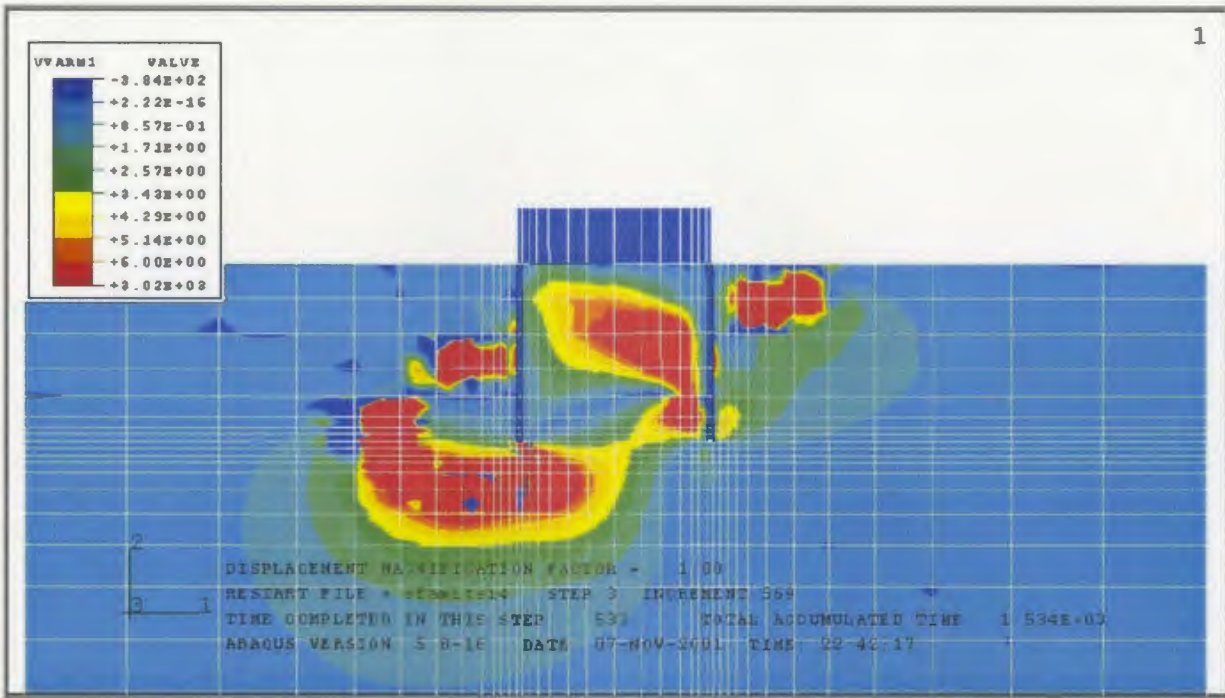


Figure 7.3.17 Contour of ratio of shear stress to shear strength based on DSS test of pullout with inclined angle of 60° and anchor point at 0.038 m below the soil surface.

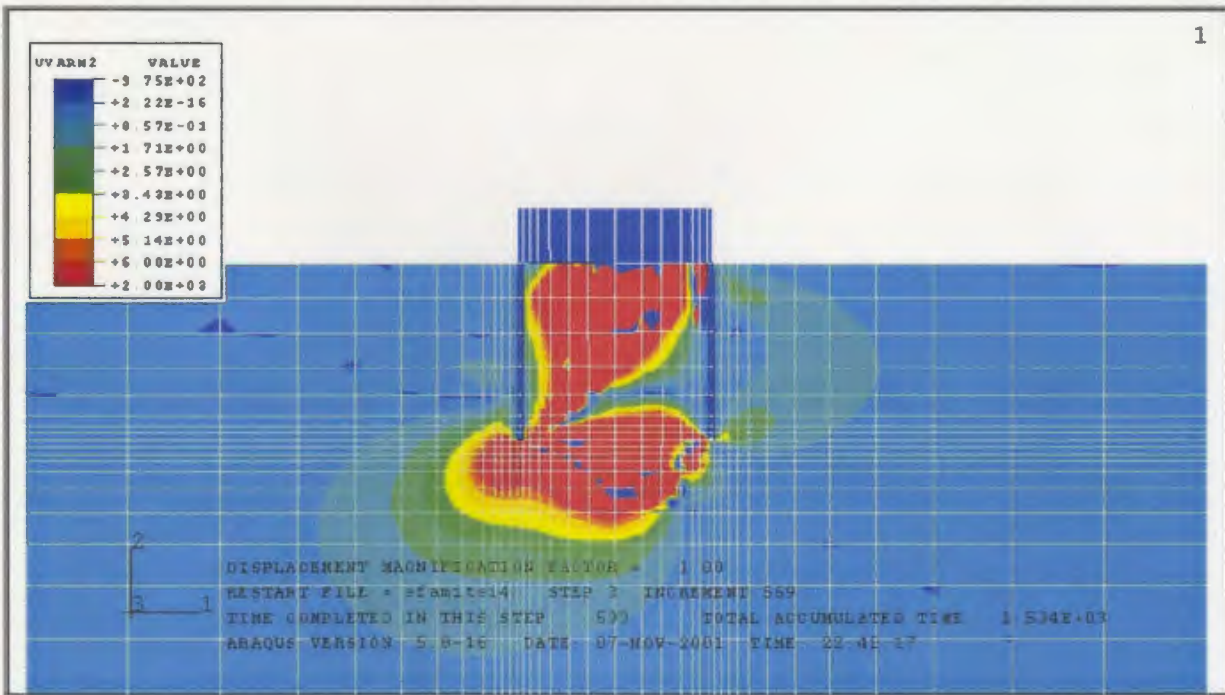


Figure 7.3.18 Contour of ratio of shear stress to shear strength based on TE test of pullout with inclined angle of 60° and anchor point at 0.038 m below the soil surface.

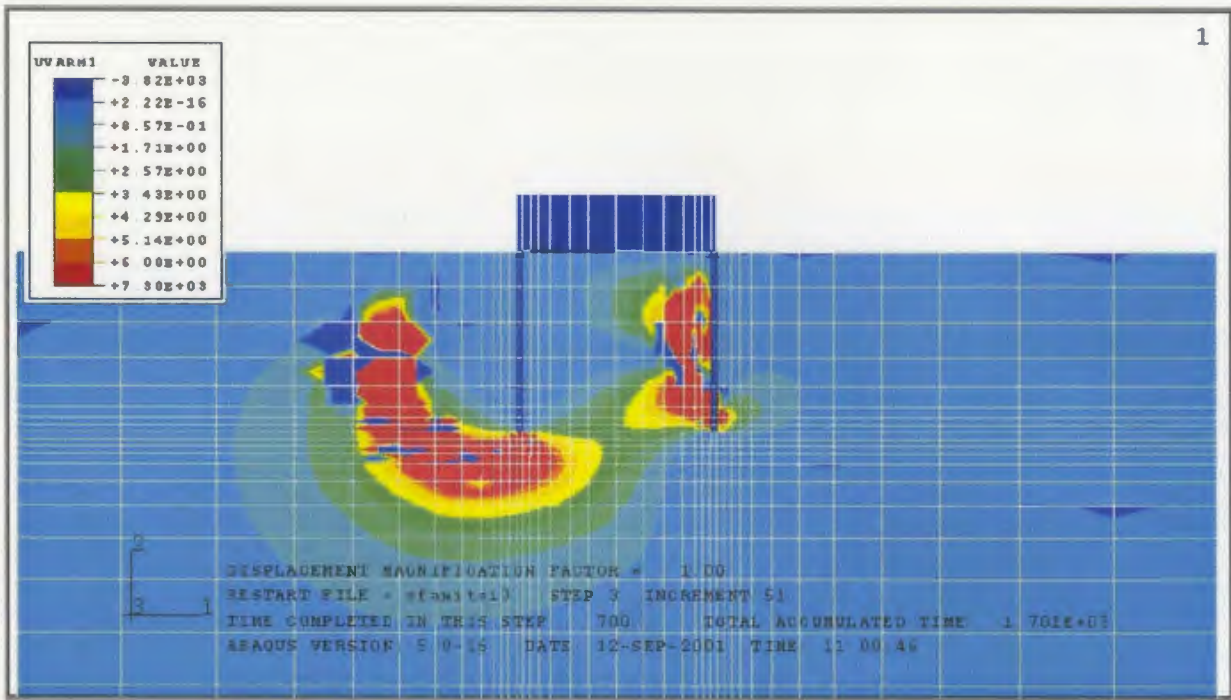


Figure 7.3.19 Contour of ratio of shear stress to shear strength based on DSS test of pullout with inclined angle of 90° and anchor point at 0.038 m below the soil surface.

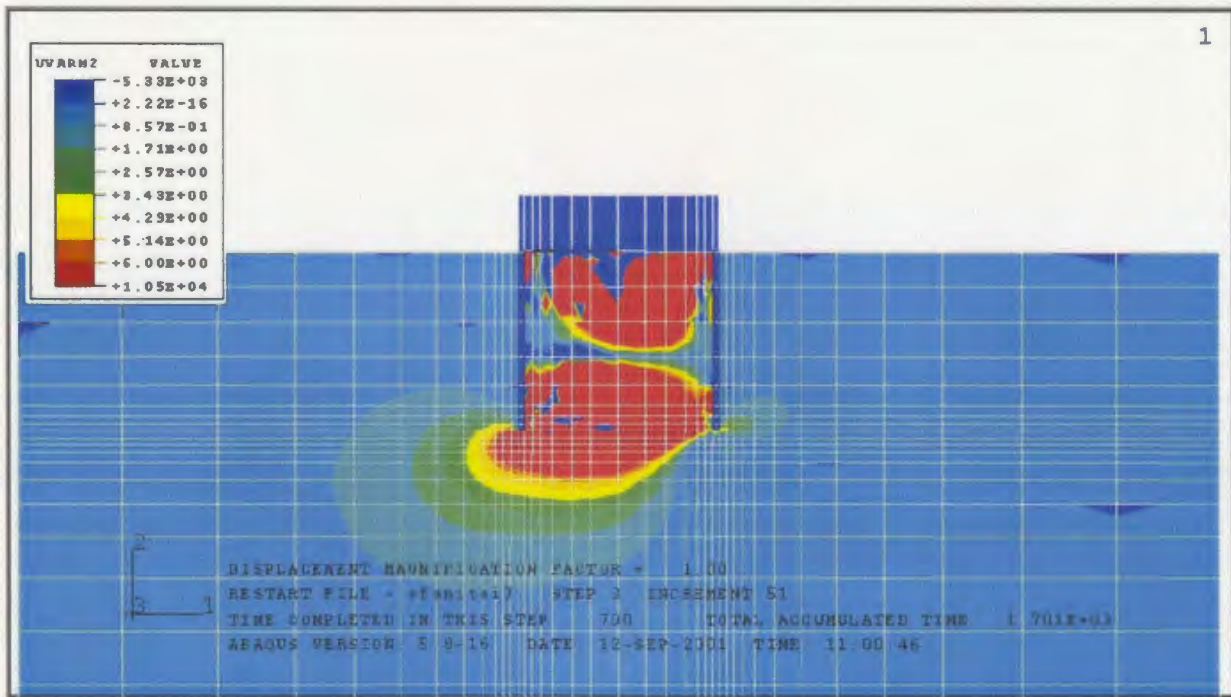


Figure 7.3.20 Contour of ratio of shear stress to shear strength based on TE test of pullout with inclined angle of 90° and anchor point at 0.038 m below the soil surface.

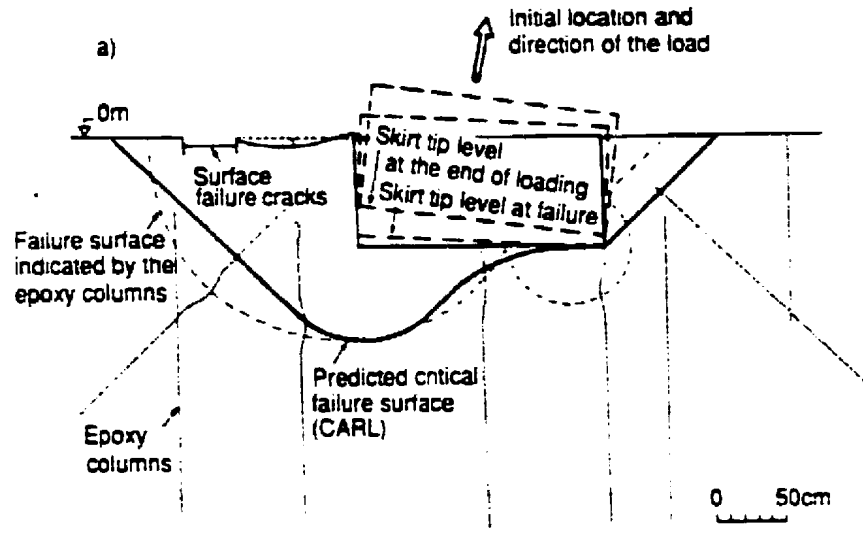


Figure 7.3.21 Failure surface of Snorre suction caisson [Andersen et al, 1993]

7.4. Summary

From the analyses presented in this chapter, the results can be summarised as in the following:

- i) The results gave correct trends for load-displacement curves with respect to the angle of pullout.
- ii) The inclined pullout model gave higher resistance than the vertical pullout model due to increased friction along walls of suction caisson. However, the percentage of suction force generated for the case of inclined pullout loads was less than that for vertical pullout loads due to increased shear deformation that occurred on the sides of the wall; thus its contribution to total resistance capacity was reduced. On the other hand, the suction force or the negative

pore pressure generated in soil body seems to give an increased contribution to soil stress, normal to the suction caisson wall, thus increasing wall shear force resistance capacity.

- iii) The failure of suction caisson seems to be governed by the reverse slope stability conditions at the back of the suction caisson and by tensile failure at the bottom of the caisson.
- iv) The combined contours of shear stress to shear strength ratio based on direct shear and triaxial extension tests, gave failure surfaces, in general, similar to the failure surfaces obtained for the Snorre suction caisson model test carried out by the Norwegian Geotechnical Institute.

Chapter 8 Conclusions and Recommendations

8.1 Overview of study

This chapter discuss the results presented in this thesis for suction caisson analysis using the ABAQUS general finite element program. Furthermore, it also presents recommendations for future work in this area. As mentioned in Chapter 1, the purpose of this work was to simulate the behaviour of suction caisson foundations including the suction pressure generation due to vertical and inclined pullout loads, and to correlate the numerical results with laboratory test results. Moreover, the failure behaviour within the soil medium was also examined and characterized.

The study used four laboratory tests carried out in different institutions, with different purposes, and different experimental set-ups. The test data used are the MIT suction caisson tests [Cauble, 1997], University of Texas at Austin suction caisson tests [El-Gharbawy, 1998], IIT Madras India friction single pile tests [Prasad, 1992], and suction caisson tests [Rao et al, 1997].

MIT tests used a special integrated apparatus that carried out pre-consolidation process, and pullout tests of suction caisson. The suction caisson model used was made of acrylic material with an outer diameter of 0.0508 m and of thickness $t_w = 0.00145$ m with a length to diameter ratio of one. Soil material used was Resedimented Boston Blue Clay (RBBC). The clay sample, into which the caisson penetrated during earlier penetration study, had a diameter of 0.305 m (the size of the test enclosure) and a pre-installation

sample height that ranged from $H_c = 0.121$ to 0.143 m with an average $H_c = 0.132$ m. A pre-compression load of 73.35 kPa (0.75 kgf/cm²) was applied with the caisson wall upper end flush with the caisson cap at the surface of the clay. The pullout tests applied different scenarios of pullout (displacement) length and waiting period, using pullout rates varying from 0.0003 m/min and 0.003 m/min. Six usable model tests were selected from this study for numerical simulation.

The University of Texas at Austin tests used suction caisson models made of acrylic material (for $L/D = 2, 4,$ and 6), and steel tubing (for $L/D = 12$). Diameters of suction caisson models were 0.1016 m (4 in) for $L/D = 2, 4,$ and 6 , and 0.0508 m (2 in) for $L/D = 12$. Model caissons had a wall diameter-to- thickness ratio (D/t) = 32 and were fitted with caisson caps. The soil sample was accommodated in a tank of approximately 0.762 m height and 0.762 m diameter. The pullout scenarios consisted of two different cases, viz., undrained pullout tests with a pullout rate of 0.0254 to 0.0508 m/sec, and drained pullout tests with a pullout loading scheme of 11.12 N to 22.24 N (per load increment) with a sustained wait of 2.5 to 3 hours.

IIT Madras India tests, on friction single piles used steel tubes (with open top) of two different diameters, viz., 0.0138 m with 0.0015 m thickness, and 0.018 m with 0.002 m thickness. Three different length-to-diameter ratios were used in the tests, viz., $L/D = 15, 25,$ and 40 , for each diameter, that gave six models to be simulated in this study. The test load was applied through the use of a strain controlled static pullout equipment. The soil used for tests was from the coastal deposits in the east coast of India. Two types of soil samples were used in the tests, and designated as soil 1 and soil 2. The pullout load

was applied on an anchor at a constant rate of 0.004 m per minute using a hydraulic jack. In this test phase, each test was continued beyond a peak failure load until noticeable failure behaviour was obtained.

IIT Madras India tests on suction caissons used steel tubes having 0.075 m diameter and 0.003 m wall thickness. The length to diameter ratio (L/D) was selected as 1.0, 1.5, and 2.0. Soil type used was a typical marine clay obtained from the coastal deposits available on the east coast of India. Three soil types were chosen for the investigation to take into account the different consistency of the soil used, giving a total of nine analyses to be carried out in this study. The tests were conducted in a cylindrical test tank of 0.75 m diameter and 0.9 m height. The pullout load was applied in increments by placing weights on the load hanger attached to the other end of the wire rope. A flexible wire rope was connected to the centre of the anchor top and then passed over a pulley arrangement in the loading frame.

Approaches for finite element analyses included application of suction force generation, based on D'Arcy's law, by implementing some user subroutines provided in ABAQUS. The application of equivalent uniformly distributed loads, to represent the average soil strength characteristics was used in the equivalent numerical models. Also, all special treatment procedures implemented during the preparation of soil sample in laboratory tests (such as waiting period, sustained wait, etc.) were simulated in the finite element analyses as close as possible by means of proper modelling procedures. Contact between suction caisson and soil surface was simulated using contact surface model. Soil material was represented as a porous medium (capable of simulating development of

internal pore pressures) and its plastic behaviour was defined using modified camclay model. Elements used in all the MIT, University of Texas, and IIT Madras tests, as well as 1g, ng, and prototype models were 8-noded isoparametric axisymmetric finite elements. However in scale model analyses the number of elements, as well as the mesh used, were the same between small scale (1g, and ng model) and prototype models, but the element size was increased several times using the scaling factor. Three-dimensional models used 20-noded solid cubic elements, with pore pressure degree of freedom on the corner nodes, for soil and no pore pressure degree of freedom for caisson. The finite element model for inclined pullout loads used 8-noded quadrilateral axisymmetric elements with asymmetric load capability, with pore pressure degree of freedom on their corner nodes for soil, and no pore pressure degree of freedom for caisson. Failure characteristics, used to determine a failure occurrence, were determined by shear stress to shear strength ratio contours of both direct simple shear tests (DSS) and triaxial extension (TE) tests, in a combined manner. Inclined pullout results were verified with the analytical formulations of Brom and Das.

8.2 Findings and Conclusions

1. Application of D'Arcy's law for fluid flow in porous medium is suitable for simulating suction pressure generation in suction caisson models. This can be seen from results of finite element analyses for MIT tests. The suction force-displacement curves (obtained with the numerical procedure developed in this thesis), for all models with different loading scenarios, were within an acceptable range of expected results defined from the MIT laboratory tests.

Also the total force-displacement curve and wall force-displacement curve met the range of upper and lower bounds obtained from the MIT laboratory tests for each component of forces (total force and wall force).

2. The generation of suction pressures (inside the caisson) increases the pore pressure difference in the area surrounding the suction caisson tip, between inside and outside wall, thus increasing the friction stress, and the total wall force resistance.
3. The suction pressure magnitudes, obtained based on the suction pressure generation approach developed in this thesis, consistently gave very close matches with results from laboratory tests of University of Texas at Austin. However, the total force-displacement curves showed a stiffer response of the finite element model compared to the laboratory results. The difference in force–displacement curves between laboratory test and finite element analysis results could be attributed to constitutive equations used for both contact surface and soil plasticity. However, the major factor seems to come from contact constitutive equation that needs to be improved to get better results.
4. Suction pressure-displacement curves obtained from finite element analysis for IIT Madras tests on suction caissons, also gave a good match with results obtained from laboratory tests. Very good matches with experimental results, for suction pressures, were obtained during the earlier part of pullout up to a certain length. The maximum suction pressures developed in finite element analyses were lower than the results obtained from laboratory tests.

5. Christensen's formulation very closely approximates the failure modes and ultimate loads of suction foundation for the MIT test cases; however, it does not accurately predict ultimate pullout capacity for neither the Texas nor the IIT Madras tests. Christensen's formulation also would require input of actual suction pressures developed inside the caisson to get good correlation with test results.
6. Application of different pullout speeds affected the total system responses. This can be seen from the scale model-prototype analyses, which gave consistent results within the expected ranges for 1g, ng, and prototype suction caissons. From the analyses of scale models, it was found that the suction pressure generation depended very much on the presence of a uniformly distributed load on the soil surface to give results comparable with experiments.
7. From scale model analysis, it is seen that 1g model can approximately simulate prototype force-displacement behaviour by applying a distributed load having a magnitude equal to the overburden stress of soil at half the height of the suction foundation.
8. From the analysis of the results of various models, it is seen that the soil stress state is properly modelled by an ng model rather than by 1g model. The error observed in suction force for ng model in this study is within 35% of the expected suction force generation (using model-prototype relationships).

9. The suction pressure development inside the caisson during pullout, was approximately modelled by the procedure developed in this thesis, giving results within 35% of expected values. It appears that 1g model tests give better suction pressure representation than ng model tests, primarily due to the conflict that arises in ng models between dynamic scaling and diffusion scaling criteria.
10. The results from 3D models gave smaller suction force than results of axisymmetric model, and the wall force of the 3D model was larger than the wall force generated by the axisymmetric model. This condition was caused by the stiffer wall resistance generated in the 3D models which restricted the slip occurring during pullout; hence 3D models gave less suction forces. However, the axisymmetric models showed a flexible wall resistance, which allowed greater slip rate to occur during pullout; hence it gave higher suction forces. This could have been avoided by the provision of a facility for including more harmonics during the Fourier series analysis in ABAQUS.
11. Differences in suction pressure generation occurred on comparison of three-dimensional model results with axisymmetric-asymmetric finite element analysis models. The condition might have been caused by the stiffness of the three-dimensional model due to the coarseness of the element mesh used, which reduces the slip occurrence in the three-dimensional models; this consequently reduces the suction force generation. In addition the non-

availability of higher order harmonics, for axisymmetric-asymmetric analysis, also could have contributed to this difference.

12. Axisymmetric-asymmetric analyses for inclined pullout gave results that matched reasonably well with those given earlier by Das and Brom.
13. Failure mode analyses gave fairly reasonable results as seen in MIT test based models for different length to diameter ratios. Reasonably good results were also obtained for suction caisson models subjected to inclined pullout loads.
14. The combined contours of shear stress to shear strength ratio based on direct shear and triaxial extension tests, gave failure surfaces, in general, similar to the failure surfaces obtained for Snorre suction caisson model tests carried out by the Norwegian Geotechnical Institute.

8.3 Recommendations for future work

Some areas for future work, for extending the study reported in this thesis, are suggested below:

1. Further study is needed on numerical modeling for scaled models as indicated in Chapter 5, with support data from laboratory (model) and field (intermediate and prototype) tests. The study should also include the improvements to suction force generation developed in this thesis, due to different gravitational and scale effect environments, as well as further observations on effect of mesh size due to application of the scale factor.

2. A further study is possible regarding failure surface or failure mode analysis especially for suction caissons using the approach given in Chapter 5, and using adaptive mesh approach [Zienkiewicz and Huang, 1995] implementing ALE (Arbitrary Lagrangian-Eulerian) finite element analysis to represent strain localization in transient problems. This is available as a new feature of ABAQUS 6.2 (and above) [HKS, 2001] and MSC MARCHENTAT 2001 [MSC, 2001], with some full sets of laboratory test results to verify the accuracy of numerical results.
3. Further studies involving the effect of inclined pullout loads on suction caisson behaviour, which can be compared with some test data from laboratory test results, to verify the correctness of suction force development.
4. Further studies could also address to suction force generation for coarse-grained soil, like sand, with support from laboratory test results.

References

- Aboim, C.A., and Roth, W.H. (1982). "Bounding-Surface Theory Applied to Cyclic Loading of Sands", *International Symposium of Numerical Models in Geomechanics*, Balkema Publication, pp. 65-80.
- Adachi, T., Oka, F., and Mimura, M. (1987). "Mathematical Structure of an Overstress Elasto-viscoplastic Model for Clay", *Soils and Foundations*, Vol.27, #3, pp. 31-42.
- Albertsen, N.D., and Beard, R.M. (1982). "State of the Art Assessment of High Capacity Sea Floor Anchors", *Offshore Moorings*, ICE, Thomas Telford LTD., London, pp. 129-142.
- Alhayari, S. (1998). "Innovative Developments in Suction Pile Technology", *Offshore Technology Conference*, Vol.1, Houston, Texas, Paper 8836, pp. 551-558.
- Amarasinghe, S.F., and Parry, H.G. (1975). "Anisotropy in Heavily Overconsolidated Kaolin", *Journal of Geotechnical Engineering Division*, ASCE, Vol.101, #GT12, pp. 1277-1293.
- American Petroleum Institute (1987). "API Recommended Practice for Planning, Designing, and Constructing Fixed Offshore Platforms", *API Production Division*.
- American Petroleum Institute (1992). "API Recommended Practice for Planning, Designing, and Constructing Fixed Offshore Platforms, RP2A", *API Production Division*, 211 North Ervay, Suite 1700, Dallas, TX 75201.
- Anandarajah, A., and Dafalias, Y.F., (1986). "Bounding Surface Plasticity. III: Application of Anisotropic Cohesive Soils", *Journal of Engineering Mechanics*, ASCE, Vol.112, #12, pp. 1292-1318.
- Andersen, K.H., Dyvik, R., Lauritzsen, R., Heien, Dag, and Hårvik, Linda (1989). "Model Tests of Gravity Platforms. II: Interpretation", *Journal of Geotechnical Engineering*, Vol.115, #11, ASCE, pp. 1550-1568.
- Andersen, K.H., Dyvik, R., and Schrøder, K. (1992). "Pull-Out Capacity Analyses of Suction Anchors for Tension Leg Platforms", *Conference on Behaviour of Offshore Structures*, Vol. I, pp. 1311-1322.

- Andersen, K.H., Dyvik, R., Schröder, K., Hansteen, Ole E., and Bysveen, Steinar (1993). "Field Tests of Anchors in Clay. II: Prediction and interpretation", *Journal of Geotechnical Engineering*, Vol.119, #10, ASCE, pp. 1532-1549.
- Andersen, J.M., and Myers, W.M. (1995). "Proceedings of The Workshop on Effects of Piles on Soil Properties", *US Army Corps of Engineers, Waterways Experiment Station, Vicksburg, VA. Appendix C.*
- Andersen, K.H., and Jostad, H.P (1999). "Foundation Design Of Skirted Foundations And Anchors in Clay", *Offshore Technology Conference*, Vol.1, Houston, Texas. Paper 10824, pp. 383-392.
- Andréasson, Bo, Christophersen, H.P., and Kvalstad, T.J. (1988). "Field Model Tests and Analyses of Suction Installed Long-Skirted Foundations", *Conference on Behaviour of Offshore Structures*, Vol. I, pp. 243-257.
- Bailey, W.A. (1961). "Effects of Salt on The Shear Strength of Boston Blue Clay", BS Thesis. Department of Civil Engineering, MIT, Cambridge, MA.
- Baker, R., Frydman, S., and Galil, J. (1982), " A Plasticity Model for Load Unload Behaviour of Sand", *Application of Plasticity and Generalized Stress-strain in Geotechnical Engineering*, Young, R.N. and Selig, E.T. (Eds.), the American Society of Civil Engineers, pp. 25-52.
- Bardet, J.P., (1986). "A Bounding Surface Model for Sands", *Journal of Engineering Mechanics*, ASCE, Vol.116, #9, pp. 1973-1994.
- Bardet, J.P. (1990), "Hypoplastic Model for Sands", *Journal of Engineering Mechanics*, ASCE, Vol.112, #11, pp. 1198-1216.
- Bardet, J.P. (1995a), "Scaled Memory Model for Undrained Behavior of Anisotropic Clays", *Journal of Geotechnical Engineering*, ASCE, Vol.121, #11, pp. 755-765.
- Bardet, J.P. (1995b). "Scaled Memory Model for Cyclic Behavior of Soil", *Journal of Geotechnical Engineering*, ASCE, Vol.121, #11, pp. 766-775.
- Bardet, J.P. (1996). "Scaled Memory Description of Hysteretic Material Behavior", *Journal of Applied Mechanics*, ASME, Vol.63, pp. 750-757.
- Bazant, Z.P., and Krizek, R.J. (1976). "Endochronic Constitutive Law for Liquefaction of Sand", *Journal of Engineering Mechanics Division*, ASCE, Vol.102, #EM2, pp. 225-299.

- Bensari, J.E. (1984). "Stress-strain Characteristics from Undrained and Drained Triaxial Tests on Resedimented Boston Blue Clay", MS Thesis, Department of Civil Engineering, MIT, Cambridge, MA.
- Biot, M.A. (1941). "General Theory of Three Dimensional Consolidation", *Journal of Applied Physics*, 12, pp. 155-164.
- Biot, M.A. (1955). "Theory of Elasticity and Consolidation for a Porous Anisotropic Solid", *Journal of Applied physics*, Vol.26, pp. 182-185.
- Biot, M.A. (1956). "Theory of propagation of Elastic Waves in a Fluid Saturated Porous Solid, I. Low Frequency Range", *Journal of the Acoustical Society of America*, Vol.28, pp. 168-178.
- Biot, M.A. (1957). "The Elastic Coefficients of a Theory of Consolidation", *Journal of Applied Mechanics*, ASME, Vol.79, pp. 594-601.
- Biot, M.A. (1962). "Mechanics of Deformation and Acoustic Propagation in Porous Media", *Journal of Applied Physics*, Vol.33, #4, pp. 1482-1498.
- Biot, M.A. (1972). "Theory of Finite Deformations of Porous Solids", *Indiana University Mathematics Journal*, Vol.21, #7, pp. 597-620.
- Biot, M.A. (1977). "Variational Langragian Thermodynamics of Non-Isothermal Finite Strain Mechanics of Porous Solids and Thermomolecular Diffusion", *International Journal of Solids and Structures*, ASCE, Vol.13, pp. 579-597.
- Biot, M.A. (1978). "Variational Langrangian Thermadynamics of Heat and Mass Transfer in Porous Solids: New Concept and Methods", *Quarterly of Applied Mathematics*, Vol.36, pp. 19-38.
- Bishop, A.W. (1966). "The Strength of Soils as Engineering Materials", *Géotechnique*, Vol.16, pp. 91-128.
- Borja, R.I., Hsieh, H.S., and Kavazanjian Jr., E. (1990). "Double-Yield-Surface Cam-Clay Plasticity Model. II: Implementation and Verification", *Journal of Geotechnical Engineering*, ASCE, Vol.116, #9, pp. 1402-1421.
- Bowen, R.M. (1982). "Compressible Porous Media Models by Use of the Theory of Mixtures", *International Journal of Engineering Science*, Vol.20, #6, pp. 697-735.
- Bowles, J.E. (1996). *Foundation Analysis and Design*, 5th Ed., McGraw-Hill Co., p.1175.

- Braathen, N-F (1966). "Investigation of Effects of Disturbance on Undrained Shear Strength of Boston Blue Clay", MS Thesis, MIT, Cambridge, MA.
- Brinch Hansen (1961). "The Ultimate Resistance of Rigid Piles Against Transversal Forces", *Geoteknisk Institut Bulletin* #12.
- Broms, B.B. (1964). "Lateral Resistance of Piles in Cohesionless Soils", *Journal of the Soil Mechanics and Foundation Division*, #SM3, ASCE.
- Brown, George. A., and Nacci, Vita A. (1971). "Performance of Hydrostatic Anchors in Granular Soils". *Offshore Technology Conference*, OTC1472, pp. 533-542.
- Cauble, D.F., (1997). "An Experimental Investigation of The Behavior of A Model Suction Caisson in A cohesive Soil", *PhD thesis*, Massachusetts Institute of Technology (MIT).
- Cheng, Y.M., and Tsui, Y., 1992, "Limitations to the Large Strain Theory", *International Journal for Numerical Methods in Engineering*, Vol. 33, pp. 101-114.
- Chohan, H.S., Sandhu, R.S., and Wolfe, W.E. (1991). "A Semi-discrete Procedure for Dynamic Response Analysis of Saturated Soils", *International Journal for Numerical and Analytical Methods in Geomechanics*, Vol.15, pp. 471-496.
- Crisfield, M.A. (1991). "Non-Linear Finite Element Analysis of Solids and Structures Vol.1", John Wiley & Sons.
- Christensen, N.H., Haahr, F., and Ramussen, J. Lorin (1991). "Breakout Resistance of Large Suction Piles", *OMAE*, Volume I-B, Offshore Technology ASME, pp. 617-622.
- Christensen, N.H. and Haahr, F. (1992). "A Computer Program To Analyze Suction Effects", *Offshore Technology Conference*, Vol.1, Houston, Texas, Paper 6845, pp. 331-338.
- Christian, J.T. (1968). "Undrained Stress Distribution by Numerical Method", *Proceeding, ASCE*, Vol.94, #SM6, pp. 1333-1345.
- Christophersen, H.P., Bysveen, S., and Støve, O.J. (1992). "Innovative Foundation Systems Selected for the Snorre Field Development", *Conference on Behaviour of Offshore Structures*, Vol. I, pp. 81-94.
- Clarke, J.I., and Guigné, J.Y. (1988). "Marine Geotechnical Engineering in Canada", *Canadian Geotechnical Journal*, Vol.25, pp. 179-198.

- Clauss, G., Lehmann, E., and Östergaard, C. (1992). *Offshore Structures – Conceptual Design and Hydromechanics*, Vol.1, Springer - Verlag.
- Clukey, E.C., and Morrison, M.J. (1993). "A Centrifuge And Analytical Study To Evaluate Suction Caissons For TLP Applications In The Gulf Of Mexico", *Geotechnical Special Publication #38*, ASCE, pp. 141-150.
- Clukey, E.C., Morrison, M.J., Garnier, J., and Corté, J.F. (1995). "The Response Of Suction Caissons In Normally Consolidated Clays To Cyclic TLP Loading Conditions", *Offshore Technology Conference*, Vol.1, Houston, Texas, Paper 7796, pp. 909-918.
- Colliat, J-L, Boisard, P., Andersen, K., and Schroeder, K. (1995). "Caisson Foundations As Alternative Anchors For Permanent Mooring Of A Process Barge Offshore Congo", *Offshore Technology Conference*, Vol.1, Houston, Texas, Paper 7797, pp. 919 - 929.
- Colliat, J.L., Boisard, P., Gramet, J-C., and Sparrevik, P. (1996). "Design and Installation of Suction Anchor Piles at a Soft Clay Site in the Gulf of Guinea", *Offshore Technology Conference*, Vol.1, Houston, Texas, Paper 8150, pp. 325-337.
- Colliat, J-L, Gramet, J-C, and Sparrevik, P. (1997). "Geotechnical Design And Installation Behaviour Of Suction Anchor Piles – Comparison With Drag Anchor ", *BOSS'97*, Vol.1, Pergamon.
- Crouch, R.S., and Wolf, J.P. (1994). "Unified 3D Critical State Bounding Surface Plasticity Model for Soils Incorporating Continuous Plastic Loading under Cyclic Paths", *International Journal for Numerical and Analytical Methods in Geomechanics*, Vol.18, pp. 735-784.
- Dafalias, Y.F., and Popov, E. (1975). "A Model of Nonlinearity Hardening Materials for Complex Loading", *Acta Mechanica*, Vol.21, #3, pp. 173-192.
- Dafalias, Y.F., and Popov, E.P. (1977). "Cyclic Loading for Materials with a Vanishing Elastic Domain", *Nuclear Engineering Design*, Vol.41, pp. 293-302.
- Dafalias, Y.F., and Herrmann, L.R. (1980). "A Bounding Surface Plasticity Model", *Proceeding of International Symposium of Soil under Cyclic Transient Load*, Swansea, A.A.Balkema Publication, Rotterdam, pp. 335-345.
- Dafalias, Y.F. (1986). "Bounding Surface Plasticity: Mathematical Foundation and Hypo-plasticity", *Journal of Engineering Mechanics*, ASCE, Vol.112, #9, pp. 966-987.
- Das, B. (1995). *Principles of Foundation Engineering*, 3rd Edition. PWS Publishing Co. p.821.

- Dickey, J.W. (1967). "A Plane Strain Shear Device for Testing Clays", MS Thesis, Department of Civil Engineering, MIT, Cambridge, MA.
- Drucker, D.C., Gibson, R.E., and Henkel, D.J. (1955). "Soil Mechanics and Work-hardening Theories of Plasticity", *Proceedings, ASCE*, Vol.81, pp. 1-14.
- Duncan, I.M., and Seed, H.B. (1966). "Anisotropy and Stress Reorientation in Clay", *Journal of Soil Mechanics and Foundation Division, ASCE*, Vol.92, #5, pp. 21-50.
- Dyvik, R., Andersen, K.H., Hansen, S.B., and Christophersen, H.P. (1993). "Field Tests of Anchors in Clay. I: Description", *Journal of Geotechnical Engineering*, Vol.119, #10, ASCE, pp. 1515-1531.
- Dyvik, R., Andersen, K.H., Madshus, C., and Amundsen, T. (1989). "Model Tests of Gravity Platforms. I: Description", *Journal of Geotechnical Engineering*, Vol.115, #11, ASCE, pp. 1532-1549.
- El-Gharbawy, S. L. (1998). "The Pullout Capacity of Suction Caisson Foundations", *PhD thesis*, University of Texas at Austin, Texas.
- El-Gharbawy, S.L., Iskander, M.G., and Olson, R.E. (1998). "Application of Suction Caisson Foundations in The Gulf of Mexico", *Offshore Technology Conference*, Vol.1, Houston Texas, Paper 8832, pp. 531-538.
- El-Gharbawy, S.L., Olson, R.E., and Scott, S.A. (1999). "Suction Anchor Installations For Deep Gulf Of Mexico Applications", *Offshore Technology Conference*, Vol.1, Houston Texas, Paper 10992, pp. 747-754.
- Erbrich, C.T., and Tjelta, T.I. (1999). "Installation Of Bucket Foundations And Caissons In Sand – Geotechnical Performance", *Offshore Technology Conference*, Vol.1, Houston Texas, Paper 10990, pp. 725-735.
- Eringen, A.C., and Ingram, J.D. (1965). "A Continuum Theory of Chemically Reacting Media (parts I and II)", *International Journal of Engineering Science*, Vol.3, pp. 197-212, and Vol.5, 1967, pp. 289-322.
- Fines, S., Støve, O.J., and Guldberg, F. (1991). "Snorre TLP Tethers and Foundation", *Offshore Technology Conference*, Vol.1, Houston, Texas. Paper 6623, pp. 587-597.
- Finn, W.D.Liam, and Byrne, P.M. (1972). "The Evaluation of the Break Out Force For a Submerged Ocean Platform", *Offshore Technology Conference*, Vol.1, Houston, Texas, Paper 1604, pp. 863-868.

- Florin, V.A. (1942). *Theory of Soil Consolidation* (in Russian), Stroyiziet, Moscow.
- Fuglsang, L.D., and Steesen-Bach, J.O. (1991). "Breakout Resistance of Suction Piles in Clay", *Centrifuge*, pp. 153-159.
- Gaboussi, J., and Momen, H. (1982). "Modeling and Analysis of Cyclic Behavior of Sand", *Soil Mechanics - Transient and Cyclic Loads*, John Wiley & Sons, New York, pp. 313-342.
- Green, A.E., and Naghdi, P.M. (1965). "A Dynamical Theory of Interacting Continua", *International Journal of Engineering Science*, Vol.3, pp. 231-241.
- Guha, Shib Nath (1978). "Breakout of Objects from Underconsolidated Sediments". *M.Eng Thesis*, Memorial University of Newfoundland, Canada.
- Hagen, D., Andenæs, E., and Korstad, G.M. (1998). "Innovative Suction Anchor Design And Installation", *Offshore Technology Conference*, Vol.1, Houston Texas, Paper 8833, pp. 539-550.
- Hansteen, O.E. and Höeg, K. (1994). "Soil Structure Interaction Analysis Of Embedded Caisson Anchor Under Tension Load ", *Geotechnic, Conference on Behaviour of Offshore Structures*, Vol.1, pp. 49-62.
- Hashiguchi, K. (1993). "Mechanical Requirements and Structures of Cyclic Plasticity Models", *International Journal of Plasticity*, Vol.2, pp. 721-748.
- Henkel, D.J. (1960). "The Relationships Between the Effective Stresses and Water Content in Saturated Clays", *Geotechnique*, Vol.10, pp. 41.
- Hicher, P.Y. (1985). "Comportement Mecanique des Argiles Saturees sur Divers Chemins De Sollicitations Monotones et Cycliques, Application a Une Modelisation Elastoplastique et Viscoplasique", These de Doctorat d'Etat, Universite Paris 6, Paris, France.
- Hill, R. (1950). *The Mathematical Theory of Plasticity*, Clarendon Press.
- HKS (1998a). *ABAQUS Theory Manual Version 5.8*, Hibbitt, Karlson & Sorensen, Inc.
- HKS (1998b). *ABAQUS/Standard User's Manual I Version 5.8*, Hibbitt, Karlson & Sorensen, Inc.
- HKS (1998c). *ABAQUS/Standard User's Manual II Version 5.8*, Hibbitt, Karlson & Sorensen, Inc.

HKS (2001). www.hks.com

Hogervorst, J.R. (1980). "Field Trails with Large Diameter Suction Piles". *Offshore Technology Conference*, Vol.1, Houston, Texas, Paper 3817, pp. 217-224.

Hsieh, H.S., Kavazanjian Jr., E., and Borja, R.I. (1990). "Double-Yield-Surface Cam-Clay Plasticity Model. I: Theory", *Journal of Geotechnical Engineering*, ASCE, Vol.116, #9, pp. 1381-1401.

Huges, T.R.J. and Winget, J. (1980). "Finite Rotation Effects in Numerical Integration of Rate Constitutive Equations Arising in Large Deformation Analysis", *International Journal of Numerical methods in Engineering*, Vol.15, pp. 1862-1867.

Iizuka, A., and Ohta, H. (1987). "A Determination Procedure of Input Parameters in Elastoviscoplastic Finite Element Analysis", *Soils and foundations*, Vol.27, #3, pp. 71-87.

Iskander, M.G., Olson, R.E., and Pavliccek, R.W. (1993). "Behaviour Of Suction Piles In Sand", *Geotechnical Special Publication #38*, ASCE, pp. 151-171.

Iwan, W.D. (1967). "On a Class of Models for the Yielding Behavior of Continuous and Composite Systems", *Journal of Applied Mechanics*, Transactions ASME, pp. 612-617.

Jackson, W.T. (1963). "Stress Paths and Strains in A Saturated Clay", MS Thesis, Department of Civil Engineering, MIT, Cambridge, MA.

Jeanjean, P., Andersen, K.H., and Kalsnes, B. (1998). "Soil Parameters For Design Of Suction Caissons For Gulf Of Mexico Deepwater Clays", *Offshore Technology Conference*, Vol.1, Houston Texas, Paper 8830, pp. 505-519.

Jones, W.C., Iskander, M.G., Olson, R.E., and Goldberg, A.D. (1994). " Axial Capacity Of Suction Piles In Sand ", *Geotechnic, Conference on Behaviour of Offshore Structures*, vol.1, Houston, Texas, pp. 63-75.

Jostad, H.P., Andersen, K.H., and Tjelta, T.I. (1997). "Analyses Of Skirted Foundations And Anchors In Sand Subjected To Cyclic Loading", *BOSS'97*, Vol.1, pp. 149-162, Pergamon.

Karal, K., Hermstad, J.M., Vigander, K. Skjong, J., and Pedersen, Ø. (1992). "Concrete Foundations for TLP's", *Offshore Technology Conference*, Vol.1, Houston, Texas, Paper 6897, pp. 217-223.

- Katona, M.G. (1984). "Evaluation of Viscoplastic Cap Model", *Journal of Geotechnical Engineering Division*, ASCE, Vol.110, #GT8, pp. 1106-1125.
- Kenney, T.C. (1964). "Sea Level Movements and Geological Histories of The Post-glacial Marine Soils at Boston, Nicolet, Ottawa, and Oslo", *Géotechnique*, 14(3), pp. 203-230.
- Khan, A.S., and Huang, S. (1995). *Continuum Theory of Plasticity*, John Wiley & Sons Inc.
- Kinner, E.B. (1970). "Load-deformation Behavior of Saturated Clay During Undrained Shear", ScD Thesis, Department of Civil Engineering, MIT, Cambridge, MA.
- Krieg, R.D. (1975). "A Practical Two surface plasticity theory", *Journal of applied mechanics*, ASME, Vol.42, pp. 641-646.
- Kulhawy, F.H., Trautmann, C.H., Beech, J.F., O'Rourke, T.D., McGuire, W., Wood, W.A., and Capano, C. (1983). "Transmission Line Structure Foundations for Uplift-compression Loading", *Report to the Electric Power Research Institute*, Report No. EI-2870, Palo Alto, CA, p. 412.
- Lacasse, S. (1999). "Ninth OTRC Honors Lecture: Geotechnical Contributions To Offshore Development", *Offshore Technology Conference*, Vol.1, Houston Texas, Paper 10822, pp. 359-371.
- Ladd, R.S. (1965). "Use of Electrical Pressure Transducers to Measure Soil Pressure", *Research Report R65-48*, No. 80, MIT, Cambridge, MA.
- Ladd, C.C., Bovee, R.B., Edgers, L., and Rixner, J.J. (1971). "Consolidated-undrained Plane Strain Shear Tests on Boston Blue Clay", *Research Report R71-13*, No. 273, Department of Civil Engineering, MIT, Cambridge, MA.
- Lambe, T.W. and Whitman, R.V. (1969). *Soil Mechanics*, John Wiley and Sons, New York.
- Larsen, P. (1989). "Suction Anchors as an Anchoring System for Floating Offshore Constructions", *Offshore Technology Conference*, Vol.1, Houston, Texas, Paper 6029, pp. 535-540.
- Le Blanc, L. (1996). "Spar-shaped drilling unit designed for 8,000 - 10,000 ft depth corridor", *Offshore Magazine*, November 1996, pp. 30-31,98.
- Lewis, R.W., and Schrefler, B.A. (1987). *The Finite Element Method in The Deformation and Consolidation of Porous Media*, John Wiley and Sons.

- Li, X., and Zienkiewicz, O.C. (1992). "Multiphase Flow in Deforming Porous Media and Finite Element Solutions", *Computers and Structures*, Vol.45, #2, pp. 211-227.
- Loth, W., and Henery, D. (1985). "The Central Cormorant UMC", *Advances in Underwater Technology and Offshore Engineering*, Vol.2, Design and Installation of Subsea Systems, Graham & Trotman Ltd., pp. 15-26.
- Luong, M.P. (1980). "Phenomenes Cycliques dans les Sols Pulverulents", *Revue Francaise de Geotechnique*, Vol.10, pp. 39-53.
- Luong, M.P., and Touati, A. (1983). "Sols Grenus sous Fortes Contraintes", *Revue Francaise de Geotechnique*, Vol.23, pp. 51-63.
- Maeno, Yoshi-hiko, Takatani, T., Hiraisi, T., and Takayama, T. (1995). "Dynamic Response of Suction Pile Anchor in Poroelastic Seabed Due to Mooring Force", *International Society of Offshore and polar Engineers*, Vol.1, pp. 420-425.
- Meroi, E.A., Schrefler, B.A., and Zienkiewicz, O.C. (1995). "Large Strain Static and Dynamic Semisaturated Soil Behaviour", *International Journal for Numerical and Analytical Methods in Geomechanics*, Vol.19, pp. 81-106.
- Meyerhof, G.G. (1982). "State of the Art Report - Limit Equilibrium Plasticity in Soil Mechanics", *Application of Plasticity and Generalized Stress-strain in Geotechnical Engineering*, Young, R.N. and Selig, E.T. (Eds.), the American Society of Civil Engineers, pp. 7-24.
- MIT (1992). "Anchoring Offshore Platforms in Deep Water", *MIT Sea Grant Quarterly Report*, Vol.14, #2, pp. 2-4.
- Mitcha, Jr.J.L., Morisson, C.E., and Oliveira, de J.G. (1996). "The Heidrun Field - Development Overview", *Offshore Technology Conference*, Vol.1, Houston, Texas, Paper 8084, pp. 495 - 520.
- Morrison, M.J., Clukey, E.C., and Garnier, J. (1994). "Behaviour Of Suction Caissons Under Static Uplift Loading ". *Centrifuge*, pp. 823-828.
- MSC (2001). http://www.mscsoftware.com/assets/94_Marc_Mentat_2000.pdf
- Mroz, Z. (1967). "On the Description of Anisotropic Workhardening", *Journal of Mechanics and Physics of Solids*, Vol.15, pp. 163-175.

- Mroz, Z. (1980). "On Hypoelasticity and Plasticity Approaches to Constitutive Modeling of Inelastic Behavior of Soils", *International Journal for Numerical and Analytical Methods in Geomechanics*, Vol.4, pp. 45-55.
- Mroz, Z., and Pietruszczak, S. (1983a). "An Constitutive Model for Sand with Anisotropic Hardening Rule", *International Journal for Numerical and Analytical Methods in Geomechanics*, Vol.7, pp. 305-320.
- Mroz, Z., and Pietruszczak, S. (1983b). "On Hardening Anisotropy of K_0 -consolidated Clays", *International Journal for Numerical and Analytical Method in Geomechanics*, Vol.7, pp. 19-38.
- Munkejord, T. (1996). "The Heidrun TLP and Concept Development for Deep Water", *International Offshore and Polar Engineering Conference*, Vol.I, pp. 1-11.
- Nagaraj, T. S. and Murthy, B.R.S. (1985). "Prediction of Preconsolidation Pressure and Recompression Index of Soils", *Geotechnical Testing Journal*, ASTM, Vol.8, No.4, pp.199-202.
- Nakai, T., and Matsuoka, H. (1983). "Constitutive Equation for Soils Based on the Extended Concept of 'Spatial Mobilized Plane' and its Application to Finite Element Analysis", *Soils and Foundations*, Vol.23, #4, pp. 87-105.
- Nakai, T., and Mihara, Y. (1984). "A New Mechanical Quantity for Soils and its Application to Elastoplastic Constitutive Models", *Soils and Foundations*, Vol.24, #2, pp. 82-94.
- Ohta, H., Iizuka, A., Omote, Y., and Sugie, S. (1991). "3-D Analysis of Soil/water Coupling Problems Using Elasto-viscoplastic Constitutive Relationships", *Computer Methods and Advances in Geomechanics*, Beer, Booker, Carter (eds.), Balkema, Rotterdam, pp. 1191-1196.
- O'Neil, D.A. (1985). "Undrained Strength Anisotropy of An Overconsolidated Thixotropic Clay", Thesis, Department of Civil Engineering, MIT, Cambridge, MA.
- Ortega, O.J. (1992). "Computer Automation of The Consolidated-undrained Direct Simple Shear Tests", MS Thesis, Department of Civil Engineering, MIT, Cambridge, MA.
- Parry, R.H.G. (1960). "Triaxial Compression and Extension Tests on Remoulded Saturated Clay", *Geotechnique*, Vol.10, pp. 166-180.
- Parry, R.G.H. (1972). *Stress-strain behaviour of Soils*, G.T. Foulis and Co., Henley, England.

- Perzyna, P. (1966). "Fundamental Problems in Viscoplasticity", *Quarterly Applied Mathematics*, Vol.9, pp. 243-377.
- Pietruszczak, S. and Pande, G. N. (1996). "Constitutive Relation for Partially Saturated Soils Containing Gas Inclusions", *Journal of Geotechnical Engineering*, ASCE, Vol. 122, No.1, pp.50-59.
- Pijaudier-Cabot, G., and Bode, L. (1995). "Arbitrary Lagrangian-eulerian Finite Element Analysis of Strain Localization in Transient Problems", *International Journal for Numerical Methods in Engineering*, Vol. 38, pp. 4171-4191.
- Prasad, Y.V.S.N. (1992). "Behaviour of Anchors in Soft Marine Clay under Static and Cyclic Loading", *PhD thesis*, Indian Institute of Technology, Madras, India.
- Preston, W.B. (1965). "The Effects of Sample Disturbance on The Undrained Strength Behavior of Boston blue Clay". MS Thesis, Department of Civil Engineering, MIT, Cambridge, MA.
- Prévost, J.H. (1977). "Mathematical Modeling of Monotonic and Cyclic Undrained Clay Behavior", *International Journal for Numerical and Analytical Methods in Geomechanics*, Vol.1, #2, pp. 195-216.
- Prévost, J.H. (1978). "Anisotropic Undrained Stress-strain Behavior of Clays", *Journal of Geotechnical Engineering Division*, ASCE, Vol.104, #GT8, Proc. Paper 13942, pp. 1075-1090.
- Prévost, J.H. (1980). "Mechanics of Continuous Porous Media", *International Journal of Engineering Science*, Vol.18, #5, pp. 787-800.
- Prévost, J.H. (1985). "A Simple Plasticity Theory for Frictional Cohesionless Soils", *Soil Dynamics and Earthquake Engineering*, 4, pp. 9-17.
- Prévost, J.H. (1987). "Dynamics of Porous Media", *Geotechnical Modeling and Applications*, Sayed M. Sayed (Ed.), Gulf Publishing Co., pp. 76-146.
- Puech, A. (1984). *The Use of Anchors in Offshore Petroleum Operations*, Houston Gulf Publication.
- Randolph, M.F., O'Neil, M.P., Stewart, D.P., and Erbrich, E. (1998). "Performance Of Suction Anchors In Fine Grained Calcareous Soils", *Offshore Technology Conference*, Vol.1, Houston Texas, Paper 8831, pp. 521-529.

- Rao, Narasimha S., Ravi, R., and Prasad, Siva B. (1997). "Pullout Behaviour of Suction Anchors in Soft Marine Clays", *Marine Georesource and Geotechnology*, 15, pp. 95 - 114.
- Rendulic, L. (1936). "Porenziffer und Porenwasserdruck in Tonen", *Bauingenieur*, 17, pp. 559-564.
- Renzi, R., Maggioni, W., Smits, F., and Manes, V. (1991). "A Centrifugal Study on the Behavior of Suction Piles", *Centrifuge*, pp. 169-176.
- Renzi, R., and Maggioni, W. (1994). "Modelling The Behaviour Of Skirt Piles", *Geotechnic, Conference on Behaviour of Offshore Structures*, Vol.1, pp. 77 - 85.
- Rice, J.R. (1975). "Continuum Mechanics and Thermodynamics of Plasticity in Relation to Microscale Deformation Mechanisms", *Constitutive Equations in Plasticity*, Argon, A.S., Editor, MIT Press, Cambridge, Massachusetts, pp. 23-79.
- Roscoe, K.H., Schofield, A.N., and Wroth, C.P. (1958). "On the Yielding of Soils". *Geotechnique*, Vol.9, pp. 22-53.
- Rowe, P.W. (1962). "The Stress-Dilatancy Relation for Static Equilibrium of an Assembly of Particles in Contact", *Proceeding of Royal Society of London*, Vol.A269, pp. 500-527.
- Saada, A.S., and Bianchini, G.F. (1975). "Strength of One Dimensionally Consolidated Clays", *Journal of Geotechnical Engineering Division*, ASCE, Vol.101, #GT11, pp. 1151-1164.
- Saga Petroleum (1997). "The Snorre Field", *Saga Petroleum Internet Home Page*.
- Sandhu, R.S., and Wilson, E.L. (1969). "Finite Element Analysis of Seepage in Elastic Media", *Journal of Engineering Mechanics Division*, ASCE, Vol.95, #EM3, pp. 641-652.
- Santagata, M. (1994). "Simulation of Sampling Disturbance in Soft Clays using Triaxial Element Tests", MS Thesis, Department of Civil Engineering, MIT, Cambridge, MA.
- Schofield, A. and Wroth, C.P. (1968). *Critical State Soil Mechanics*, McGraw-Hill, New York.
- Scott, R.F. (1979). "Cyclic Static Model Pile Tests in a Centrifuge", *Proceedings, 11th Offshore Technology Conference*, Houston, Texas, OTC 3492, pp.1159-1163.

- Scott, R.F. (1985). "Plasticity and Constitutive Relations in Soil Mechanics", *Journal of Geotechnical Engineering*, ASCE, Vol.111, #5, pp. 563-605.
- Scott, R.F. (1994). "Review of Progress in dynamic Geotechnical Centrifuge Research", *Dynamic Geotechnical Testing II*, ASTM STP 1213, R.J. Ebelhar, V.P. Drnevich, and B.L. Kutter, Eds., pp.305-329.
- Seah, T-H (1990). "Anisotropy of Resedimented Boston Blue Clay", PhD Thesis, Department of Civil Engineering, MIT, Cambridge, MA.
- Sekiguchi, H., and Ohta, H. (1977). "Induced Anisotropy and Time Dependency in Clays", *Proceeding, Specialty Session 9, 9th ICSMFE*, pp. 289-292.
- Senpere, D., and Auvergne, G.A. (1982). "Suction Anchor Piles - A Proven Alternative to Driving or Drilling", *Offshore Technology Conference*, Vol.1, Houston, Texas, Paper 4206, pp. 483-493.
- Schiffman, R., Chen, A., and Joreau, J. (1964). "An Analysis of Consolidation Theories", *Journal of Soil Mechanics and Foundation Division*, ASCE, Vol. 95, #SM1, pp. 285-312.
- Senneset, K. and Janbu, N. (1985). "Shear Strength Parameters Obtained from Static Cone Penetration Tests", *Strength Testing of marine Sediments: laboratory and In-Situ Measurements*, ASTM STP 883, R.C. Chaney and K.R. Demars Eds., pp.41-82.
- Sheahan, T.C. (1991). "An Experimental Study of The Time-dependent Undrained Shear Behavior of Resedimented Clay using Automated Stress Path Triaxial Equipment", ScD Thesis, Department of Civil Engineering, MIT, Cambridge, MA.
- Skempton, A. W. (1957). "The Planning and Design of New Hong Kong Airport", *Proceedings, The Institute of Civil Engineers*, London, Vol.7, pp. 305-307.
- Simon, B.R., Zienkiewicz, O.C., and Paul, D.K. (1984). "An Analytical Solution for the Transient Response of Saturated Porous Elastic Solids", *International Journal for Numerical and Analytical Methods in Geomechanics*, Vol.8, pp. 381-398.
- Steesen-Bach, J.O. (1992). "Recent Model Tests With Suction Piles in Clay and Sand", *Offshore Technology Conference*, Vol.1, Houston, Texas, Paper 6844, pp. 323 - 330.
- Støve, O.J., Bysveen, S., and Christophersen, H.P. (1992). "New Foundation Systems for the Snorre Development", *Offshore Technology Conference*, Vol.1, Houston, Texas, Paper 6882, pp. 75-83.

- Svanø, G., Eiksund, G., Kavli, A., Langø, H., Karunakaran, D., and Tjelta, T.I. (1997). "Soil Structure Interaction Of The Draupner E Bucket Foundation During Storm Conditions", *BOSS'97*, Vol.1, Pergamon, pp. 163-176.
- Terzaghi, K. (1943). *Theoretical of Soil Mechanics*, John Wiley & Sons.
- Tjelta, T.I., Guttormsen, T.R., and Hermstad, J. (1986). "Large-Scale Penetration Test at a Deepwater Site", *Offshore Technology Conference*, Vol.1, Houston, Texas, Paper 5103, pp. 201-212.
- Tomlinson, M.J. (1994). *Pile Design and Construction Practice*, 4th Ed., E & FN Spon, New York, p. 411.
- Truesdell, C., and Taupin, R. (1960). "The Classical Field Theories", *Hanbuch der physik. S Flugge* (ed.), Springer-Verlag Berlin, Vol. III/1., pp.
- Ulbricht, W.R., Ripping, M.A., Doyle, E.H., Stevens, J.W., and Mayfield, J.G. (1994). "Design, Fabrication, and Installation of the Auger TLP Foundation System", *Offshore Technology Conference*, Vol.1, Houston, Texas, Paper 7626, pp. 589-598.
- Valanis, K.C., and Read, H.J.E. (1982). "A New Endochronic Plasticity Model for Soils", *Soil Mechanics - Transient and Cyclic Loads*, G.N.Pande & O.C.Zienkiewicz (Eds.), John Wiley & Sons, pp. 375-417.
- Varallyay, J. (1964). "The Effects of Stress System Variables on The Undrained Strength of Boston Blue Clay", MS Thesis, Department of Civil Engineering, MIT, Cambridge, MA.
- Wang, M.C, Nacci, V.A., and Demars, K.R. (1975). "Behavior of Underwater Suction Anchor in Soil", *Ocean Engineering*, Vol.3, pp. 47-62.
- Wroth, C.P. and Wood, D.M. (1978). "The Correlation of Index Properties with Some Basic Engineering Properties of Soils", *Canadian Geotechnical Journal*, Vol. 15, No. 2, pp. 137-145.
- Zienkiewicz, O.C., and Corneau, I.C. (1974). "Visco-plasticity - Plasticity and Creep in Elastic Solids - a Unified Numerical Solution Approach", *International Journal for Numerical Methods in Engineering*, Vol.8, pp. 821-845.
- Zienkiewicz, O.C., Humpheson, C., and Lewis, R.W. (1975). "Associated and Non-associated Visco-plasticity and Plasticity in Soil Mechanics", *Geotechnique*, Vol.25, #4, pp. 671-689.

- Zienkiewicz, O.C., Humpheson, C., and Lewis, R.W. (1977). "A unified Approach to Soil Mechanics problems Including Plasticity and Viscoplasticity", *University of Wales, Dep. Of Civil Eng., C/R/250/75*, Swansea, also *Chapter 4* in G. Gudehus (Ed.), *Finite Element in Geomechanics*, Wiley, pp. 157-178.
- Zienkiewicz, O.C. (1977). *The Finite Element Method*, Third Edition, McGraw-Hill.
- Zienkiewicz, O.C., Chang, C.T., and Bettess, P. (1980). "Drained, Undrained Consolidating and Dynamic Behaviour Assumptions in Soils; Limits of Validity", *Geotechnique*, 30, pp. 385-395.
- Zienkiewicz, O.C., and Bettess, P. (1982). "Soils and other Saturated Media under Transient, Dynamic Conditions; General Formulation and the Validity of Various Simplifying Assumptions", *Soil Mechanics - Transient and Cyclic Loads*, G.N.Pande & O.C.Zienkiewicz (Eds.), John Wiley & Sons., pp. 1-16.
- Zienkiewicz, O.C., and Shiomi, T. (1984). "Dynamic Behaviour of Saturated Porous Media; the Generalized Biot Formulation and its Numerical Solution", *International Journal for Numerical and Analytical Methods in Geomechanics*, Vol.8, pp. 71-96.
- Zienkiewicz, O.C., and Taylor, R.L. (1985). "Coupled Problems - a Simple Time-stepping Procedure", *Communications of Applied Numerical Methods*, 1, pp. 233-239.
- Zienkiewicz, O.C., Chan, A.H.C., Pastor, M., Paul, D.K., and Shiomi, T. (1990a). "Static and Dynamic Behaviour of Soils: a Rational Approach to Quantitative Solutions. I. Fully Saturated Problems.", *Proceeding of Royal Society of London*, Vol. A 429, pp. 285-309.
- Zienkiewicz, O.C., Xie, Y.M., Schrefler, B.A., Ledesma, A., and Bicanic, N. (1990b). "Static and Dynamic Behaviour of Soils: a Rational Approach to Quantitative Solutions. II - Semi-saturated Problems", *Proceeding of Royal Society of London*, Vol.A 429, pp. 311-321.
- Zienkiewicz, O.C., and Huang, M. (1995). "Localization Problems in Plasticity using Finite Elements with Adaptive Remeshing", *International Journal for Numerical and Analytical Methods in Geomechanics*, Vol.19, pp. 127-148.

Appendix A1

Subroutines used for suction force generation

The subroutines used in suction force generation consist of ABAQUS internal subroutines that are provided by ABAQUS as USER SUBROUTINES, and an additional subroutine to control flow and status of the analysis. The user subroutine can be defined using FORTRAN or C programming language. This Appendix is aimed to give a more in depth view of every user subroutine used in the analysis for suction force generation. Therefore, for additional details of various aspects of user subroutines, one should consult ABAQUS/STANDARD USER'S MANUALS.

As previously stated in Chapter 3, user subroutines that are provided by ABAQUS used for the suction force generation, consist of DFLOW, DLOAD, URDFIL, and UVARM.

DFLOW is an user subroutine used to define non-uniform fluid flow velocity across a porous medium face at a certain time in an analysis. This facility is used to define the fluid flow information as an input based on change of pore pressure status, for every increment during analysis.

DLOAD is a user subroutine used to define a non-uniform distributed load on a solid face at a certain time in an analysis. This capability is used to define non-uniform distributed load as an input based on pore pressure status on soil surface under the caisson cap for every increment during analysis.

URDFIL is a user subroutine to facilitate the user accessing output (result file .fil) of analysis results for every increment, to be used as input and control of the analysis procedure. This capability would assist the user to access results of analysis at every time/load increment, i.e., accumulated fluid, displacement, based on database code used by ABAQUS.

UVARM is a user subroutine that defines new user defined material definition and is called for all material calculation points of elements when the material definition in the input file (.inp) includes the ***USER DEFINED VARIABLES**.

GETVRM is an internal routine that is called as a utility routine to provide access to material point information for user subroutine **UVARM** and **USDFLD**.

SPRIND is an internal routine that is called as utility routine to determine both the principal values and direction for a given stress or strain tensor.

POSFIL is a utility routine to define pointer of access in output database.

DBFIL is a utility routine to initiate and define access to an output database.

The list of typical subroutine program to define suction force generation is given in the following.

```
      SUBROUTINE UVARM(UVAR, DIRECT, T, TIME, DTIME, CMNAME, ORNAME,
1     NUARM, NOEL, NPT, LAYER, KSPT, KSTEP, KINC, NDI, NSHR)
C23456
C      INCLUDE 'ABA_PARAM.INC'
      implicit real*8(a-h,o-z)
      parameter (nprecd=2)
C
      CHARACTER*8 CMNAME, ORNAME, FLGRAY(15)
      DIMENSION UVAR(NUARM), DIRECT(3,3), T(3,3), TIME(2)
```

```

        DIMENSION ARRAY(15),JARRAY(15)
        DIMENSION SX1(6),SPX1(3),ANX1(3,3)
C
        DIMENSION PORV(4)
C Error counter:
        JERROR = 0
        NHIT=0
        DO 1000 I=1,4
1000    PORV(I)=0.
C Stress tensor:
        IF(KSTEP.LT.3) GOTO 3000
        IF(CMNAME.NE.'FOUND') THEN
            CALL GETVRM('S',ARRAY,JARRAY,FLGRAY,JRCD)
            JERROR = JERROR + JRCD
            SX = ARRAY(1)
            SX1(1)=ARRAY(1)
C            UVAR(3)=SX
            SY = ARRAY(2)
            SX1(2)=ARRAY(2)
C            UVAR(4)=SY
            SZ = ARRAY(3)
            SX1(3)=ARRAY(3)
C            UVAR(5)=SZ
            SXY = ARRAY(4)
            SX1(4)=ARRAY(4)
            SXZ = ARRAY(5)
            SX1(5)=ARRAY(5)
            SYZ = ARRAY(6)
            SX1(6)=ARRAY(6)
            CALL GETVRM('IE',ARRAY,JARRAY,FLGRAY,JRCD)
            XIE12=ARRAY(4)
            LSTR=1
            CALL SPRIND(SX1,SPX1,ANX1,LSTR,NDI,NSHR)
            SXYZ=SX+SY+SZ
            UVAR(1)=ABS(SXY/(0.2*SX))
            UVAR(2)=ABS(SXY/(0.13*SY))
            IF(KSTEP.LT.2) GOTO 2000
2000    CONTINUE
            JERROR = JERROR + JRCD
C
            UVAR(3)=ABS(SXY/(0.2*SPX1(1)))
            UVAR(4)=ABS(SXY/(0.2*SPX1(2)))
            UVAR(5)=ABS(SXY/(0.2*SPX1(3)))
            UVAR(6)=ABS(SXY/(0.2*SY))
            UVAR(7)=ABS(SXY/(0.13*SPX1(1)))
            UVAR(8)=ABS(SXY/(0.13*SPX1(2)))
            UVAR(9)=ABS(SXY/(0.13*SPX1(3)))
            UVAR(10)=ABS(SXY)
            UVAR(11)=ABS(XIE12)
        ENDIF
C        JERROR=JERROR+JRCD
C If error, write comment to .DAT file:
        IF(JERROR.NE.0) THEN
            WRITE(6,*) 'REQUEST ERROR IN UVARM FOR ELEMENT NUMBER ',

```

```

1      NOEL, 'INTEGRATION POINT NUMBER ', NPT
      ENDIF
3000  RETURN
      END
C
C23456789
      SUBROUTINE URDFIL(LSTOP, LOVRWRT, KSTEP, KINC, DTIME, TIME)
C      INCLUDE 'ABA_PARAM.INC'
      implicit real*8(a-h,o-z)
      parameter (nprecd=2)
      DIMENSION ARRAY(513), JRRAY(NPRECD, 513)
      COMMON/KKK/XKOPEN(1000, 2), XKVOL, XKDE, XKDX1, PORE
      EQUIVALENCE(ARRAY(1), JRRAY(1, 1))
C
C      FIND CURRENT INCREMENT
C
      CALL POSFIL(KSTEP, KINC, ARRAY, JRCD)
      KSWOP=0
      KSWSO=0
      DO K1=1, 99999
          CALL DBFILE(0, ARRAY, JRCD)
          IF(JRCD.NE.0) GOTO 110
          KEY=JRRAY(1, 2)
C
C      RECORD 1521, ATTRIB. 1: CONTAIN CONTACT CLEARANCE
C
          IF((KSWOP.GT.0).AND.(KSWSO.GT.0)) GOTO 110
          IF(KEY.EQ.1521)THEN
              IF(KSWOP.GT.0) GOTO 1100
              KSWOP=KSWOP+1
              XKOPEN(KINC, 1)=ARRAY(3)
              CALL ACHAIN(KINC, 200)
              GOTO 1100
          ENDIF
C
C      RECORD 1591, ATTRIB. 1: CONTAIN SECTION SOP
C
          IF(KEY.EQ.1591)THEN
              IF(KSWSO.GT.0) GOTO 1100
              KSWSO=KSWSO+1
              IF((KINC.EQ.1).AND.(ARRAY(3).LT.0)) XKVOL=0.
              XKVOL=XKVOL+ARRAY(3)
              XKDX1=ARRAY(3)
              IF(XKOPEN(KINC, 1).GT.0) XKOPEN(KINC, 2)=XKOPEN(KINC, 1)-XKVOL/20.43
              CALL ACHAIN(KINC, 200)
              WRITE(6, *) 'XKVOL:', XKVOL, ' XKOPEN1: ', XKOPEN(KINC, 1),
1          ' XKOPEN2:', XKOPEN(KINC, 2), ' SOP:', ARRAY(3)
              ENDIF
1100      CONTINUE
          END DO
110      CONTINUE
C
      RETURN
      END

```

```

C
C23456789
  SUBROUTINE DLOAD(F,KSTEP,KINC,TIME,NOEL,NPT,LAYER,KSPT,
1 COORDS,JLTYP)
C
C   INCLUDE 'ABA_PARAM.INC'
C   implicit real*8(a-h,o-z)
C   parameter (nprec=2)
C
C   DIMENSION TIME(2),COORDS(3)
C   COMMON/KKK/XKOPEN(1000,2),XKVOL,XKDE,XKDX1,PORE
C
C   DEFINE F:P3NU
C   XKDE: SPEED OF PULLOUT FLOW; XKDX1: SPEED OF INCREMENT FLOW
C
C234567
  F=-PORE
C
C   RETURN
C   END
C
C   SUBROUTINE ACHAIN(KINC,NSW)
C
C   INCLUDE 'ABA_PARAM.INC'
C   implicit real*8(a-h,o-z)
C   parameter (nprec=2)
C   COMMON/KKK/XKOPEN(1000,2),XKVOL,XKDE,XKDX1,PORE
C   IF(KOUNT1.GT.10) GOTO 1100
C   IF(NSW.EQ.100) KOUNT1=KOUNT1+KINC/KINC
C   IF(KOUNT1.EQ.1) XKOPEN(KINC,1)=0.
1100 CONTINUE
  RETURN
  END
C
C23456789
  SUBROUTINE DFLOW(FLOW,U,KSTEP,KINC,TIME,NOEL,NPT,
1 COORDS,JLTYP)
C
C   implicit real*8(a-h,o-z)
C   parameter (nprec=2)
C
C   DIMENSION TIME(2),COORDS(3)
C   COMMON/KKK/XKOPEN(1000,2),XKVOL,XKDE,XKDX1,PORE
C
C   PORE=U
C   PATHL=14.*(5.D0-XKOPEN(KINC,1))/5.D0
C   FLOVEL=2.37D-7*10.13/(PATHL*0.00981)
C   FLOW=FLOVEL
C
C   RETURN
C   END
C

```

Appendix A2

MIT Models Analyses Results [Cauble, 1997]

As mentioned in Chapter 4, 6 models of MIT test results are selected in these analyses. The difference is related to pullout scenario of every model as seen in the following Table A.2.1.

Table A.2.1. Tests loading schedule of MIT laboratory tests

Test ID	Consolid. at 73.5 kPa	Suction Driving	Equil. I and sustained loading 149 N	Monotonic Pullout I m/min.	Equil. II and sustained loading 149 N	Monotonic Pullout II m/min.
CET3	24 hr.	L = 0.051 m; 0.003 m/min.	24 hr.	0.0003 m/min to L=0.003 m; 0.003 m/min to extraction	-	-
CET4	28 hr.	L = 0.051 m; 0.003 m/min.	18 hr.	0.0003 m/min to L=0.003 m; 0.003 m/min to extraction	-	-
CET5	48 hr.	L = 0.051 m; 0.003 m/min.	24 hr.	0.0003 m/min to L=0.003 m	67 hr.	0.0003 m/min to L=0.003 m

L = length of suction driving or pullout.

Table A.2.1. Tests loading schedule of MIT laboratory tests (cont'd)

Test ID	Consolid. at 73.5 kPa	Suction Driving	Equil. I and sustained loading 149 N	Monotonic Pullout I m/min.	Equil. II and sustained loading 149 N	Monotonic Pullout II m/min.
CET6	25.5 hr.	L = 0.0105 m; 0.0001 m/min.; L = 0.0405 m; 0.003 m/min.	30 hr.	0.0003 m/min to L=0.003 m	66.6 hr.	0.0003 m/min to L=0.004 m
CET7	24.9 hr.	L = 0.051 m; 0.003 m/min.	25.6 hr.	0.0003 m/min to L=0.003 m	24.1 hr.	0.0003 m/min to L=0.003 m; 0.003 m/min to extraction
CET8	25.8 hr.	L = 0.051 m; 0.003 m/min.	33.3 hr.	0.0003 m/min to L=0.003 m; 0.003 m/min to extraction		

L = length of suction driving or pullout.

The results from all finite element analyses gave results for different scenarios as given in Table A.2.1, and some of the results, given in Table A.2.2, were very close to the experimental values, while some others were not. This difference between laboratory test and numerical analysis results may be attributed to different constraints that may apply to the set-up of each test. However in the finite element analysis these different constraints could not be included since they were not quantified exactly in the experimental results. It

is also seen from Table A.2.2 that the finite element results gave stiffer responses. Even though the displacement at peak loads did not agree very well with the experimental results, the theoretical load-displacement curves showed an excellent agreement with the experimental load-displacement curves as seen in Figures A.2.1 to A.2.18.

The results of finite element models, were in the expected test results range, based on the bounds given for the original experimental data.

Table A.2.2 Finite element analysis results of MIT model tests.

Monotonic Pullout I: 0.0003 m/min.; Values at Peak Total Force				
Results given in brackets indicate the results obtained from laboratory tests.				
CET Test no.	Wall displacement at top (m)	Wall Force (N)	Cap Force (N)	Total Force (N)
3	6.5502E-04 (17.2E-04)	107.20 (124.56)	109.55 (64.53)	216.75 (189.09)
4	4.4514E-04 (22.7E-04)	105.14 (140.25)	111.22 (82.48)	216.36 (222.73)
5	6.4695E-04 (23.5E-04)	109.65 (149.08)	110.44 (85.82)	220.09 (234.90)
6	4.4514E-04 (30.0E-04)	105.14 (107.89)	111.22 (110.83)	216.36 (218.72)
7	4.4514E-04 (18.7E-04)	105.14 (69.05)	111.22 (103.96)	216.36 (173.01)
8	4.4514E-04 (23.4E-04)	105.14 (132.41)	111.22 (87.29)	216.36 (219.70)

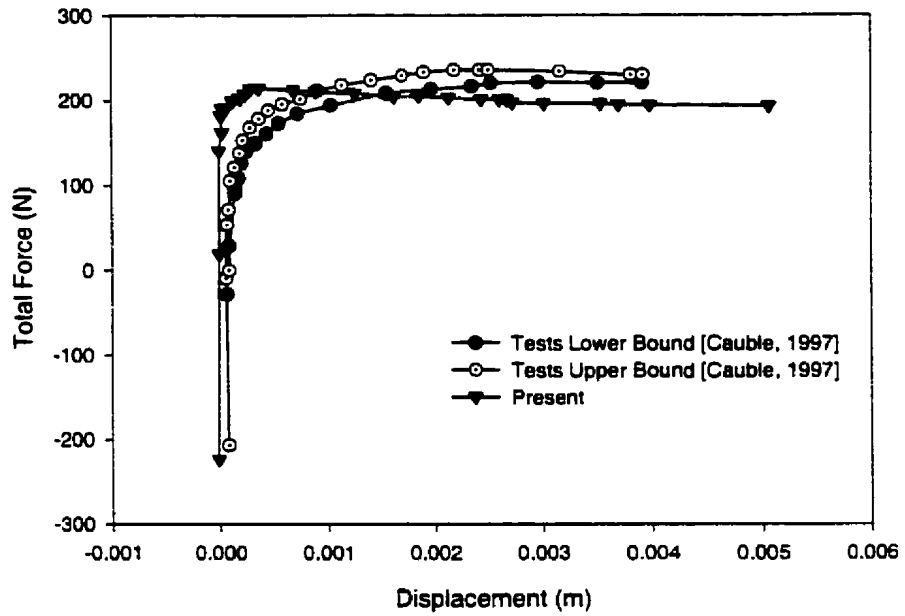


Figure A.2.1 Total force-displacement curves of laboratory test results (CET3) and FEM analysis results

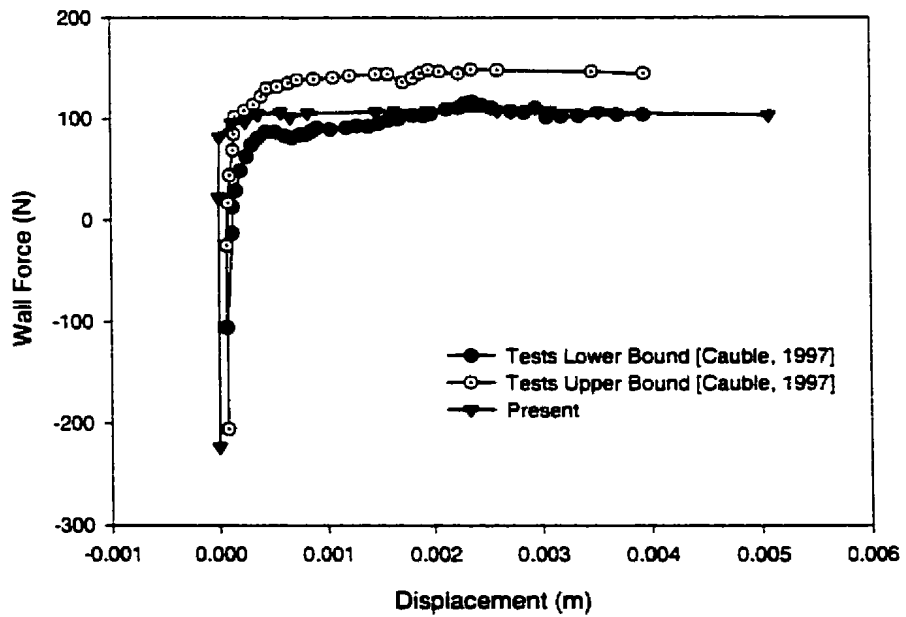


Figure A.2.2 Wall force-displacement curves of laboratory test results (CET3) and FEM analysis results

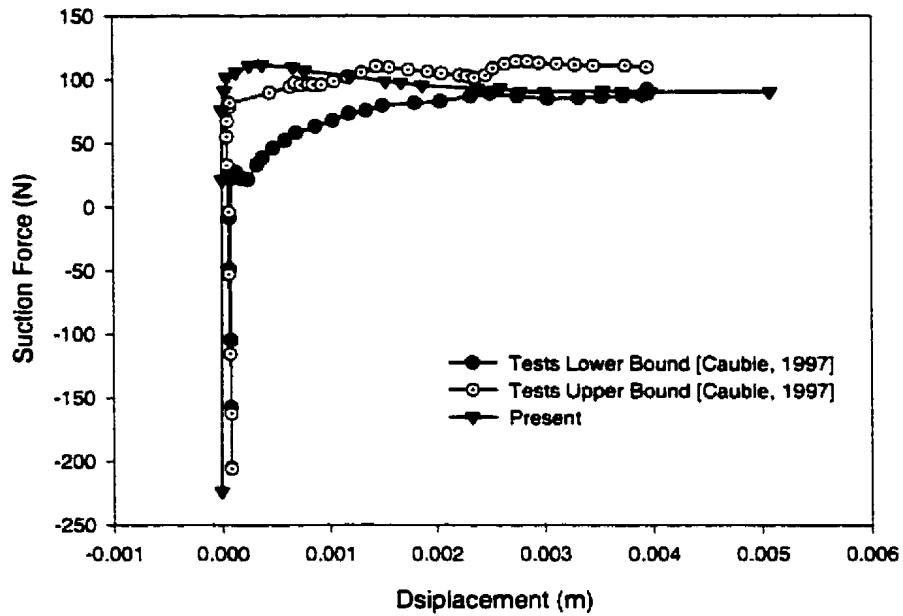


Figure A.2.3 Suction force-displacement curves of laboratory test results (CET3) and FEM analysis results

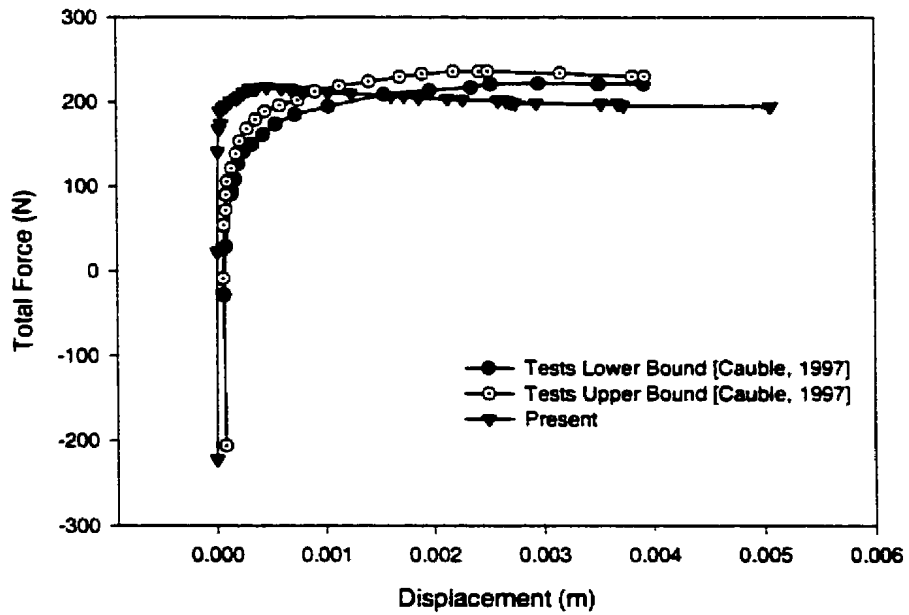


Figure A.2.4 Total force-displacement curves of laboratory test results (CET4) and FEM analysis results

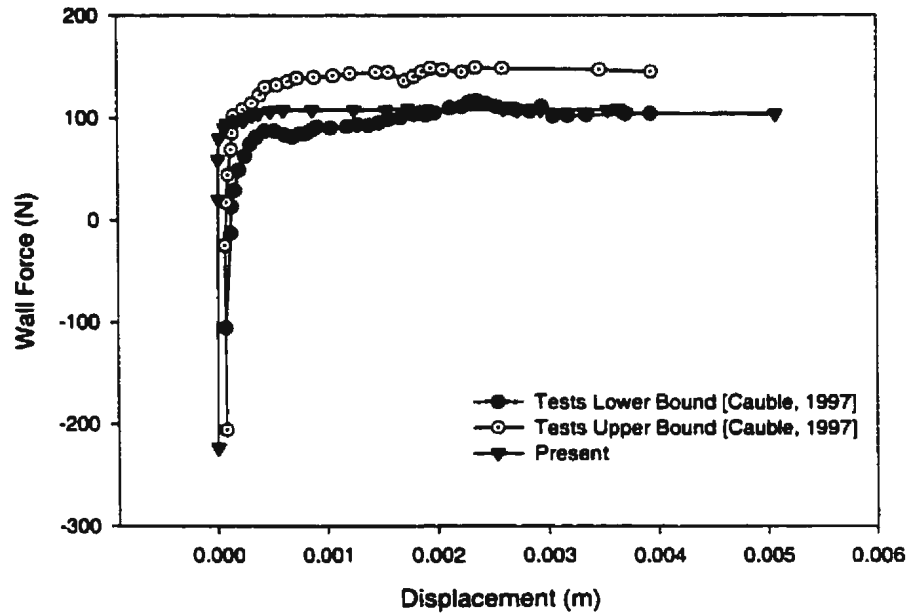


Figure A.2.5 Wall force-displacement curves of laboratory test results (CET4) and FEM analysis results

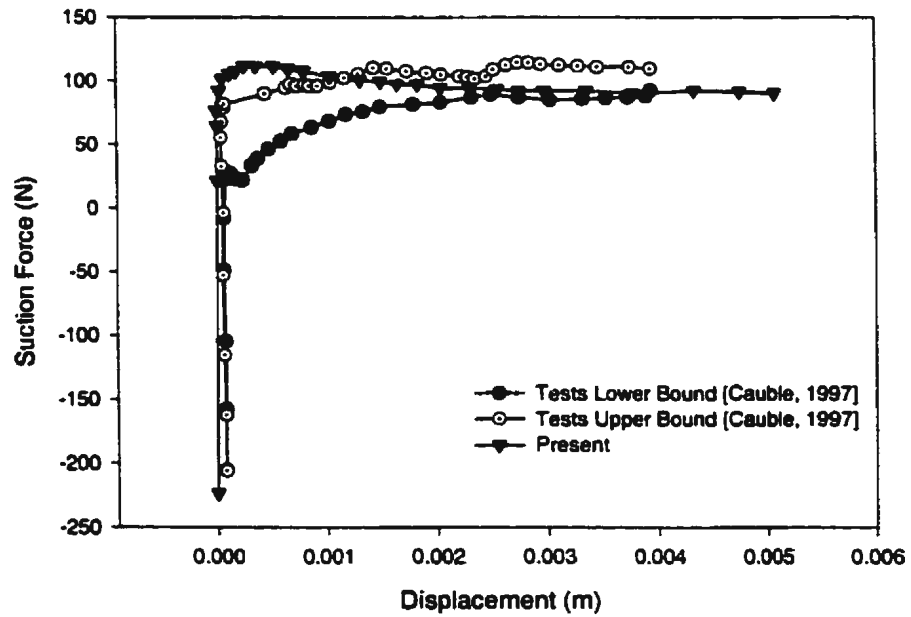


Figure A.2.6 Suction force-displacement curves of laboratory test results (CET4) and FEM analysis results

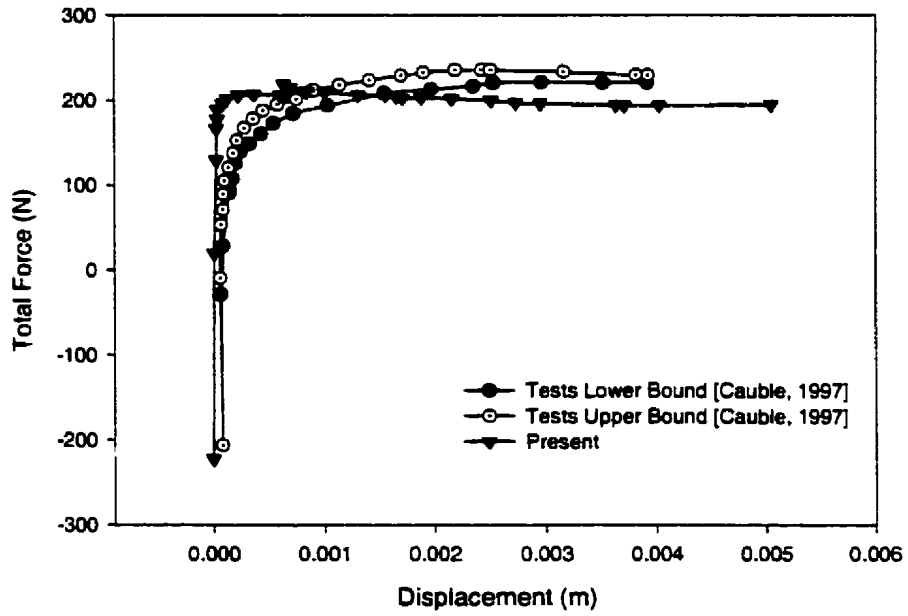


Figure A.2.7 Total force-displacement curves of laboratory test results (CET5) and FEM analysis results

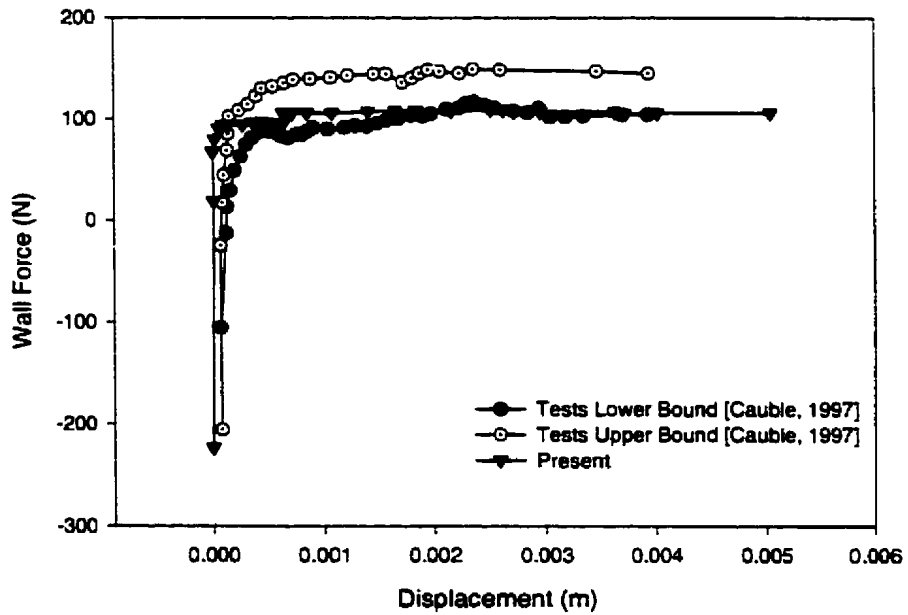


Figure A.2.8 Wall force-displacement curves of laboratory test results (CET5) and FEM analysis results

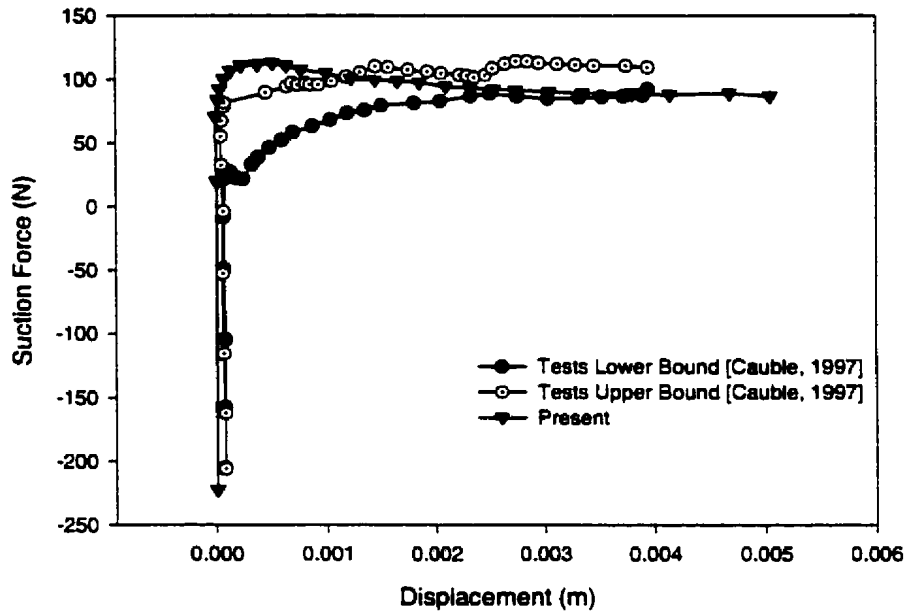


Figure A.2.9 Suction force-displacement curves of laboratory test results (CET5) and FEM analysis results

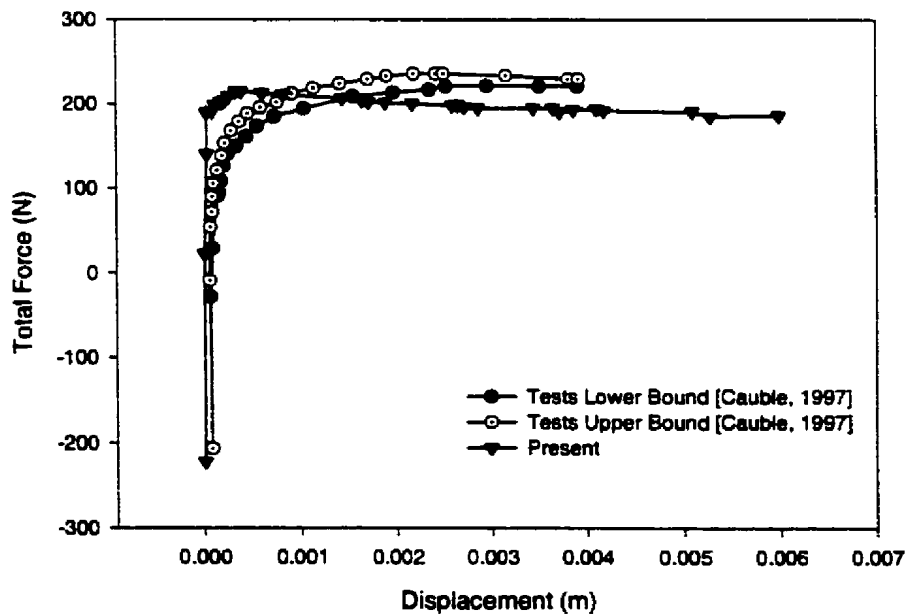


Figure A.2.10 Total force-displacement curves of laboratory test results (CET6) and FEM analysis results

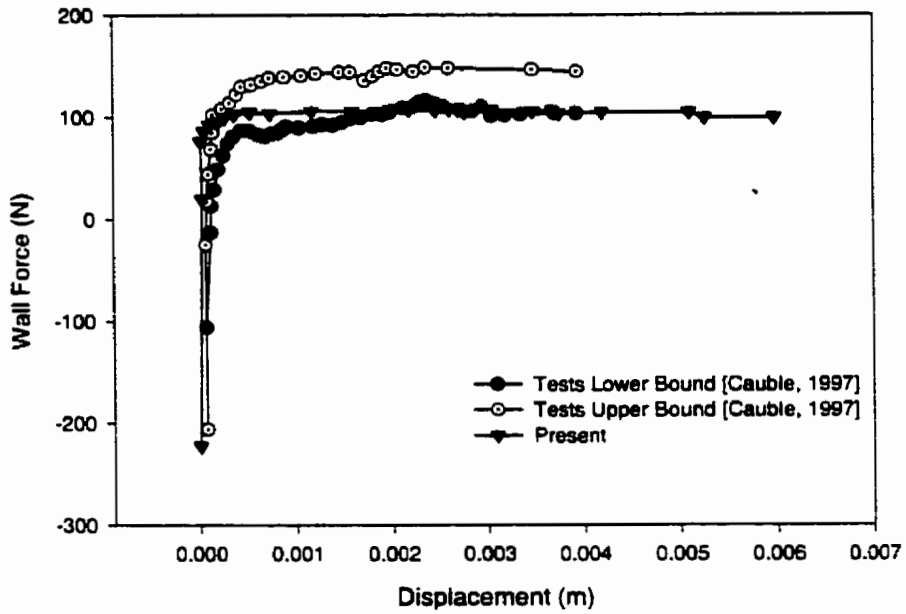


Figure A.2.11 Wall force-displacement curves of laboratory test results (CET6) and FEM analysis results

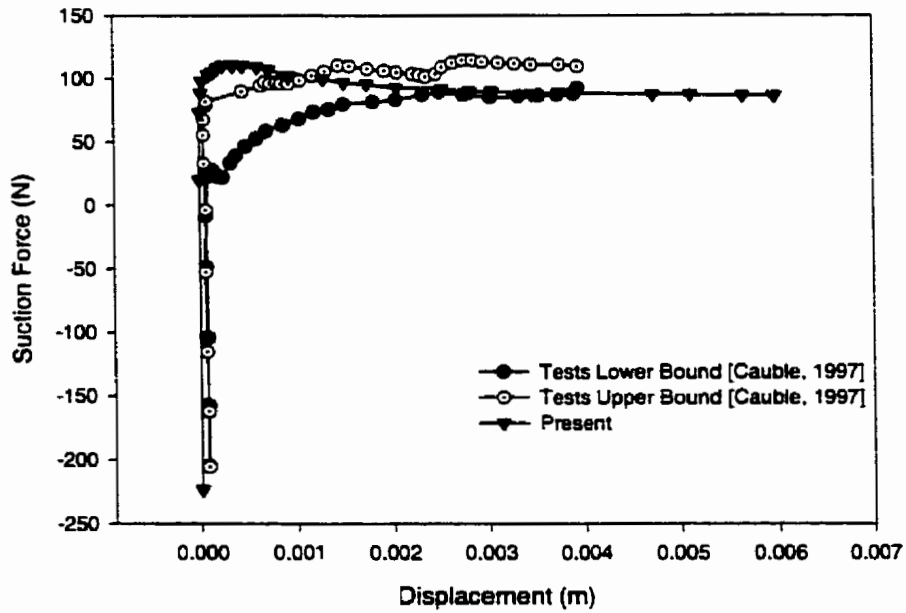


Figure A.2.12 Suction force-displacement curves of laboratory test results (CET6) and FEM analysis results

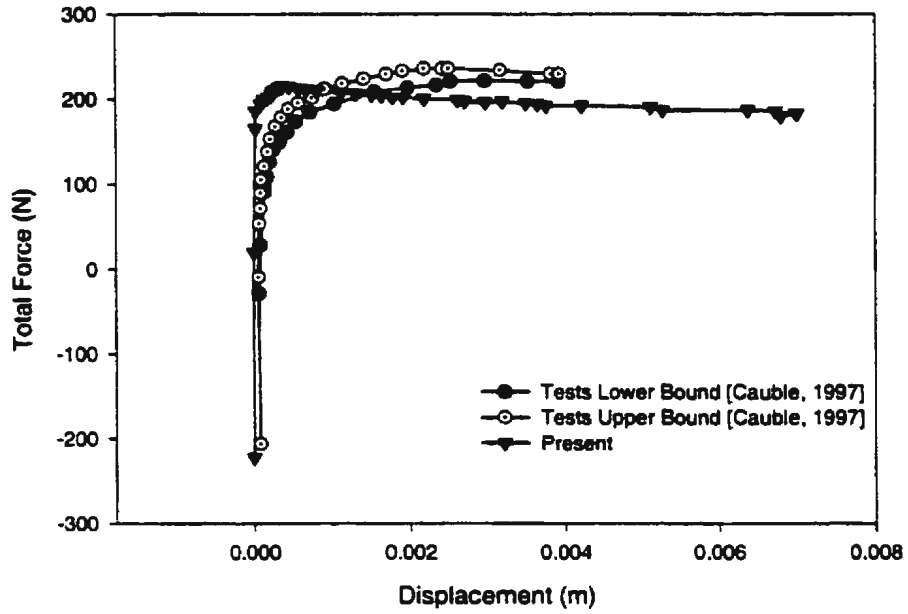


Figure A.2.13 Total force-displacement curves of laboratory test results (CET7) and FEM analysis results

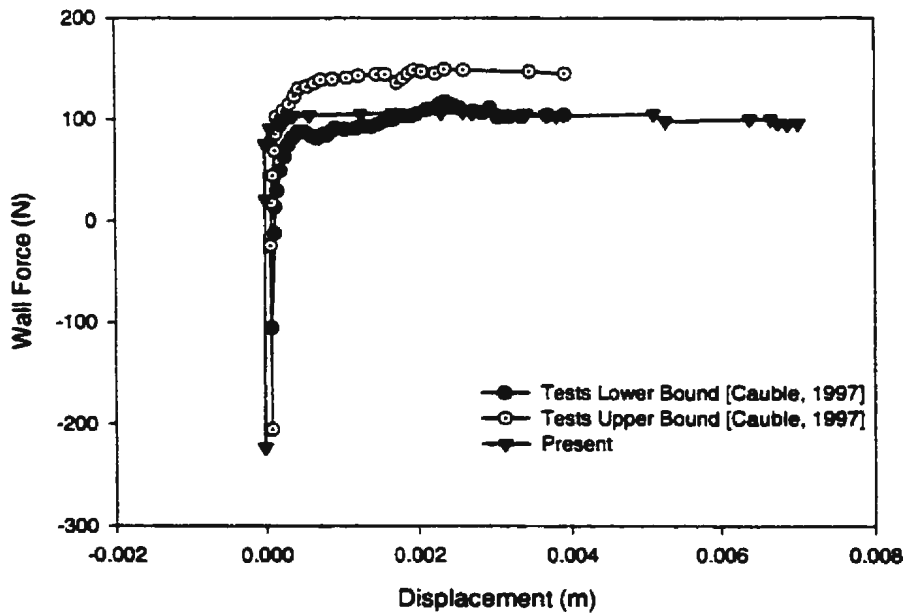


Figure A.2.14 Wall force-displacement curves of laboratory test results (CET7) and FEM analysis results

NOTE TO USERS

Page(s) not included in the original manuscript are unavailable from the author or university. The manuscript was microfilmed as received.

297

This reproduction is the best copy available.

UMI

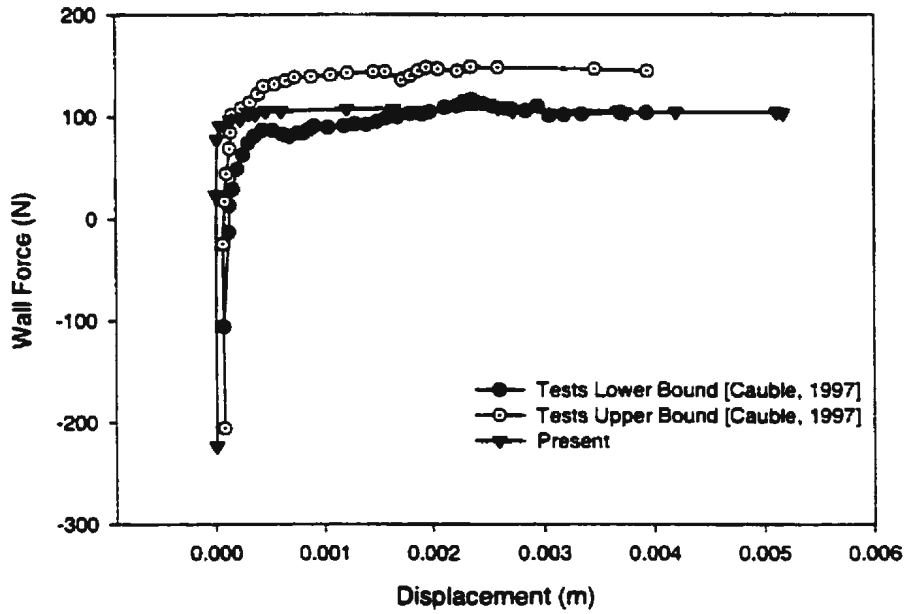


Figure A.2.17 Wall force-displacement curves of laboratory test results (CET8) and FEM analysis results

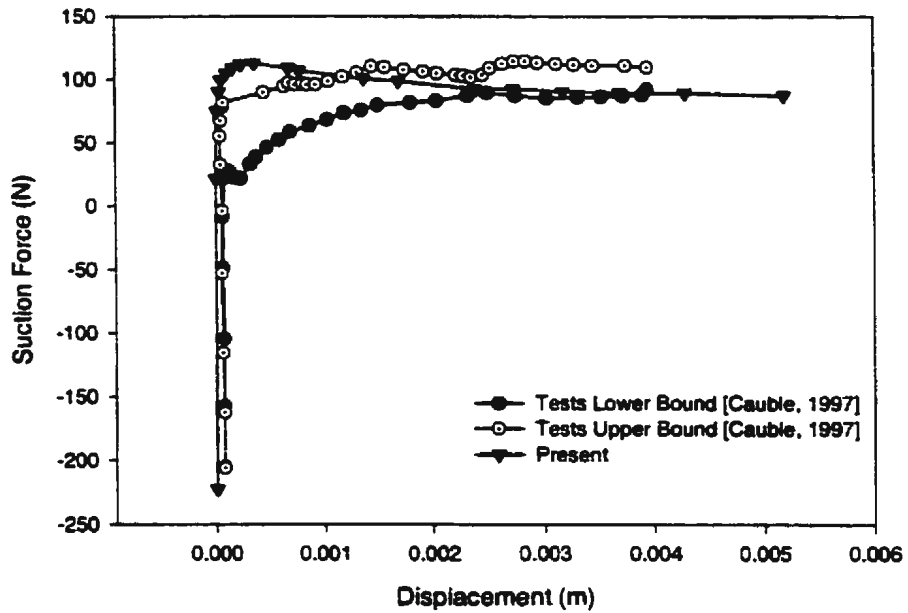


Figure A.2.18 Suction force-displacement curves of laboratory test results (CET8) and FEM analysis results

Appendix A3

Results from Analyses of Texas Models [El-Gharbawy, 1998]

As mentioned in Chapter 4, two major groups of tests were carried out, viz., (i) Short term pullout (undrained loading); and (ii) Long term pullout (drained loading). The details of selected test loading scenarios are given in the following tables (Tables A.3.1 and A.3.2).

Table A.3.1 Short-term pullout (undrained loading)

Test ID	L/D ratio	Pullout speed (m/sec)
STCC2	2	0.0508
STCC4	4	0.0254 – 0.0508
STCC6	6	0.0254 – 0.0508
STCC12	12	0.0254 – 0.0508

Table A.3.2 Long-term pullout (drained loading)

Test ID	L/D ratio	Loading/Treatment
STCC2	2	11.12 N increment, wait 3 hr. for drainage
STCC4	4	22.24 N increment, wait 30 min. for drainage
STCC4a	4	22.24 N increment, wait 2.5 hr. for drainage, maintained load 133.44 N
STCC4b	4	22.24 N increment, wait 3 hr. for drainage, loading history: 111.2, 133.44, 137.89 N
STCC4c	4	22.24 N increment, wait 2.5 - 3 hr. for drainage, loading history: 111.2, 124.54 N
STCC6	6	22.24 N increment, 3 hr. for drainage
STCC12	12	22.24 N Increment, wait 3 hr. for drainage

The results from all finite element analyses gave results for different scenarios: short-term pullout (shown in Table A.3.1), and long-term pullout (shown in Table A.3.2), gave results given in Table A.3.3 and A.3.4. From finite element analyses, it was found that the responses of the model were stiffer than these found in laboratory test results. It was also observed that the maximum pullout capacity forces of the FEA (finite element analysis) were close to the experimental ones, except in the case of STCC12 for drained loading. It was observed from the load applied on top of the soil body that it was equal to a soil height of 10.35 m, which gave a model to prototype ratio of 101. This closely simulates the results of L/D ratio equal to 2, where an excellent agreement has been obtained for load-displacement behaviour (Table A.3.3). For other L/D ratios, the load to be applied on the top had to be different to obtain values closer to experimental values. Hence it is observed that the suction pressure applied at the bottom in the University of Texas tests should have been different for different L/D ratios to give a better fit with the analytical results.

Table A.3.3 Short term pullout (undrained loading) analysis results

Test ID	Suction Pressure at top cap (kPa)	Maximum Pullout Capacity (N)	Displacement at maximum load (m)
STCC2	14.48 (-)	163.24 (164.57)	0.0026 (0.0030)
STCC4	18.61 (20.68)	349.17 (382.53)	0.0040 (0.0246)
STCC6	16.54 (20.68)	663.19 (596.03)	0.0067 (0.0216)
STCC12	16.54 (-)	246.86 (177.92)	0.0017 (0.0305)

Results given in brackets indicate the results obtained from laboratory tests.

Table A.3.4 Long-term pullout (drained loading) analysis results

Test ID	Maximum Pullout Capacity (N)	Displacement at maximum load (m)
STCC2	77.84 (88.96)	0.0016 (0.0033)
STCC4	200.16 (151.23, 160.13)	0.0017 (-)
STCC6	200.16 (177.92)	0.0023 (0.0038)
STCC12	200.16 (88.96,129)	0.0009 (0.0007)

Results given in brackets indicate the results obtained from laboratory tests.

Test results of force–displacement relationships for undrained tests (of STCC2) are given in Figure A.3.1, showing a good match with the results from laboratory tests. However, the other results gave peak resistances closer to test results but the displacements did not match very well. It can be seen from the short-term model analyses of STCC4, STCC6, and STCC12 shown in Figures A.3.2 to A.3.4 that the forces were close to that observed in experiments, while the displacements were different. Figure A.3.5 gives results from undrained test simulation of STCC2 where the model was pulled at a load increment of 11.12 N with a waiting time (for drainage to take place) of 3 hours. From the figure it is seen that there were 7 load increments applied during simulation starting at 11.12 N and giving a total load of 77.84 N, which is closer to 88.94 N, obtained in laboratory test. Other long-term model analyses of STCC4, STCC6, and STCC12 given in Figures A.3.6 to A.3.8, show that they can simulate closely the load results of laboratory tests.

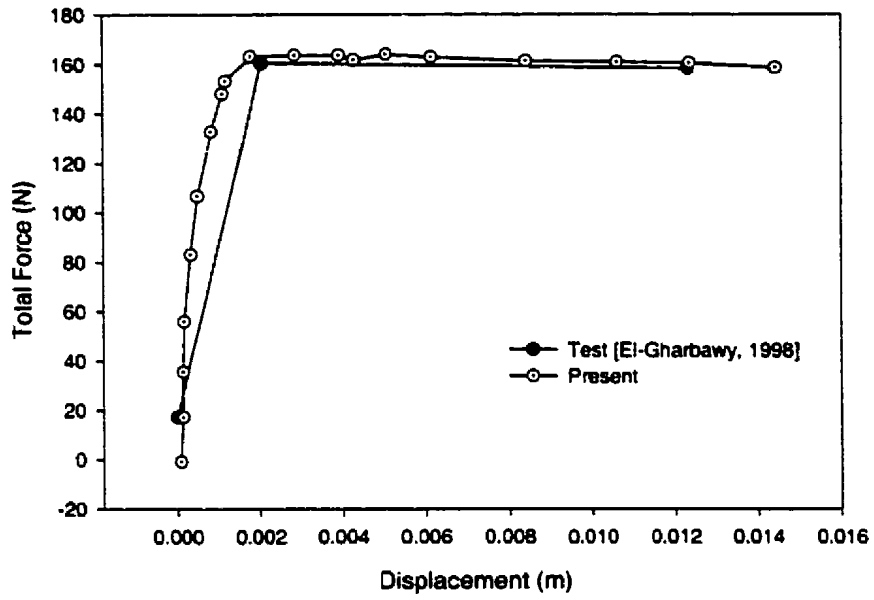


Figure A.3.1 Force-displacement curve of STCC2 for undrained loading

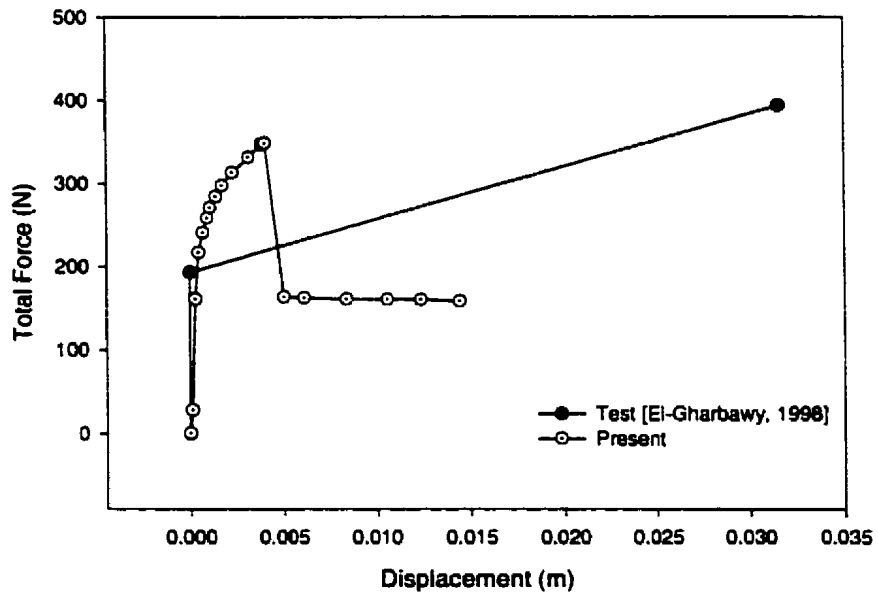


Figure A.3.2 Force-displacement curve of STCC4 for undrained loading

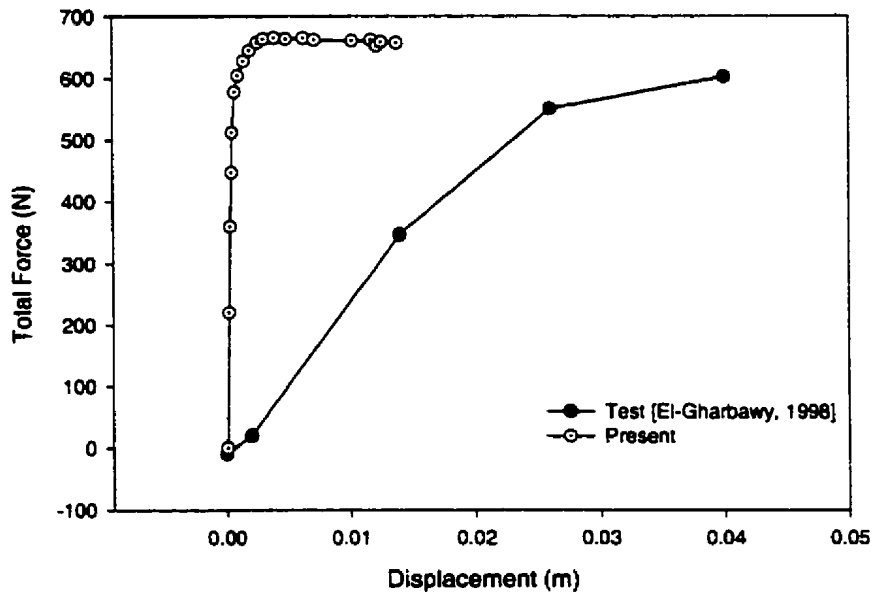


Figure A.3.3 Force-displacement curve of STCC6 for undrained loading

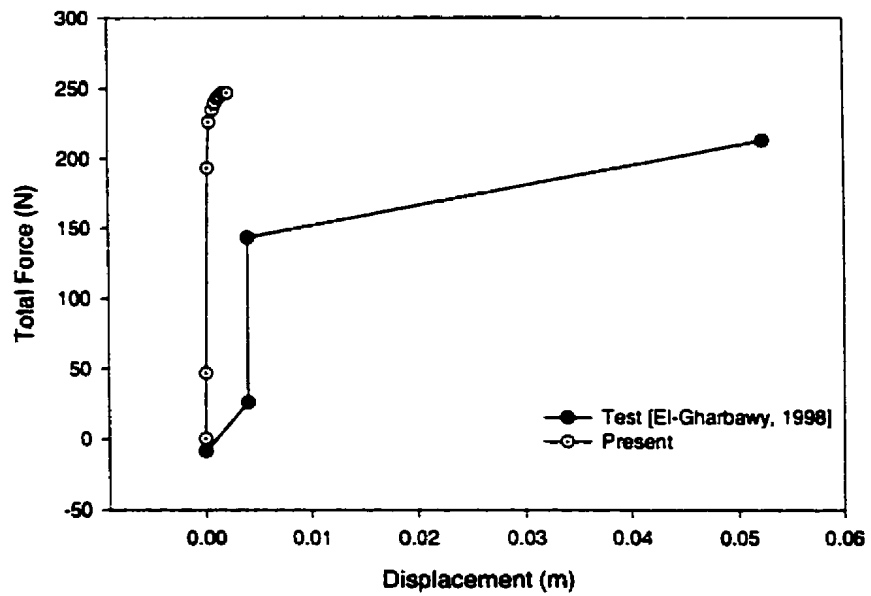


Figure A.3.4 Force-displacement curve of STCC12 for undrained loading

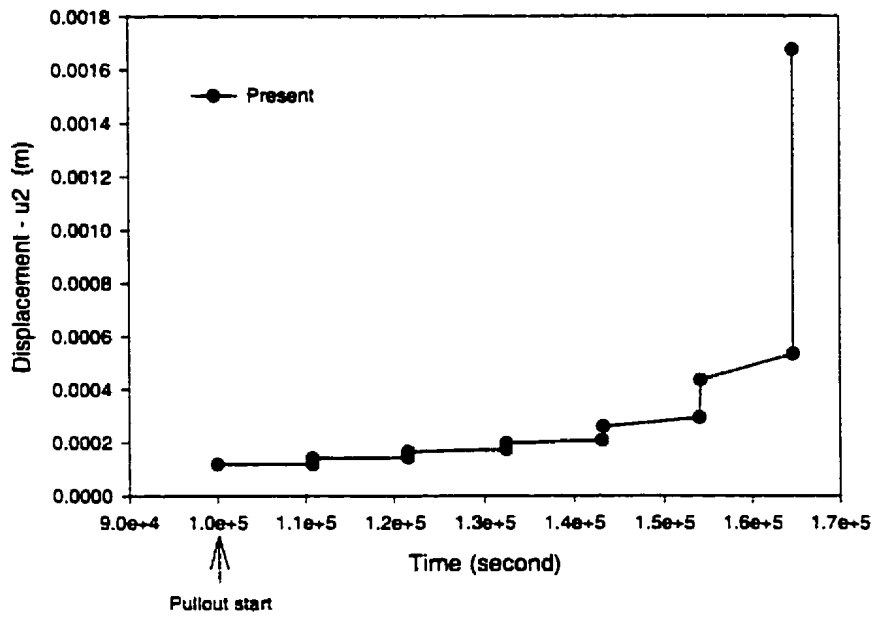


Figure A.3.5 Displacement-time curve of STCC2 for drained loading (at caisson head top center)

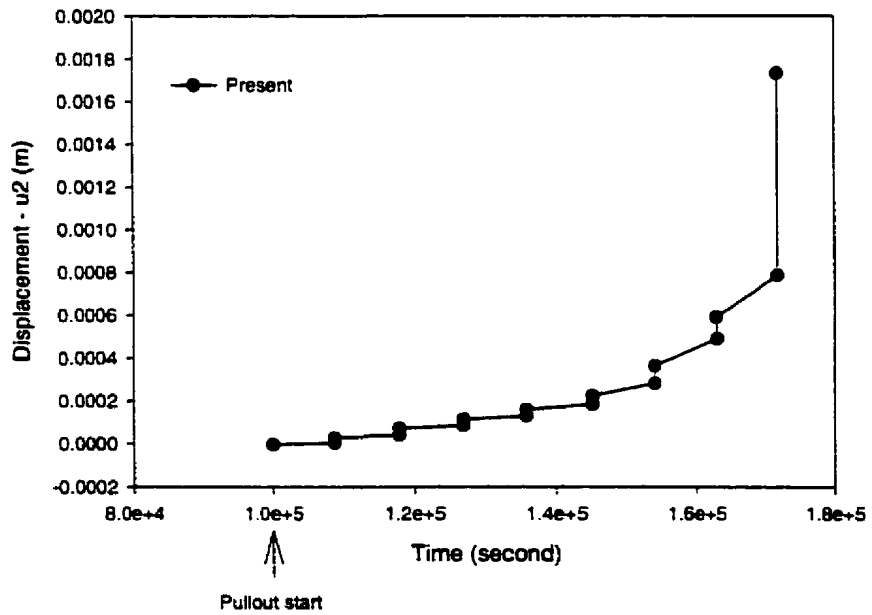


Figure A.3.6 Displacement-time curve of STCC4 for drained loading (at caisson head top center)

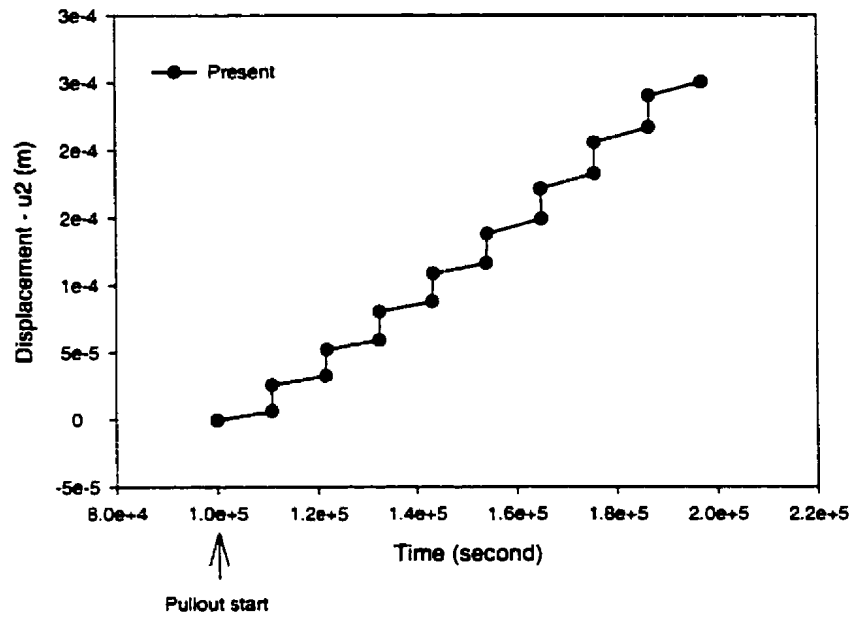


Figure A.3.7 Displacement-time curve of STCC4 for drained loading (at caisson head top center)

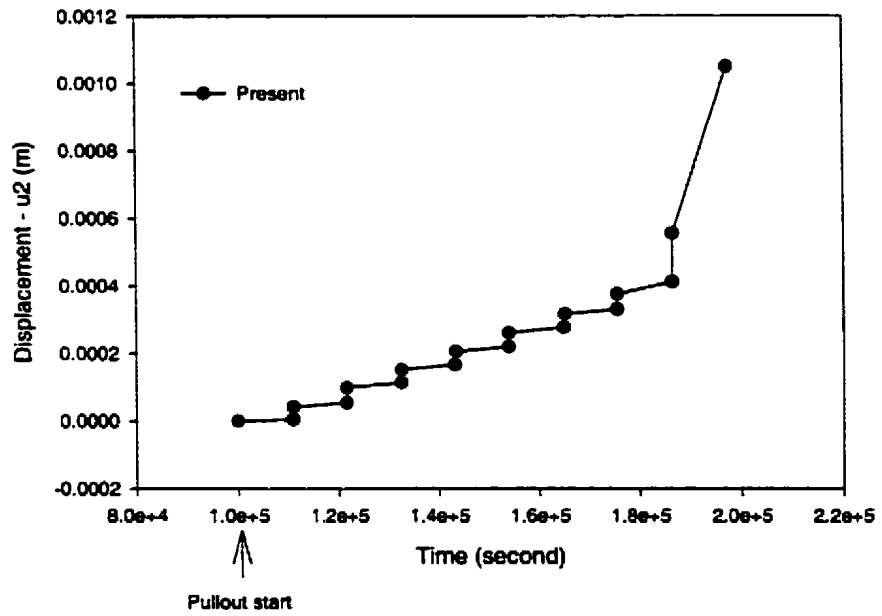


Figure A.3.8 Displacement-time curve of STCC4 for drained loading (at caisson head top center)

Appendix A4

Results from Analyses of India Institute of Technology (IIT) Models [Prasad, 1992]

As mentioned in Chapter 4, only single pile tests were selected to be used in this study, to represent the friction pile behaviour subjected to vertical pullout loads. Six tests results, of two different diameters and three different length to diameter (L/D) ratios, were available for comparing with results of numerical simulation. The test load was applied through the use of strain controlled static pullout equipment. The pullout load was applied on the suction caisson at a constant rate of 0.004 m per minute using a hydraulic jack. In this test phase, each test was continued beyond a peak failure load until well-noticed failure behaviour was obtained.

Results (obtained from finite element analysis) are given in Table A.4.1. The analytical results obtained are slightly lower than the experimental values for lower L/D ratios and higher for higher L/D ratios. Also the correlation between experiment and analysis seems to be better for the L/D ratio equal to 25. From the given c_u value of 5 kPa, the soil data given simulated very closely the analytical results for $L/D = 25$.

Table A.4.1 Results from finite element analysis (Laboratory test values)

Test ID	Diameter (mm)	L/D	Max Pullout Capacity (N)	At Displacement (mm)
1	13.8	15	43 (52)	0.35 (0.50)
2	13.8	25	72 (71)	0.34 (0.40)
3	13.8	40	117 (90)	0.49 (0.75)
4	18	15	72 (80)	0.36 (0.40)
5	18	25	123 (110)	0.36 (0.40)
6	18	40	200 (130)	0.14 (0.25)

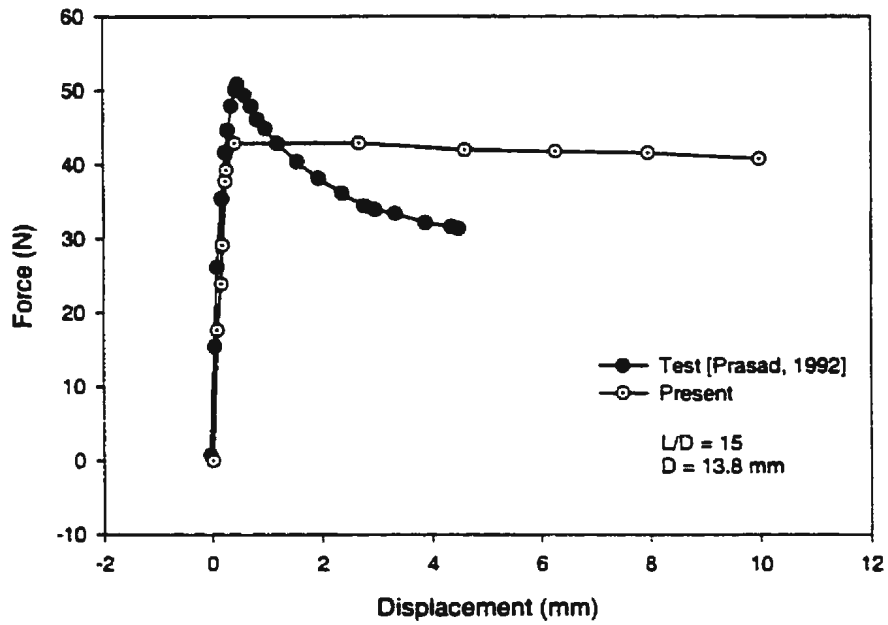


Figure A.4.1 Force-displacement curve of single pile pullout test, Dia.: 13.8 mm, L/D = 15, IIT Madras model.

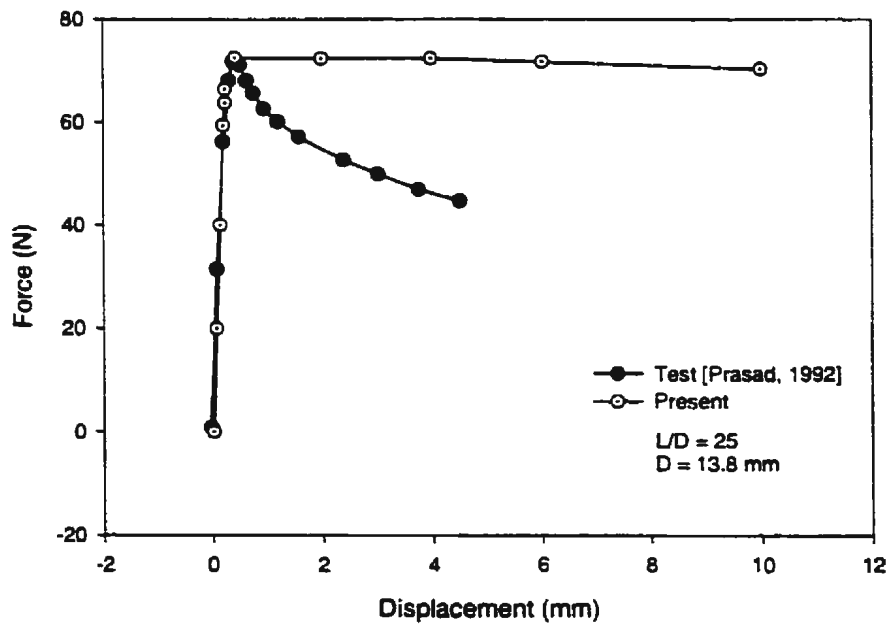


Figure A.4.2 Force-displacement curve of single pile pullout test, Dia.: 13.8 mm, L/D = 25, IIT Madras model.

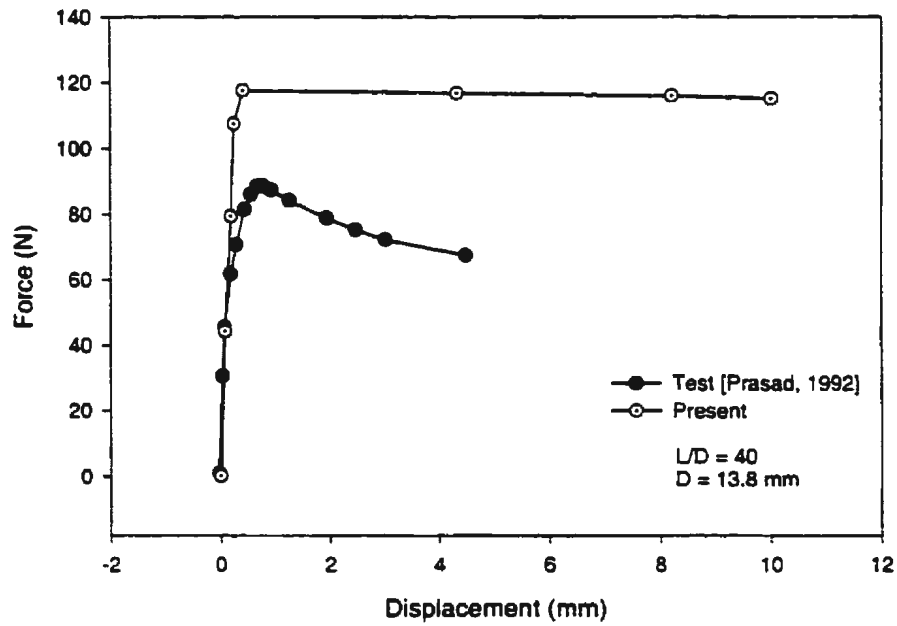


Figure A.4.3 Force-displacement curve of single pile pullout test, Dia.: 13.8 mm, L/D = 40, IIT Madras model.

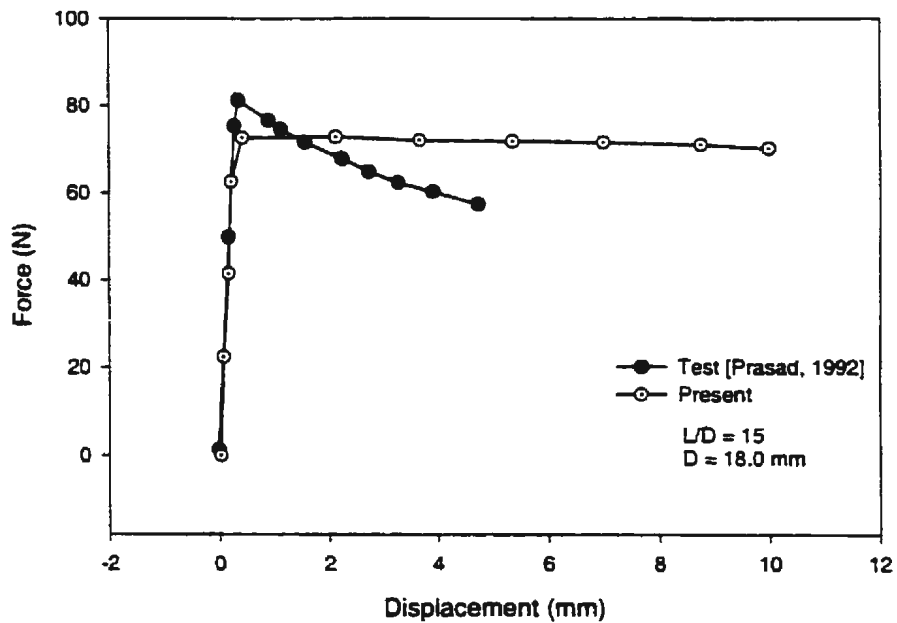


Figure A.4.4 Force-displacement curve of single pile pullout test, Dia.: 18.0 mm, L/D = 15, IIT Madras model.

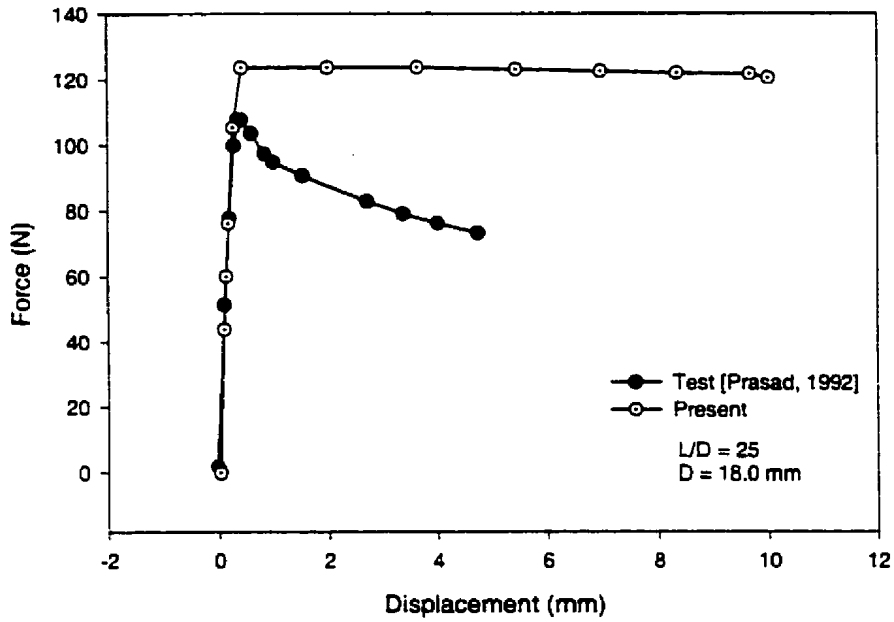


Figure A.4.5 Force-displacement curve of single pile pullout test, Dia.: 18.0 mm, L/D = 25, IIT Madras model.

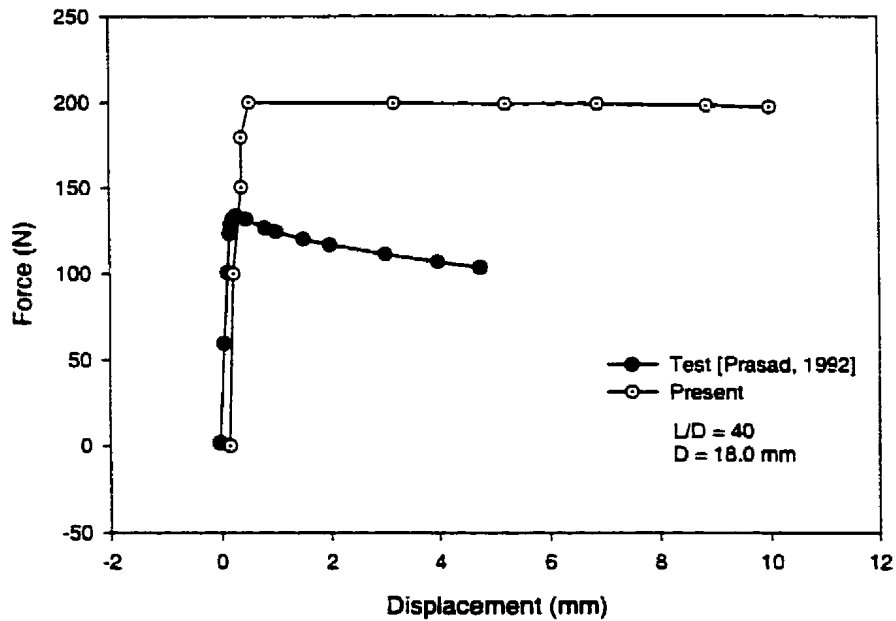


Figure A.4.6 Force-displacement curve of single pile pullout test, Dia.: 18.0 mm, L/D = 40, IIT Madras model.

Appendix A5

Results of Analyses of India Institute of Technology (IIT) Models [Rao et al., 1997]

As previously mentioned in Chapter 4 Section 4.6.5, three different model geometries and three different soil properties were chosen to carry out the finite element analyses. Therefore nine results (in total) were obtained to be compared with the results from laboratory tests [Rao et al., 1997].

The loading tests used a flexible wire rope connected to the centre of the suction caisson top and then passed over a pulley arrangement in the loading frame. For static loading, the pullout load was applied in increments by placing weights on the load hanger attached to the other end of the wire rope. However in the finite element analysis, the load application used displacement-controlled approach with a pullout rate of 0.015 m/min, that was assumed fast enough to represent the static pullout rates used in laboratory tests.

Results from finite element analyses are given in the following Table A.5.1 along with experimental values that were extracted from previous Figures 4.5.1 to 4.5.4 in Section 4.5. It is observed from the results given in Table A.5.1 that $L/D = 1$ very closely simulates the analysis and test results (see Figures A.5.1 to A.5.2).

From Figures A.5.3, A.5.7, A.5.8, A.5.9, it is seen that the model of $L/D = 1.5$ gave odd results that were far beyond the range obtained from laboratory tests. Also, the model showed a very stiff behaviour for the suction caisson model. However, other

model results seemed to give approximately close results to laboratory tests (see Figures A.5.4 to A.5.6).

Table A.5.1 Results from finite element analysis (laboratory test values)

Test Models	Ultimate Pullout Capacity of Suction Caisson Model (N)		
	LI = 0.8	LI = 0.6	LI = 0.4
L/D = 1	52 (56.11)	98 (115.55)	150 (162.78)
L/D = 1.5	168 (56.67)	221 (136.36)	289 (176.67)
L/D = 2	84 (83.33)	136 (170.45)	N/A (210)

Results given in brackets indicate the results obtained from laboratory tests

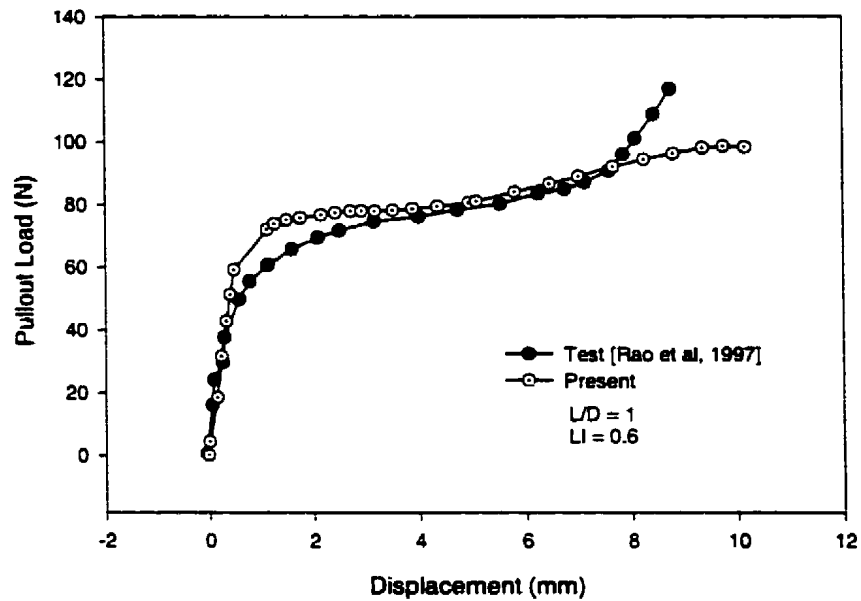


Figure A.5.1 Pullout load–displacement curve, for L/D = 1, LI = 0.6

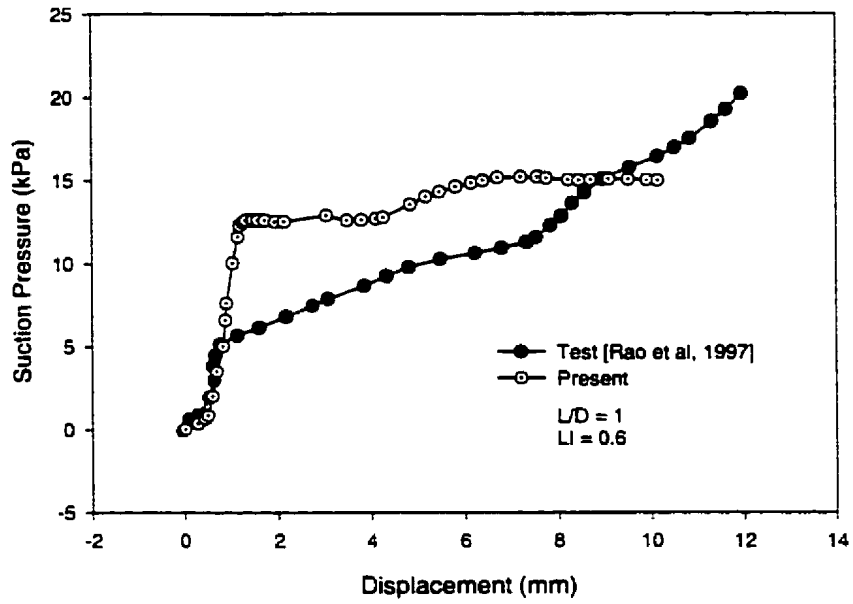


Figure A.5.2 Suction pressure–displacement curve, for $L/D = 1$, $LI = 0.6$

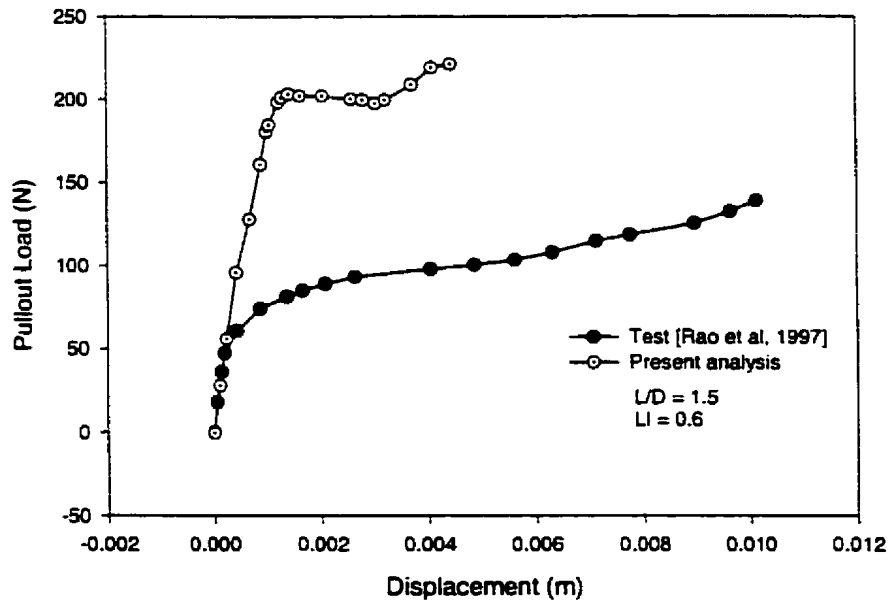


Figure A.5.3 Pullout load–displacement curve, for $L/D = 1.5$, $LI = 0.6$

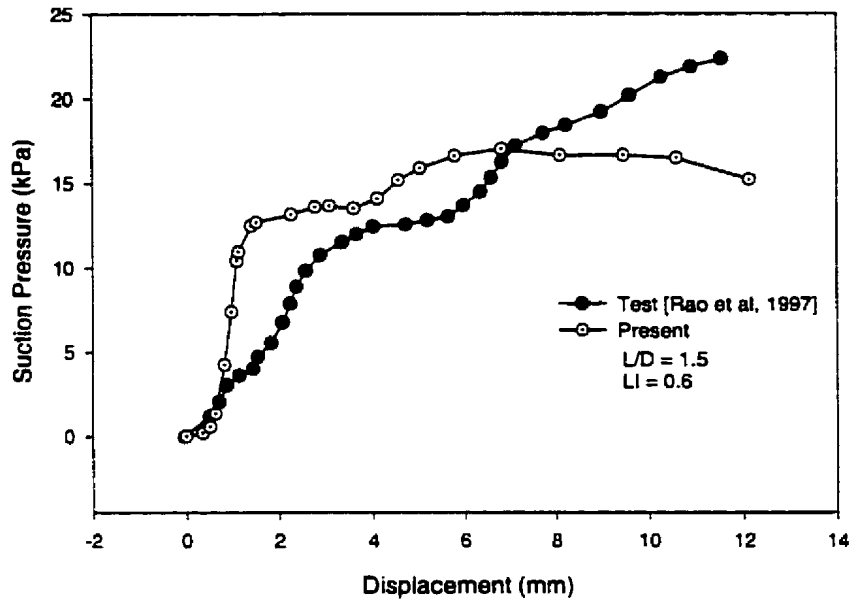


Figure A.5.4 Suction pressure–displacement curve, for $L/D = 1.5$, $LI = 0.6$

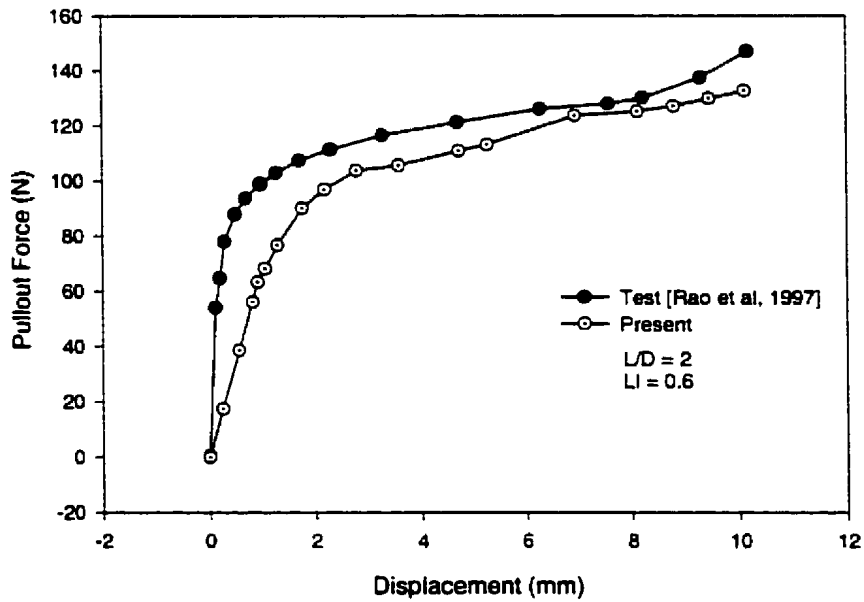


Figure A.5.5 Pullout load–displacement curve, for $L/D = 2$, $LI = 0.6$

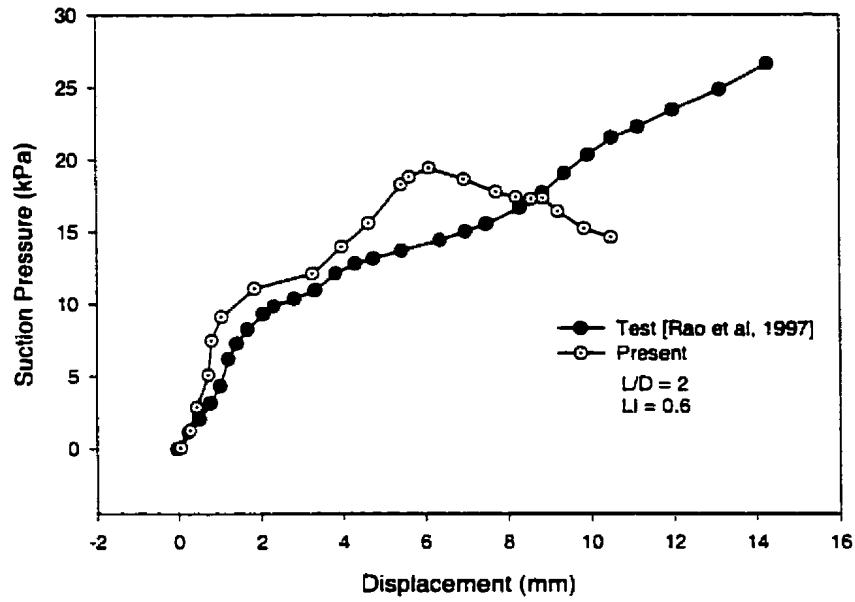


Figure A.5.6 Suction pressure–displacement curve, for $L/D = 2$, $LI = 0.6$

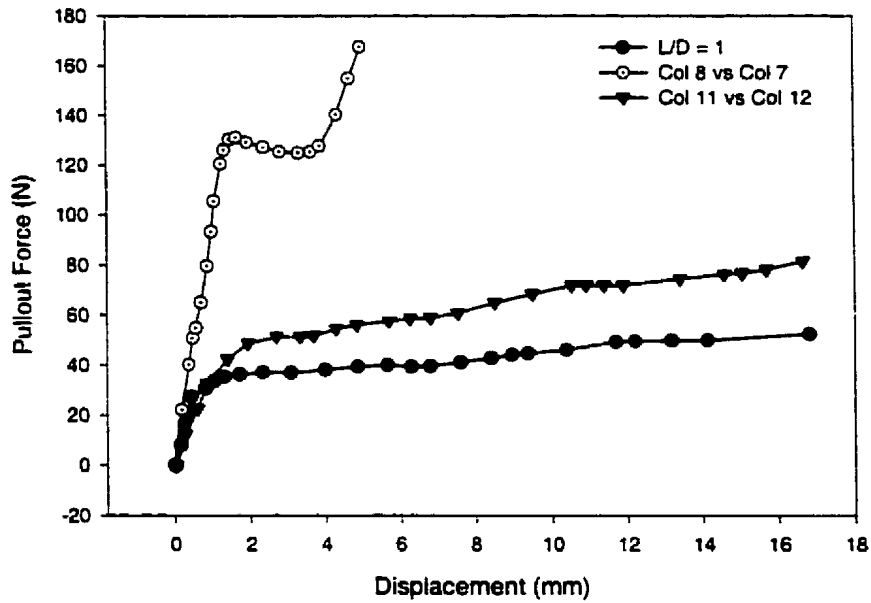


Figure A.5.7 Pullout load–displacement curves obtained from analyses, for $LI = 0.8$

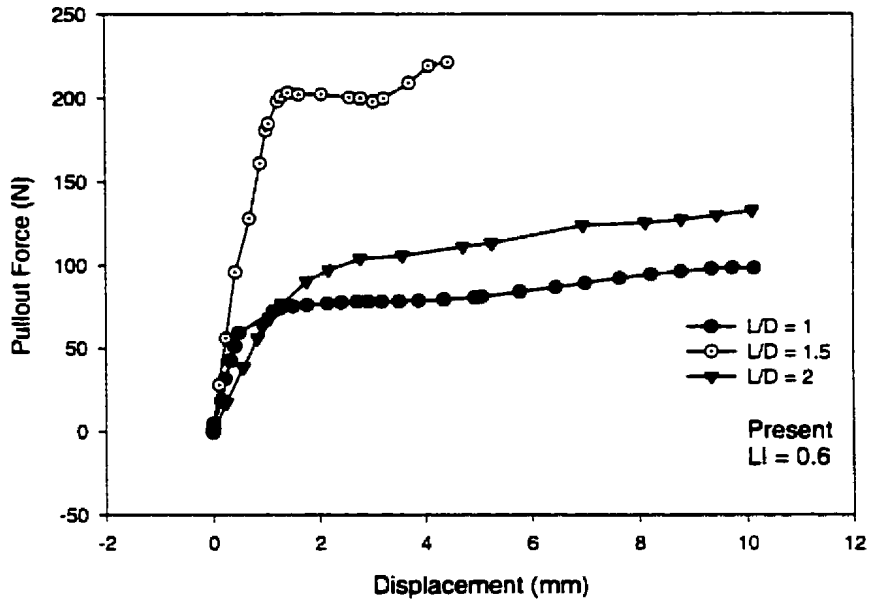


Figure A.5.8 Pullout load–displacement curves obtained from analyses, for LI = 0.6

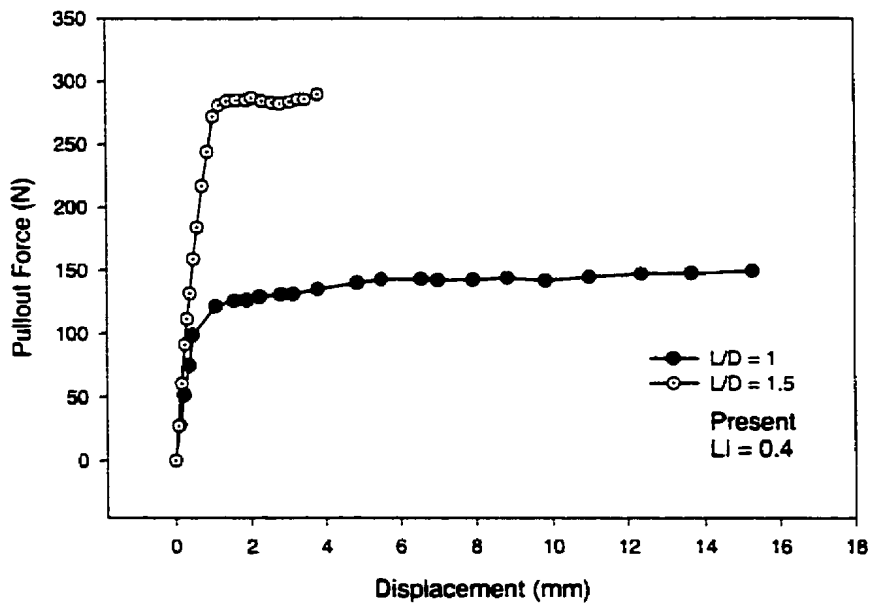


Figure A.5.9 Pullout load–displacement curves obtained from analyses, for LI = 0.4

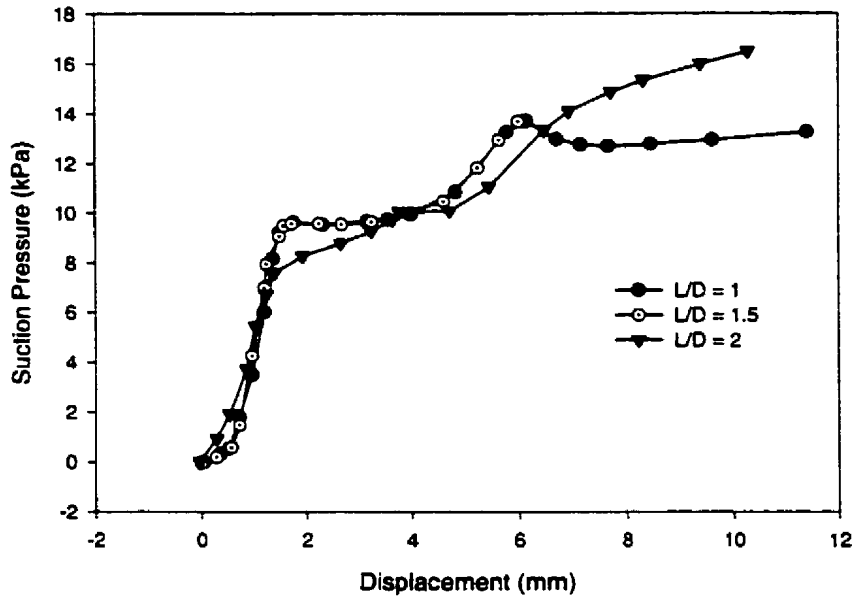


Figure A.5.10 Suction pressure–displacement curves obtained from analyses, for LI = 0.8

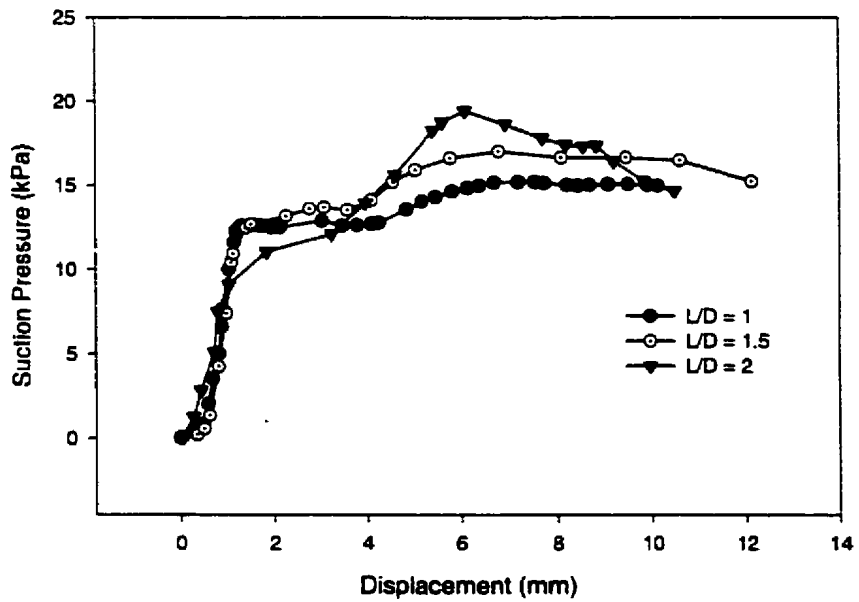


Figure A.5.11 Suction pressure–displacement curves obtained from analyses, for LI = 0.6

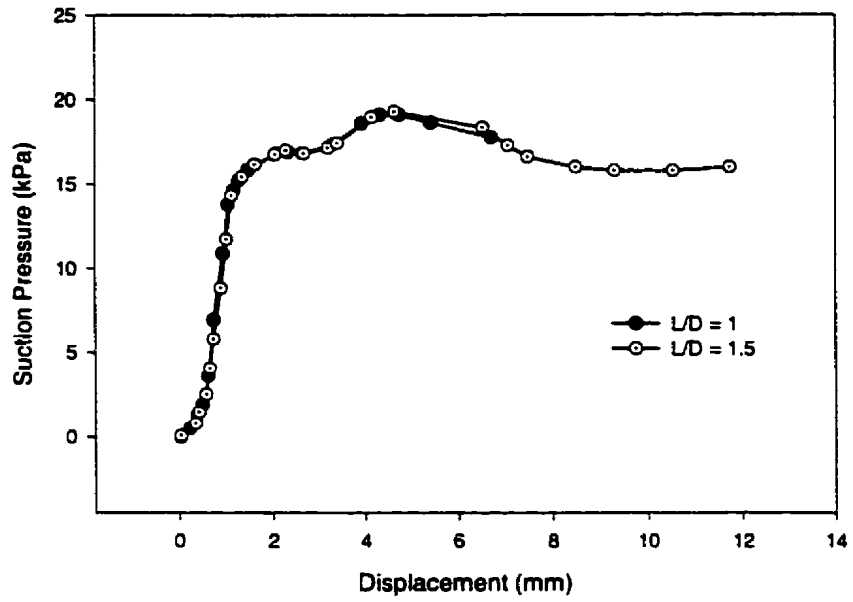


Figure A.5.12 Suction pressure–displacement curves obtained from analyses, for LI = 0.4



